UNSTEADY TURBULENT THERMAL CONVECTION

BY

ROGERIO TADEU DA SILVA FERREIRA

Ing. Mec., Universidade Federal de Santa Catarina, 1970
M.S.M.E., Universidade Federal de Santa Catarina, 1973

THESIS

Submitted in partial fulfillment of the requirements
for the degree of Doctor of Philosophy in Mechanical Engineering
in the Graduate College of the
University of Illinois at Urbana-Champaign, 1978

Urbana, Illinois

ACKNOWLEDGEMENTS

The author wishes to express his sincere appreciation to his advisor and his thesis director, Professor B. G. Jones and Professor R. J. Adrian, respectively, for their invaluable guidance, suggestions and encouragement during the course of this research.

A special note of appreciation should go to Professor W. F. Stoecker for all the arrangements during the enrollment at the University of Illinois and also for his guidance during the first stages of the author's PhD studies.

Gratitude is also expressed to the Conselho Nacional de Desenvolvimento Cientifico e Tecnologico (CNPq), Universidade Federal de Santa Catarina (UFSC) and IBM do Brasil for providing the author's financial support during his doctoral studies.

Finally, the author wishes to thank his children, Rogerio, Fernando and Rodrigo for the happiness they brought to this period of his life, and his wife, Elisabete, whose patience and understanding made this task infinitely easier.

TABLE OF CONTENTS

LIST OF SYMBOLS

A,E	ensemble average of the set of runs
A_m, E_m	mean of the record for one run
a,e	fluctuating signal with respect to A or E
a_m, e_m	fluctuating signal with respect to A_m or E_m
a'_m, e'_m	total signal of one run
a	particle radius
A_s	external area of the sensor
C_p	specific heat at constant pressure
d_f	spacing between fringes
$d_{e^{-2}}$	diameter of the laser beam at e^{-2} points
d_m	transverse dimension of the measurement volume contained in the plane of the axis of the two beams
d_{ph}	diameter of the pinhole
F_u,F_w,F_θ	power spectrum of the horizontal velocity, vertical velocity or temperature signal
f_c	cut off frequency of the filter
g_i	acceleration of gravity vector (0,0,-g)
$\hat{G}_k$	raw estimate of one-sided power spectrum
h	mean heat transfer coefficient
h_m	height of the measurement volume measured perpendicularly to the plane of the axis of the two beams
H_0	mean heat flux through the lower plate
k_i	wave number vector of the i^{th} beam
L	total number of points for power spectrum calculations
l_m	length of the measurement volume contained in the plane of the axis of the two beams

M	magnification of the collecting lens system
mc	capacitance heat mass of the sensor
Nu	Nusselt number
N	total number of points in the record
N_i	total number of points for the i^{th} condition of the conditional average
n	refractive index of the medium
N_{FR}	number of fringes in the measurement volume
N_{ph}	number of fringes in the measurement volume as seen by the photodetector
p'	total pressure minus the mean hydrostatic pressure
p	pressure fluctuation
Pr	Prandtl number
P	mean pressure
Pe	Peclet number
q^2	twice the value of the kinetic energy of the fluctuations per unit of mass
Q_0	kinematic heat flux
$r_{w\theta}$	correlation coefficient of w and θ
R_x^c	circular autocorrelation function
$\overline{R_i}$	conditional average for the i^{th} condition
Ra	Rayleigh number
Re	Reynolds number
$\hat{S}_k$	raw estimate of two-sided power spectrum
S	sensitivity of the fequency-to-voltage converter
T	local value of the mean temperature
T_1	mean temperature

T_1'	total temperature
T_∞	core temperature
T_W	mean temperature at the wall
T_f	fluid temperature
T_{RW}	temperature indicated by the resistance wire
t	time
U	scanning speed
U_i, U_j	mean velocity vector (U,V,W)
u_i', u_j'	total velocity vector (u',v',w')
u_i, u_j	fluctuating velocity vector (u,v,w)
u_p	particle velocity
u_f	fluid velocity
V	settling velocity for the particles
V_X	velocity perpendicular to the fringes
w_*	convective velocity scale
w_0, w_d	conductive velocity scale
$(\overline{w\theta})_0$	kinematic heat flux at the lower plate measured from the records
X_k	Fourier transform of x_n
z^*	total layer depth
z_0, z_d	conductive length scale
α	thermometric conductivity
β	volumetric coefficient of thermal expansion
$\dot{\Phi}$	equivalent input phase noise
Δf_D	e^{-1} bandwidth of the power spectrum of the photocurrent due to transit time broadening
Δt, h	digitization time interval
ε	rate of dissipation of kinetic energy

ε_θ	rate of dissipation of thermal variance
$\varepsilon_{w\theta}$	rate of dissipation of kinematic heat flux
κ	half of the angle between two laser beams
λ	wavelength of the light in the vacuum
λ_{H_2O}	wavelength of the light in water
μ	viscosity of the fluid
ν	kinematic viscosity
ν_D	Doppler frequency
ν_i	frequency of the light of the i^{th} beam
ν_{ij}	frequency of the light scattered from the intersection of the i-j pair of beams
ν_0	frequency of the main beam
ν_c	intermediate carrier frequency
ρ_0	mean density
ρ_f	fluid density
ρ_p	particle density
σ_w	RMS vertical velocity
σ_θ	RMS temperature
σ_u	RMS horizontal velocity
τ	time constant of the probe
θ	temperature fluctuation
θ_*	convective temperature scale
θ_0, θ_d	conductive temperature scale

CHAPTER I

INTRODUCTION

1.1 Statement of the Problem

This is a study of a particular form of thermal convection in which a horizontal layer of water is confined between a heated lower plate and an insulated upper plate and the turbulent Reynolds number is large. The flow can be used to model many aspects of convection in the planetary boundary layer and is perhaps the simplest form of turbulent convection.

Thermal convection is important in atmospheric modeling and also in engineering systems. This work provides direct empirical data on the behavior of such systems. In addition, the data can be used in the development and testing of calculational models of turbulent flows in which buoyant production of energy is significant. The emphasis in the study has been on the structure of turbulent flows, especially measurements of the higher order moments and their relationship to lower order quantities.

Measurements of the local, instantaneous values of the temperature, the vertical velocity and horizontal velocity were performed using a scanning thermocouple probe and a laser Doppler velocimeter. The various terms in the equations for kinetic energy, thermal variance and kinematic heat flux were calculated and flow visualization and conditional averaging techniques were employed to infer certain properties of the active fluid transport mechanisms. Power laws in a possible equilibrium layer were calculated and power spectrum estimates were used to evaluate

the rate of dissipation functions when inertial subranges existed in the wave number space.

1.2 Retrospective Theoretical Analysis

From dimensional analysis, it is found that the non-dimensional heat flux is proportional to Rayleigh number to the 1/3 power, provided that the Prandtl number is irrelevant and that the boundary temperature gradient is independent of the distance between plates. Measurements of Silveston (1958), Globe and Dropkin (1959), Chu and Goldstein (1973) and Goldstein and Chu (1969), support this analysis for $Ra > 10^5$, though a Prandtl number dependence has been found. The same conclusions were obtained by Long (1976), by assuming a buoyancy defect law in the interior of the layer analogous to the velocity defect law in pipe and channel flows.

Theoretical studies of turbulent thermal convection can probably be classified into four categories:

In one category are similarity and mixing length studies in which maximum use is made of experimental results and minimum use is made of the important differential equations. Examples are the similarity theory of Priestley (1954), and mixing length theory of Kraichnan (1962).

The similarity theory of Priestley (1954) predicts that in the region where the direct influence of molecular viscosity is unimportant and the turbulent heat flux is constant with height, and where the effect of an upper boundary is not felt relative to the influence of a lower boundary, the mean temperature gradient has a -4/3 power law and the RMS temperature and vertical velocity fluctuations have a -1/3 and

1/3 power laws respectively. Thomas and Townsend (1957) and Townsend (1959) found a (z^{-2}) dependence for $\partial T/\partial z$ which Bryson (1955)got a ($z^{-3/2}$) profile based on an essentially kinematic analysis of non-entraining symmetric plumes.

Kraichnan's work (1962) is a generalization of the mixing length theory which attempted to explain Prandtl number effects in turbulent thermal convection. The heat flux and vertical profiles of mean temperature, temperature variance and vertical velocity variance are predicted for certain heights and for either large or small Prandtl numbers. The mixing length is taken as the vertical distance from a boundary. Such theories have only limited regions of validity arising from the limited regions where the important assumptions are valid.

In a second category of theories, the hierarchy of relevant non-linear equations describing averaged properties of the turbulence, and containing usually several more unknowns than equations, is closed by suitable assumptions. The theory of Malkus (1954) can be included into this category although the only second order moment equations utilized were those for velocity and temperature variances.

The theory of Malkus sought to provide the magnitude of the heat flux transfer relation and to describe the mean temperature profile for fully turbulent convection. Malkus found a (-2) power law for the gradient of the mean temperature.

Following the same line as Malkus, Howard (1964) solved the variational problem for the heat flux through a horizontally infinite layer of fluid heated from below by maximizing the heat flux subject to

two integral constraints derived from the equations of motion and continuity.

A slight different approach but following the same lines of the second category are the works of Lundgren (1967), (1969). Instead of dealing with moment equations, the equations governing the probability density functions for turbulent velocities in isothermal turbulence were derived. This approach cannot avoid the closure problem, because the equation for f_1 (probability density for velocities at one point) in the flow, contains the two point probability density f_2. Certain class of flows with isothermal turbulence, where dissipation function could be eliminated, had the f_1 equations closed. Generally good results were obtained as pointed out by Adrian (1972).

In a third category are numerical integrations with respect to time of the basic hydrodynamic and thermodynamic equations. Arbitrary initial conditions are imposed and the integration is continued until a statistically steady state is obtained. This approach seems promising if the main interest is with those features of the turbulence which depend most strongly upon the larger scales of the motion. One simplification of this category consists in discarding all non-linear terms in the equations except the vertical transport of horizontally averaged mean temperature and the vertical divergence of large scale eddy heat flux. Following this line are the works of Herring (1963), (1964), (1966), (1969) and Elder (1969).

A second example in this category is the quasi-normal approximation of Millionshchikov (1941), Proudman and Reid (1954) and Tatsumi (1957) in which the fourth order correlations are related to second order

correlations by assuming that velocity is a Gaussian random variable. The quasi-normal approximation leads to the non-physical development of negative energy as pointed out by O'Brien and Francis (1962) and Ogura (1962a), (1962b), (1963).

The clipping approximation of André et al. (1975a), (1975b) is a modification of the quasi-normal approximation which enforces realizability conditions for third order correlations between velocity and/or temperature thereby insuring positive values of energy.

An alternative method which partially avoids the use of a higher order closure technique is the so-called sub-grid theory, Deardorff (1972), in which the closure assumption is less crucial since the grid size is then sufficiently small to allow explicit description of most of the energy containing turbulent structures. This requires a 3-D simulation and the memory capacity of the computer restricts considerably the size of the domain which can be simulated.

In a fourth category the convective plumes are studied separately and with mutual interactions and mixing in a convective field. The study does not start from the hydrodynamic and thermodynamic equations, but sets up the hypothesis that a plume element with a sharp boundary and a statistically uniform interior is an adequate basis for a mathematical description of real convection. Examples of this category are the works by Telford (1967), Turner (1963), (1969), Manton (1975) and many others.

Table 1 presents some of the more important theoretical works in each category of the previous classification that, in some way, followed, contributed or confirmed some of the results in each line.

Table 1

Some of the Works in Each Theoretical Category

I	II	III	IV
Priestley (1953)	Malkus (1954a)	Herring (1962)	Turner (1963)
Priestley (1954)	Malkus (1954b)	Herring (1964)	Telford (1966)
Kraichnan (1962)	Spiegel (1962)	Deardorff (1964)	Telford (1967)
	Townsend (1962)	Deardorff (1965)	Warner and Telford (1967)
	Howard (1964)	Herring (1966)	
	Lundgren (1967)	Herring (1969)	Turner (1969)
	Lundgren (1969)	Elder (1969)	Manton (1975)
	Adrian (1972)	Deardorff (1970)	Manton and Cotton (1977)
	Mellor (1973)	Deardorff (1972)	
	Zeman and Lumley (1976)	Deardorff (1974)	
	Zeman and Tennekes (1977)	Wyngaard and Coté (1974)	
		André et al (1975)	
		Petersen (1976)	

1.3 Experimental Studies

As all theories of turbulent thermal convection have been concerned with statistically steady, horizontally homogeneous convection, it is worthwhile to briefly mention the few pertinent laboratory studies in which the investigators have gone beyond the relatively simple measurements of the mean heat flux. Table II summarizes the measured and calculated quantities and the different features in each experimental study, with respect to the following characteristics:

1. Mean heat flux.
2. Mean temperature profile.
3. Gradient of the mean temperature.
4. RMS of temperature fluctuations.
5. RMS of velocity fluctuations.
6. Kinetic energy budget.
7. Thermal variance budget.
8. Kinematic heat flux.
9. Power laws in the convective layer.
10. Viscous dissipation.
11. Thermal dissipation.
12. Spectral and/or correlation function analysis.
13. Mean density deficit profile
14. Probability density function for temperature signal.
15. Probability density function for velocity signal.
16. Horizontal scales of the flow.

Some of the experimental measurements performed in the atmosphere are reported by Telford and Warner (1964), Lenschow and Johnston

Table 2 - More Significant Laboratory Experimental Works

RESEARCHER YEAR	CHARACTERISTICS 1	2	3	4	5	6	7	8	9	10	11	12	13	14	15	16	ASPECT RATIO	FLUID	TEMPERATURE PROBE	VELOCITY PROBE	TYPE OF CONVECTION
Malkus (1954)	X				X												-	water	-	suspended particles	Rayleigh
Thomas and Townsend(1957)	X	X	X	X								X					5 x 1	air	Resistance Thermometer	-	Rayleigh
Townsend(1958)	X	X	X	X								X					.7 x 1	air	Resistance Thermometer	-	Rayleigh open top
Croft (1958)	X	X	X														-	air	Interferom.	-	Rayleigh heated surface
Globe and Dropkin (1959)	X																-	various	Thermocouple	-	Rayleigh
Townsend(1964)	X	X		X													1 x 1	water	Thermistor	suspended particles	water over ice
Sommerscales & Dropkin (1965)	X	X		X													4 x 1	silicone oils	Thermocouple	-	Rayleigh
Deardorff & Willis (1967)	X			X	X	X	X	X		X	X	X					3 x 1	air	Thermocouple	X-anemom.	Rayleigh
Deardorff and Willis (1967)	X	X	X						X								3 x 1	air	Resistance wire	-	Rayleigh
Deardorff and al. (1969)	X	X															1.5 x 1	water	Resist. wire Thermocouple	-	Unsteady penetrative
Sommerscales & Gazda (1969)	X	X		X													4 x 1	silicone oils	Thermocouple	-	Rayleigh
Adrian (1972) and (1975)		X		X	X			X					X	X	X		1.7 x 1	water	Thermocouple	LDV	water over ice
Caron and Goldstein (1973)	X				X												2 x 1	water	-	LDV	Rayleigh
Chu and Goldstein (1973)	X	X	X						X								1.5 x 1	water	Interferom.	-	Rayleigh
Willis and Deardorff (1974)	X	X		X	X	X	X	X	X	X	X	X					2 x 1	water	Thermocouple	suspended particles	Unsteady penetrative
Carrol (1976)	X	X	X	X								X					3 x 1	air	Thermocouple	-	Rayleigh
Fitzjarrald (1976)	X			X	X			X				X				X	5 x 1	air	Platinum wire	X-anemom.	Rayleigh
Boberg (1976)	X	X	X	X					X								7.5 x 1	water	Thermocouple Resist. wire	-	Unsteady non-penetrative

(1968), Lenschow (1970), Warner (1972), Hall, Edinger and Neff (1975), Benech (1976) and Kaimal et al. (1976). For a variety of reasons, not least of which is the difficulty in performing such measurements, atmospheric data do not correlate very well with laboratory experiments.

1.4 Motivations

This work encompasses the study of the turbulent thermal convection in a layer of water between a large, horizontal, uniformly heated surface and a horizontal, thermally insulating upper plate. The mean temperature of the convective layer increases with time at a constant rate. The investigations concentrated on the properties of a buoyancy driven flow that is generated by a large upward heat flux at the lower boundary and a small or vanishing heat flux at the upper boundary, which is referred as unsteady, non-penetrative convection. Unsteady because the temperature is steadly increasing, non-penetrative because the flow is bounded by rigid surfaces. Although the temperature is unsteady, the dynamics of the flow are steady, that is, the fluctuating moments of the turbulence are statistically stationary in time and (ideally) in horizontal planes.

The motivations for studying such a flow are as follows:

1. The structure of the atmospheric boundary layer can be illuminated by a simplified laboratory model where the boundary conditions could be controlled and the experiment could be repeated as often as necessary in order to obtain good vertical profile resolution and to reduce the experimental uncertainty.

Some of the important applications of this type of flow are:

i) Dispersion of particles in atmospheric pollution.

ii) Formation of clouds.

iii) Prediction of optical information loss generated by the turbulent temperature fluctuations in areas such as solar observation and aerial reconnaissance.

iv) Convection in lakes and oceans.

2. Available data need to be supplemented in order to validate the conjectures and hypothesis of theoretical studies or numerical models. As this is a simple flow, without mean motion, methods of study which fail to predict or explain this simple type of turbulence cannot be expected to explain atmospheric turbulent convection.

3. Despite for the qualitative description of Elder (1969) and Foster (1965) of the structure of the convective elements and the laboratory experiments of Deardorff and Willis (1967), Adrian (1972), Willis and Deardorff (1974) and Fitzjarrald (1976), and the atmospheric measurements of Telford and Warner (1964), Lenschow and Johnston (1968), Lenschow (1970), (1974), Warner (1972), Hall et al. (1975) and Kaimal et al. (1976), it is still unclear how closely unsteady thermal convection in the laboratory can simulate convection in the atmosphere. However, it seems that a method which could adequately describe the important features of parallel convection might be gradually extended to explain much of the atmospheric case.

4. A parallel numerical investigation was carried out by Mr. M. K. Chung (TAM Dept.) and the data was also intended to provide information for his numerical analysis.

5. This experiment was the first step in a series of three basic laboratory experimental configuration:

a) Convection with zero entrainment, b) convection with a finite entrainment, and c) convection under a stable layer. Data from this work will provide basic information to study the more complicated models.

CHAPTER II

GOVERNING EQUATIONS AND SCALING

2.1 Governing Equations

The governing equations follow the Boussinesq approximation as the variations of velocity were small compared with the speed of sound and variations of density were also small compared with the average density.

Following Townsend (1976), the momentum equation is

$$\frac{\partial u_i'}{\partial t} + u_j' \frac{\partial u_i'}{\partial x_j} = - \frac{1}{\rho_0} \frac{\partial p'}{\partial x_i} - \beta g_i \theta + \nu \frac{\partial^2 u_i'}{\partial x_j \partial x_j} , \tag{2.1}$$

The enthalpy equation, neglecting viscous heating, is

$$\frac{\partial T_1'}{\partial t} + u_i' \frac{\partial T_1'}{\partial x_i} = \alpha \frac{\partial^2 T_1'}{\partial x_j \partial x_j} , \tag{2.2}$$

and the continuity equation is

$$\frac{\partial u_i'}{\partial x_i} = 0 , \tag{2.3}$$

where ρ_0 is the mean density of the fluid, ν is its kinematic viscosity, α is the thermometric conductivity, g_i is the gravitational vector $(0,0,-g)$, β is the volumetric coefficient of thermal expansion of the water and p' is the total pressure minus the mean hydrostatic pressure.

Separating the total dependent variables into its mean and fluctuating parts,

$$u_i' = U_i + u_i \ , \tag{2.4a}$$

$$p' = P + p \ , \tag{2.4b}$$

$$T_1' = T_1 + \theta, \tag{2.4c}$$

substituting (2.4a), (2.4b) and (2.4c) into equations (2.1), (2.2) and (2.3), and ensemble averaging, gives

$$\frac{\partial U_i}{\partial t} + U_j \frac{\partial U_i}{\partial x_j} + \frac{\partial}{\partial x_j} \langle u_i u_j \rangle = - \frac{1}{\rho_0} \frac{\partial P}{\partial x_i} + \nu \frac{\partial^2 U_i}{\partial x_j \partial x_j} \ , \tag{2.5}$$

$$\frac{\partial T_1}{\partial t} + U_i \frac{\partial T_1}{\partial x_i} + \frac{\partial}{\partial x_i} \langle u_i \theta \rangle = \alpha \frac{\partial^2 T_1}{\partial x_j \partial x_j} \ , \tag{2.6}$$

$$\frac{\partial U_i}{\partial x_i} = 0 \ . \tag{2.7}$$

The equations governing the fluctuations are obtained by subtracting the equations for the ensemble averages from the instantaneous governing equations

$$\frac{\partial u_i}{\partial t} + U_j \frac{\partial u_i}{\partial x_j} + u_j \frac{\partial u_i}{\partial x_j} + u_j \frac{\partial U_i}{\partial x_j} - \frac{\partial}{\partial x_j} \langle u_i u_j \rangle =$$

$$= - \frac{1}{\rho_0} \frac{\partial p}{\partial x_i} - \beta g_i \theta + \nu \frac{\partial^2 u_i}{\partial x_j \partial x_j} \ , \tag{2.8}$$

$$\frac{\partial \theta}{\partial t} + U_j \frac{\partial \theta}{\partial x_j} + u_j \frac{\partial \theta}{\partial x_j} + u_j \frac{\partial T_1}{\partial x_j} - \frac{\partial}{\partial x_j} \langle u_j \theta \rangle = \alpha \frac{\partial^2 \theta}{\partial x_j \partial x_j} \ , \tag{2.9}$$

$$\frac{\partial u_j}{\partial x_j} = 0 \ . \tag{2.10}$$

Equations for the mean kinetic energy of the turbulent velocity fluctuations and the mean square temperature fluctuations (thermal variance) are obtained by multiplying equations (2.8) and (2.9) by u_i and θ respectively, and ensemble averaging,

$$\frac{\partial}{\partial t}\left(\frac{1}{2}q^2\right) + U_j \frac{\partial}{\partial x_j}\left(\frac{1}{2}q^2\right) + \frac{\partial}{\partial x_j}\left\langle u_j \frac{1}{2}q^2\right\rangle + \langle u_i u_j\rangle \frac{\partial U_i}{\partial x_j} =$$

$$= -\frac{1}{\rho_0}\frac{\partial}{\partial x_j}\langle u_j p\rangle - \beta g_i \langle u_i \theta\rangle + \nu \frac{\partial^2\left(\frac{1}{2}q^2\right)}{\partial x_j \partial x_j} - \varepsilon, \qquad (2.11)$$

where $q^2 = \langle u_i u_i\rangle$,

and

$$\varepsilon = \nu \left\langle \frac{\partial u_i}{\partial x_j}\frac{\partial u_i}{\partial x_j}\right\rangle .$$

The equation for thermal variance is

$$\frac{\partial}{\partial t}\left\langle\frac{1}{2}\theta^2\right\rangle + U_j \frac{\partial}{\partial x_j}\left\langle\frac{1}{2}\theta^2\right\rangle + \frac{\partial}{\partial x_j}\left\langle u_j \frac{1}{2}\theta^2\right\rangle + \langle u_j\theta\rangle \frac{\partial T_1}{\partial x_j} =$$

$$= \alpha \frac{\partial^2\left\langle\frac{1}{2}\theta^2\right\rangle}{\partial x_j \partial x_j} - \varepsilon_\theta , \qquad (2.12)$$

where $\varepsilon_\theta = \alpha \left\langle \frac{\partial \theta}{\partial x_i}\frac{\partial \theta}{\partial x_i}\right\rangle$.

The main assumptions governing the present flow situation are:

i) There is no mean flow inside the layer.

ii) Mean quantities depend only on the vertical direction, that is, the flow is statistically homogeneous in horizontal planes.

iii) There is a statistically steady state in which all moments except the mean temperature are independent of time, aside from slow variations due to the Prandtl number changing with mean temperature.

iv) Ensembles can be formed such that ensemble averages are equivalent to averages over horizontal planes or horizontal lines.

Therefore, equation (2.6) yields

$$\frac{\partial T_1}{\partial t} + \frac{\partial}{\partial z}(\overline{w\theta}) = \alpha \frac{\partial^2 T_1}{\partial z^2}. \tag{2.13}$$

When the statistically steady state is achieved,

$$T_1(t,z) = T(z) + \frac{dT_\infty(t)}{dt}(t-t_0) , \tag{2.14}$$

where T_∞ is the temperature of the core of the fluid layer.

Performing a thermal energy balance on the layer and assuming that the top plate is perfectly insulated

$$Q_0 = \frac{H_0}{\rho_0 C_p} = z^* \frac{dT_\infty}{dt} \tag{2.15}$$

where H_0 is the mean heat flux through the lower boundary of the fluid and z^* is the depth of the layer.

Using equation (2.15) and integrating equation (2.13) with respect to z, one has a

$$\overline{w\theta} - \alpha \frac{dT}{dz} = Q_0\left(1 - \frac{z}{z^*}\right) \tag{2.16}$$

Equation (2.11) for the mean kinetic energy of the fluctuation reduces to

In thermal convection, the major contributor for those pressure fluctuations is the temperature fluctuation effect, which has its main influence close to the lower boundary extending over the conduction layer up to 0.10 z*. Therefore, in analyzing the terms of equations (2.17), (2.18) and (2.19) in the convective region, the terms involving pressure fluctuations will be neglected from the equations, hoping they are small compared to the others.

The kinetic energy equation (2.17) is a balance of transport of turbulent kinetic energy plus turbulent pressure energy by vertical velocity fluctuations, gain of energy through production by the buoyancy forces and transformation of fluctuation energy to heat plus a smaller amount of energy diffusion by the viscous stress fluctuations.

Equation (2.18) represents the balance of the production of mean square temperature fluctuations by turbulent flux of heat along the gradient of mean temperature, the vertical turbulent convection of mean square temperature fluctuations, the diffusion of mean square temperature fluctuations and the destruction of the temperature fluctuations by heat conduction down local temperature gradients.

The rate of change of convective heat flux in equation (2.19) is a balance between transport by the vertical velocity fluctuations, generation due to the vertical velocity fluctuating along the mean temperature gradient, transport of the pressure fluctuations, buoyant generation in the gravitational field and the dissipation by viscous and thermal effects.

2.2 Scaling

In order to correlate data obtained under different conditions, the appropriate scales must be used.

The convective process developed between rigid boundaries show a layered type structure characterized by different scales of length, velocity and temperature. In the region close to the lower plate, molecular transport is important and the temperature gradient shows very high values, on the order of $(-Q_0/\alpha)$. This is referred as the conduction layer. In the central region, molecular transport is unimportant and the buoyancy forces generate energy at a local rate on the order of $\beta g Q_z$ where Q_z is the local convective heat flux. In this so called convective region, the velocity fluctuations reach a maximum, the mean temperature gradient is negligible and the temperature fluctuations are small. The geometry of the boundaries determine the large scales of the flow, and, in particular, the layer depth z_* determines the scale of the turbulent motions.

Deardorff (1970) proposed the following set of length, velocity and temperature scales for the convection layer:

$$z_* \ , \tag{2.21a}$$

$$w_* = (\beta g Q_0 \ z_*)^{1/3} \ , \tag{2.21b}$$

$$\theta_* = Q_0/w_* \ . \tag{2.21c}$$

These scales are derived from dimensional analysis on the assumption that the important external parameters are the flux of buoyancy, $\beta g Q_0$ and the length scale z_* imposed on the large scale

motions by the layer depth. The molecular diffusivities ν and α are excluded on the basis that Reynolds number and the Peclet number are large in the convection layer. There is now considerable evidence to show that Deardorff's convection scales do correlate the turbulence moments in high Reynolds number convection layers after the studies of Willis and Deardorff (1973), Adrian (1975), Fitzjarrald (1976), Boberg (1977) and many others.

Townsend (1959) proposed the following scales for the wall layer region:

$$w_0 = (\beta g Q_0 \alpha)^{1/4} \tag{2.22a}$$

$$z_0 = \alpha / w_0 \tag{2.22b}$$

$$\theta_0 = Q_0 / w_0 \tag{2.22c}$$

The assumptions underlying the development of these scales are that the wall layer is independent of z^*, but dependent on $\beta g Q_0$ and the thermal diffusivity α. Townsend's scales are not the only possible scales for the wall layer. In fact, when the Prandtl number is different from unity there are an infinite number of scales that can be defined by multiplying the factor α in equation (2.22a), (2.22b) and (2.22c) by various powers of Pr. For example, Kraichnan (1962) defines a set of viscous scales by replacing α with ν in equations (2.22a-c). Also Chung (1978) has shown that the following mixed diffusion scales can be used to correlate mean temperature profiles for various fluids with Prandtl numbers greater than 0.7:

$$w_d = (\beta g Q_0 \alpha^2 / \nu)^{1/4} \tag{2.23a}$$

$$z_d = \alpha/w_d \tag{2.23b}$$

$$\theta_d = Q_0/w_d \tag{2.23c}$$

There exist in the literature numerous sets of wall layer scales that are defined differently from those cited above, as reported in Kraichnan (1962), Sommerscales and Gazda (1969), Chu and Goldstein (1973), Fitzjarrald (1976), but they are often essentially, albeit indirectly, related to w_0, θ_0, z_0 by simple factors of Prandtl number to some power.

Kraichnan's (1962) analysis and recent work by Adrian and Chung (1978) suggested that in addition to the w_0, θ_0, z_0 scales, at least two other sets of molecular scales, the viscous scales and the mixed diffusion scales may be needed to describe completely all of the sublayer regions of the wall layer. Thus, a full understanding of the wall layer may require a complicated analysis of the data. However since the present experiments deal primarily with the convective layer, and moreover, since they are performed at nearly constant Prandtl number, it will suffice to use w_0, z_0, θ_0 to characterize the wall layer.

It is customary to use the Rayleigh number

$$Ra = \frac{\beta g z^3 \Delta T}{\alpha \nu} \tag{2.24}$$

the Prandtl number

$$Pr = \nu/\alpha \tag{2.25}$$

and the Nusselt number

$$Nu = \frac{Q_0 z^*}{\alpha \Delta T} \tag{2.26}$$

to describe the state of convection over horizontal surfaces. However, since the Rayleigh number is more pertinent to the stability problem than to the dynamics of buoyancy driven turbulence, it has been suggested by Adrian (1975), that a more appropriate parameter would be the turbulent Reynolds number

$$Re_* = \frac{w_* z_*}{\nu} \tag{2.27}$$

and the Prandtl number, or equivalently the turbulent Reynolds number and the turbulent Peclet number

$$Pe_* = \frac{w_* z_*}{\alpha} \tag{2.28}$$

The relationship between these parameters are:

$$w_* = \frac{\alpha}{z_*} (PrRaNu)^{1/3} , \tag{2.29}$$

$$\theta_* = \Delta T \left(\frac{Nu^2}{RaPr}\right)^{1/3} , \tag{2.30}$$

$$Re_* = \frac{(RaNu)^{1/3}}{Pr^{2/3}} . \tag{2.31}$$

Using the empirical relationship $Nu \propto Ra^{1/3}$, one sees that $Re_* \propto Ra^{4/9}/Pr^{2/3}$.

The relationship between the convection layer scales and the conduction layer scales are

$$\frac{z_*}{z_0} = (Re_* Pr)^{3/4} \tag{2.32a}$$

$$= (NuRaPr)^{1/4} \tag{2.32b}$$

$$\frac{w_*}{w_0} = (Re_* Pr)^{1/4} \tag{2.33a}$$

$$= \left(\frac{z_*}{z_0}\right)^{1/3} \tag{2.33b}$$

$$= (NuRaPr)^{1/12} \tag{2.33c}$$

$$\frac{\theta_*}{\theta_0} = (Re_* Pr)^{-1/4} \tag{2.34a}$$

$$= \left(\frac{z_*}{z_0}\right)^{-1/3} \tag{2.34b}$$

$$= (NuRaPr)^{-1/12} \tag{2.34c}$$

A number of useful results can be obtained by examining the dimensionless governing equation in this limit of asymptotically large turbulent Reynolds number and Peclet number. In this limit, equation (2.32a) imples that $z_0 \ll z_*$.

Using the molecular scales to non-dimensionalize equation (2.16) one gets

$$\overline{\theta_m w_m} - \frac{dT_m}{dz_m} = 1 - Pe_*^{-3/4} z_m \tag{2.35}$$

where $\theta_m = \theta/\theta_0$, $w_m = w/w_0$ and $z_m = z/z_0$.

In the limit when Pe_* is large enough and $z_m = O(1)$ (very close to the lower wall):

$$\overline{\theta_m w_m} - \frac{dT_m}{dz_m} = 1 \tag{2.36}$$

Hence, in the wall layer, the total heat flux is essentially constant and the mean temperature must obey the following law of the wall:

$$\frac{T_w - T}{\theta_0} = f(z/z_0) \tag{2.37}$$

where f is a universal function and T_w is the wall temperature.

Similarly, using convective scales, yields

$$\overline{\theta_c w_c} - \frac{1}{Pe_*}\frac{dT_c}{dz_c} = 1 - z_c \tag{2.38}$$

where $\theta_c = \theta/\theta_*$, $w_c = w/w_*$ and $z_c = z/z_*$. In the limit when Pe_* is large enough and $z_c = O(1)$

$$\overline{\theta_c w_c} = 1 - z_c \tag{2.39}$$

This equation states that the convective heat flux is linearly decreasing in the layer and the conductive heat flux is $O(Pe_*^{-1})$ outside the wall region.

Since all the terms in (2.39) depend only on z_c, the following "law of the core" can be stated:

$$\frac{T - T_\infty}{\theta_*} = g(z/z_*) \quad \text{for } z_c = O(1), \tag{2.40}$$

where g is a universal function within a given class of flows and T_∞ is the nearly constant temperature in the convection layer.

The large difference between the length scales z_* and z_0 in the limit $Re_* \to \infty$ is reminiscent of a singular perturbation problem and suggests the use of asymptotic matching techniques as suggested by Adrian (1977). Less mathematically, there should exist a matching layer between the low Reynolds number in the conduction layer and the high Reynolds number in the convection layer in which the turbulent motions make an adjustment from the very small length z_0 and the much larger length scale z_*. This layer should exist for heights such that $z_0 << z << z_*$. The structure is very similar to that in turbulent boundary layers wherein the log law region provides a matching between the viscous wall layer and the outer wakelike layer as presented in White (1974).

Adrian (1977) has shown that in thermal convection the Priestley similarity laws can be obtained by requiring the gradient of the mean temperature profiles given by equations (2.37) and (2.40) to match for arbitrary large values of Re_*Pr.

The gradient matching gives

$$\frac{dg}{dz_c} = - \left(\frac{z_*}{z_0}\right)^{4/3} \frac{df}{dz_m} \tag{2.41}$$

where $(z_*/z_0)^{4/3} = Re_*Pr$ from equation (2.32a). In order to achieve matching independent of Re_*Pr, equation (2.41) must be rearranged to read

$$\left(\frac{z}{z_*}\right)^{4/3} \frac{dg}{dz_c} = - \left(\frac{z}{z_0}\right)^{4/3} \frac{df}{dz_m} = \frac{1}{3} C \tag{2.42}$$

where C is a constant. Therefore,

$$g = - C z_c^{-1/3} + A , \tag{2.43a}$$

$$f = C z_m^{-1/3} + B . \tag{2.43b}$$

The gradient matching technique can also be extended to other moments of the velocity and temperature fields. For the RMS vertical velocity, σ_w and the RMS temperature σ_θ.

Adrian (1977) obtained the Priestley power laws,

$$\sigma_\theta = C_\theta \theta_* (z/z_*)^{-1/3} + \text{const.} \tag{2.44a}$$

$$= C_\theta \theta_0 (z/z_0)^{-1/3} + \text{const.} \tag{2.44b}$$

and

$$\sigma_w = C_w w_* (z/z_*)^{1/3} + \text{const.} \tag{2.45a}$$

$$= C_w w_0 (z/z_0)^{1/3} + \text{const.} \tag{2.45b}$$

CHAPTER III

DESCRIPTION OF THE FACILITIES, EXPERIMENTAL PROCEDURES AND DATA ANALYSIS

3.1 Description of the Facilities

3.1.1 Test Section

The test section was a box filled with water, heated from below with insulating side walls and upper boundary c.f. Figure 3.1. The main points to be achieved by the test section were:

a) Aspect ratio of infinity, i.e., negligible effects of the lateral walls in generating mean flow circulations.

b) Uniform temperature of the lower plate, or inexistence of cold and hot spots that could generate recirculating cells.

c) A constant mean heat flux through the lower plate.

d) Negligible heat losses through the top and side walls of the test section.

e) Parallel and horizontal plates.

The accomplishment of those requirements would reinforce the validity of the hypothesis of horizontal homogeneity in the flow.

There existed a compromise between a deep convective layer of fluid, that would produce high values of Reynolds number, with a favorable width-height aspect ratio that would avoid any influence of the lateral walls on the flow. The minimum aspect ratio employed in the present experiments was 7.2 x 1, a much higher value than other laboratory thermal convection experiments.

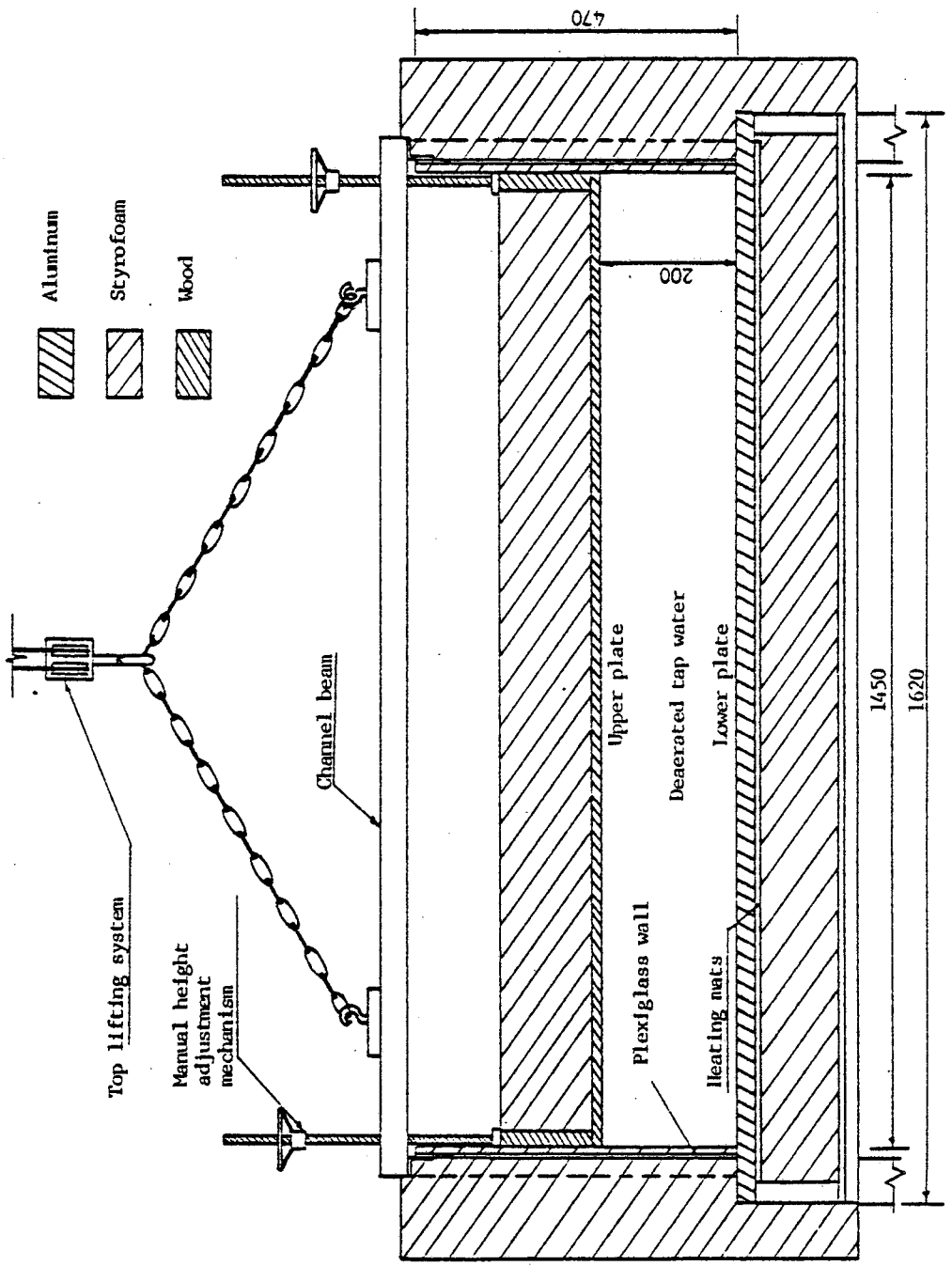

Figure 3.1 - Cross section of the test section. Dimensions in mm.

Boberg (1977) conducted tests to check the magnitude of surface temperature variations over the entire lower boundary using a chromel-constatan thermocouple probe. A maximum value of 0.5^{o} C peak-to-peak was observed and from this, at least 50% was due to the fluid-lower plate interactions, in the form of time variations. The standard deviation of the multipoint temperature measurements at the upper surface of the aluminum lower plate averaged 0.09^{o} C while the surface-to-mixed layer temperature difference had an average value of 2^{o} C.

Calibration tests to determine the heat flux through the lower boundary by measuring the rate of the temperature rise in the convective region showed a constant slope after the warm-up period (first 15-20 minutes) indicating a constant supply of heat flux with respect to time. The heater stability was monitored by checking the Thermac voltage before and after each set of runs. By set it is understood the group of individual runs at a certain height from the lower plate, a certain heat flux and a certain layer thickness.

Measurements of the heat losses through the top and side walls done by Boberg (1977) and measurements of the mean temperature profile in the water close to the upper plate indicated less than 5% heat loss through the boundaries for the worst situation.

The lower and upper plates are parallel within 1.5 mm or at most 1.25% of the layer depth. The mean slope of the upper plate due to warpage is 0.021 to 1.

Therefore, based on those evaluations, the test section was found adequate to produce data comparable with the theoretical assumptions.

The test section consisted of a 162 cm x 152 cm x 2.5 cm lower aluminum plate, two plane 10 mm thick glass front and back walls and two 6 mm thick plexiglass side walls of 47 cm height. The interior dimensions of the test section were 150 cm x 145 cm - length x width.

The upper plate was constructed of wood and plywood and filled with 15 cm thick slabs of styrofoam. Two U-shaped steel bars resting on the side walls held the upper plate in position. By rotating four threaded long rods the top could be adjusted to produce the necessary depth in the horizontal layer of deaerated tap water and keep it parallel to the lower plate as well.

Both lower and upper plates were painted with Pratt and Lambert Yellow Palgard epoxy paint. Due to the adverse environment of water and relatively high temperatures, the lower plate showed some imperfections in the paint due to plate roughness and dirty particles. Fortunately those defects were not concentrated in certain regions nor encountered too often that would change the conditions of the lower plate to a rough surface. The effect of the roughness was considered negligible as the maximum height of the surface irregularities was of the order of 25 μm.

Due to the constant contact with the water, the upper plate warped slightly, showing 1.5 mm difference between the heights from the lower plate measured in the center and close to the lateral walls.

All lateral walls were externally insulated by 15 cm thick panels of styrofoam and the plexiglass walls were insulated by 2.5 cm thick plates of styrofoam on the interior sides in order to minimize lateral heat transfer. A thin window 10 cm x 120 cm - height x length, was

cut in the external styrofoam panel of the front glass wall to provide access for the laser beams and collection of the scattered light. The upper plate had a 80 cm x 2 cm slot situated 42 cm from the front glass wall which was used to insert the thermocouple probe into the fluid in order to measure the temperature fluctuations during the scans and a circular hole ϕ2 cm used to introduce the mercury-in-glass thermometer to measure the mean core temperature of the layer.

In order to avoid reflections of the light at the glass water interface of the back wall, a thin curtain of black plastic was hung from the upper plate down to the lower plate.

The thermal energy to the test section was supplied by nine 50 cm x 50 cm Ohmweave, 40Ω nominal, electrically insulated heating mats in parallel arrangement. As measured by Boberg (1977), the mats showed a mean resistance of 38.46Ω $\pm$ 0.22Ω at 25° C and an equivalent value of 4.0Ω when connected in parallel. The mats were positioned directly below the lower plate and insulated underneath with 15 cm slabs of styrofoam in order to increase the efficiency of the heating process. The power controller used to supply the heating mats was a RI Research, Inc., Thermac model 5212 with an output voltage controlled up to 165 V that corresponded to a maximum heat flux of 2.6 kW/m^2. A thermistor probe series 400 and a proportional controller Versa-Therm model 2156 produced by Cole-Parmer Instrument Co. were used to shut the power down when the test section achieved its maximum design temperature of 43° C.

Four jack screws were used to adjust the lower plate to a horizontal plane to within 0.03° of horizontal by measuring the water layer depth at each corner.

3.1.2 Temperature Measurements

3.1.2.1 Vertical Temperature Profile

The mean temperature of the fluid at different heights was measured utilizing a teflon coated Alumel wire (Omega Engineering, Inc.) strung across a stainless steel ring as shown in Figure 3.2. The wire had the following characteristics: length = 3200 mm, diameter of wire = 0.0762 mm, thickness of the insulation = 0.0762 mm, resistance = 188 ohms at 25° C, sensitivity = 0.370 ohm/°C. A Wheatstone bridge amplifier was used to convert the resistance variations with temperature into voltage. All the measurements were performed with a fixed gain of 200 and a cut off frequency of 100 Hz. The combined probe and bridge amplifier sensitivity was 2.28 °C/V, obtained by calibration. The time constant of the resistance wire was 228 ± 24 ms for a vertical scan rate of 0.478 cm/s in water.

3.1.2.2 Instantaneous Temperature

The thermocouple probe used to measure the fluctuating temperature signal was constructed from a Omegaclad Chromel-Constantan duplex wire (Omega Engineering Inc.). The hot junction was spot welded. The characteristics of the probe were: resistance = 440 ohms at 25° C, diameter of wires = 0.0381 mm, sheat material = type 304 stainless steel, sheat diameter = 0.254 mm. Figure 3.3 shows the upper plate and the lower plate probes.

The reference junction was established in the ambient room air because only the rapid fluctuating part of the temperature signal was of interest.

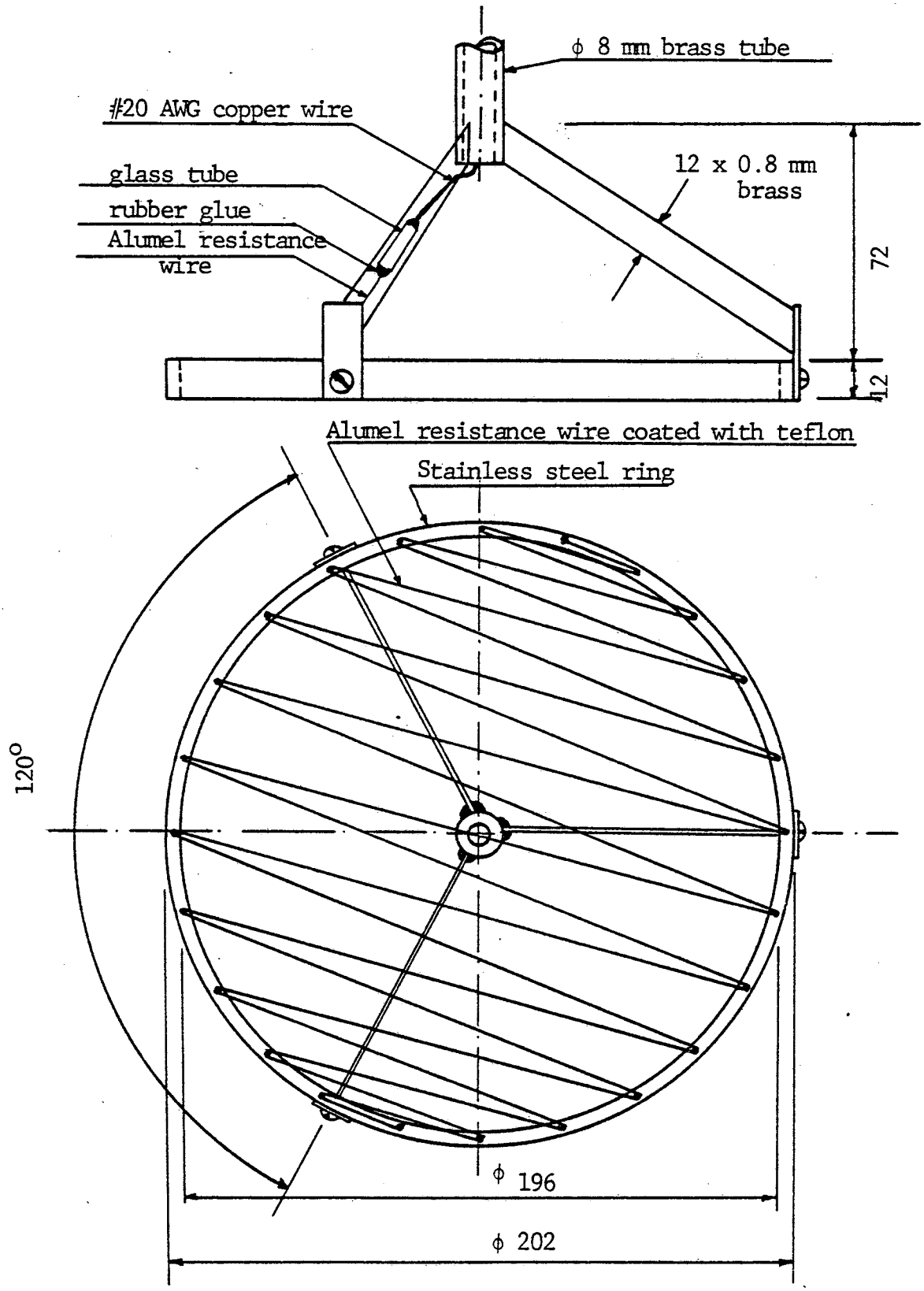

Figure 3.2 - Mean temperature probe. Dimensions in mm.

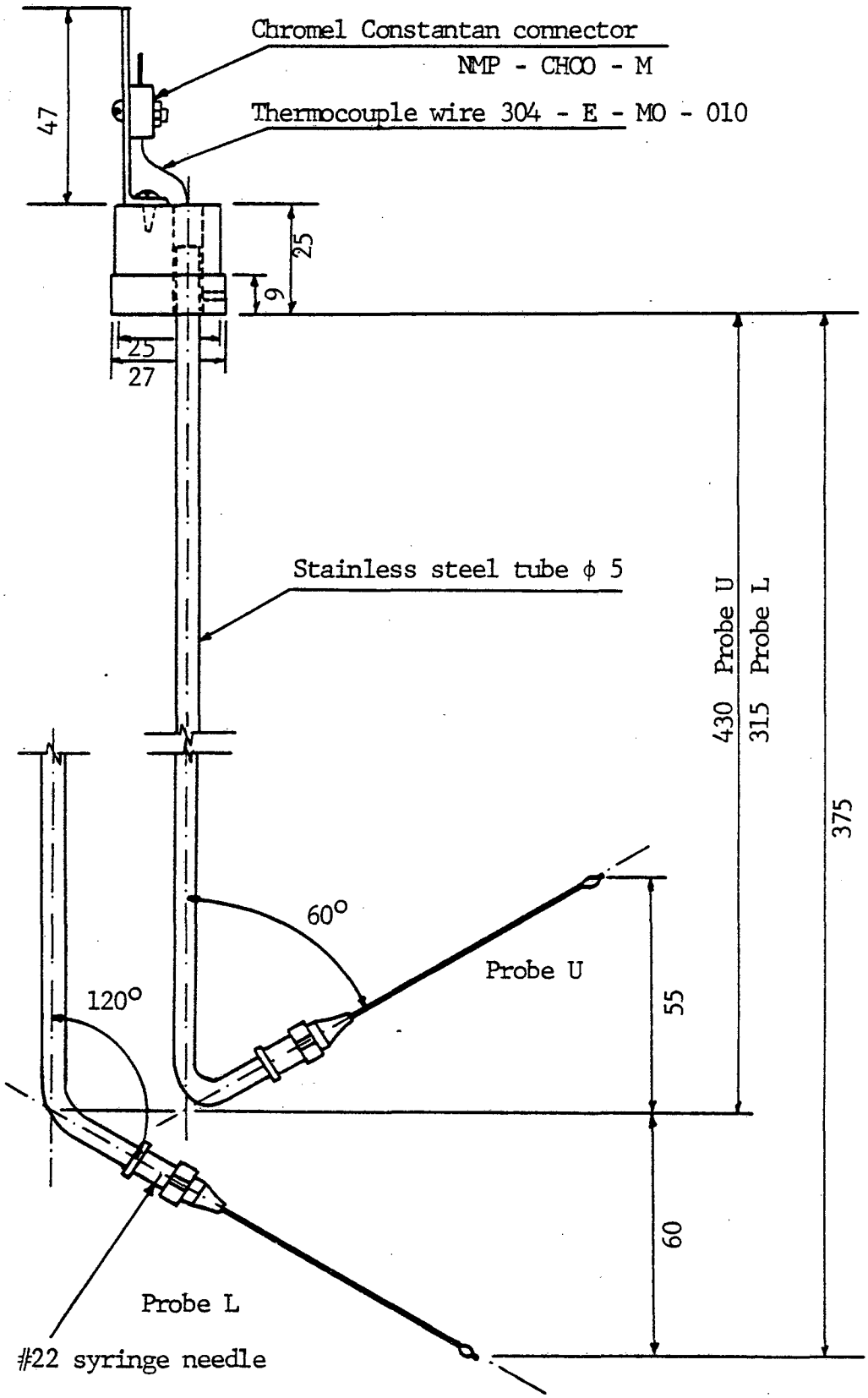

Figure 3.3 - Thermocouple probes. Dimensions in mm.

The amplifier used was an Ectron 560 operating with a gain of 1000, AC mode, i.e., the input signal is capacitively coupled with a time constant of 31.83 s ± 0.64 s, and a cut off frequency of 100 Hz. The time constant of the thermocouple was 3.2 ms ± 0.3 ms for a scan rate of 0.478 cm/s, corresponding to 49.7 Hz. As the scanning speed used in the experiments was 5 times that of for calibration, it was expected a frequency response for the probe greater than 50 Hz. The sensitivity of the amplifier probe was 16.15 ^{o}C/V in the range of 25 to 45^{o} C.

3.1.2.3 Core Temperature

The test section core temperature was measured with a mercury-in-glass thermometer Sargent model S-80 210-B with an accuracy up to 0.05^{o}C. Those measurements were taken before and after each set of runs at certain conditions. The mean core temperature was used to evaluate the physical properties of the fluid.

The kinematic heat flux through the lower boundary was calculated by measuring the core temperature variation with time. The curves presented in Figure 3.4 are ensemble averages of three different runs each one.

As can be easily seen, an energy balance over the whole layer produces

$$Qo = z^{*} \frac{dT_{\infty}}{dt} \qquad (3.1)$$

for the steady state condition in which dT_{∞}/dt is constant.

For the same setting in the power supply of the heating mats, $z^{*}\ dT_{\infty}/dt$ should be constant for different layer depths.

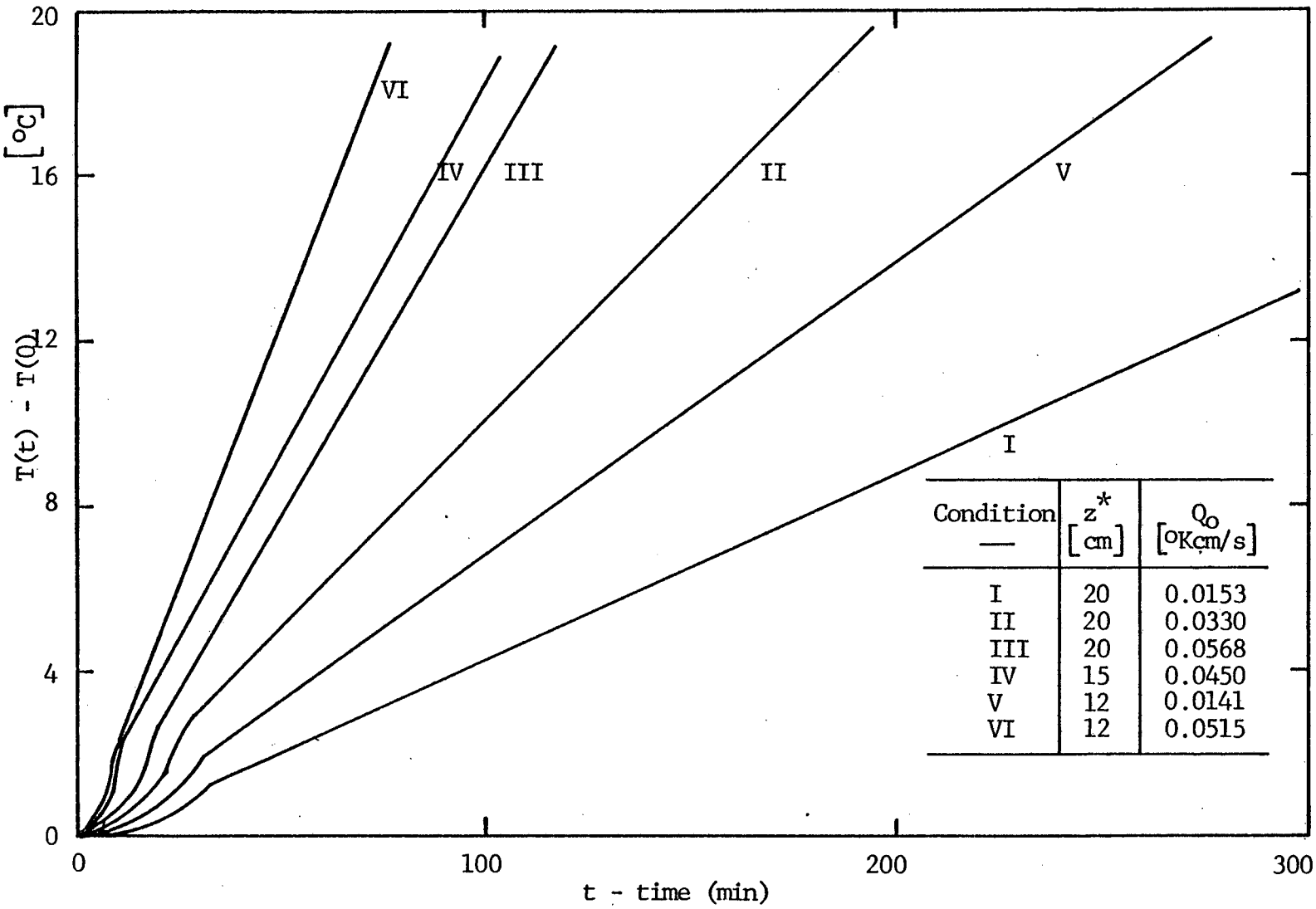

Condition	z^* [cm]	Q_o [°Kcm/s]
I	20	0.0153
II	20	0.0330
III	20	0.0568
IV	15	0.0450
V	12	0.0141
VI	12	0.0515

Figure 3.4 - Kinematic heat flux calculation.

Measurements with 20 cm and 12 cm layer depths were generally consistent with this situation but z^* dT_∞/dt was approximately 10% lower in the latter case.

In order to see if the slot in the upper plate was producing cold region in the water layer, the heating experiments were run with the thermometer placed under the slot. The resulting kinematic heat fluxes were reproduced within 1% of the values obtained with the thermometer far from the slot.

3.1.3 Velocity Measurements

The u and w components of the instantaneous velocity were measured with a two component, fringe mode, laser Doppler velocimeter. When two coherent waves intersect, they interfere to generate fringes in the volume defined by their intersection. The plane of the fringes is perpendicular to the plane of the intersecting beams and parallel to the line bisecting the angle between the beams. A particle passing through this volume with a certain velocity V will alternately cover and uncover bright and dark fringes. When the light scattered from such a particle is observed in any direction, its intensity will oscillate sinusoidally with a frequency equal to the component of the velocity perpendicular to the fringes V_x divided by the fringe spacing.

The spacing d_f between these fringes is given by

$$d_f = \frac{\lambda}{2} \frac{1}{\sin \kappa} \tag{3.2}$$

Where λ is the wavelength of the light in the fluid and 2κ is the angle between the beams.

The frequency shift is given by

$$\nu_D = 2 \frac{V_x}{\lambda} \sin \kappa \qquad (3.3)$$

The geometry of the illuminating beams in the present fringe mode LDV is the three beam configurations reported in Adrian (1975) and shown in solid lines in Figure 3.5. The frequency of the beams ν_1, ν_2 and ν_3 were different, but all beams were plane polarized in the same direction, resulting in three distinct signals from the interference fringe patterns produced by each pair of beams.

The light scattered from a stationary particle residing at the intersection of a pair of beams with frequencies ν_1 and ν_2, would consist of a wave of frequency ν_1 and another at frequency ν_2. The mixing of the waves at a photodetector then produced a sinusoidal photo-current having frequencies $(\nu_2 - \nu_1)$ and a positive or negative motions of the particle appeared as positive or negative Doppler shift relative to $(\nu_2 - \nu_1)$. The frequency ν_1 was the characteristic frequency ν_o of the laser light (583×10^{12} Hz) and this beam will be called main beam hereafter. The frequencies ν_3 and ν_2 of the other two beams were obtained from the main beam by using an accousto optic modulator or Bragg cell which shifted the main beam to 30 and 40 MHz , respectively, and generated the so-called 30 and 40 MHz beams.

From the standard Doppler shift formula, and reported by Adrian (1975), the signal frequencies were given by

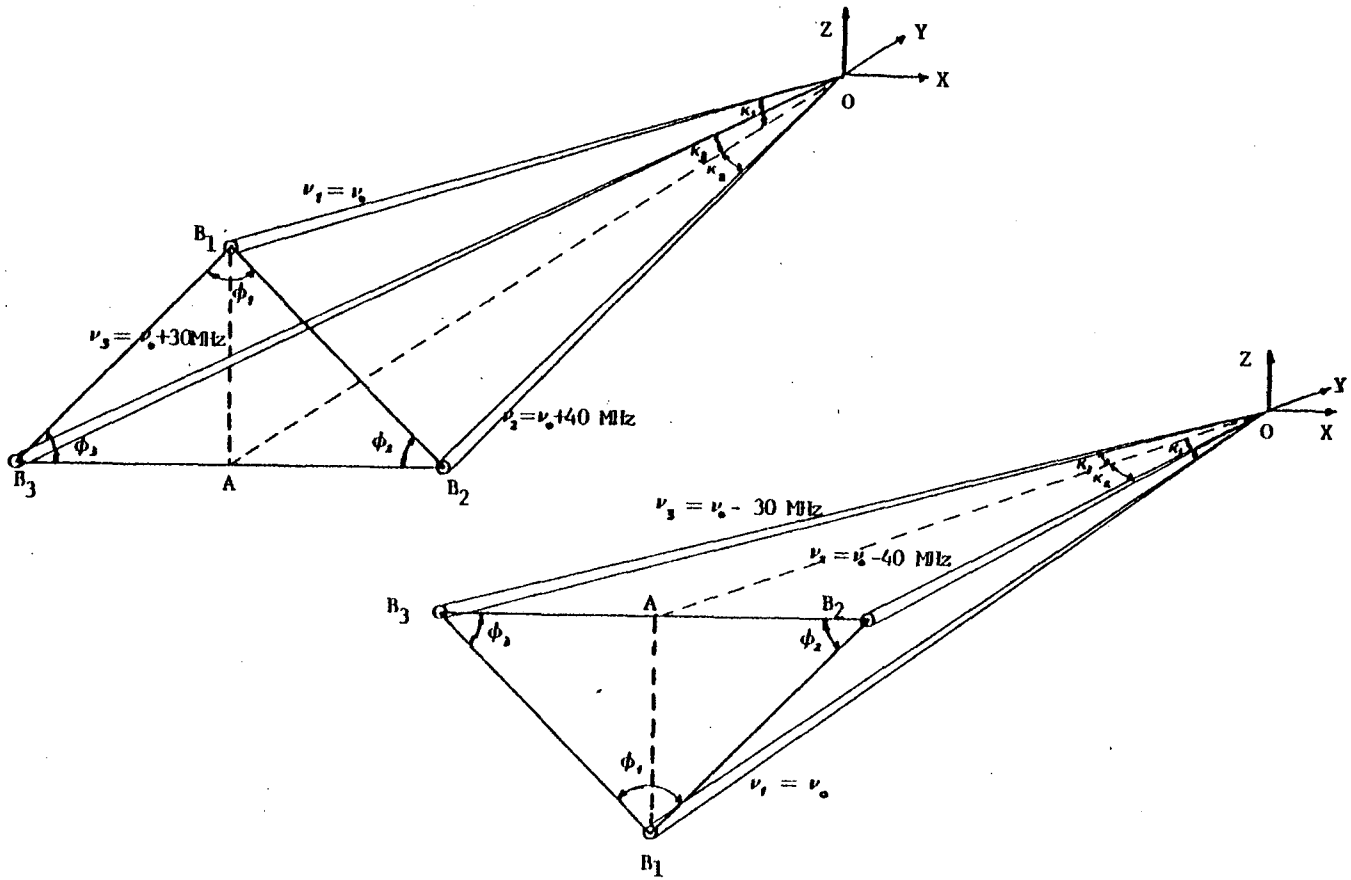

Figure 3.5 - Beams geometry for measurements close to the lower and upper plates.

$$\nu_{21} = \nu_2 - \nu_1 - \underset{\sim}{u} \cdot (\hat{k}_2 - \hat{k}_1) \tag{3.5a}$$

$$\nu_{31} = \nu_3 - \nu_1 - \underset{\sim}{u} \cdot (\hat{k}_3 - \hat{k}_1) \tag{3.5b}$$

$$\nu_{23} = \nu_2 - \nu_3 - \underset{\sim}{u} \cdot (\hat{k}_2 - \hat{k}_3) \tag{3.5c}$$

where $\underset{\sim}{u} = (u, v, w)$ is the vector velocity of the fluid and k_i is the wave number vector of the i^{th} beam ($| k_i | = \lambda^{-1}$), and ν_{ij} is the frequency of the signal derived from the i-j pair of beams. When $\kappa_1 = \kappa_2 = \kappa_3 = \kappa$, as shown on Figure 3.5, the frequencies are given by

$$\nu_{21} = \nu_2 - \nu_1 + \frac{\sin \kappa}{\lambda} (u - w) \tag{3.6a}$$

$$\nu_{31} = \nu_3 - \nu_1 + \frac{\sin \kappa}{\lambda} (-u - w) \tag{3.6b}$$

$$\nu_{23} = \nu_2 - \nu_3 + 2 \frac{\sin \kappa}{\lambda} u \tag{3.6c}$$

By summing and subtracting ν_{21} and ν_{31}, the normal components, u and w, could be calculated.

The light source was an Argon Ion laser (Coherent Radiation Model CR-2) which nominally produced 1500 mW multimode and 600 mW in the single frequency mode at 514.5 nm. The laser power decreased with age. The best output power of the laser was achieved at the beginning of the experiment being 750 mW multimode and 300 mW single mode at 514.5 nm. Fifty percent of this power reached the measurement volume. As the collection of the light was made in off-axis back scatter mode, (30^{o} with respect to the y-axis as shown in Figure 3.6), high power was needed to

produce adequate SNR (signal-to-noise ratio) therefore the single frequency mode operation of the laser was abandoned. At the end of the experiment the output power of the laser was 380 mW multimode.

Details of the optical system and a functional diagram of the signal processing system are shown in Figures 3.6 and 3.7 respectively.

As previously mentioned the 30 and 40 MHz beams were generated by diffraction in a Bragg cell (Zenith M40-R) that was driven by the sum of sinusoidal outputs of separated 30 MHz and 40 MHz quartz crystal oscillators. The Bragg cell was oriented at an angle that was intermediate to the Bragg angles for these frequencies (4.05 mrd for the 30 MHz and 5.4 mrd for the 40 MHz), and its output consisted of the undiffracted main beam at frequency ν_o, two primary diffracted beams, 30 and 40 MHz beams, with frequencies $30 + \nu_o$ MHz and $40 + \nu_o$ MHz respectively, and a series of much weaker diffracted beams spaced at 10 MHz intervals. The intensity of the three primary beams were not equalized because the RF power amplifier (Larkton MP-100) did not have enough gain (only 10 dB). The power of each one of the shifted beams was approximately 50% of the main beam.

As the angle between adjacent beams is about 1.25 mrd for a 10 MHz spacing, long path lengths were needed to separate the beams spatially. A 622 mm lens Lo, placed ahead of the Bragg cell and a set of apertures A_1, located at the focal plane of Lo separated the three beams from the subsidiary diffracted ones. The beams separator is located 762 mm away from the spacial filter which permitted adequate beam isolation. The beams are then recollimated by 865 mm lenses L_1, L_2 and L_3 and

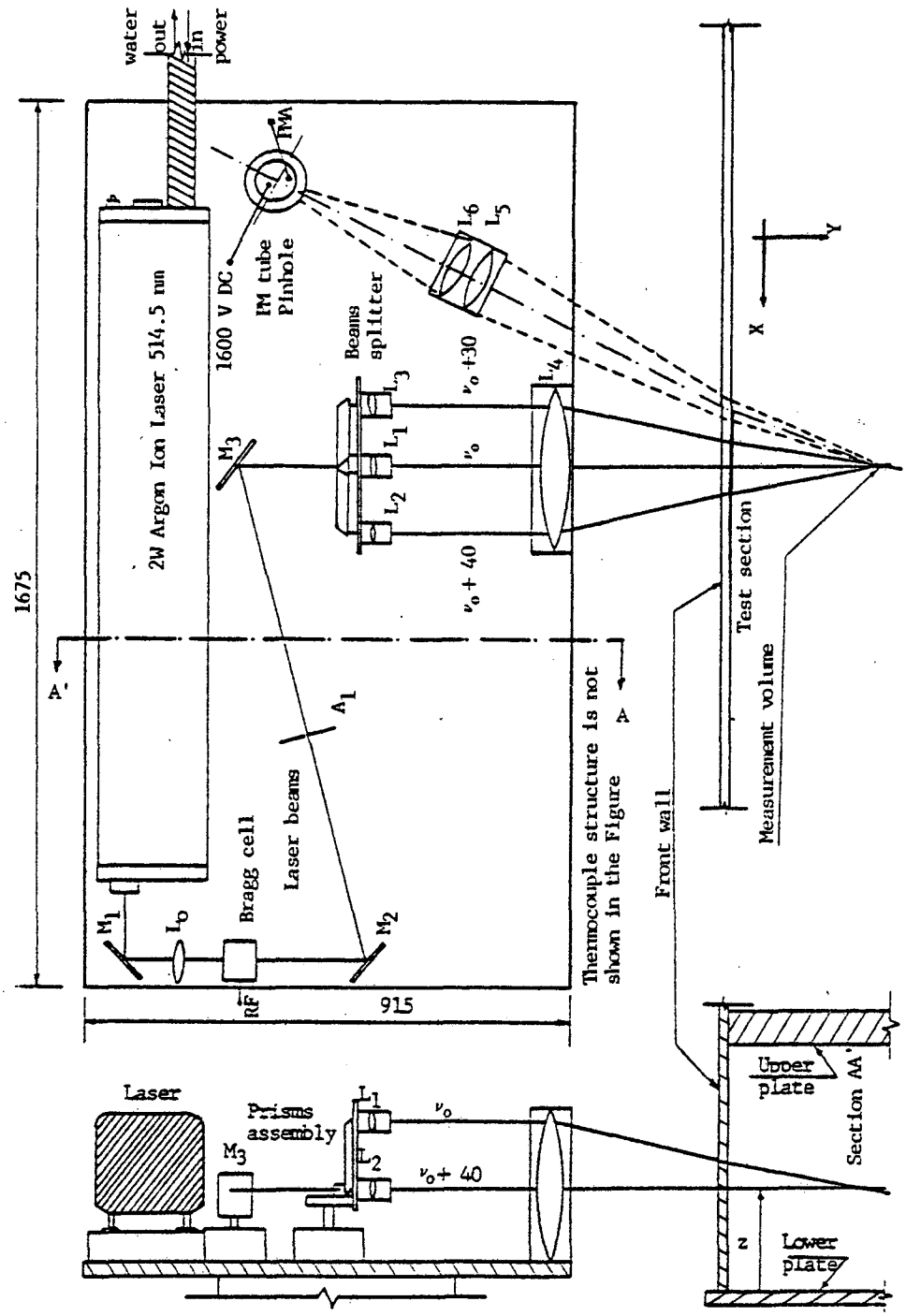

Figure 3.6 - Scanning table with optical components. Not in scale.

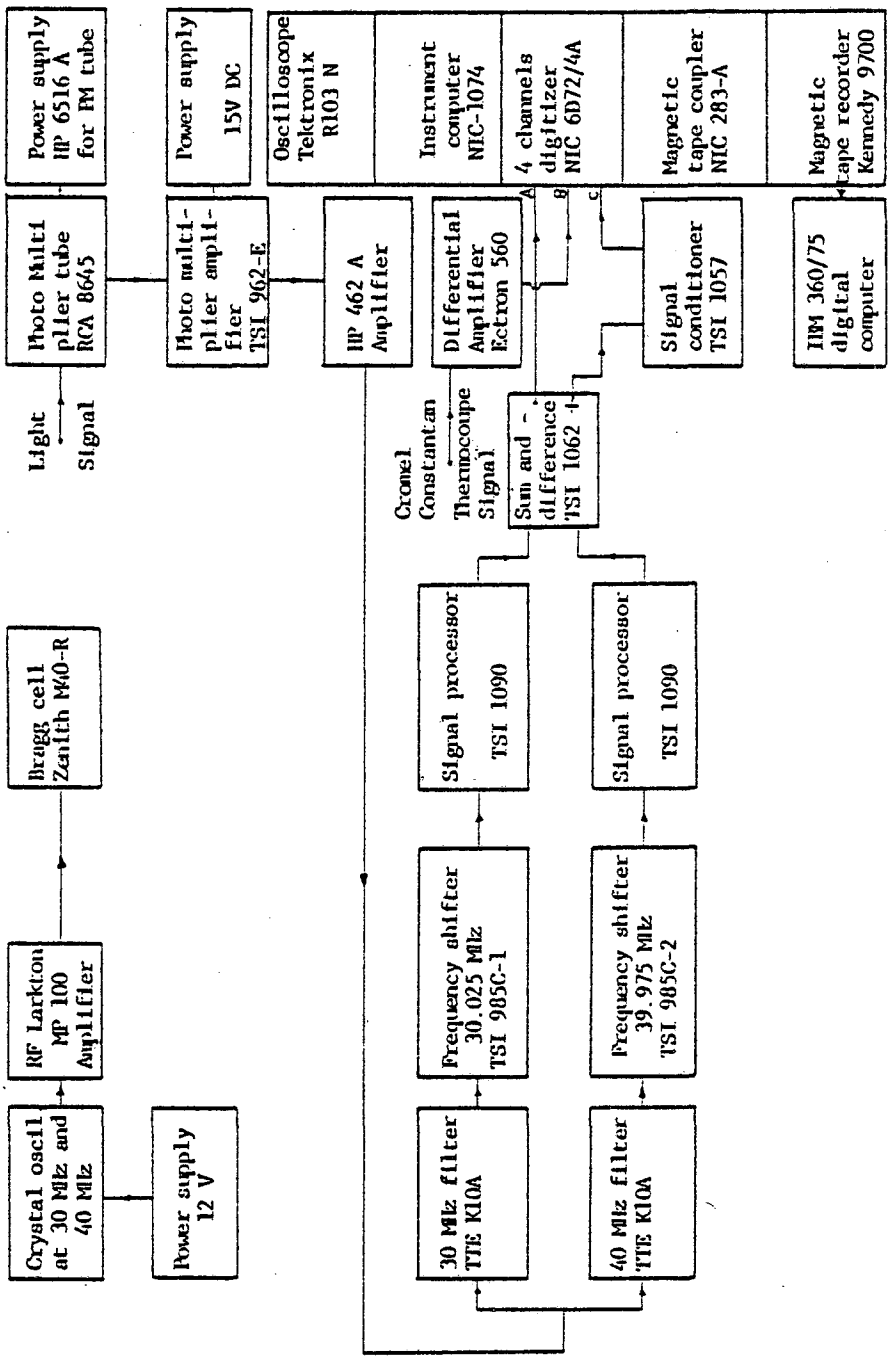

Figure 3.7 - Functional diagram of the signal processing system.

focused to a common intersection by L_4, a 628 mm focal length objective. Six micrometers acting on the lenses L_1, L_2 and L_3 permitted fine adjustments of the beam positions at the intersection.

Back scattered light is collected by L_5 a 870 mm lens, focused onto aperture A_2 by a 350 mm lens L_6, and detected by the photomultiplier tube (RCA 8645). A_2 is a 0.35 mm pinhole which limits the field of view to a region slightly smaller than the beam intersection. The light collection is off-axial to reduce flare from the lens L_4 and the test section windows.

After amplification by a photomultiplier amplifier (TSI model 962 E with a gain of 1500 V/A and bandwidth over 100 MHz and an amplifier Hewlett-Packard model 462 A operating at a gain of 40 dB and bandwidth of 50 MHz, the signal from the PM tube was separated into two channels that are bandpass filtered at 30 MHz and 40 MHz by TTE miniature filters (Model K10A). The maximum measurable Doppler shift is limited by the 30 MHz filter which had a bandwidth of ± 1.5 MHz corresponding to u = 2.8 m/s for a typical angle of $\kappa = 6^{\circ}$ and a wavelength of 514.5 nm, which is a much higher value for the typical velocities in this experiment as reported by Adrian (1975).

The carrier frequencies on each channel are shifted down to an intermediate frequency ν_c = 25 kHz by mixing the respective signals with local oscillators at 39.975 MHz and 30.025 MHz by using TSI 985C-2 and TSI 985C-1 frequency shifters. The signal frequencies are subsequently converted to voltages by signal processors of the frequency locked loop type TSI 1090. The center frequency of the FLL trackers was set at

25 kHz and its sensitivity is 10V/50 kHz. The net frequency drift of the local oscillators and the Bragg cell is less than $\pm$ 500 Hz.

After the voltages from the frequency trackers output had been added and subtracted together in a TSI 1063 Sum and Difference module, the sum voltage is level shifted to remove the DC component associated with the scanning speed and the intermediate frequencies using a TSI 1057 Signal Conditioner.

Appendix A-1 shows the calculation of the scaling factor converting volts to cm/s for three different situations of the geometry of the beams.

Appendix A-2 contains the calculations of the parameters of the measurement volume.

The particles used to seed the flow in order to generate good Doppler signals were Dow Saran microspheres or thermoplastic vinylidene chloride acrylonitrile copolymer monocells with average diameter of 5-8 μm and specific gravity of 1.333.

Those particles produced good signals, followed the flow well as shown in Appendix A-3, were cheap, non-corrosive, non-abrasive, and chemically inactive.

3.1.4 Digitizer and Data Storage Equipment

All velocity and temperature data were digitized by a 9 bit resolution, Four Channel Signal Digitizer (Nicolet model SD-72/4A). The horizontal sweep was controlled by a Wide Range Sweep Control Nicolet model SW-71B, and the memory and display control was done by a Display Control Nicolet NIC 1074. The data was stored in a memory with a capacity

of 4096 points. The display unit was a Tektronix 5103 N Power Supply/ Amplifier, a D10 Single Beam display and two 5A24N utility plug-in units that provided simple access to either the vertical or horizontal deflection system.

A Magnetic Tape Coupler model NIC-283A interfaced the digitizer memory and the magnetic tape, which was recorded by a Kennedy model 9700 tape recorder. The Magnetic Tape Coupler generated two tag words used to identify the record.

The tapes used to record the data were 7" white reel, 1/2" x 600', 9 track magnetic tapes.

The same equipment mentioned above was used to record the mean temperature profiles but instead of the Four Channel Signal Digitizer SD-72/AA, a Single Channel 12 Bit Digitizer SD-71B was utilized.

3.2 Experimental Procedures

The following quantities were measured: (i) vertical velocity fluctuations, (ii) horizontal velocity fluctuations using the laser Doppler anemometer, (iii) temperature fluctuations using the thermocouple probes, and (iv) mean temperature profiles close to the upper and lower plates using the resistance wire probes.

The wall close to the measurement line and parallel to the scanning direction is called the front wall and all the references are made from an observer outside the test section looking at the front wall.

A 167.6 cm x 91.4 cm x 2.5 cm table containing the laser, the optical components of the system and a support for the thermocouple probe was rigidly mounted on the cross-slide of the carriage of a lathe and

driven by a monophase electric motor (1/4 HP, 3450 rpm) and a Boston gear reductor with a 10:1 reduction ratio through the original lead screw of the lathe.

The data was taken along a line, 50 cm long and parallel to the front wall, by scanning the table horizontally from right to left at a speed of 2.36 cm/s.

Several test scans at different heights and different distances from the front wall were performed to check for any dependence of the statistics of the signal on the Y direction as defined in Figure 3.6. No trend was observed beyond the normal scatter of the data.

Preliminary data was taken in order to determine the ensemble size and the performance of the system. By calculating the RMS values of the signals, an ensemble of 10 scans at each height with 90% of confidence interval was enough to collapse the data very well. Therefore, at the beginning of the experiment smaller ensembles were used. When the higher order moments were calculated, a need for larger ensembles was evident and then 15 scans were taken at each height.

Vibrations of the optical units and variations in the table speed caused small spurious fluctuations in the velocity signals. Installation of a universal coupling between the reduction unit and the lead screw and stiffening the prism assembly reduced the RMS equivalent input velocity noise due to vibrations to 1 mm/s, typically.

The digitization rate of the data was set at 5000 μs for a four channel module, corresponding to an interval between points of 0.02 s and a Nyquist frequency of 25 Hz. The time constant of the filters was 10 ms corresponding to a cut-off frequency of 16 Hz.

Those settings were a compromise between measuring over 50 cm long lines in order to get good horizontal averages and a reasonable frequency response that would enable power spectrum analysis.

The data was taken only when the carriage, moving to the left, had a constant speed of 2.36 cm/s which was achieved in less than 2 s after the start of each scan. The digitizer was timed to complete the recording prior to the traverse shutdown. The use of only one direction to take the data was dictated mainly by the positioning of the thermocouple with respect to the measurement volume. In order to minimize probe interference the thermocouple junction was located 2.0 mm to the right of the center of the measurement volume, on the same line used to get the velocity data and no interference was desired in the velocity measurements. When scanning the table to the right, the crossing volume of the beams would be located in the wake of the thermocouple wires. The Reynolds number based on the double diameter of the wires and the scanning speed was 2.25 which corresponded to a region of influence of 50.8 μm ahead of the probe.

The positioning of the probe with respect to the measurement volume was done by first placing the hot junction of the thermocouple at the center of the intersection of the three beams, which was visually checked with the aid of a 15X microscope eyepiece and a reticle mounted on the photomultiplier base, and then moved back horizontally using a precise translation device.

The alignment of the beams was the most important factor in the process of getting good signals. For this reason, the procedure used is summarized in the following steps:

1) With the Bragg cell, beam splitter and objective removed, adjust the laser beam to propagate horizontally with respect to the table. The mirrors M1, M2 and M3 are adjusted to maintain horizontal propagation and direct the beam perpendicularly to the test section. The lens Lo is then inserted and adjusted to reproduce the previous conditions.

2) Introduce the Bragg cell in the circuit and adjust its proper angle with respect to the incoming beam in order to produce the 30 MHz and 40 MHz beams with equal intensity. Position the spatial filter at the focal point of Lo and get three clean beams with no generation of interference or reflection fringes.

3) Introduce the beam splitter unit into the optical circuit and position the prism assembly to produce good separation of the beams. There is a small (less than 3%) leakage of the light from one beam to the other. The leaking light intensity should be about the same in both beams. This is checked by turning alternatively the 30 and 40 MHz crystal oscillators off.

4) Measuring the heights and distances of the beams across the test section, the table is then adjusted in a plane parallel to the lower plate of the test section (which should already be horizontal) keeping the beams perpendicular to the front wall.

5) Place the objective L4 in the circuit and position it in order to introduce no deflection in the horizontal beams.

6) As the beams will not cross at one single point, adjust the

position of the lenses L_1, L_2 and L_3 using the micrometers and cross the beams at their waists generated by the objectives. This is most easily accomplished by placing a target in the focal plane of L_4. The fringes generated at the waist of the beams are equally spaced.

7) With the target at the crossing point rotate lenses L_5 and L_6 about a vertical axis in order to compensate for refraction at the air-glass-water interface. Optimal compensation is achieved when the target has least distortion.

8) Position the photomultiplier base such that the pinhole is centered on the image of the target. When focused, the pinhole should be located in a position corresponding to the circle of least confusion of the image.

9) Take the target out of the test section and seed the flow with particles. If the alignment of the beams and collection of the scattered light are good, the particles can be seen passing through the measurement volume when observed through the eyepiece microscope set at the PM base.

10) Set the PM tube in its base and turn it on. If signal is received by looking at the output of the mixers, loose the locking screws of the PM tube and finely adjust its position in order to receive the highest rate of signals.

11) Very fine adjustments of the position of the beams may be made at this stage in order to get the highest and equal rate of signals in both channels.

12) Repeat steps 6 to 11 as many times as necessary to get the best signal. Normally long periods were spent in this operation.

It is difficult to get and distinguish a good signal at the beginning. A good indication can be given by rates of 3 to 4 bursts per second for fluid velocities of 1 cm/s and Saran microspheres (5-8 μm) at normal concentration and amplitudes of 30 to 40 mV peak-to-peak. By normal concentration it is meant a concentration such that scanning the table 400-500 samples per second were received at the meter of TSI-1090.

Good performance of the LDA also requires small hum pick up in the form of interferences in the electronic equipment due to ground loops, electromagnetic fields, electromagnetic radiation, reflections, etc. The FLL trackers do not track the signal if the peak-to-peak voltage at the output of the TSI mixers is greater than 2.5 mV. In order to keep this hum picked up at low values (less than 1.0 mV p.p. is recommended) some points should be verified:

1) The case of the PM tube should be capacitively grounded to the table (0.1 pF).

2) The racks containing the electronic equipment, the lathe bed and the test section should be connected to a common ground.

3) The case of the photomultiplier amplifier TSI 962 E should be grounded to the table by direct contact.

4) The oscillator crystals and the RF amplifier should be set up in a single rack close to the Bragg cell.

5) The braided shield of the thermocouple extension wires should be grounded at the rack.

6) By moving and making loops in the cables connecting the Bragg

cell and the RF amplifier and the PM amplifier and the HP amplifier, the signal pick up can be decreased considerably.

The gain of the signal input in the FLL trackers should be set such that the indicating light just flashes. This procedure avoids the FLL to lock in the hum.

All electronic equipment was carefully tested and calibrated before it was used. Description of such calibrations will not be presented as they followed the normal procedures indicated by the manufacturer's manuals.

After each scan, the data was visually inspected and if any unlock transient or drop out could be detected, the data was rejected and not transferred to the magnetic tape. By this means, about 80% of the imperfections with the data acquisition process could be eliminated.

The mean temperature scans were made using a vertical constant speed traverse of 0.475 cm/s. The starting transient was minimized by letting the motor reach the operating speed before the probe began to move. This was accomplished by using a spring-slide system designed and described by Boberg (1977). The spring-slide system enabled the traverse to travel beyond the point of plate-probe contact. After starting the motor, the resistance wire remained in contact with the plate until previously compressed helical springs were completely released, at which point the whole system abruptly moved upwards. This procedure reduced the effects of the starting transient to acceptable levels. Prior to the probe lift off, a microswitch was used to trigger the digitizing unit. By increasing the gain of the horizontal and vertical displays of the

signal, the zero position could be very well identified. And yet by knowing the traverse speed and the digitization rate the vertical position could be well defined.

The time constant of the resistance wire probe was determined by two methods:

i) Passing the probe and a thermocouple with much smaller time constant ($\sim$ 5 ms) through a temperature discontinuity, at a constant speed of 0.475 cm/s.

ii) Moving the resistance wire and the thermocouple in a constant temperature gradient medium.

Sixteen scans of each method yielded an average time constant of 0.228 ± 0.024 s.

The test section had to be cleaned once a month so the use of distilled water was not feasible. After one month of use, the viscosity of the water of the test section was measured at two different temperatures and excellent agreement was found with the values given in the handbooks. Therefore the tabulated values for the physical properties were used in the data reduction.

When the test section was cleaned the operating fluid was changed. Before taking the data, the water in the test section was completely deaerated by repeatedly warming up the test section and scraping the air bubbles from the lower plate. Six to seven repetitions of this procedure were normally needed.

In order to accelerate the cooling of the test section after each day of tests, the upper plate was lifted 3 cm above the water level

and the insulating panels were removed. The next day the height of the layer of the fluid was checked with the upper plate in position and refilled if necessary.

Prior to injecting the Saran microspheres into the test section, the larger particles were removed by allowing 10% of the suspension of particles to settle in a beaker for 30 minutes. The particles were then injected through the slot on the upper plate and equally distributed along its whole length 10 minutes after the heat had been turned on, in order to achieve a good mixing and rapid diffusion through the water. After injecting the particles,10 minutes were required to achieve uniform dispersion. When new particles were injected during the tests, a minimum of five minutes was allowed before resuming the measurements.

The first solution was made with 15 g of particles in 800 ml of tap water. After 30 minutes, 10% of the solids settled down and the rest was used to inject in the flow. From one day of tests to the next, the particles remaining in the flow settled down and new ones needed to be injected. The first injection each day was about 100 ml of the solution for 20 cm layer of water. When correction in the particle concentration was needed, 25 ml of the solution was spread along the slot each time. As mentioned before, the good concentration was determined when about 400 samples of signal per second were obtained in the TSI 1090 in both channels when scanning the table.

All the data were digitized and stored on a 9-track magnetic tape. Each data record was recorded under a filing scheme using the octal tagword settings on the Nicolet Coupler unit. For each different

condition of height in the layer and heat flux at the lower plate, the tagword 1 was changed. The tagword 2 changed automatically at each scan. For different conditions the tagword 2 was reset to start from 1. Tagword 1 was selected by turning 6 thumbwheels in an octal base. The assignment of a file was done based on the following convention. The first digit on the left identified the person responsible for the data, the next three digits referred to the day of the year in which the data had been taken, in octal, and the last two digits indicated the order of the file in that specific day. For example: T_1 = 122503 refers to the author (1), to data taken on the 149th day of the year (May 29) and this was the third set of data taken that day. The general thought behind labeling subsequent data records was to increment T_2 for each scan and change T_1 only when a new condition began.

The stored data was easily retrieved for playback by selecting the display mode of operation on the digitizer unit and the appropriate tagword 1 to identify the record.

The tapes containing the data were analyzed using IBM 360/75 and the respective Fortran IV and Assembler programs that will be discussed later.

3.3 Data Analysis

All data records from horizontal scans were used to calculate the following mean central moments: $< \overline{w^2} >$, $< \overline{\theta^2} >$, $< \overline{u^2} >$, $< \overline{w\theta} >$, $< \overline{u\theta} >$, $< \overline{uw} >$, $< \overline{w^3} >$, $< \overline{\theta^3} >$, $< \overline{u^3} >$, $< \overline{u^2 w} >$, $< \overline{w\theta^2} >$, $< \overline{w^2\theta} >$, $< \overline{w^4} >$, $< \overline{\theta^4} >$, $< \overline{u^4} >$ where the bar indicates temporal averaging over

the whole scan length and the brackets indicate mean ensemble average over all the scans at certain conditions. That is, for each run the time average was calculated and then all the time averages of one set, representing a certain height above the lower plate, a certain heat flux at the lower boundary and a certain depth of the water layer, were ensemble averaged to produce one point in the vertical profile of the considered central moment. The standard deviation of the time averages was also calculated representing a measure of the variability at each condition.

In order to transform the finite record of one run to calculate the central moments, a new mean of the record had to be defined. As each one of the means for the same variable were different from run to run, corrections were applied to the moment calculations as follows. Define E_m as the mean of the record for one run, E the ensemble average of the set of runs, e'_m the total signal of one run, e_m the fluctuation with respect to E_m and e the fluctuating signal with respect to the ensemble average of the E'_ms. Therefore,

$$e = e'_m - E, \tag{3.7a}$$

$$e_m = e'_m - E_m. \tag{3.7b}$$

The calculation of the ensemble of the mean square value of the signal is given by

$$\langle e^2 \rangle = \langle (e'_m - E)^2 \rangle \tag{3.8}$$

Adding and subtracting E_m to (3.8), one has

$$< e^2 > = < e_m^2 > + < (E_m - E)^2 > \quad (3.09)$$

because $< e_m > = 0$ by definition.

For the higher order moments one has

$$< e^3 > = < e_m^3 > + 3 < (E_m - E) > < e_m^2 > + < (E_m - E)^3 > \quad (3.10)$$

$$< e^4 > = < e_m^4 > + 4 < (E_m - E) > < e_m^3 > + 6 < (E_m - E)^2 > < e_m^2 > +$$

$$+ < (E_m - E)^4 > \quad (3.11)$$

and for the cross moments, calling the other signal $a'_m = a_m + A_m$ (3.12)

$$< ea > = < e_m a_m > + < (E_m - E) \cdot (A_m - A) > \quad (3.13)$$

$$< e^2 a > = < e^2_m a_m > + 2 < e_m a_m > < (E_m - E) > + < (E_m - E)^2 (A_m - A) > \quad (3.14)$$

The first three quarters of the memory for each run were filled with the vertical velocity (Channel A), the temperature (Channel B) and the horizontal velocity (Channel C) data.

The data reduction was done using the IBM 360/75 digital computer of the Digital Computer Laboratory of the University of Illinois.

The Assembler program used to read the tape and convert the data into machine language was available from Boberg (1977).

The flow chart diagram of the program used to calculate the moments is shown in Figure 3.8.

No corrections for noise or other sources of errors were applied to the data due to the uncertainty of their values at each different

$$< e^2 > = < e_m^2 > + < (E_m - E)^2 > \quad (3.09)$$

because $< e_m >=0$ by definition.

For the higher order moments one has

$$< e^3 > = < e_m^3 > + 3 < (E_m - E) > . < e_m^2 > + < (E_m - E)^3 > \quad (3.10)$$

$$< e^4 > = < e_m^4 > + 4 < (E_m - E) > . < e_m^3 > + 6 < (E_m - E)^2 > . < e_m^2 > +$$

$$+ < (E_m - E)^4 > \quad (3.11)$$

and for the cross moments, calling the other signal $a'_m = a_m + A_m$ (3.12)

$$< ea > = < e_m a_m > + < (E_m - E) \cdot (A_m - A) > \quad (3.13)$$

$$< e^2 a > = < e^2_m a_m > + 2 < e_m a_m > . < (E_m - E) > + < (E_m - E)^2 (A_m - A) > \quad (3.14)$$

The first three quarters of the memory for each run were filled with the vertical velocity (Channel A), the temperature (Channel B) and the horizontal velocity (Channel C) data.

The data reduction was done using the IBM 360/75 digital computer of the Digital Computer Laboratory of the University of Illinois.

The Assembler program used to read the tape and convert the data into machine language was available from Boberg (1977).

The flow chart diagram of the program used to calculate the moments is shown in Figure 3.8.

No corrections for noise or other sources of errors were applied to the data due to the uncertainty of their values at each different

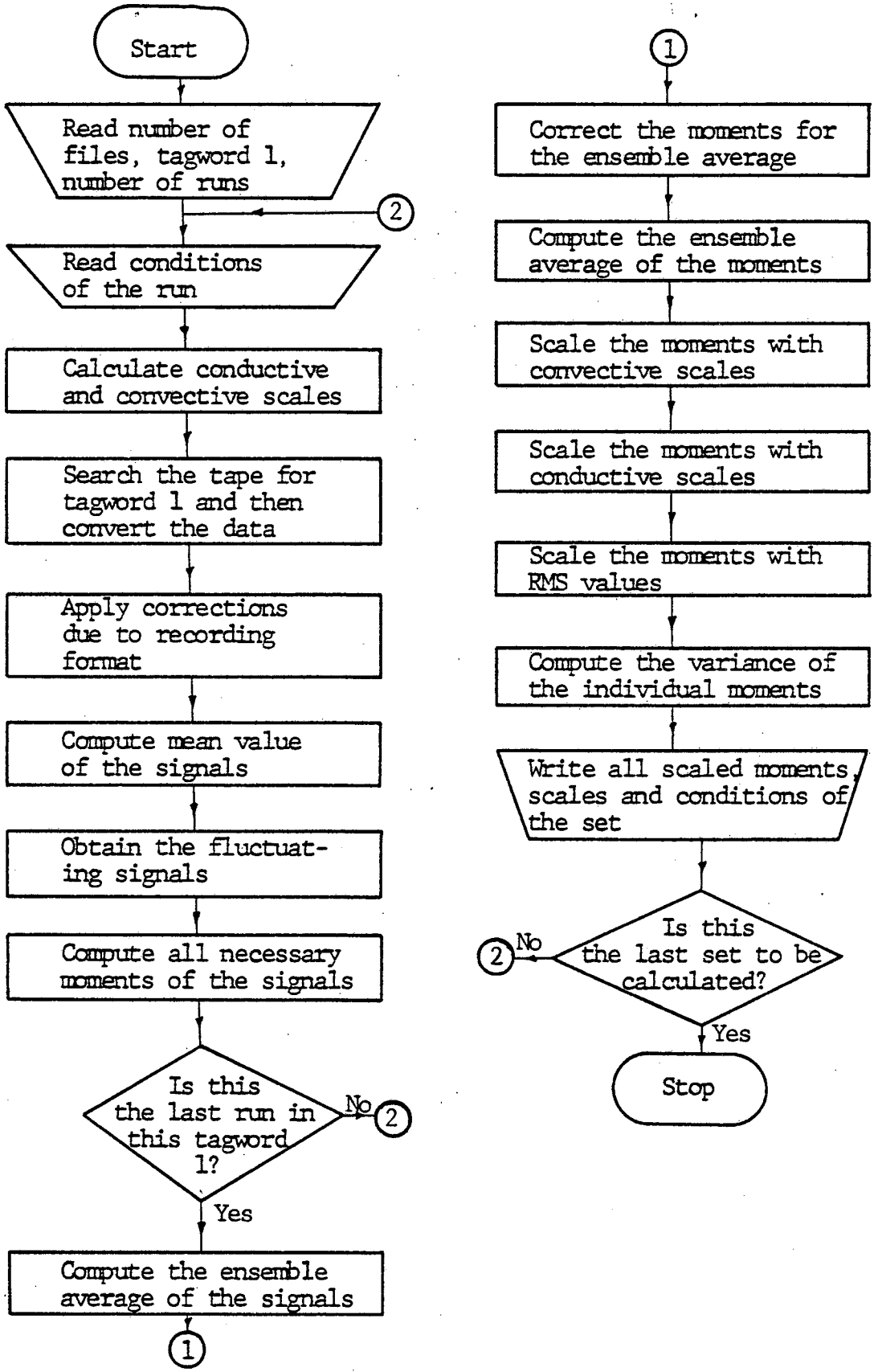

Figure 3.8 - Flow chart diagram for moments calculation.

situation. Appendix A-2 presents a discussion of the estimated noise in those experiments.

Sampling errors probably represented the largest single source of error in the experiments. Estimates of the sampling errors required reasonably accurate knowledge of the auto-covariance function over long time delays (Bendat and Piersol, 1971, p. 172-4), and this quantity itself could not be obtained due to the short sampling periods ($\sim$ 20s).

The selection of which moments to calculate was determined by the terms involved in the kinetic energy, kinematic heat flux and temperature variance governing equations, previously presented in Chapter 2.

The vertical scans of mean temperature close to the upper and lower boundaries were processed in the IBM 360/75 computer. The derivative of each raw temperature profile was calculated and after being multiplied by the time constant, the product was added to the value of the raw profile in each point, as discussed in Appendix A-4.

Eight scans were used to produce the ensemble averaged temperature profile. The flow chart diagram of the computer program is shown in Figure 3.9.

The harmonic analysis of the data - power spectrum and autocorrelation function, was done on the horizontal records of w, θ and u. The Fast Fourier Transform subroutine used was a 4 + 2 radix and was reported by Brumbach (1968).

The main steps of the power spectrum and autocorrelation functions calculation were:

i) Taper the records with a cosine taper function with a cosine

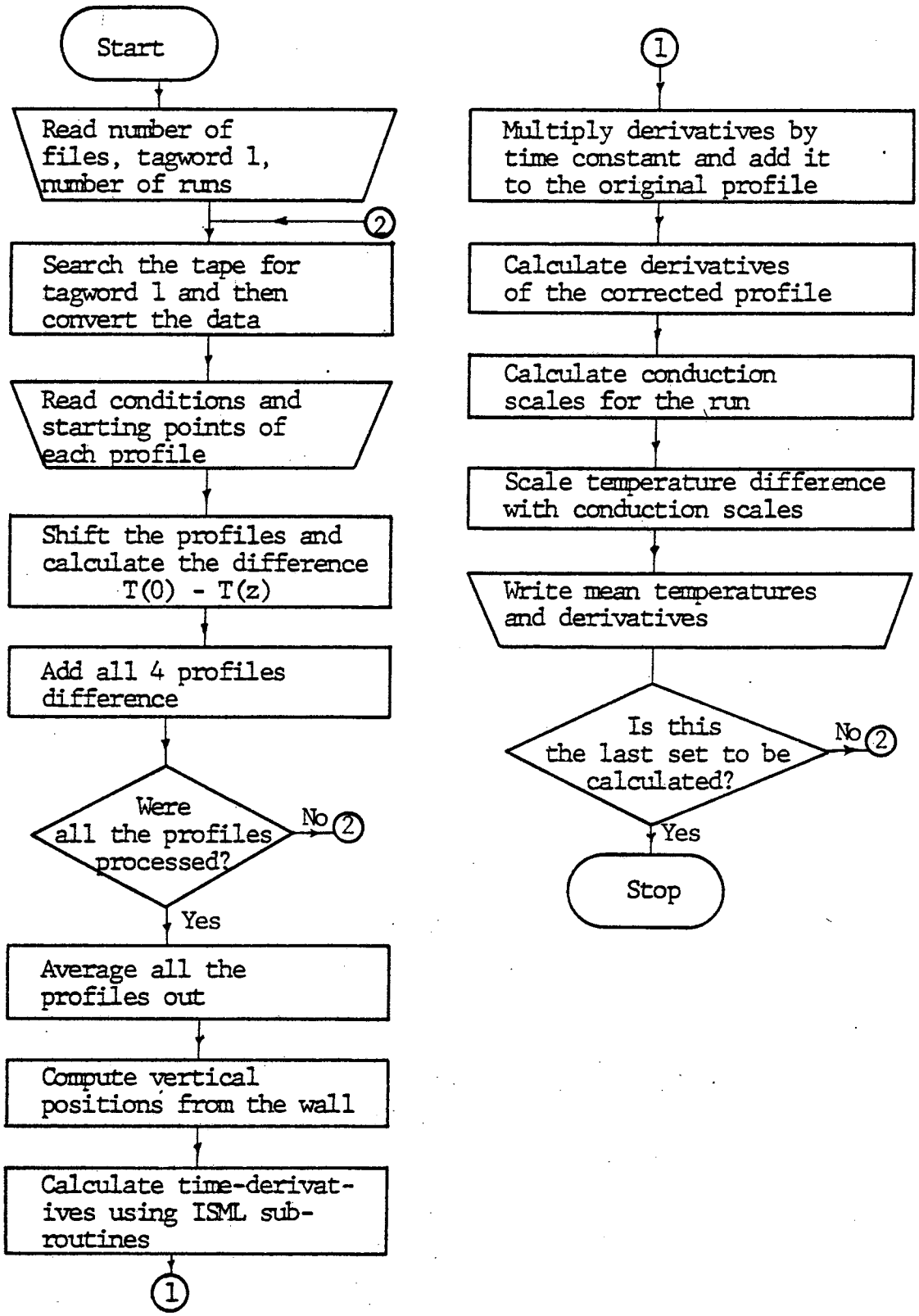

Figure 3.9 - Flow chart diagram for mean temperature calculations.

bell at one tenth the length of the data at the beginning and end of the record.

For data stretching from t = 0 to t = T-1, the expressions of such a taper window would be

$$\frac{1}{2}\left(1 - \cos\frac{\pi t}{0.1T}\right) \qquad \text{for } 0 < t < 0.1T \qquad (3.15a)$$

$$1 \qquad \text{for } 0.1T < t < 0.9T \qquad (3.15b)$$

$$\frac{1}{2}\left[1 - \cos\frac{\pi(T - t)}{0.1T}\right] \qquad \text{for } 0.9T < t < T \qquad (3.15c)$$

ii) Add N zeros to the record in order to separate the calculated circular autocorrelation function where N is the number of data points.

iii) Fourier transform the sequence using FFT24 subroutine, Brumbach (1968) and get

$$X_k = \sum_{n=0}^{2N-1} x_n \exp\left[-i\frac{2\pi kn}{N}\right] \qquad k = 0,1.... 2N-1 \qquad (3.16)$$

iv) Compute the raw estimate of the power spectrum for k = 0,1 ....N-1.

$$\tilde{G}_k = \frac{1}{N\,\Delta t}\left|X_k\right|^2 \qquad (3.17)$$

v) Adjust these estimates for the scale factor due to tapering, e.g., by replacing $\tilde{G}_k$ by 1.14286 $\tilde{G}_k$.

vi) Compute the inverse FFT of $\tilde{S}_k = \frac{\tilde{G}_k}{2}$ to obtain R^c_x (rh)

for r = 0, 1, ... 2N-1.

vii) Discard the last half of R_x to obtain results for r = 0,1. .... N-1.

viii) Multiply the R_x by the scale factor $\frac{N\Delta t}{N-r}$.

ix) Smooth the raw estimates of the power spectrum by averaging in blocks of 19 consecutive points.

Power spectrum and autocorrelation function calculated here follow the same definitions presented in Bendat and Piersol (1971).

The flow chart diagram of this computer program is shown in Figure 3.10.

Analyzing the results of the convective heat transfer, $< \overline{w\,\theta} >$ showed lower values than the expected theoretical values based on mean rate of temperature increase measured directly.

In order to search for the reasons of this anomalous behavior, the joint probability functions and conditional averages of the signals w-θ, u-θ and u-w were calculated.

The flow chart of this computer program is shown in Figure 3.11.

The conditional averaging techniques were the same used by Adrian (1975) in analyzing water over ice convection.

Two types of conditional averages were calculated:

Type 1 - Given any function R(w, θ), the conditional average $\overline{R_i}$ was the mean value of R for points belonging to the i^{th} group.

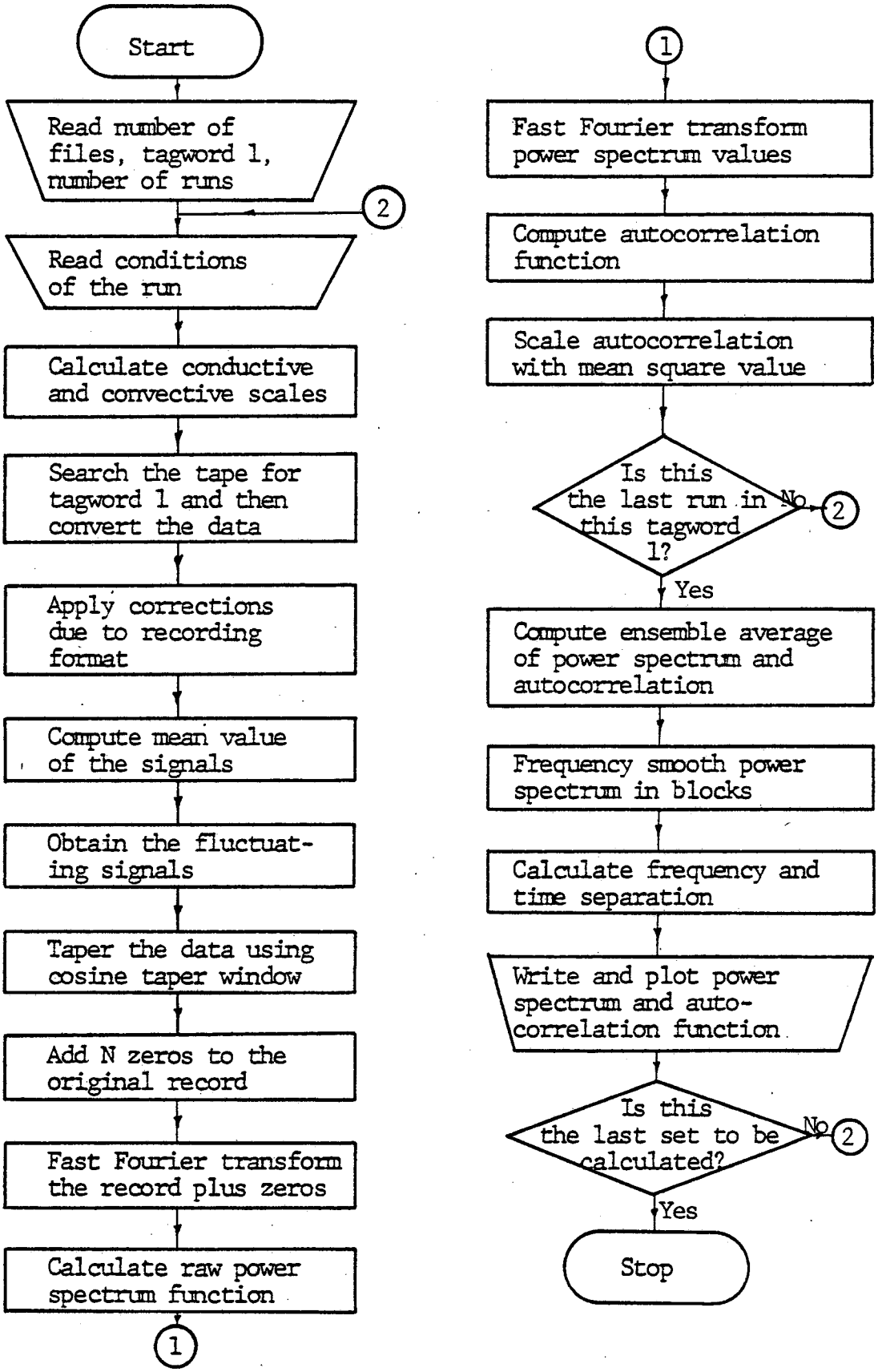

Figure 3.10 - Flow chart diagram for power spectrum and auto-correlation functions calculation.

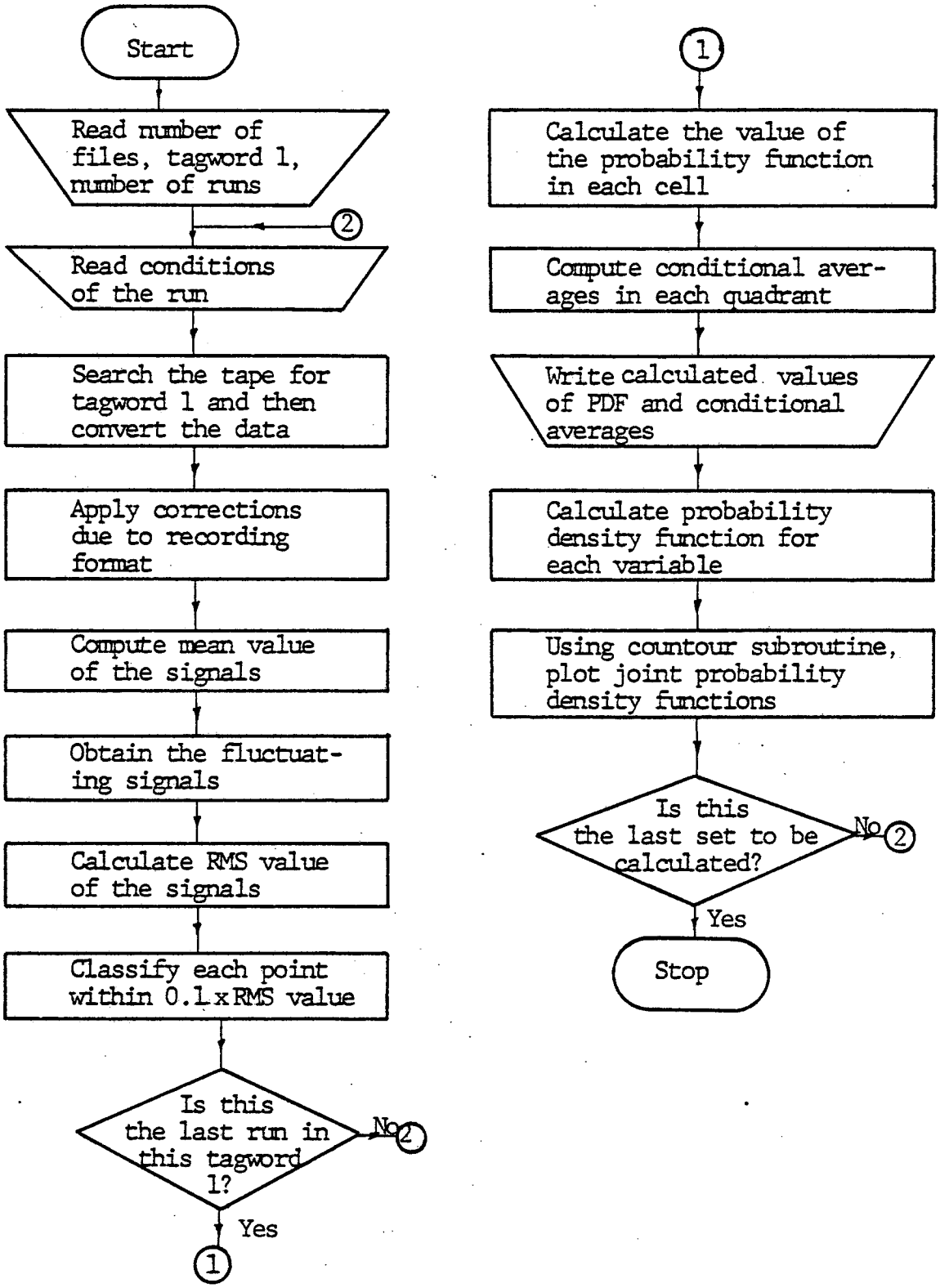

Figure 3.11 - Flow chart diagram for joint PDF and conditional averages calculation.

$$\overline{R_i} = \frac{1}{N_i} \sum_{a \in i} R\,(w_a, \theta_a) \qquad i = I, \ldots V \tag{3.18}$$

where data points in the w-θ plane were classified into five groups according to the following inequalities

$$\left.\begin{array}{lll} \text{(I)} & w > 0 \;, & \theta > 0 \\ \text{(II)} & w < 0 \;, & \theta > 0 \\ \text{(III)} & w < 0 \;, & \theta < 0 \\ \text{(IV)} & w > 0 \;, & \theta < 0 \end{array}\right\} \text{ and } |w\theta| > 0.1\,\sigma_\theta\,\sigma_w$$

$$\text{(V)} \qquad |w\theta| < 0.1\,\sigma_w\sigma_\theta \tag{3.19}$$

where σ_w and σ_θ are the RMS values of the vertical velocity and temperature fluctuations respectively.

Type 2 - The second type of average represented the fractional contribution made by the fluctuations in a given class of fluid to the total mean value of the fluctuation. It was related to the conditional average by

$$\frac{1}{N\overline{R}} \sum_{a \in i} R\,(w_a, \theta_a) = \frac{N_i\,\overline{R_i}}{N\,\overline{R}} \qquad i = I, II \ldots V \tag{3.20}$$

Using just w and θ signals, for $w > 0$, $\theta > 0$ and $|w\theta| > 0.1\,\sigma_w\sigma_\theta$ conditional averages of types 1 and 2 are

$$\overline{(w\theta)_I}\Big|_1 = \frac{\sigma_\theta\,\sigma_w}{N}\left(\frac{1}{\overline{N}_I}\right)\cdot\sum_{a \in I}\left(\frac{w}{\sigma_w}\right)_a\left(\frac{\theta}{\sigma_\theta}\right)_a \tag{3.21}$$

$$\overline{(w\theta)_I}\Big|_2 = \frac{1}{N\, r_{w\theta}} \cdot \sum_{a \in I} \left(\frac{w}{\sigma_w}\right)_a \left(\frac{\theta}{\sigma_\theta}\right)_a \qquad (3.22)$$

where $r_{w\theta}$ is the correlation coefficient of that run.

Separated horizontal runs using half of the memory for w signal and the other half for θ signal were performed in order to calculate the space-time correlation functions for w-θ for different separations of the thermocouple probe and the velocity measurement volume.

Those runs intended to produce a correction factor for the convective heat flux calculation due to the spatial separation of the probes. The flow chart diagram of the computer program is presented in Figure 3.12.

The main points of the program are:

i) In order to save computer time, two records x(n) and y(n) were Fourier transformed at a time and separated by

$$X(k) = \frac{Z(k) + Z^*(N-k)}{2} \qquad (3.23$$

$$Y(k) = \frac{Z(k) - Z^*(N-k)}{2i} \qquad (3.24)$$

$$k = 0,1 \ldots N-1$$

where $z(n) = x(n) + iy(n)$ (3.25)

$$Z(k) = \sum_{k=0}^{N-1} z(n) \exp\left[-i\,\frac{2\pi kn}{N}\right] \qquad (3.26)$$

and $Z^*(k)$ is the complex conjugate of Z(k). This technique is explained in Bendat and Piersol (1971 - p. 308).

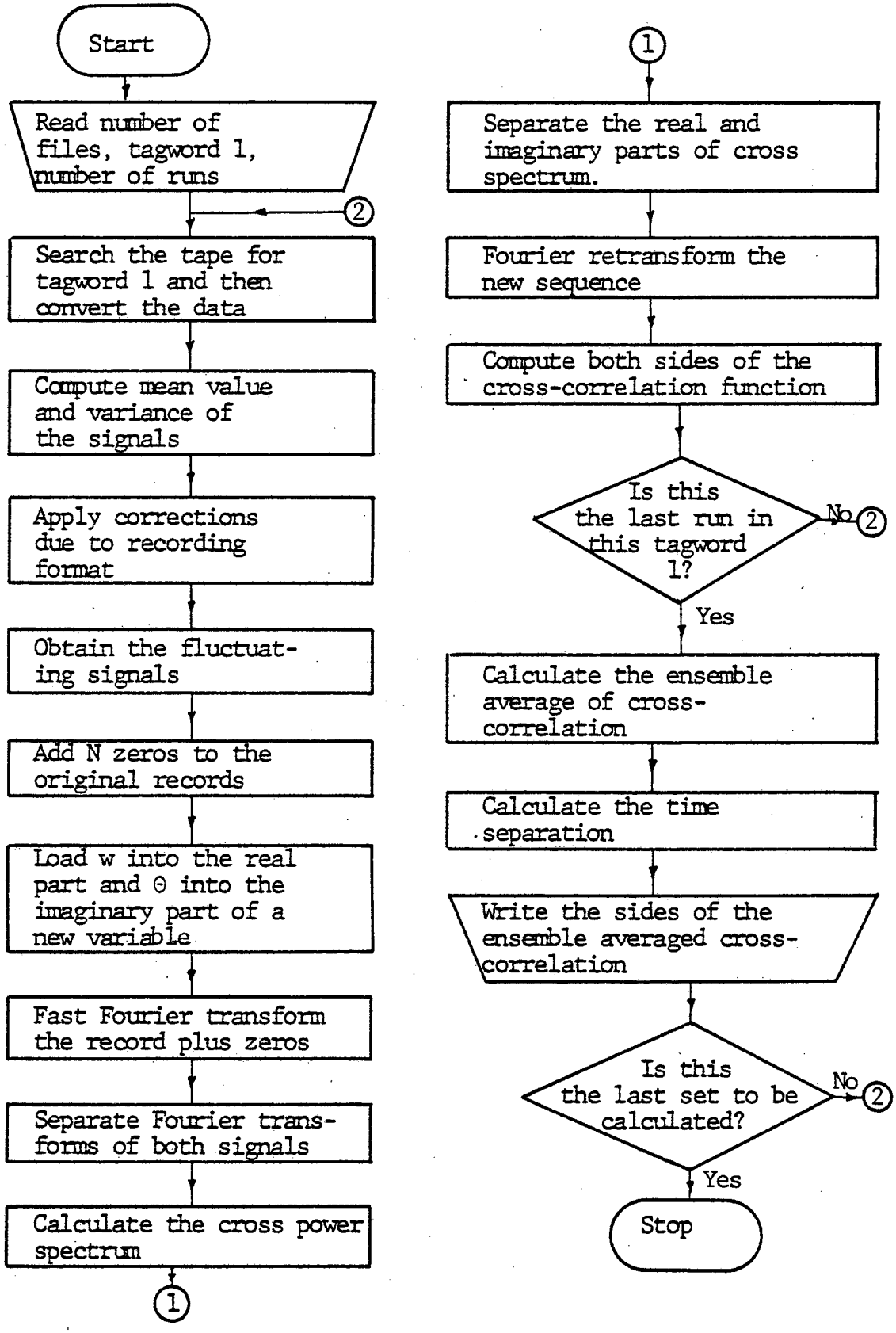

Figure 3.12 - Flow chart diagram for cross-correlation function calculation

ii) As suggested by Brumbach (1968), a faster method to compute the cross-correlation function of two records is used.

By definition

$$R_{xy}(\tau) = \frac{1}{N\Delta t} \sum_{k=0}^{N-1} X(k)\, Y^{*}(k) \exp\left[\frac{2\pi i k\tau}{N}\right] \qquad (3.27)$$

$$\tau = 0,1 \ldots M$$

and

$$R_{xy}(-\tau) = \frac{1}{N\Delta t} \sum_{k=0}^{N-1} X^{*}(k)\, Y(k) \exp\left[\frac{2\pi i k\tau}{N}\right] \qquad (3.28)$$

Multiply (3.28) by $i = \sqrt{-1}$ and adding it to (3.27)

$$R_{xy}(\tau) + i\, R_{xy}(-\tau) = \frac{1}{N\Delta t} \sum_{k=0}^{N-1} \left\{ X(k)\, Y^{*}(k) + i\, Y(k) X^{*}(k) \right\} \exp\left[\frac{2\pi i k\tau}{N}\right] \qquad (3.29)$$

Equation (3.29) shows that only one Fourier transformation produces both sides of $R_{xy}(\tau)$.

CHAPTER IV

RESULTS

4.1 Flow Visualization

Flow visualization was performed in an auxiliary rectangular small test section 510 mm x 510 mm x 560 mm (width x length x height) filled up to 200 mm with deaerated tap water and electrically heated from below. The lower plate was a 12 mm thick aluminum plate and upper boundary was made of plywood and filled with 15 cm slabs of styrofoam. The lateral walls were 10 mm thick plexiglass and externally insulated with 15 cm thick panels of styrofoam. The kinematic heat flux used to visualize the flow was 0.038 ^{o}Kcm/s, in a 20 cm layer. Two windows 100 x 150 mm were made in two adjacent lateral panels. One window was used to illuminate the test section with a 1000 W Sylvania CTT and the other, situated 90^{o} with respect to the illuminating window, was used to observe the flow. Pictures were taken using a Tri-X - 400 ASA Kodak film and a Vivitar N/AI 75-205 mm f 3.8 close focusing mode and mounted on a tripod at an angle of 15 - 20^{o} with respect to the horizontal plane. Dow plastic pigment 722 - Polysterene Latex with specific gravity of 1.05 was used as the dye tracer for visualization purposes. After initially filling the test section with water and letting it still completely, a thin layer of the pigment (0.5 mm thick) was carefully introduced into the tank to cover the central region of the lower plate. The pigment was slightly heavier than the water and it was not completely transported into the convective region by the initial motions, but remained for a time on the bottom, serving as a continuous source of flow tracer.

Sufficient pigment remains along the bottom plate to allow detailed observations of the convective patterns for about 20 minutes after the onset of motion. It is expected that the turbulence and convective patterns have reached a statistically quasi-steady state well within this time interval.

The main characteristics of the flow observed in the thermal convection experiment are related as follows:

i) When the thermal convection starts, the latex on the lower plate initially forms stationary ridges due to the accumulation of dye in regions of flow convergence. As the turbulent Reynolds number increases, those ridges start wandering about the surface in a random fashion. When enough hot fluid is accumulated in a ridge, it breaks away from the horizontal lower boundary as a long sheet of buoyant fluid. The sheets are less than 1 mm thick and about 0.5-1 layer depth long. The ridges are good indicators of the action of the cold fluid over the horizontal lower plate.

ii) When kinks are formed along the front, more tracer is ejected from the boundary layer and long columns of hot fluid could be devised, as reported by Townsend (1959) and (1976). Only at the beginning of the experiment (about 4 minutes after the heat had been turned on) could individual thermals, as reported by Sparrow, Husar and Goldstein (1970) be identified. Individual thermals were not observed at any other time. The intersection of two or more ridges detached large amounts of hot fluid in columnar forms that were eroded by contact with the surrounding water which was in vigorous turbulent motion.

iii) There existed about 10 ridges in half of the area of

the lower plate, where the latex pigment was accumulated. Contrary to observations reported by Willis and Deardorff (1977), the ridges were not connected together in one region showing horizontal planforms with dendritic shapes. The method of illuminating the flow may not have permitted this observation.

iv) The motion of the hot fluid from the lower plate was not always exactly vertical. There was a tendency to upward movement generated by the buoyancy forces. The cold fluid, acting on the hot fluid sheets, deflected them to the sides showing occasionally inclinations up to 60° from the vertical direction.

v) In the central third of the fluid layer, the upward motion of the hot fluid followed an irregular path. In the upper third of the fluid layer, the vertical motion was greatly decelerated and the flow was dominated by large horizontal motions. Some of the hot masses of fluid had so much inertia that they could not be decelerated during their approach to the upper boundary. Upon hitting the upper plate, they were deflected to the sides. If the upper plate showed any imperfection, mean motions could be easily set up.

vi) There were no preferential directions for the movement of the ridges on the lower plate, nor did the release of thermals occur at specific points. (By thermal, it is understood a mass of fluid, driven by buoyancy, that moves away from a bounding surface into the bulk of the fluid layer). At high Reynolds number, the mass flux of hot fluid from the lower boundary still showed a nearly intermittent, rather than steady, pattern. Occasionally, there were extremely active periods corresponding to the bursting away of a thermal.

vii) As a rule, the ascending hot fluid was deflected by the cold descending fluid and had to find out new paths in its way up. When the hot fluid was unable to penetrate cold regions, it spread horizontally to the sides until enough fluid accumulated to overcome the imposed cold fluid resistance.

Many of the observations reported above cannot be perfectly seen in the sequence of prints taken 2 seconds apart and shown in Figures 4.1 and 4.2, because as the tracer spread rapidly over the layer. Figure 4.1 shows the flow 6 minutes after the onset of convection. The detachment of a thermal from the lower boundary is shown by the sequence of photographs in Figure 4.2, taken 2 seconds apart.

4.2 Mean Temperature

The mean temperature of the layer was measured using the alumel resistance wire probes described in section 3.1.2.1. The mean temperature profiles in Figures 4.3 and 4.4 show the ensemble averages of eight independent runs close to the lower and upper plates respectively, for different conditions of layer depths and heat flux at the lower plate.

The convention for labelling the conditions is

Label	Z_* {cm}	Qo {^oKcm/s}	Z_*/Zd	Pe_*
I	20	0.0153	452	6090
II	20	0.0330	566	7840
III	20	0.0568	676	9370
IV	15	0.0450	444	6000

For all the runs, one can observe in Figure 4.3 that 95% of

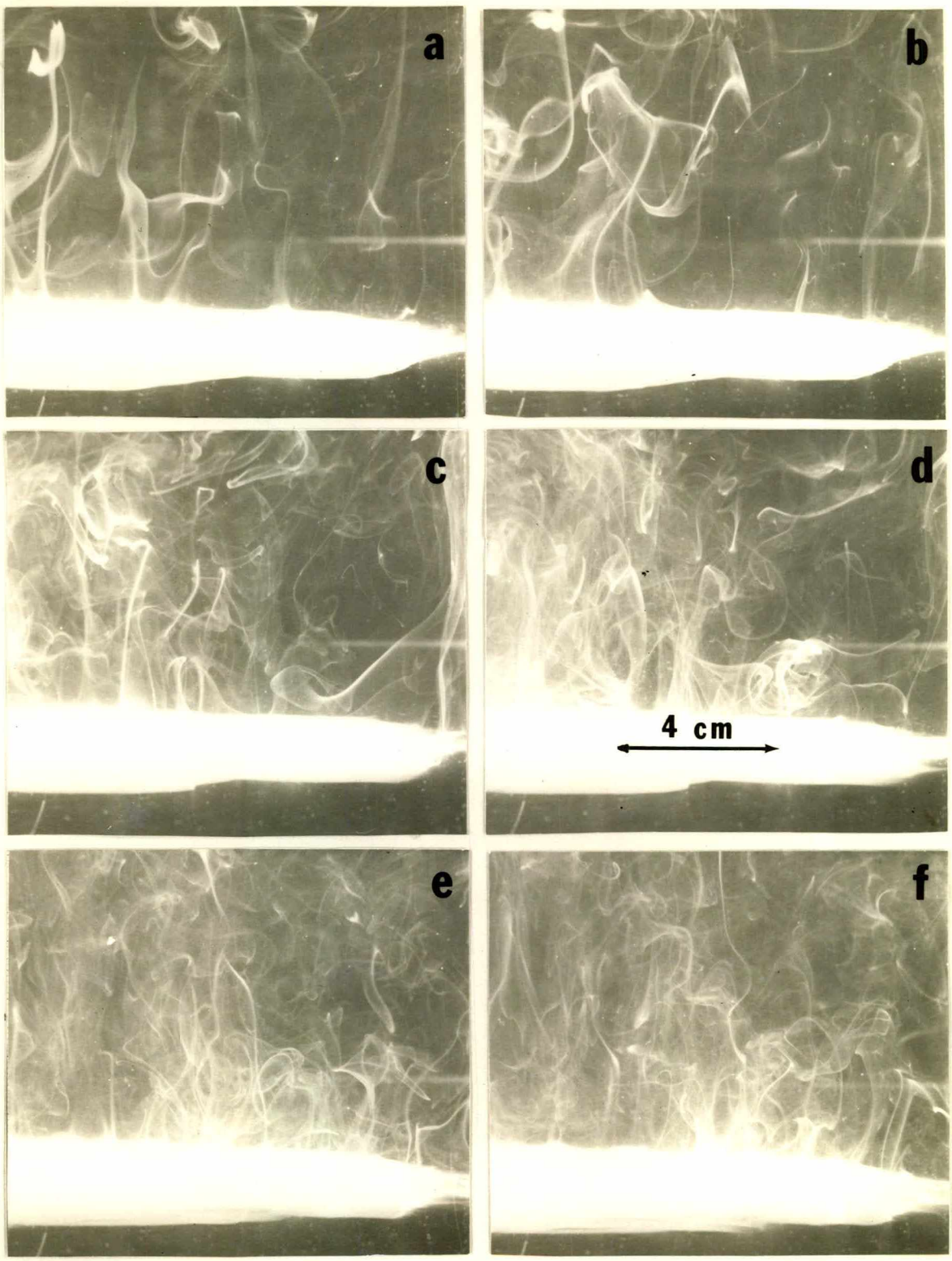

Figure 4.1—Evolution of the thermal convection flow

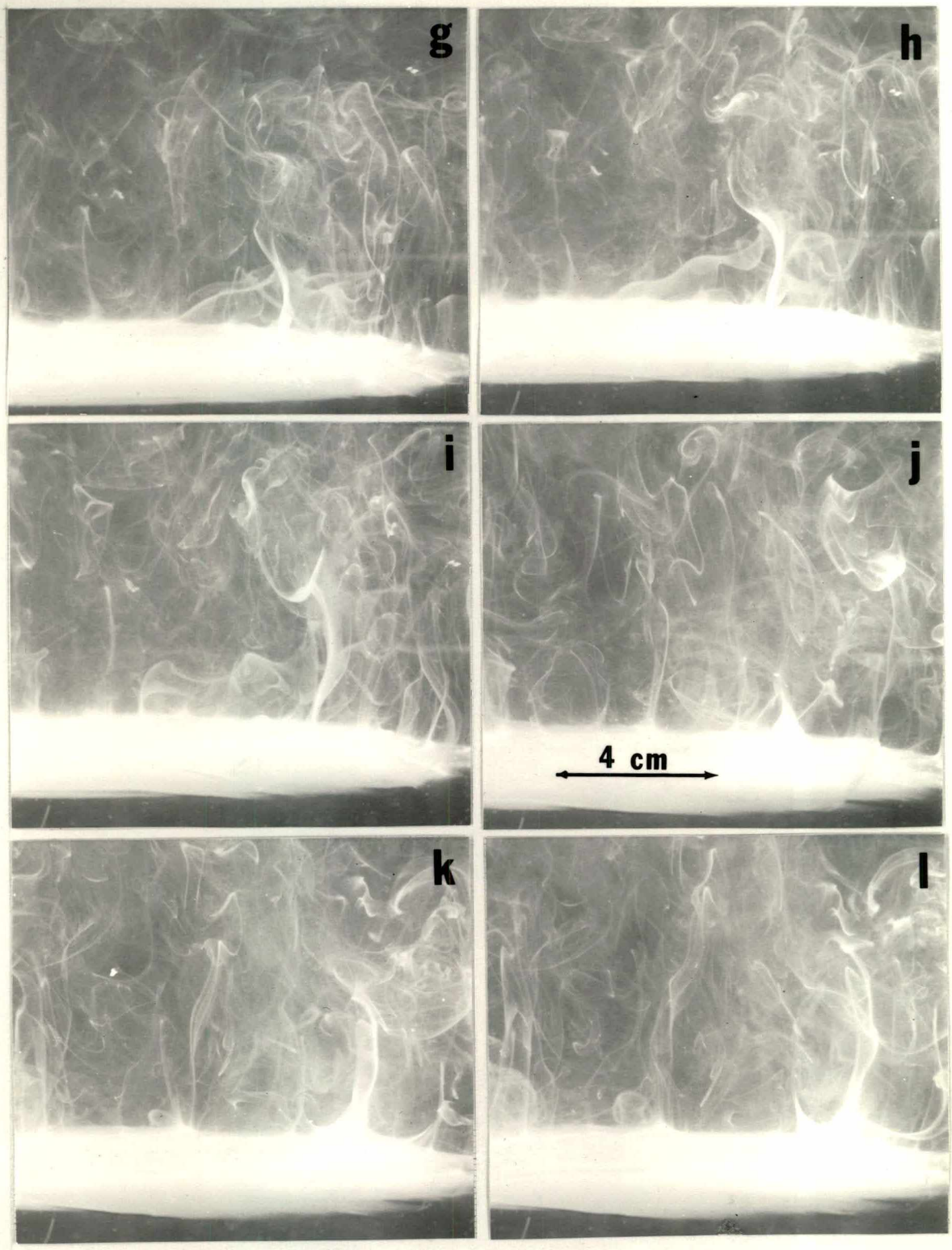

Fig. 4.1 (cont.)–Evolution of the thermal convection flow

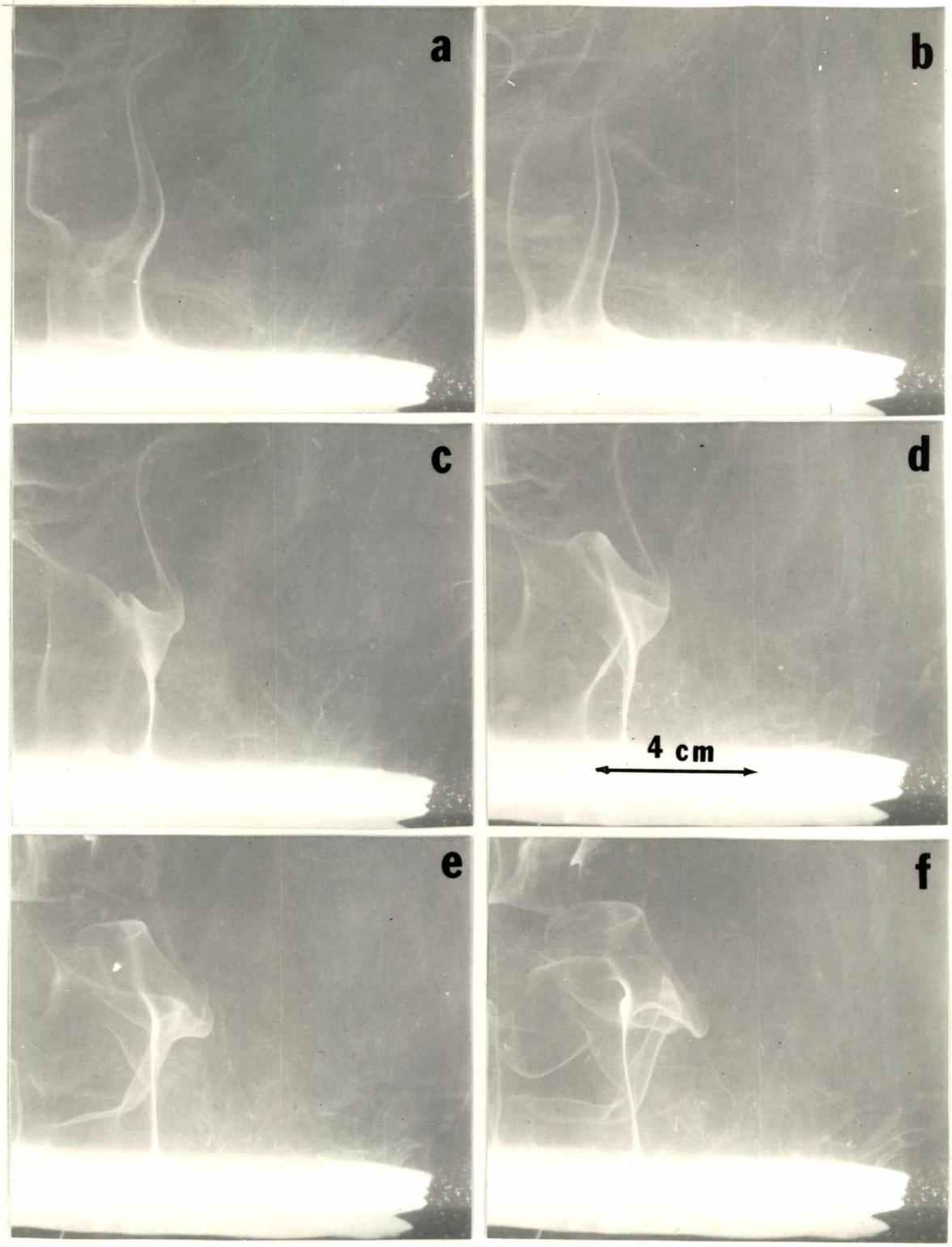

Figure 4.2 — Development of a thermal

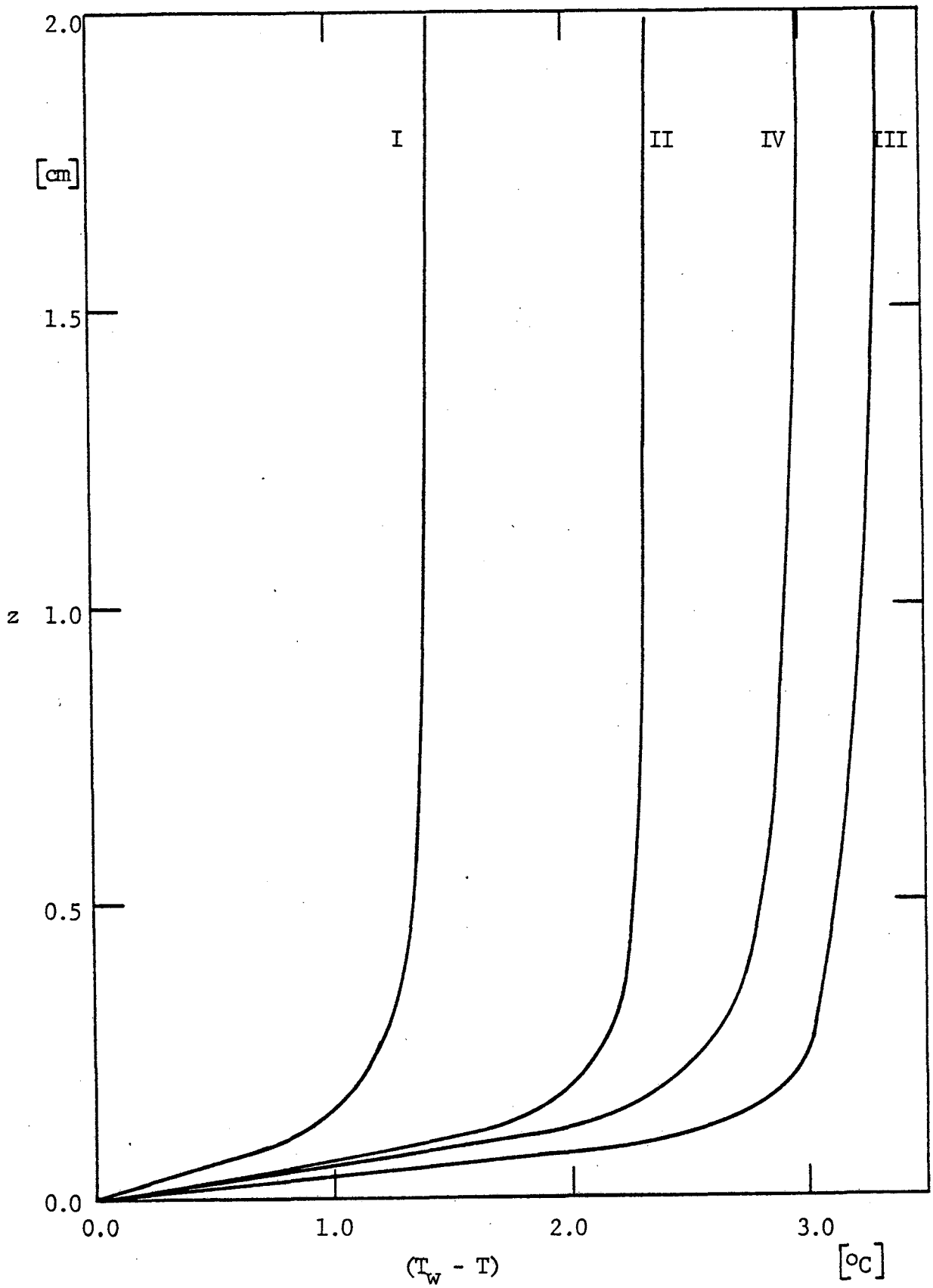

Figure 4.3 - Temperature profiles close to the lower plate.

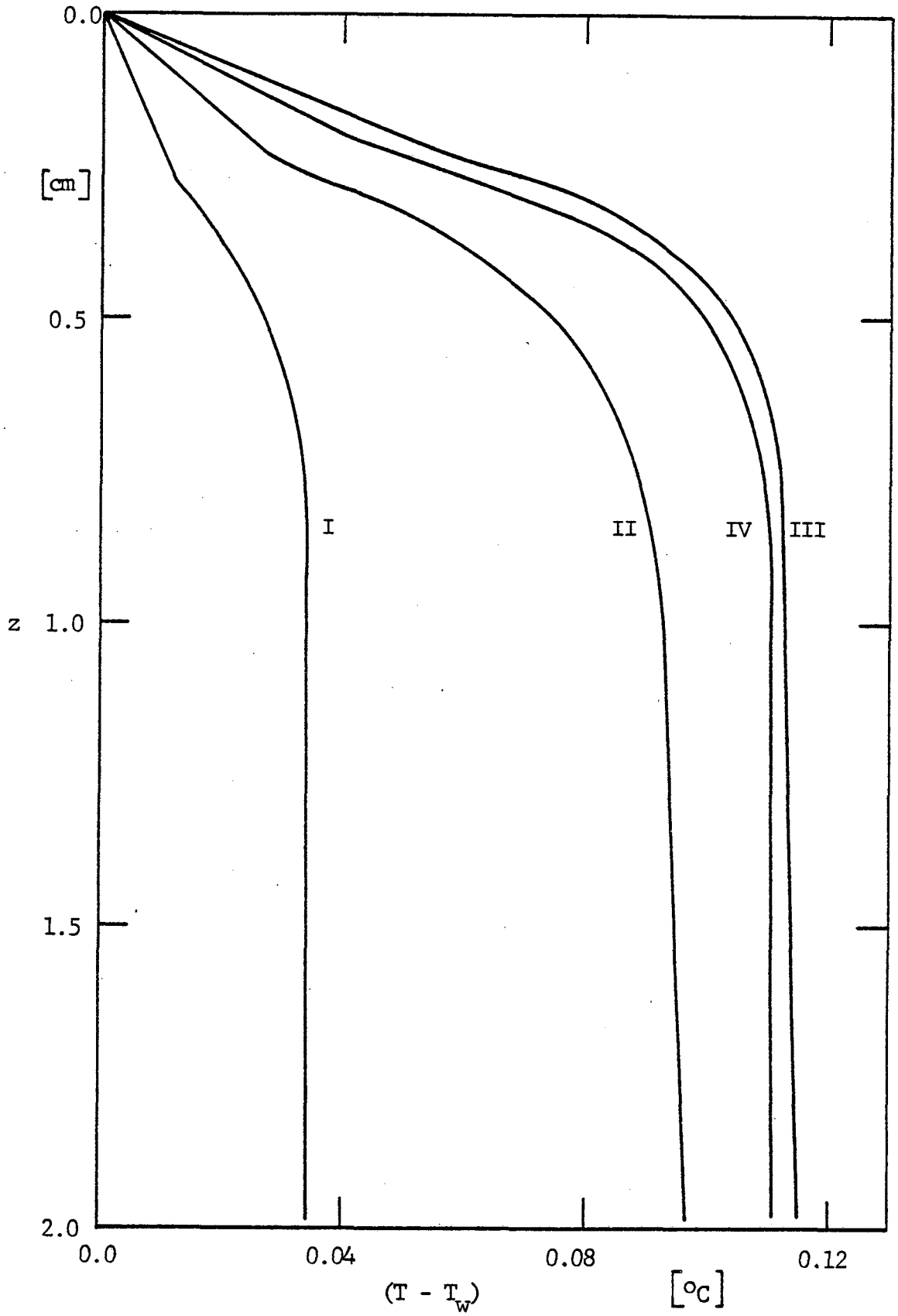

Figure 4.4 - Temperature profile close to the upper plate.

the total temperature difference ($T_w - T_\infty$) occurs in the first 5 mm of the layer. Close to the upper plate, due to the small heat loss, the gradients extended up to 8 mm inside the layer. The heat losses through the upper plate were

Condition	Q loss {$^oKcm/s$}	Q loss/Qo x 100%
I	0.000061	0.40
II	0.000179	0.54
III	0.000326	0.57
IV	0.000268	0.60

The temperature difference between the core and the upper plate is less than 0.12^oC for the worst case (III), demonstrating the adequacy of the insulation on the upper plate.

The change in the gradient of the temperature profile close to the upper plate in Figure 4.4 may have been caused by inadequate spatial averaging. Figure 4.5 shows the temperature profile close to the lower plate scaled by the convective scales for the same layer depth $Z^* = 20$ cm.

Using the scales defined in equations (2.23a) through (2.23c), the log-log graphs of the ensemble averaged temperature profiles shown in Figure 4.5 correlated very well up to $Z/Zd = 8$. Beyond that point, each profile showed a slightly different behavior.

The digitization settings for the mean temperature profile runs were:

Resolution - 12 bits

Vertical Display - $\pm$ 1/2V and $\pm$ 1V full scale

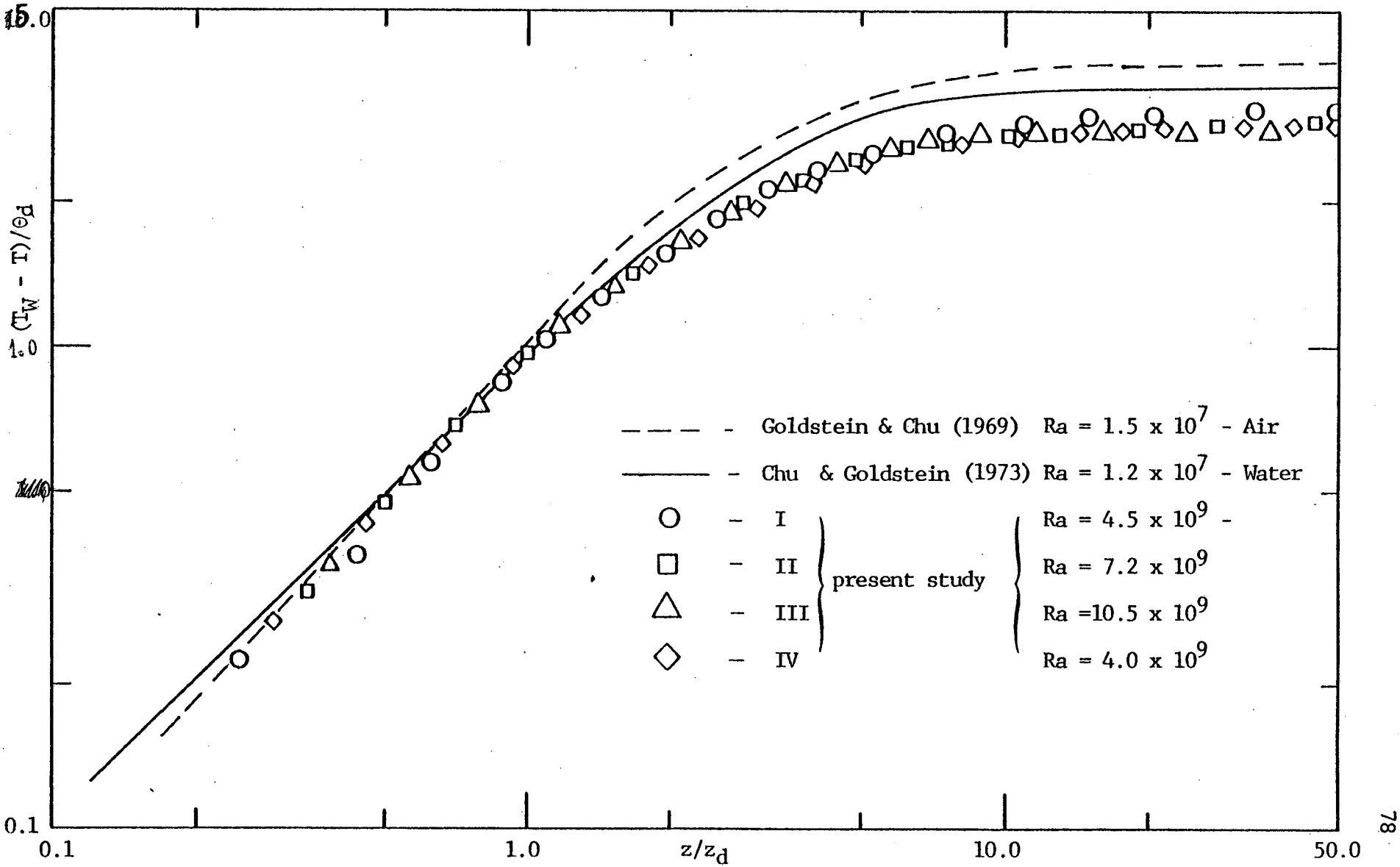

Figure 4.5 - Temperature profile using Chung's (1978) scales.

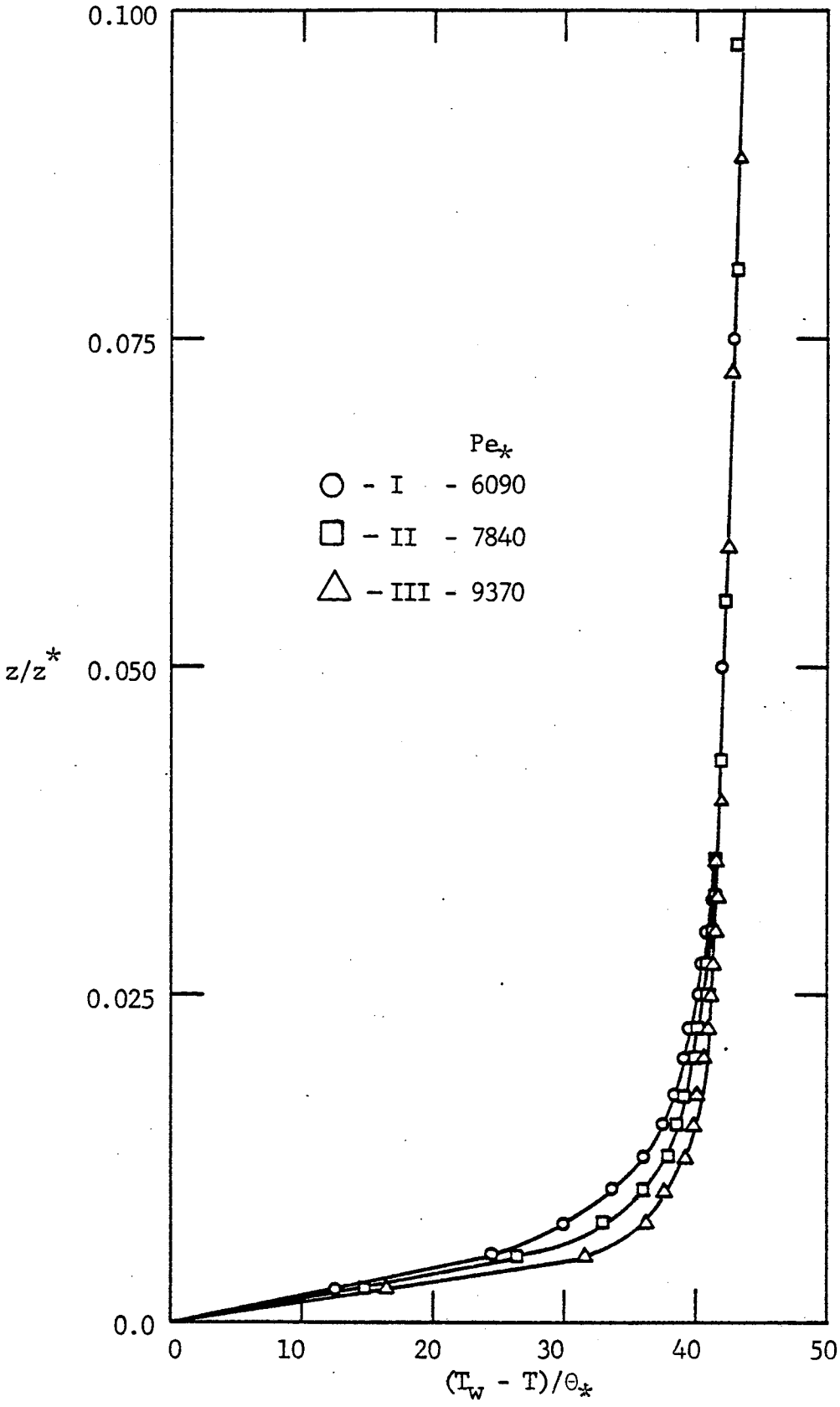

Figure 4.5A- Temperature profile close to the lower plate using convective scales.

Low Pass Filter - 100 Hz.

Dwell Time - 16 667 μs

Three other sets of data for the 20 cm layer depth were taken with dwell time of 2000 μs and were scaled using equations (2.23a) through (2.23c). They showed the same behavior as presented in Figure 4.5.

The asymptotic values of the graphs after $z/z_d = 50$ are lower than the values reported by Chu and Goldstein (1973) and Goldstein and Chu (1969) when the same scales were employed. This difference may be due to the fact that a different kind of flow is being analyzed and the constant heat flux in Rayleigh convection is not encountered in the unsteady non-penetrative convection.

One can define an equivalent Rayleigh number that permits the comparison between Rayleigh convection and unsteady non-penetrative thermal convection, as

$$Ra_{eq} = \frac{\beta g (2\Delta T)(2z*)^3}{\alpha\nu} \qquad (4.1)$$

The following equivalent Rayleigh numbers have been calculated

Condition	Equivalent Rayleigh Number
I	4.55×10^9
II	7.22×10^9
III	10.52×10^9
IV	3.98×10^9

Records of the spatially averaged mean temperature furnished by the resistance wire probe sitting still 1 mm from the lower plate are presented in Figure 4.6. These discouraged any attempt to measure the

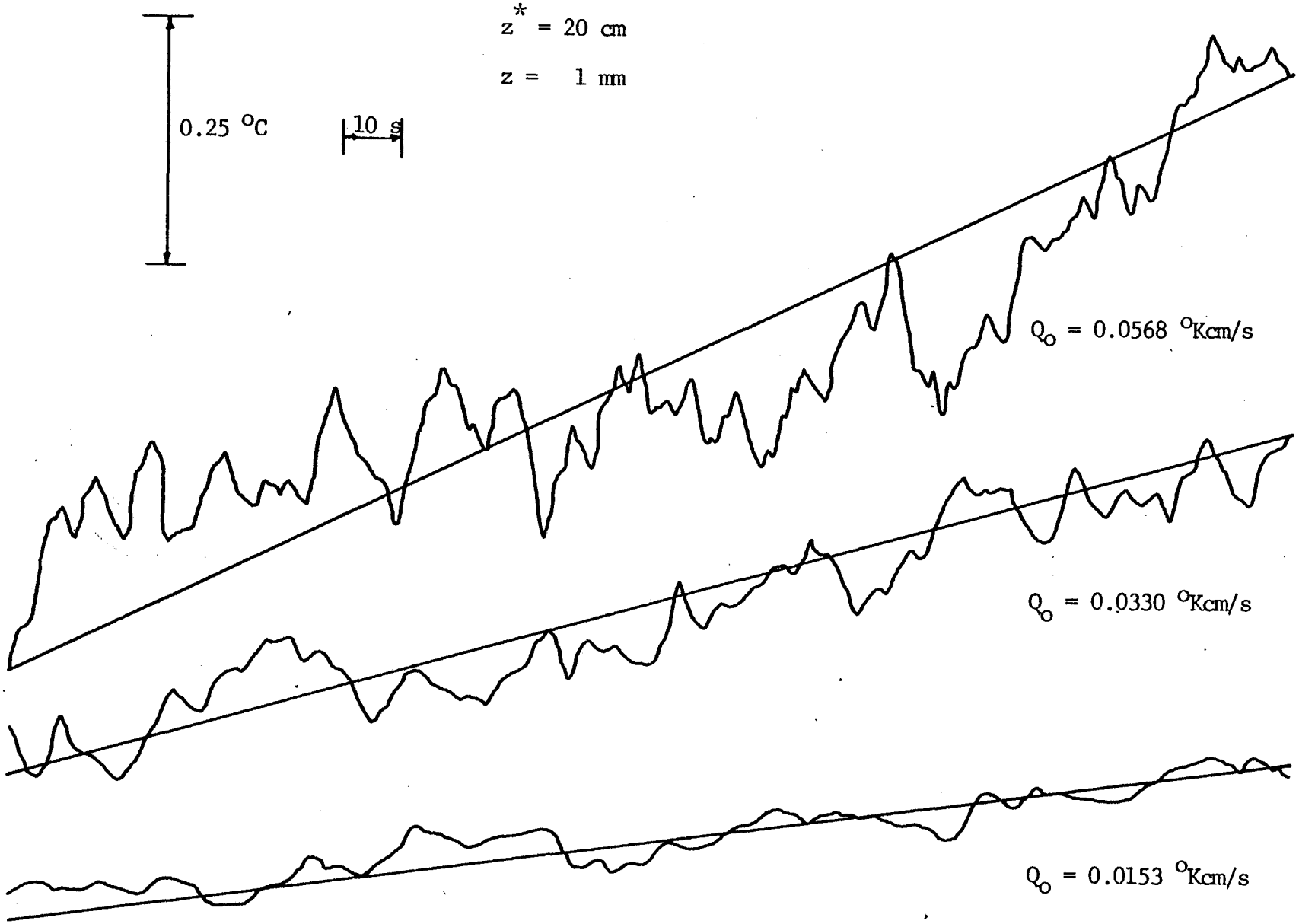

Figure 4.6 - Resistance wire signal sitting still at z = 1 mm.

temperature profile by gradually moving the probe and waiting a certain time interval until the temperature stabilized at that height.

4.3 Joint Probability Density Function

The joint probability density function (JPDF) of the records w-Θ, u-Θ, and w-u were calculated. Typical contours of equal probability at three different heights are shown in Figures 4.7 through 4.18.

The JPDF analysis helps to visualize and calculate the distribution of the signal with respect to their mean values. The axes extend 5 standard deviations to each side and the minimum discrete dimension of each cell was 0.1 standard deviations. Each plot calculation of the JPDF uses all the runs (typically 14 runs) in one set.

Close to the lower boundary, most of the points for w-Θ records concentrate in the first and third quadrants resulting a net positive kinematic heat flux.

The joint distribution of u-w is nearly symmetric in all quadrants resulting an overall balance close to zero and a small correlation of both components of the velocity.

With respect to the Θ axis, u is distributed symmetrically in the u-Θ joint distribution and Θ still shows the long tail in the positive side (high temperature skewness) of the Θ axis. The maximum of the Θ distribution happens at approximately one standard deviation to the negative side, indicating the value shown by the temperature signal most of the time during the scans. Typical record of simultaneous w, Θ and u are shown in Figures 4.19 to 4.24.

At higher levels, for example $z/z^* = 0.5$, the destruction of the w-Θ correlation by the highly turbulent field produces smaller

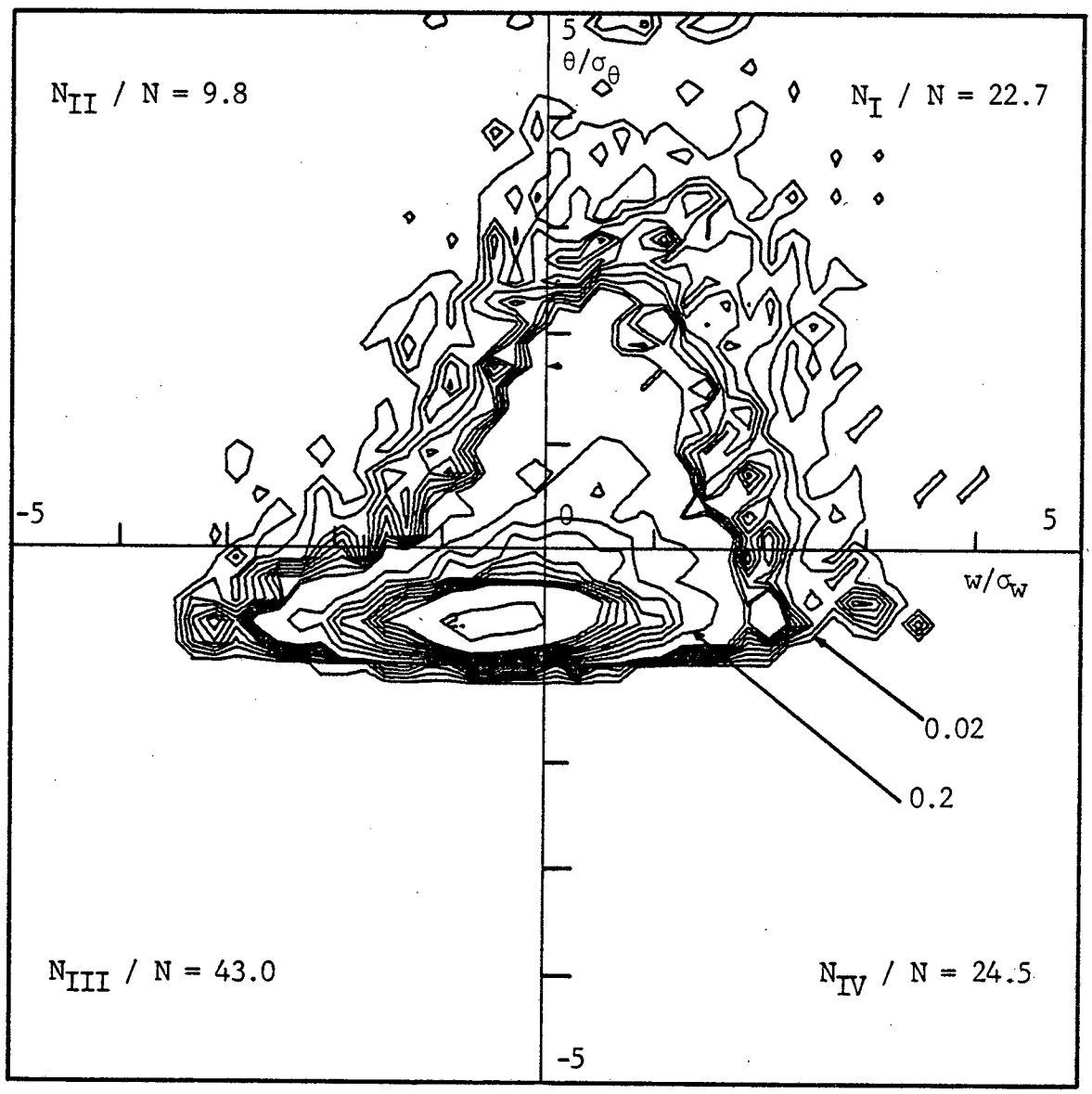

Figure 4.7 - w-θ joint probability density function, $z/z^* = 0.0175$. Condition III.

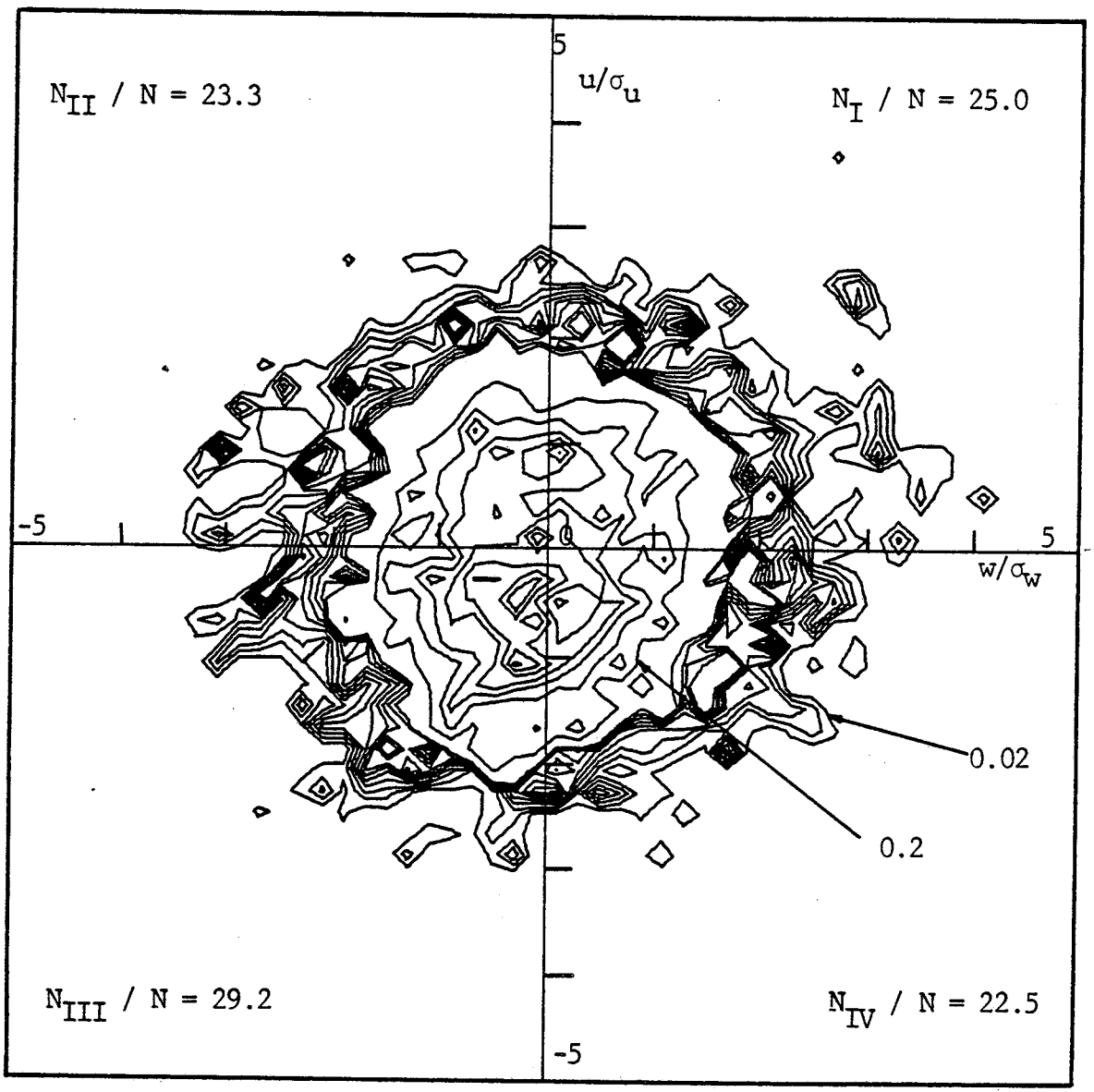

Figure 4.8 - u-w joint probability density function, $z/z^* = 0.0175$. Condition III.

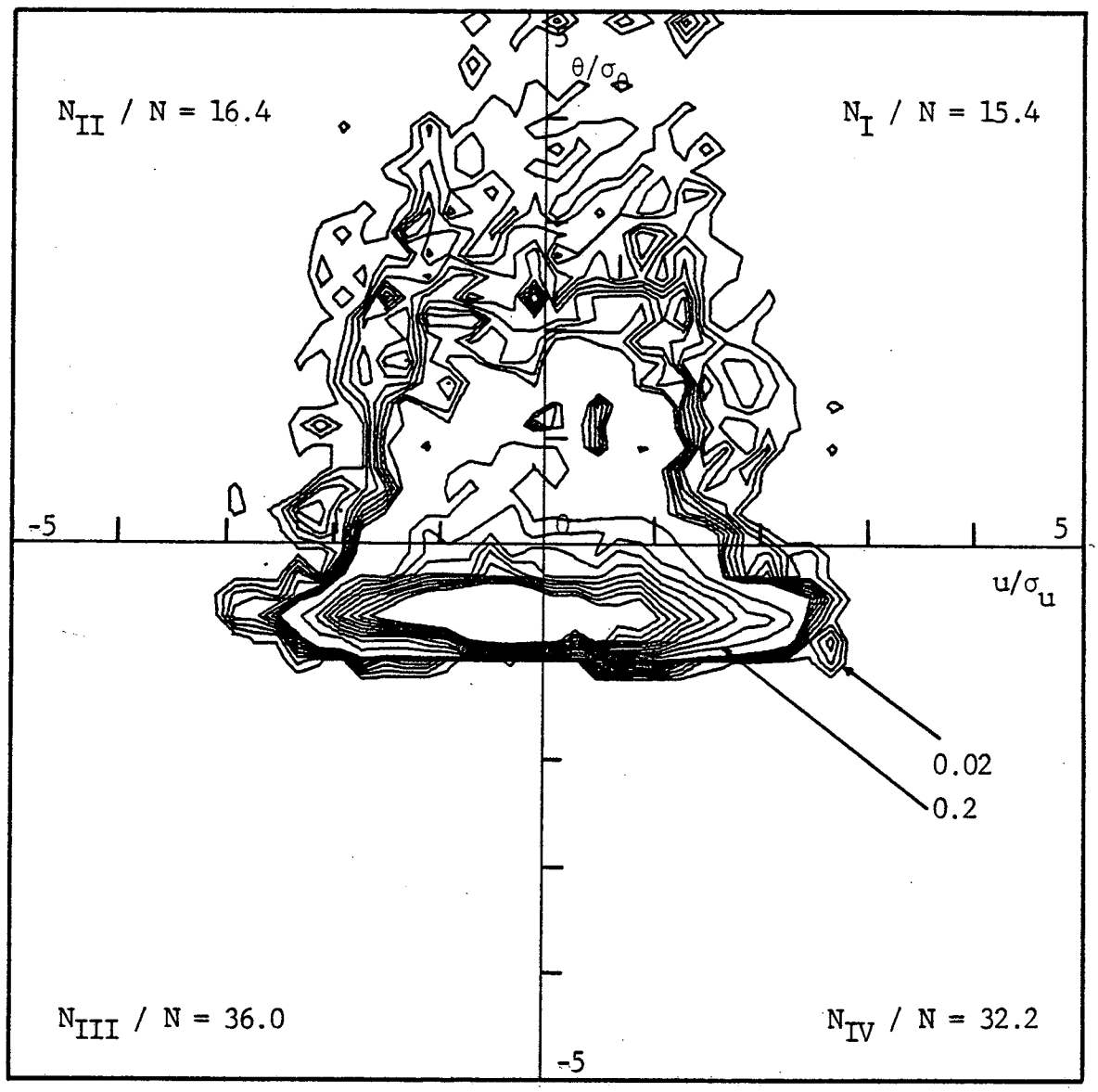

Figure 4.9 - u-θ joint probability density function, $z/z^* = 0.0175$. Condition III.

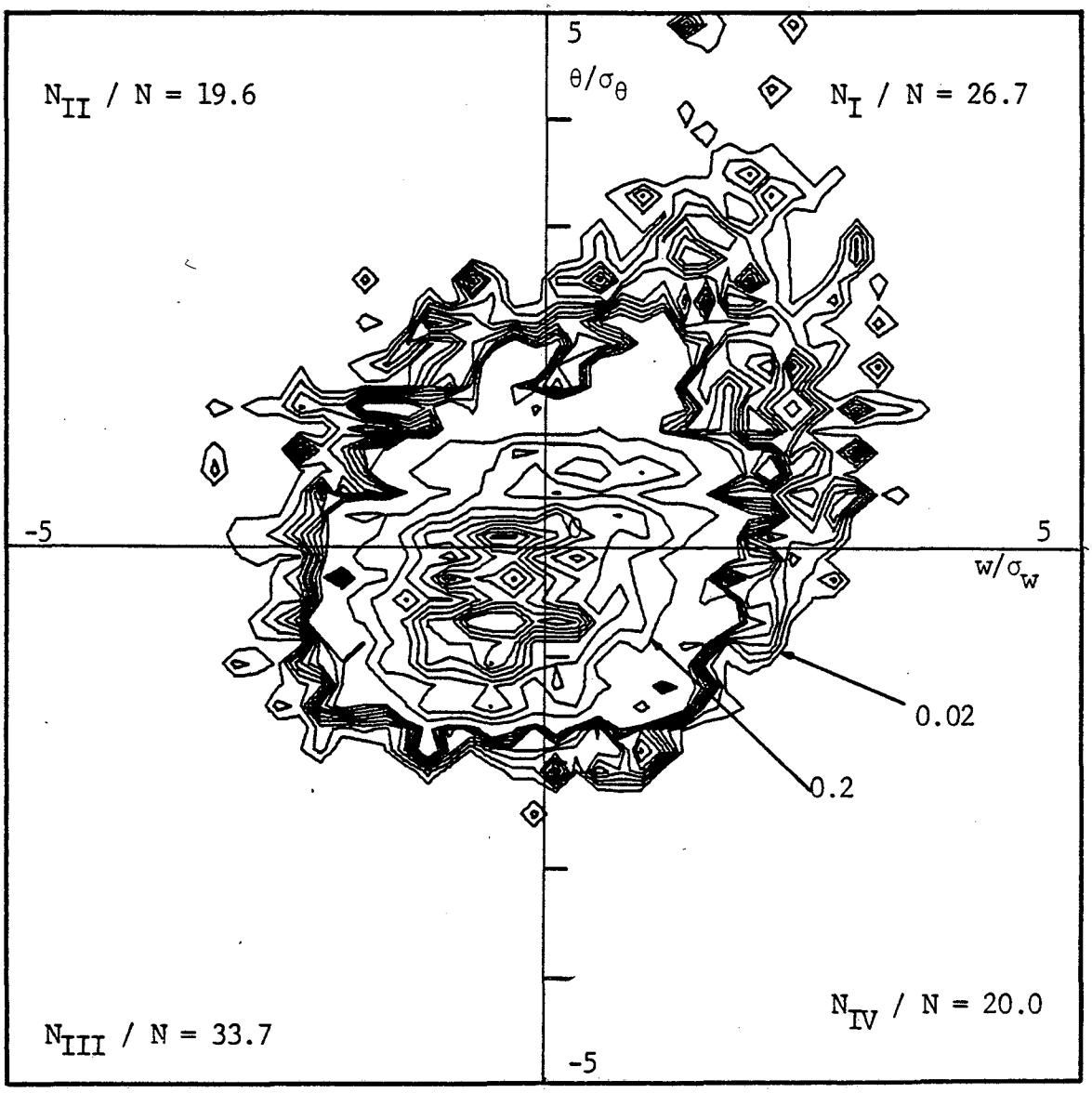

Figure 4.10 - w-θ joint probability density function, $z/z^{*} = 0.5025$. Condition III.

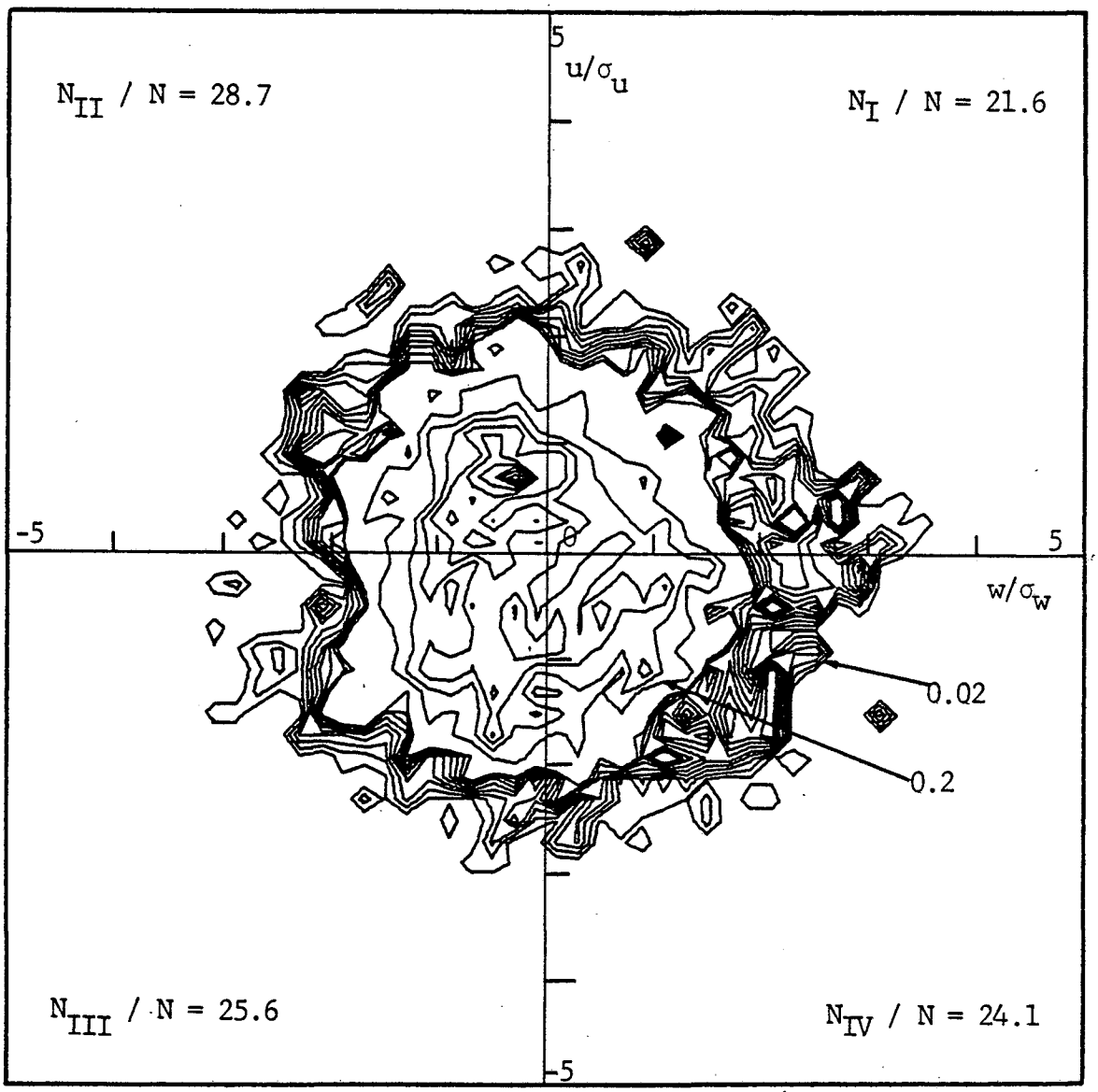

Figure 4.11 - u - w joint probability density function, $z/z^* = 0.5025$. Condition III.

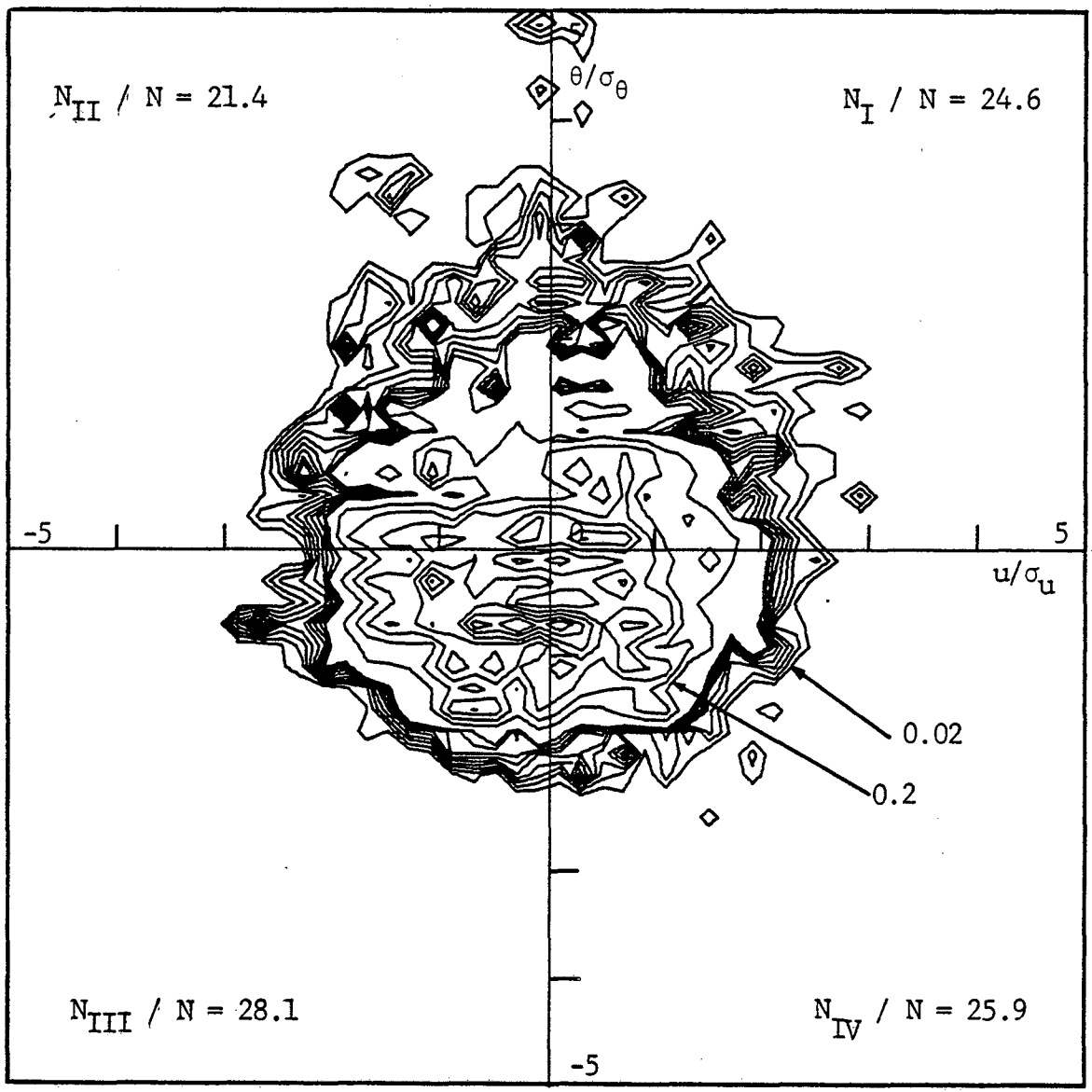

Figure 4.12 - u - θ joint probability density function, $z/z^* = 0.5025$. Condition III.

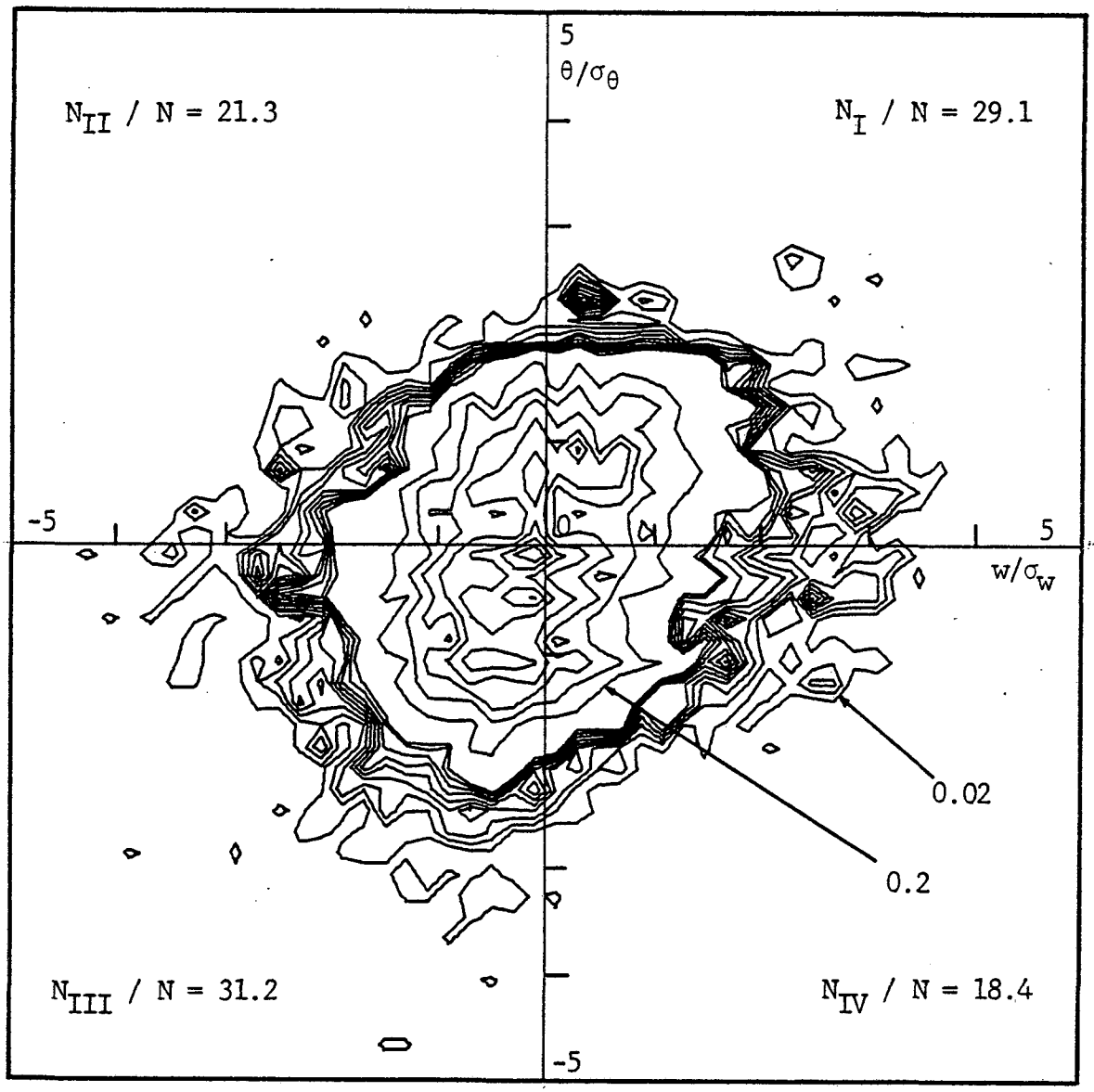

Figure 4.13 - w-θ joint probability density function, $z/z^{*} = 0.960$. Condition III.

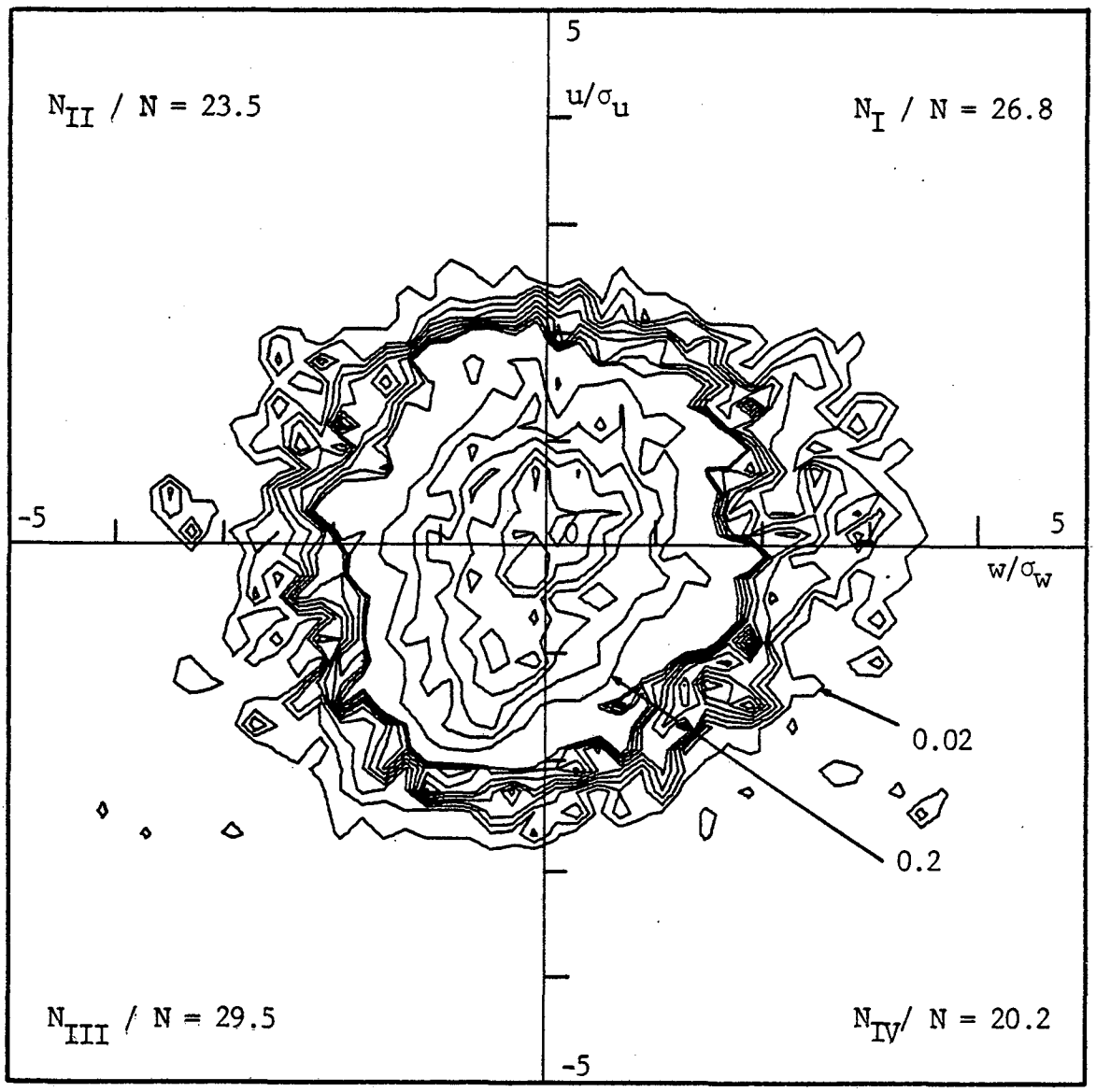

Figure 4.14 - w-u joint probability density function, $z/z^* = 0.960$. Condition III.

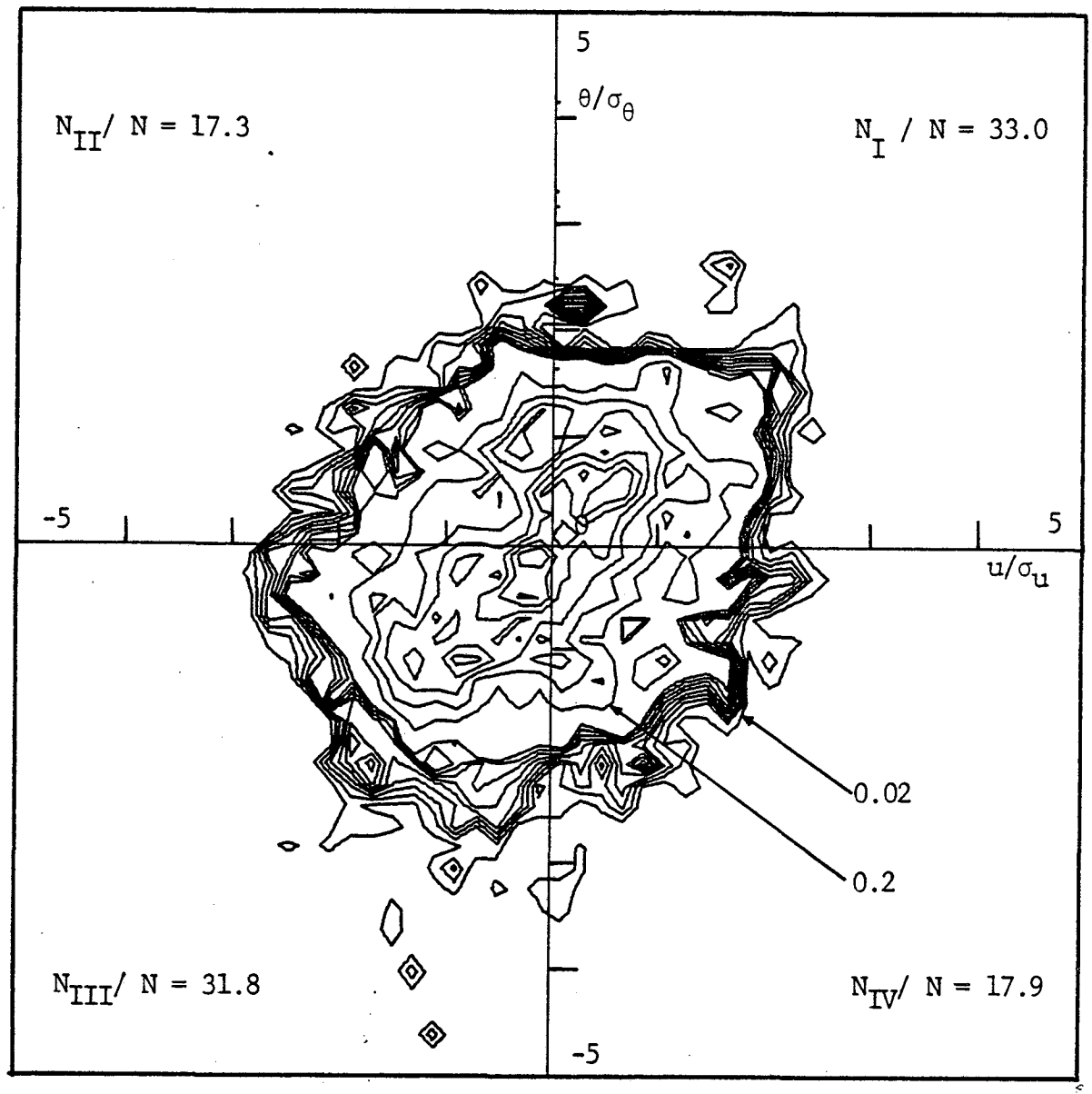

Figure 4.15 - u-θ joint probability density function, $z/z^* = 0.960$. Condition III.

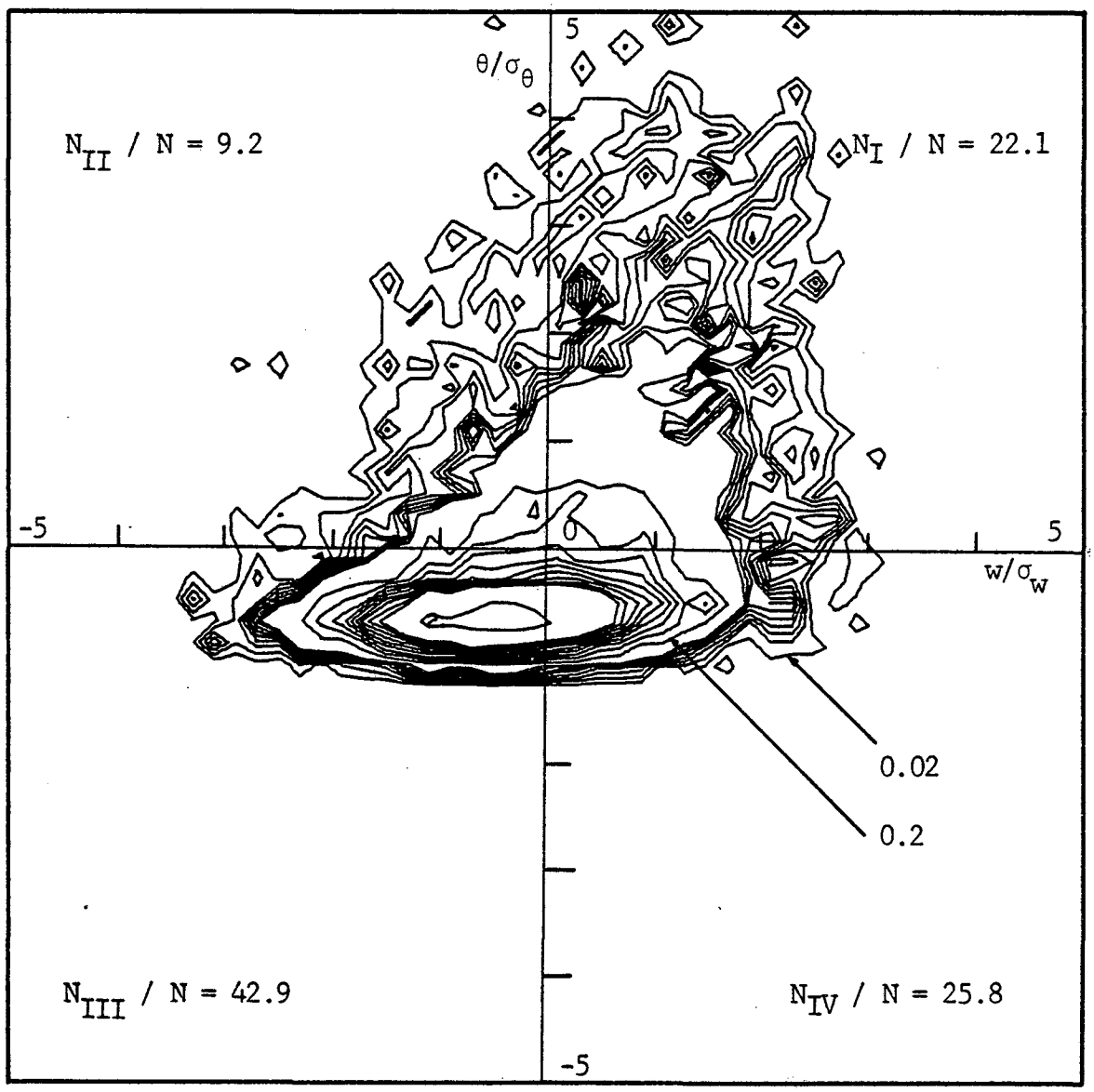

Figure 4.16 - w-θ joint probability density function, $z/z^* = 0.0175$. Condition I.

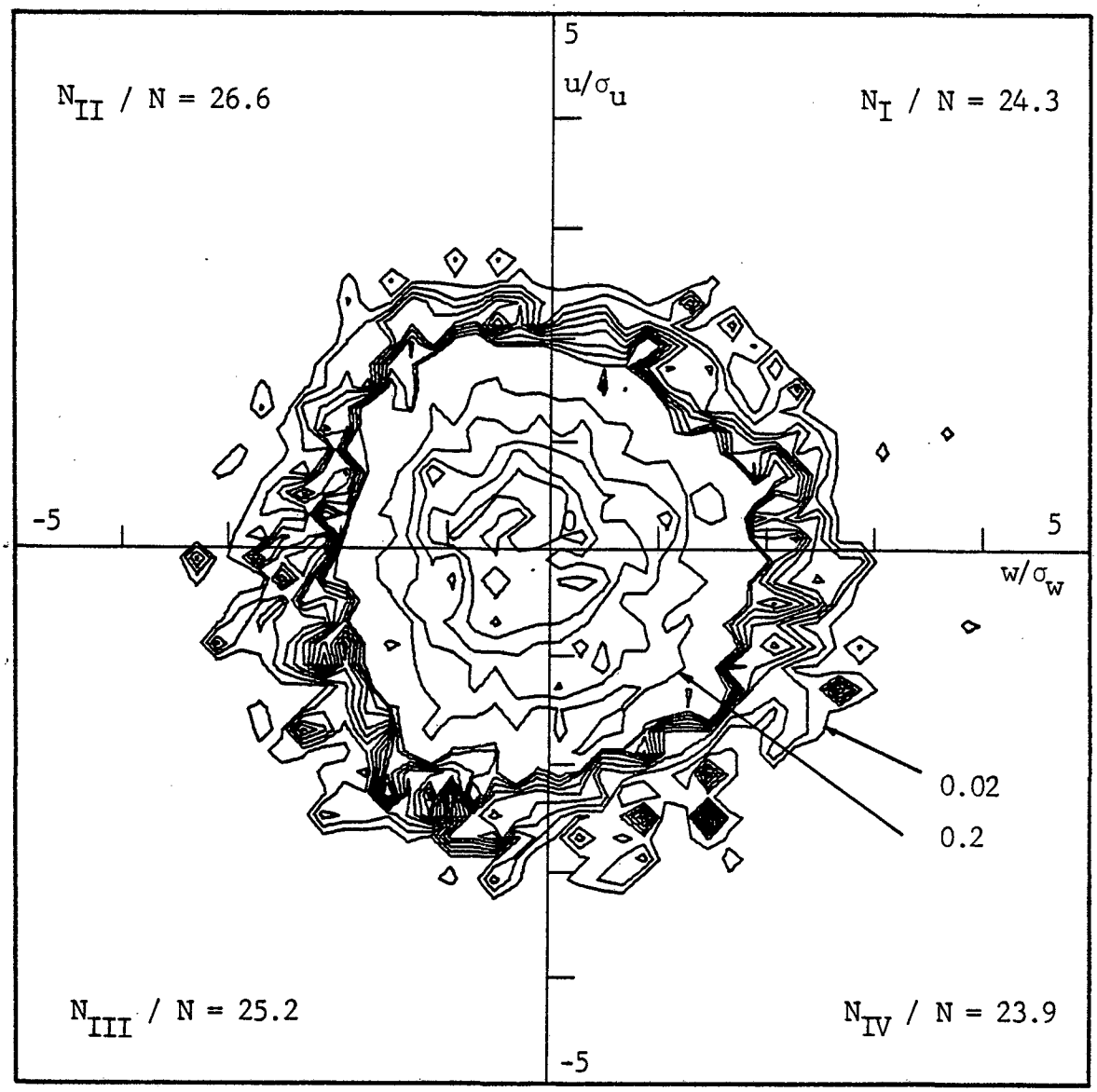

Figure 4.17 - w - u joint probability density function, $z/z^* = 0.0175$. Condition I.

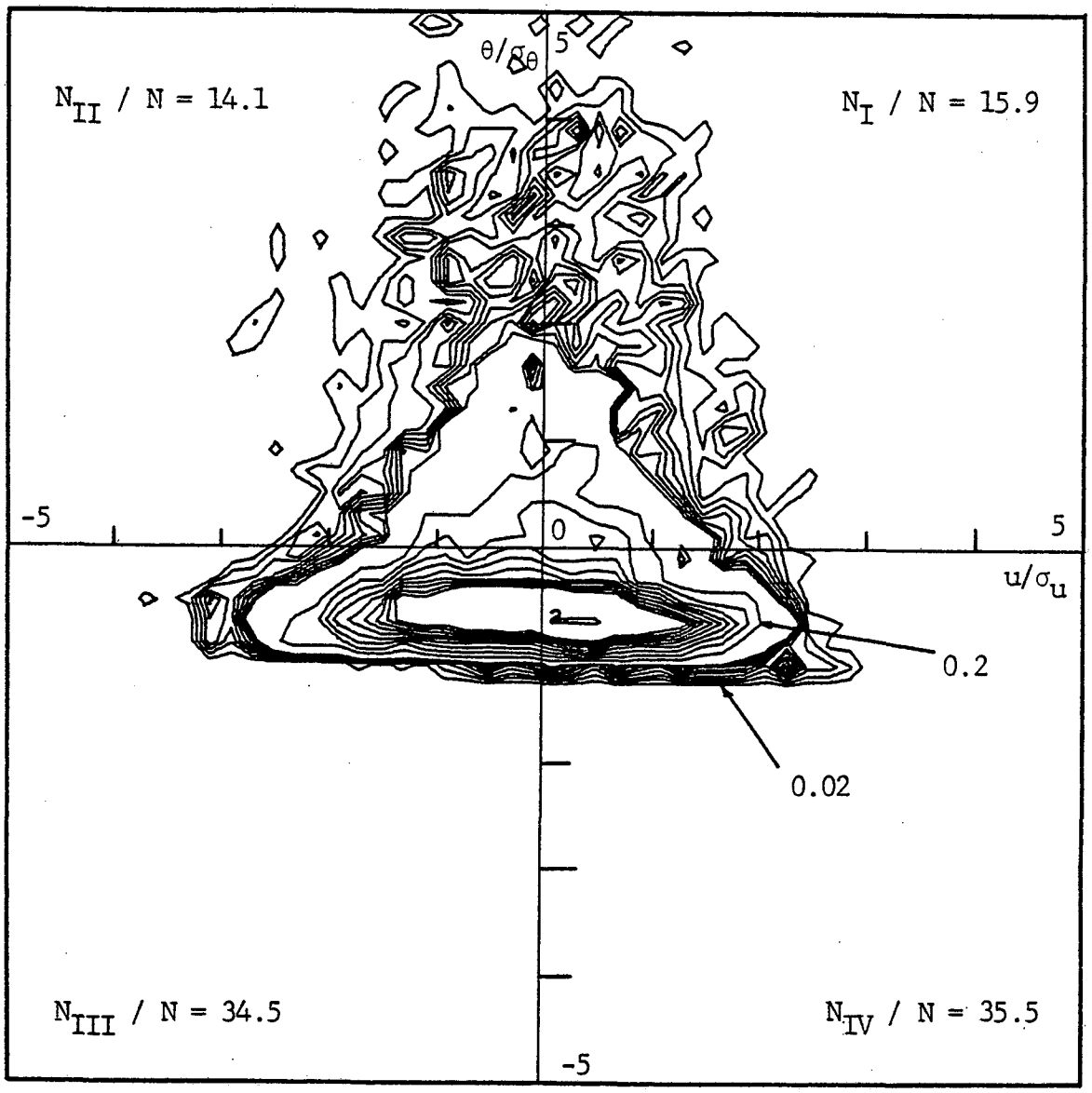

Figure 4.18 - u - θ joint probability density function, $z/z^* = 0.0175$. Condition I.

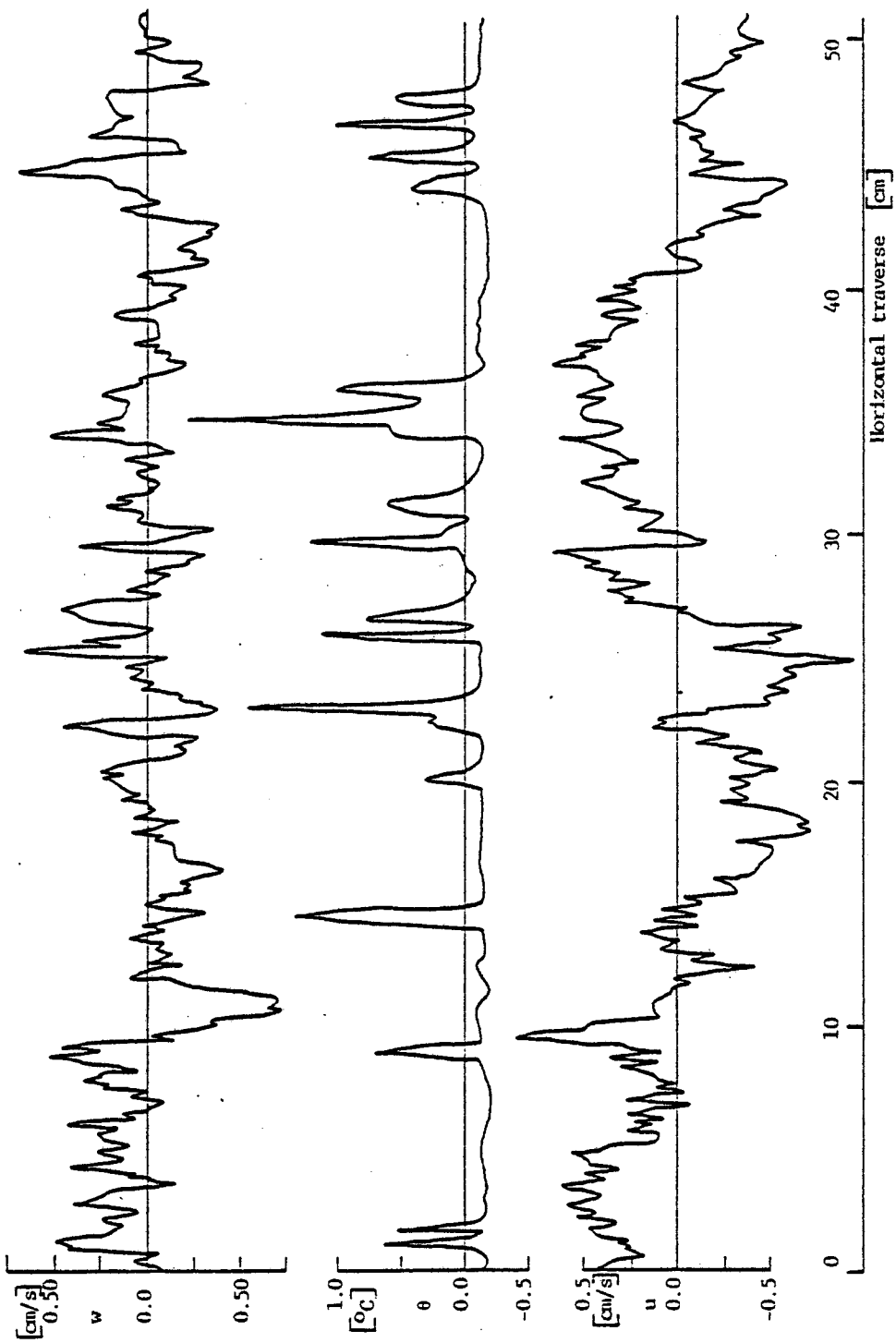

Figure 4.19 - Typical records of w-θ-u at z= 3.5 mm. Condition III.

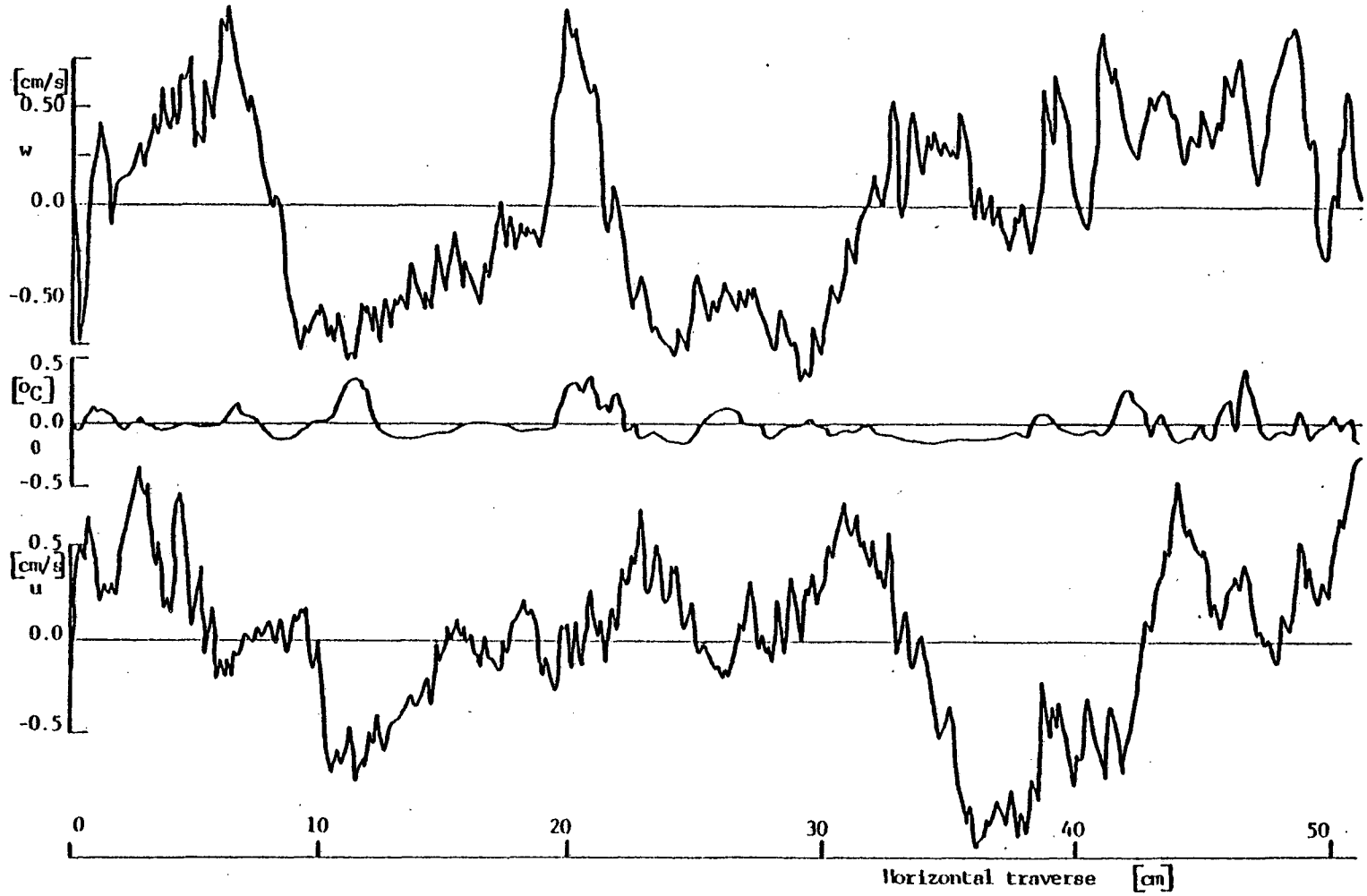

Figure 4.20 - Typical records of w-θ-u at z = 35 mm. Condition III.

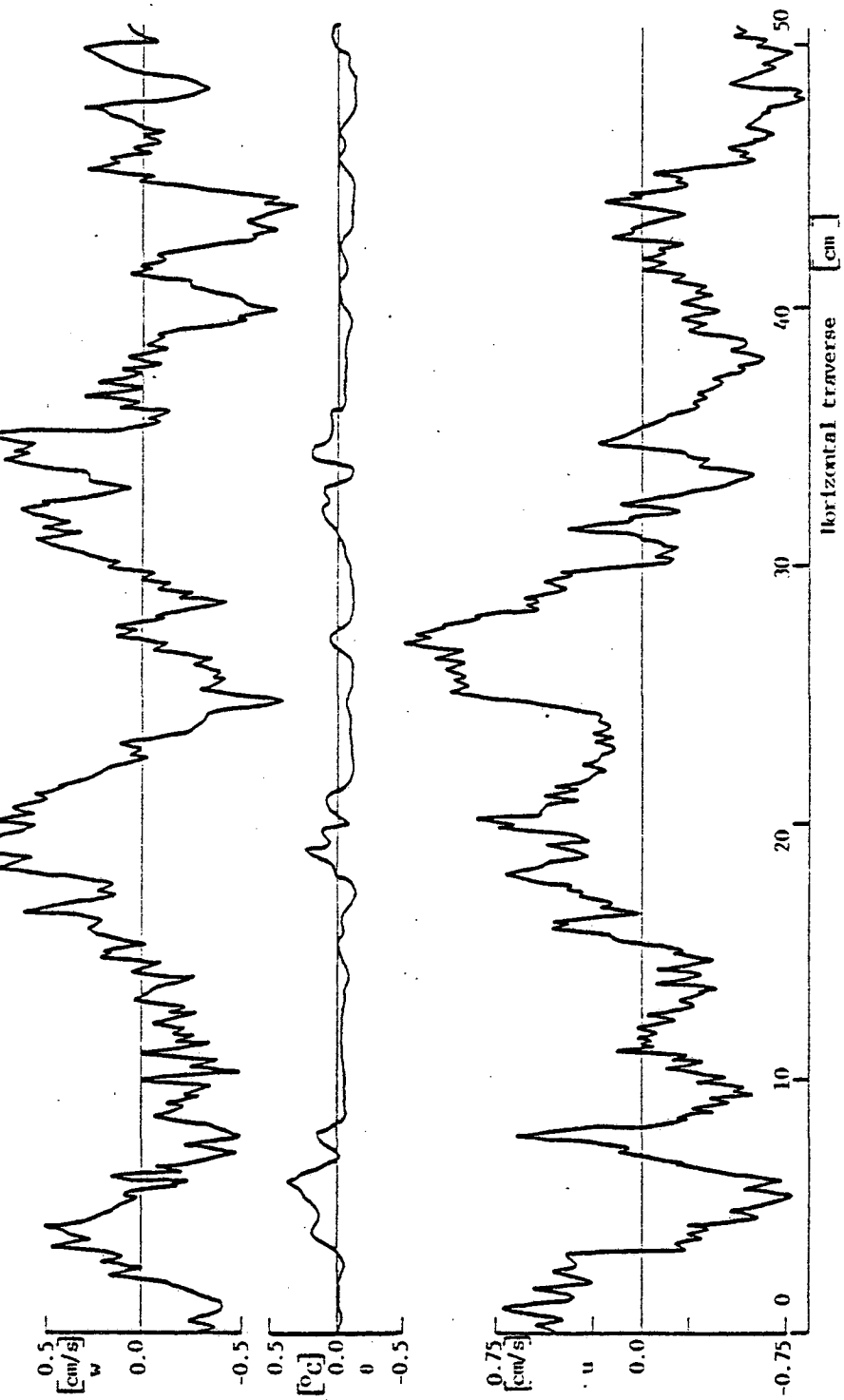

Figure 4.21 - Typical records of w-θ-u at z = 60 mm. Condition III.

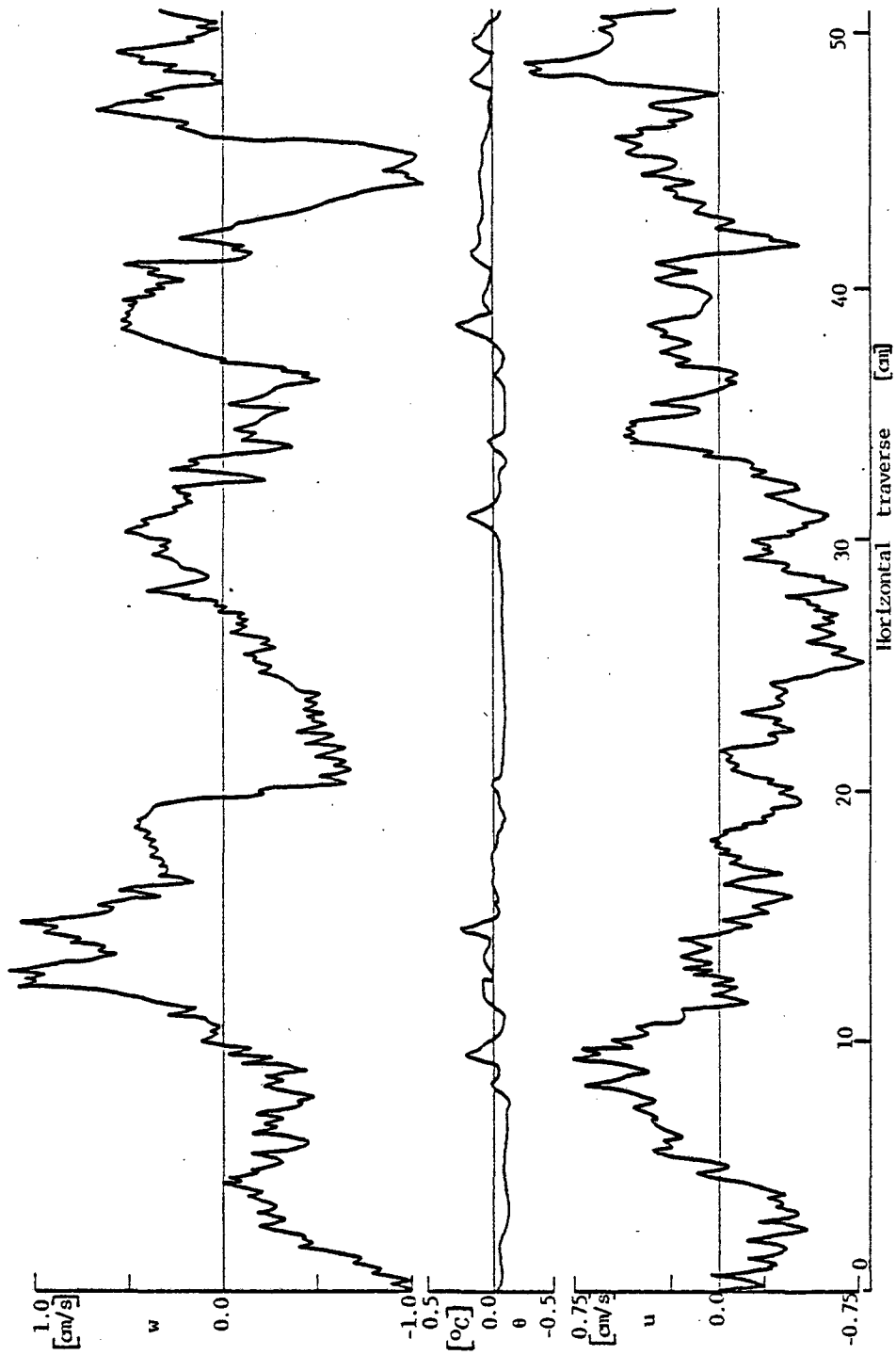

Figure 4.22 - Typical records of w-θ-u at z = 100.5 mm. Condition III.

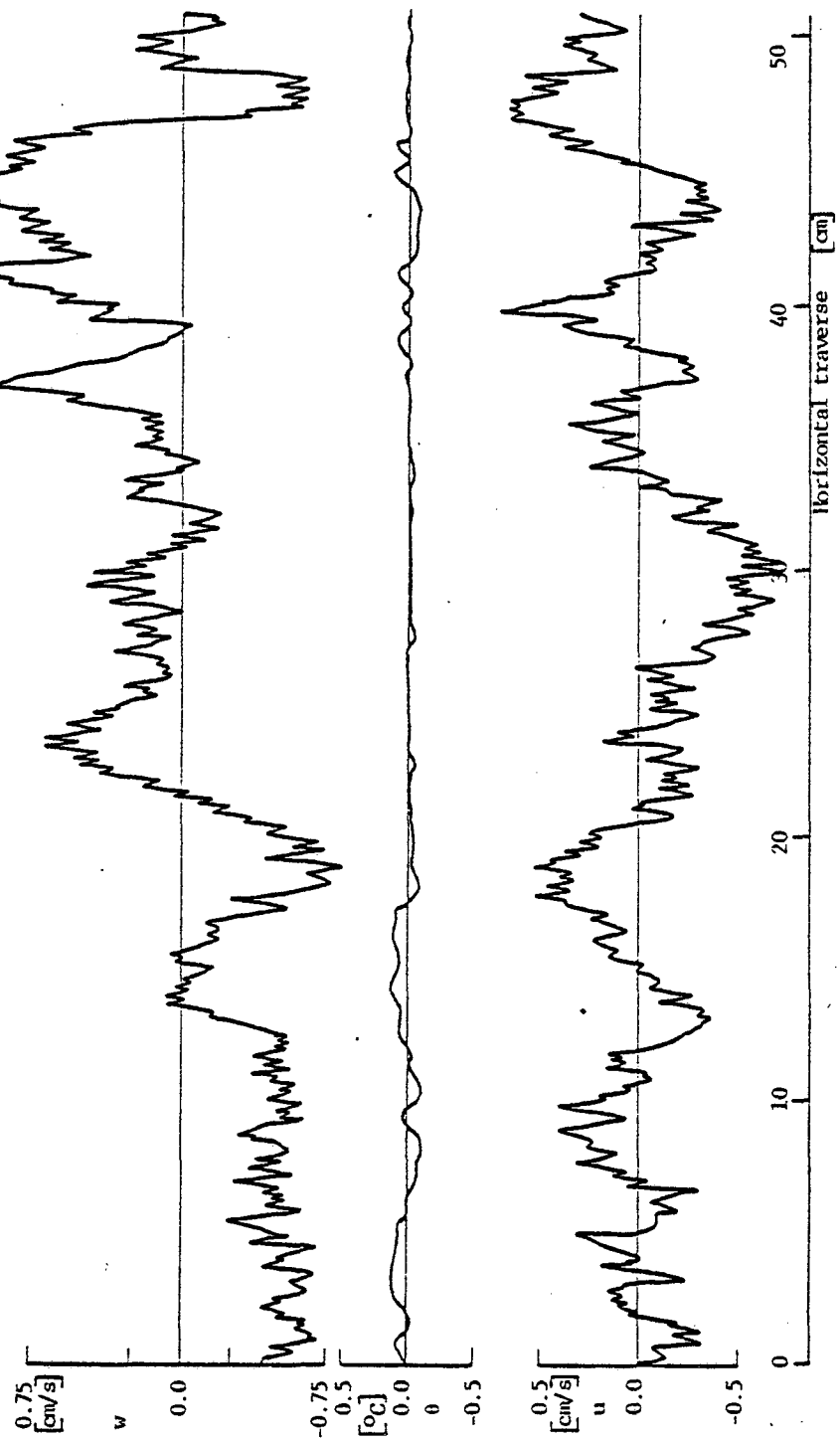

Figure 4.23 - Typical records of w-θ-u at z = 144.5 mm. Condition III.

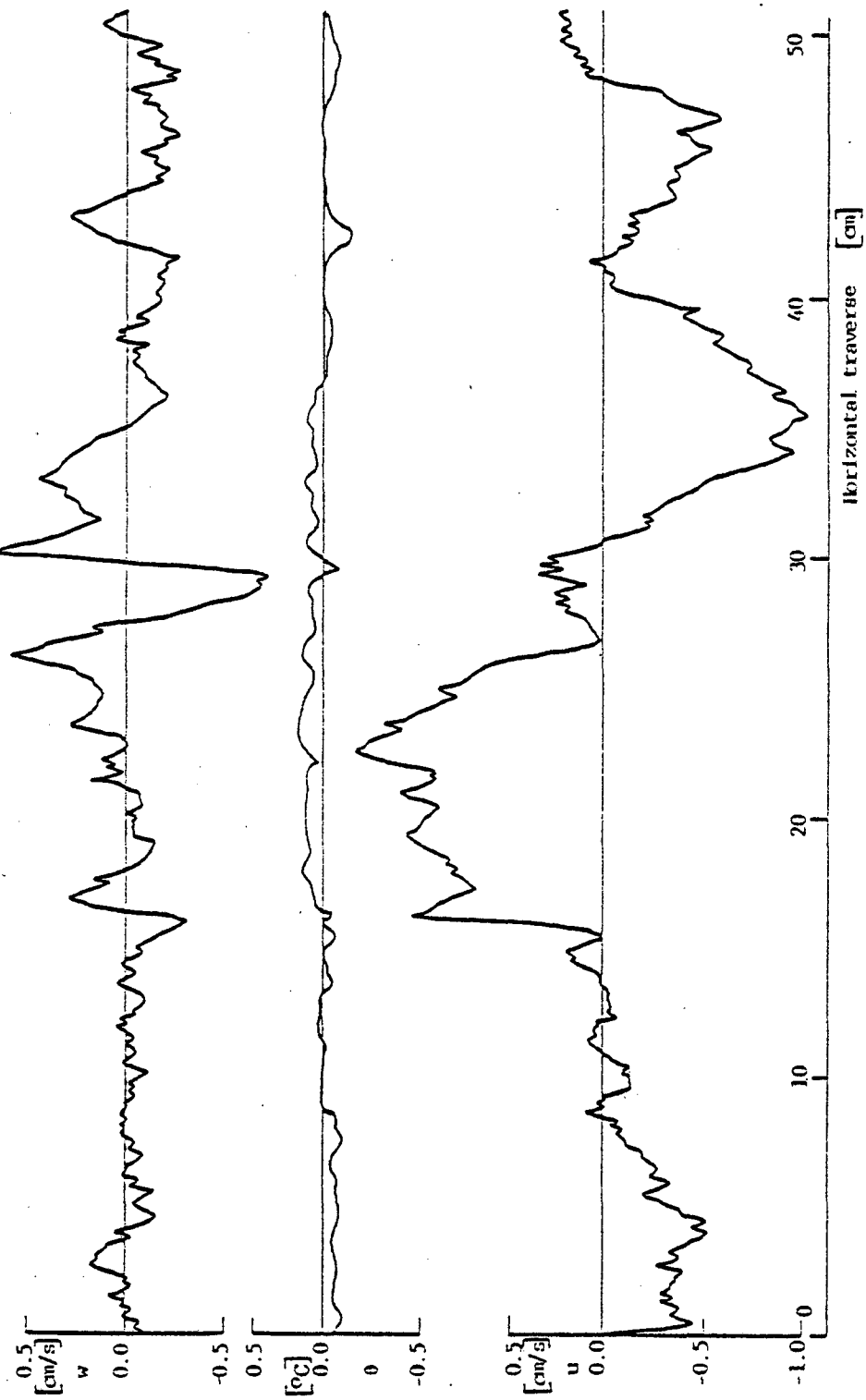

Figure 4.24 - Typical records of w-θ-u at z = 192 mm. Condition III.

transport of kinematic heat flux. The asymmetry of the temperature density function is diminished but vertical velocity fluctuations continue to have high values. The w-u and u-θ distributions show essentially the same features as was previously pointed out.

Close to the upper plate, w-θ JPDF is almost circular showing a little eccentricity in the positive heat flux direction (1st and 3rd quadrants), and u-θ also show a positive net balance in the same direction.

As the heat flux is increased, the joint probability density function at the same heights shows features similar to those previously described.

4.4 Central Moments

All the data used to compute the central moments are related in Appendix A-5 with the specification of the main parameters of the runs, tagword 1, number of runs and tape in which it is recorded.

Besides giving information about the shape of the distribution and density functions, the moments are used to evaluate the terms of the kinetic and thermal energy equations.

Table 3 shows the important parameters of the different conditions under which the measurements were performed, the turbulent Reynolds number and the symbols representing each condition in the vertical profile of the central moments.

Figures 4.25 through 4.41 show the vertical profiles of some of the moments scaled by the convective scales and RMS values.

Table 3

Important Parameters in Different Conditions

Condition	Q_o [^oKcm/s]	w^* [cm/s]	z^* [cm]	θ^* [^oK]	z_o [cm]	w_o [cm/s]	θ_o [^oK]	$Pe_* = (z^*/z_o)^{4/3}$	Symbol in the plots
I	0.0153	0.450	20	0.034	0.029	0.051	0.300	6090	○
II	0.0330	0.581	20	0.057	0.024	0.062	0.532	7840	□
III	0.0568	0.696	20	0.082	0.021	0.071	0.800	9370	△
IV	0.0450	0.585	15	0.077	0.022	0.067	0.672	6000	⬡
V	0.0141	0.369	12	0.038	0.030	0.050	0.282	2950	▽

Properties were evaluated at 30^oC.

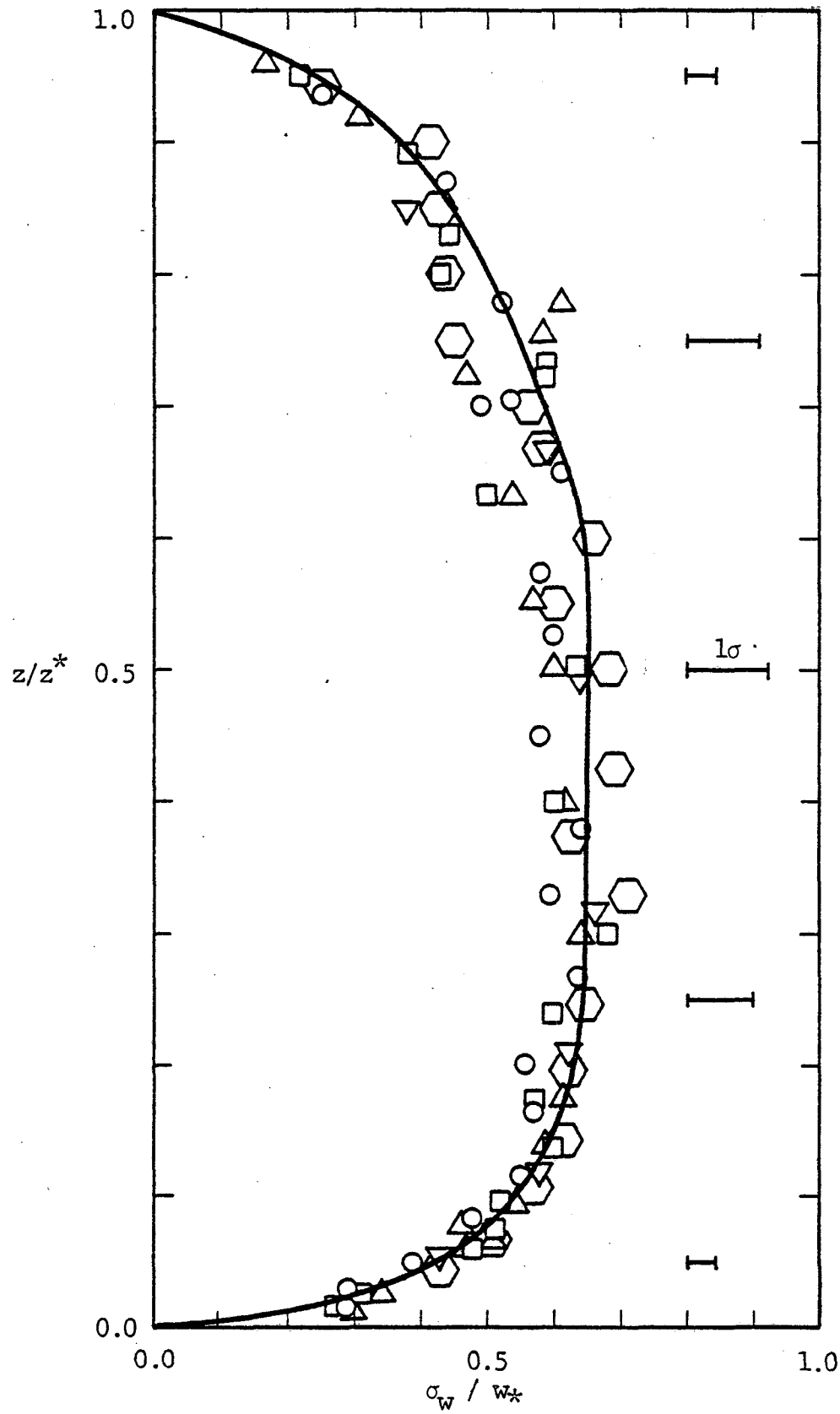

Figure 4.25 - Profile of RMS vertical velocity fluctuations.
○ - Pe_* = 6090, □ - Pe_* = 7840, △ - Pe_* = 9370,
⬡ - Pe_* = 6000, ▽ - Pe_* = 2950.

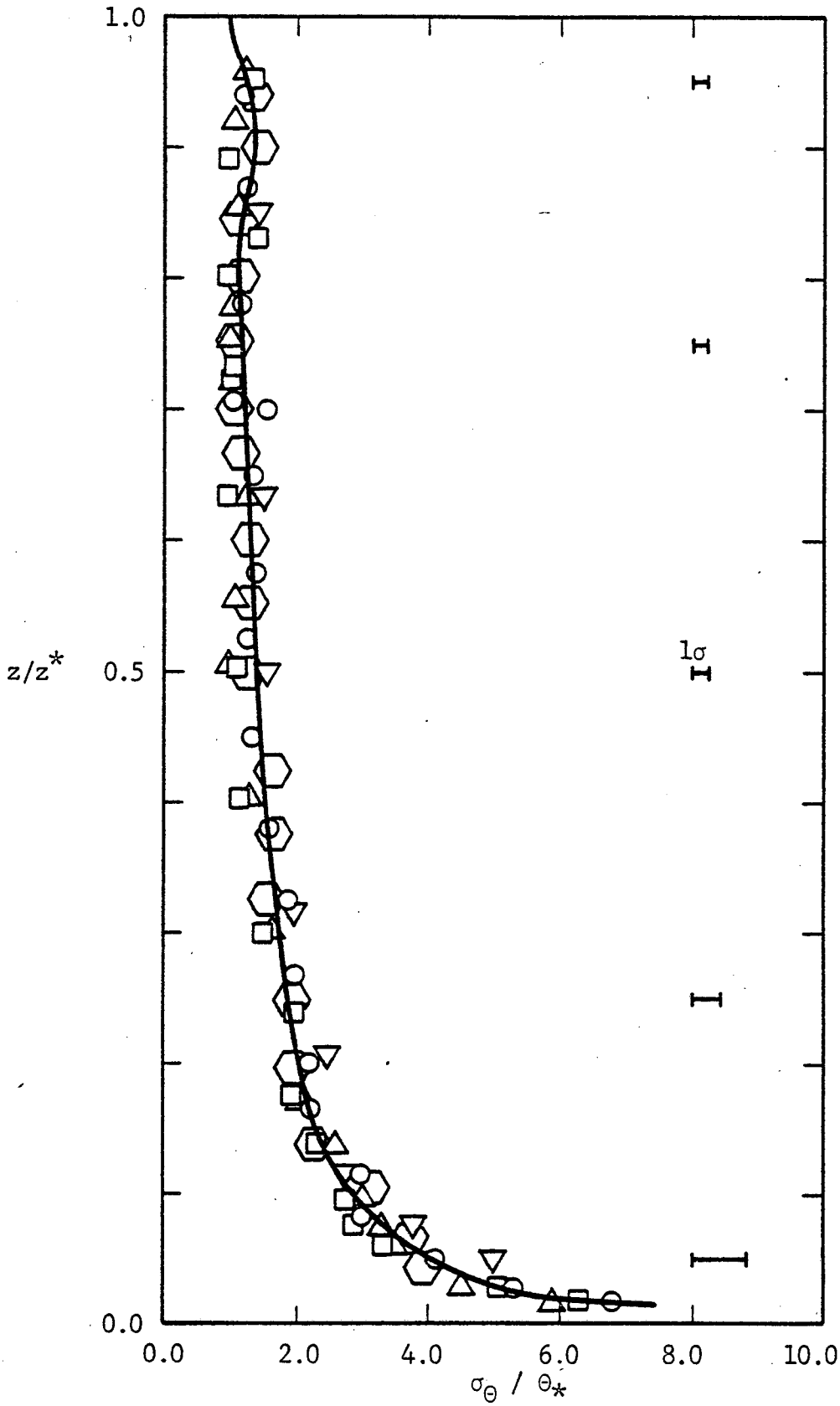

Figure 4.26 - Profile of RMS temperature fluctuations. Symbols defined in Figure 4.25.

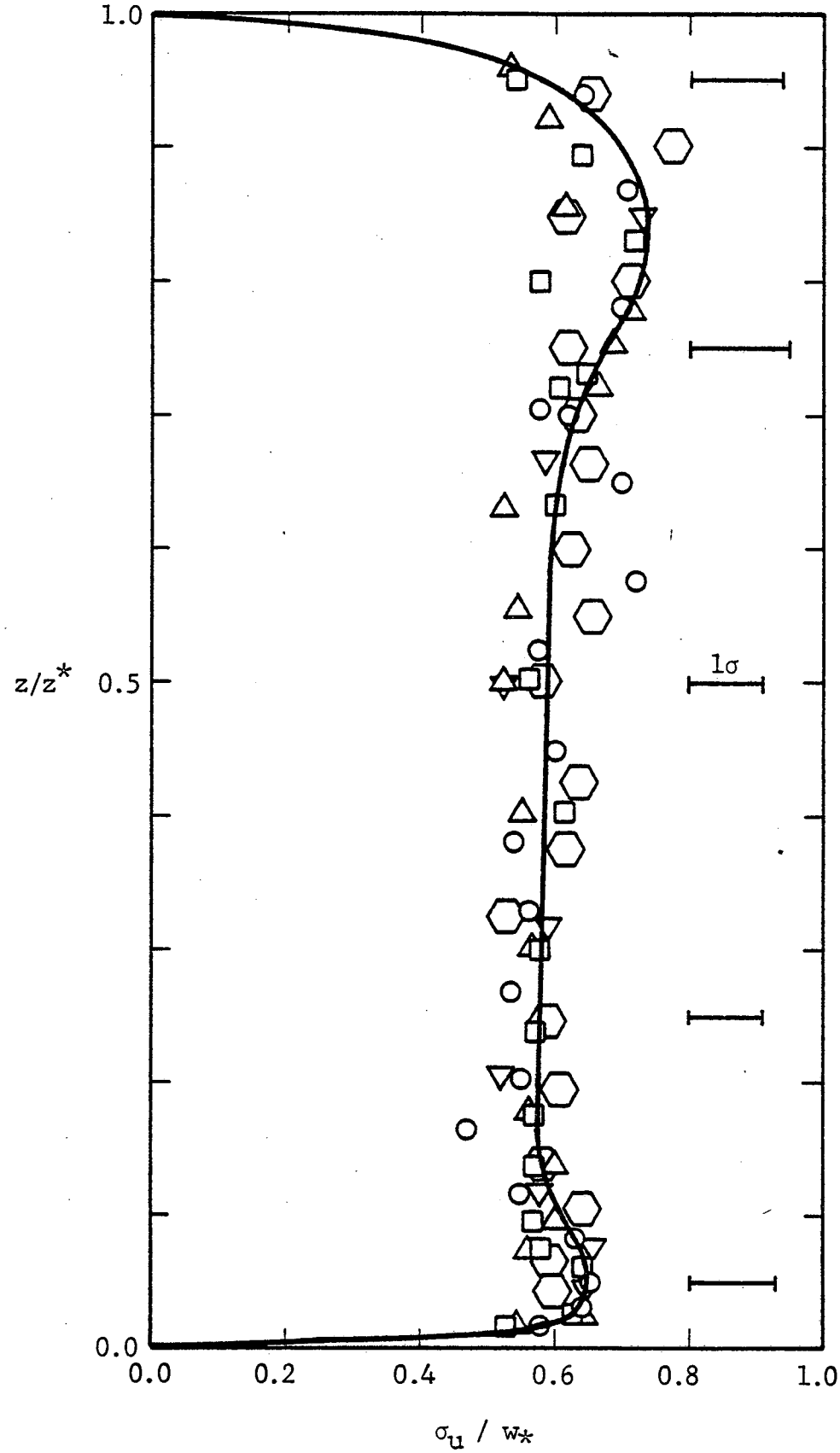

Figure 4.27 - Profile of RMS horizontal velocity fluctuations. Symbols defined in Figure 4.25.

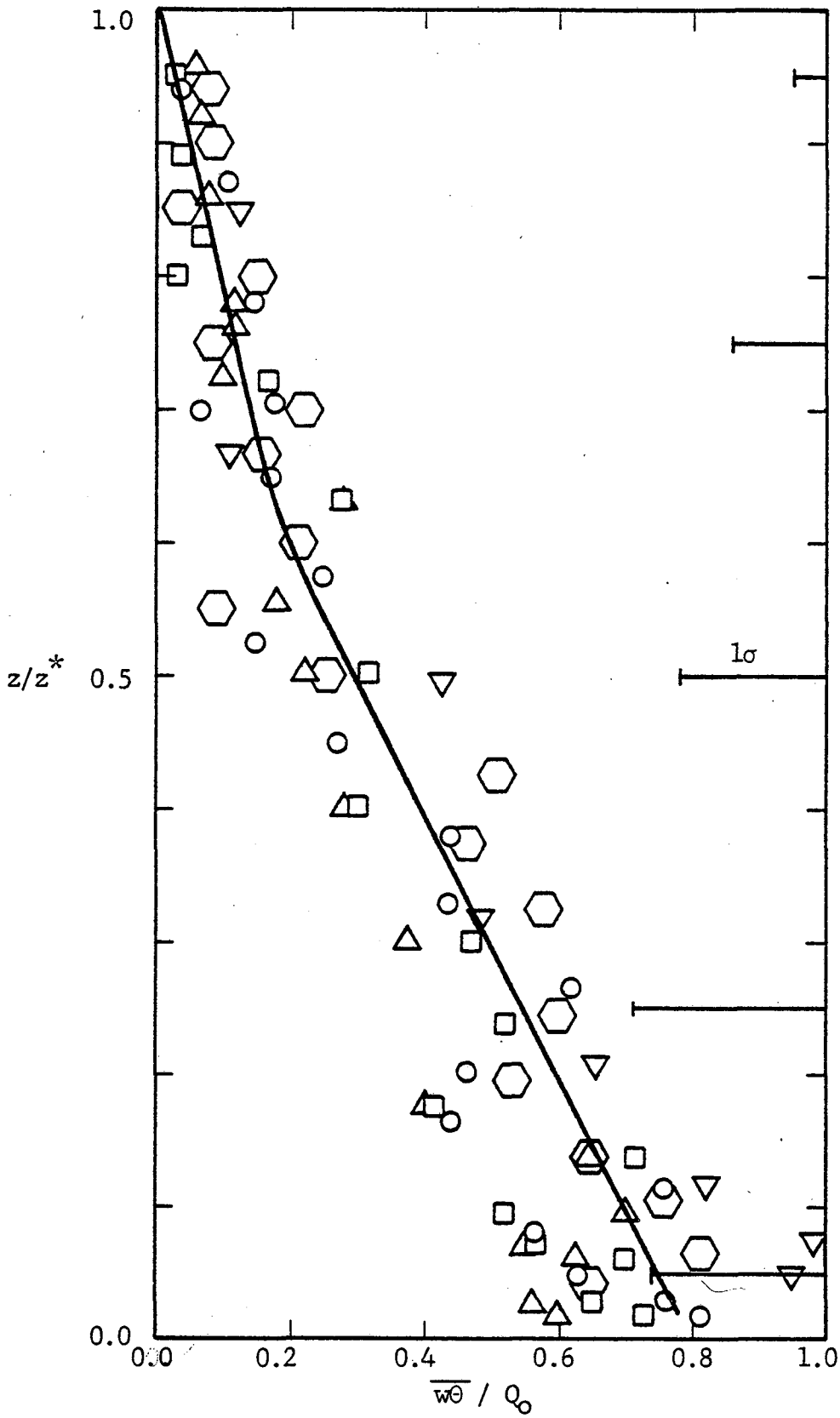

Figure 4.28 - Kinematic heat flux - Symbols defined in Figure 4.25.

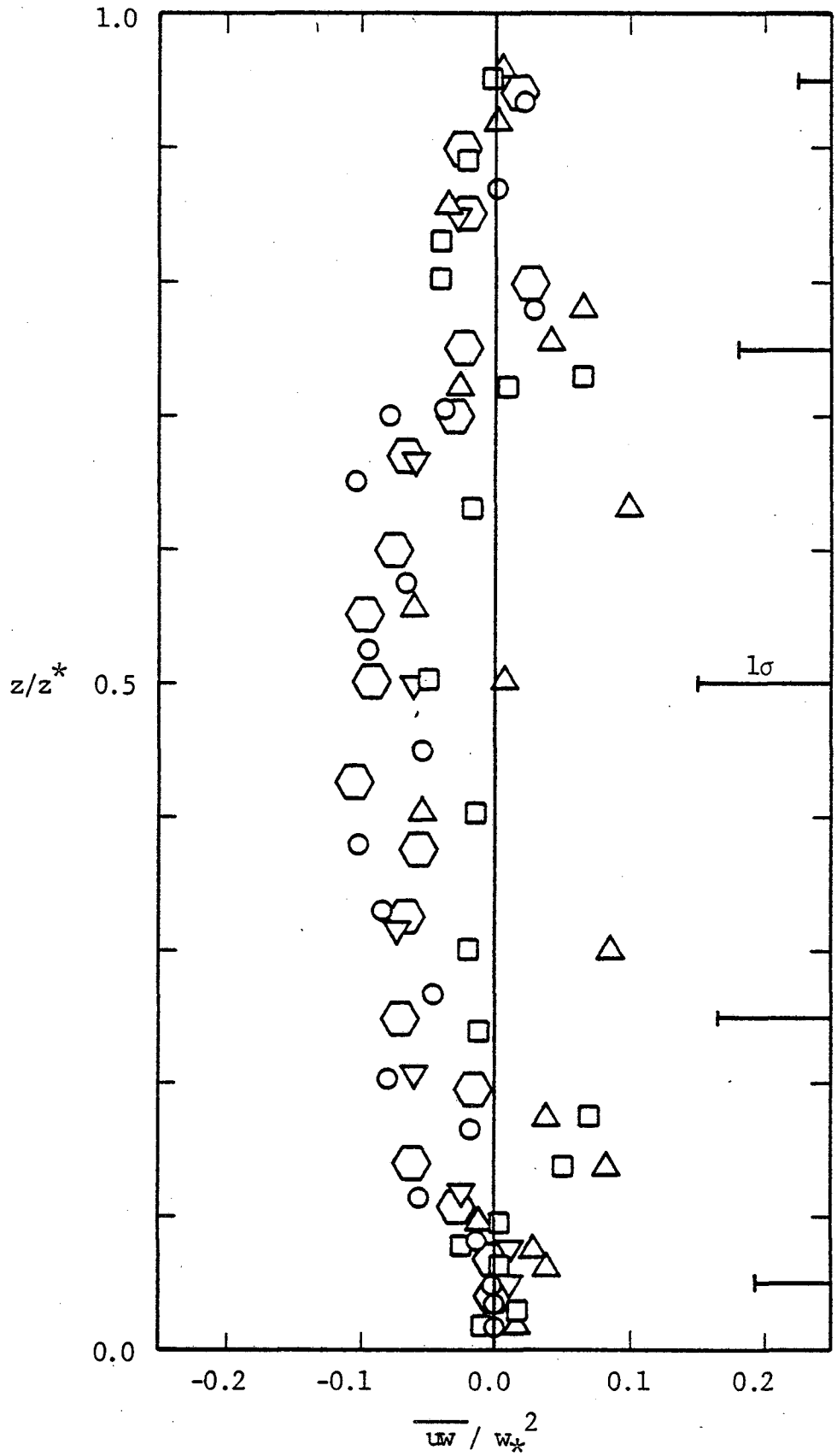

Figure 4.29 - Cross-moment of horizontal and vertical velocities. Symbols defined in Figure 4.25.

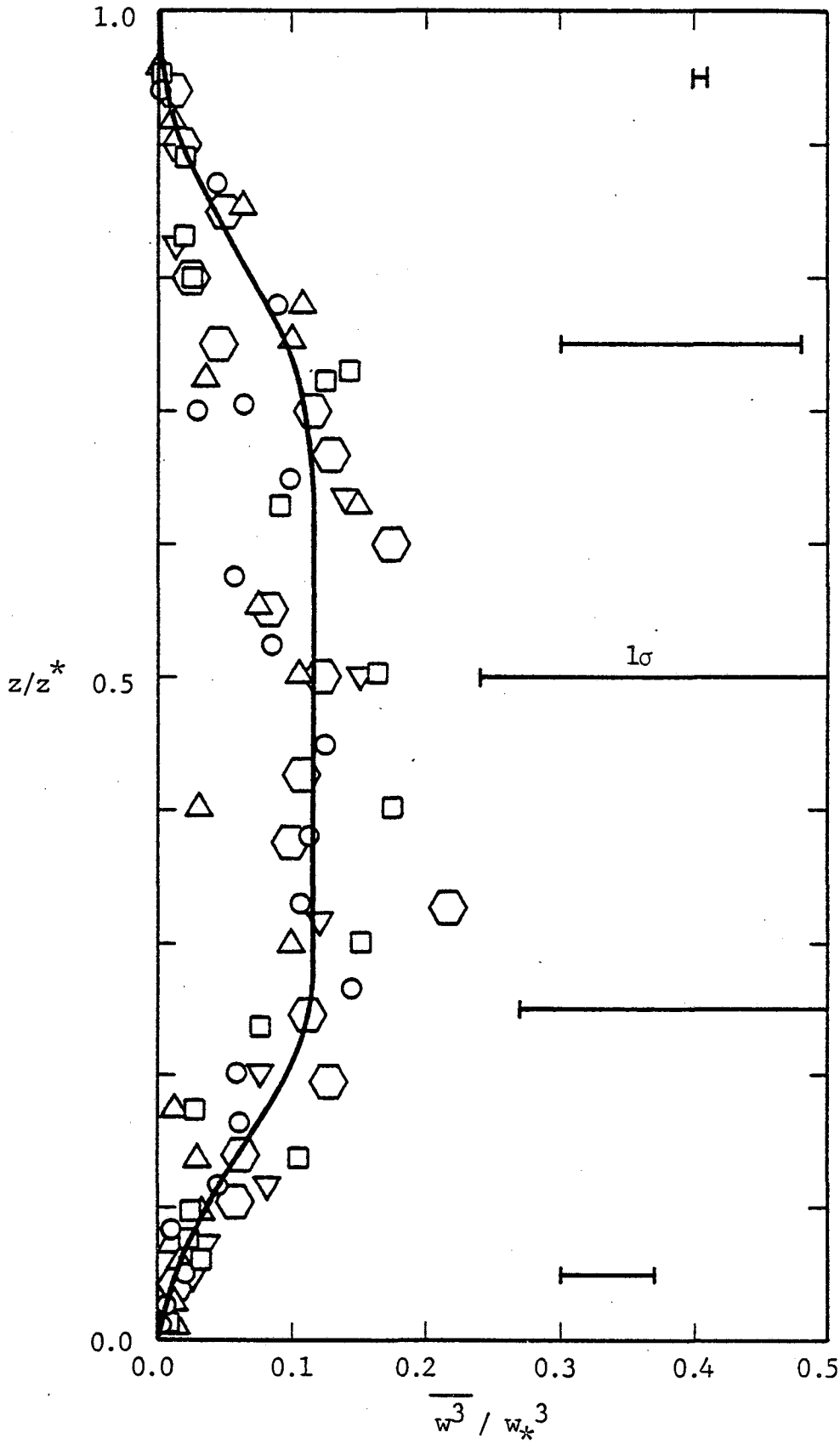

Figure 4.30 - Third order moment of vertical velocity. Symbols defined in Figure 4.25.

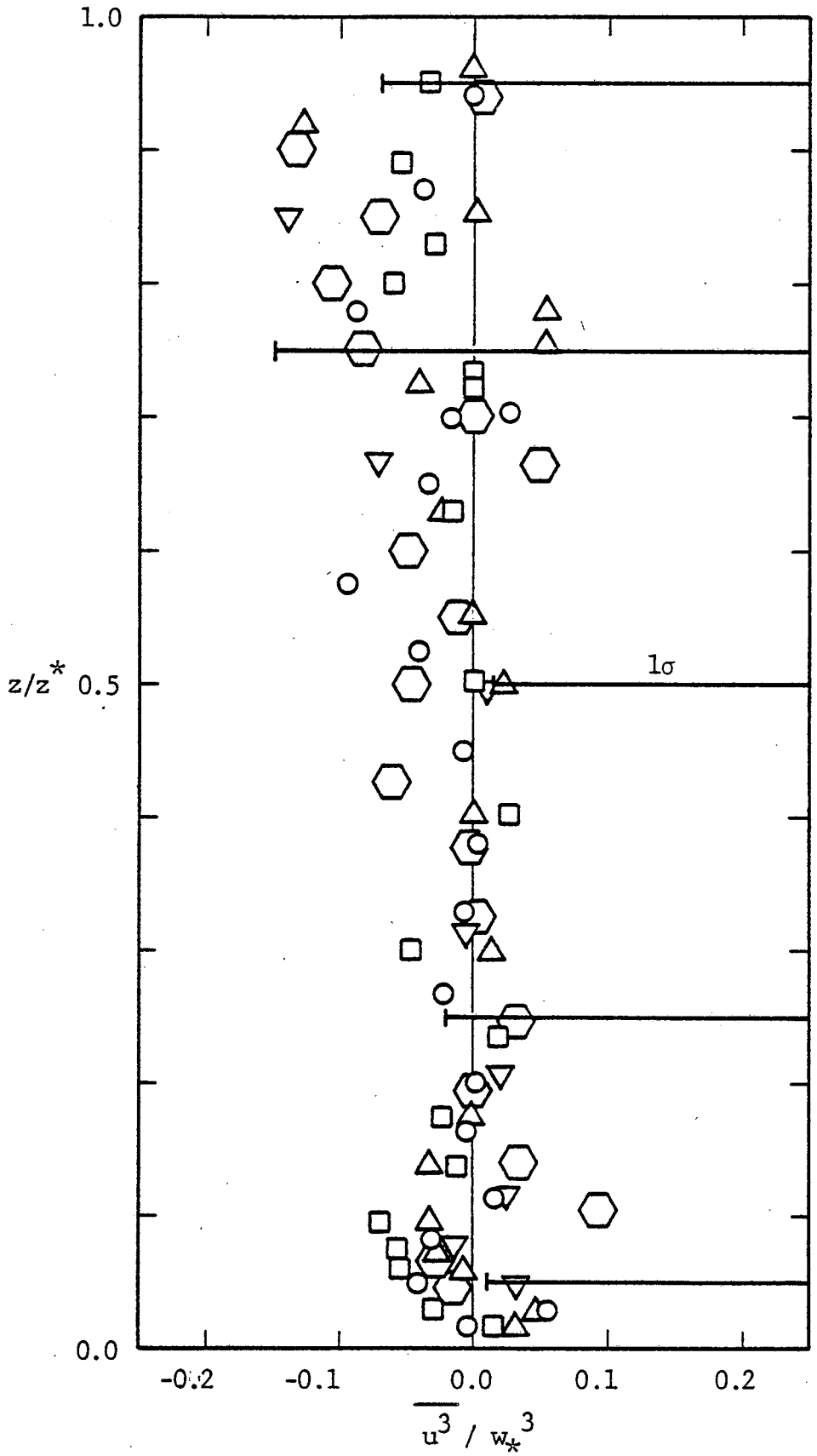

Figure 4.31 - Third order moment of horizontal velocity. Symbols defined in Figure 4.25.

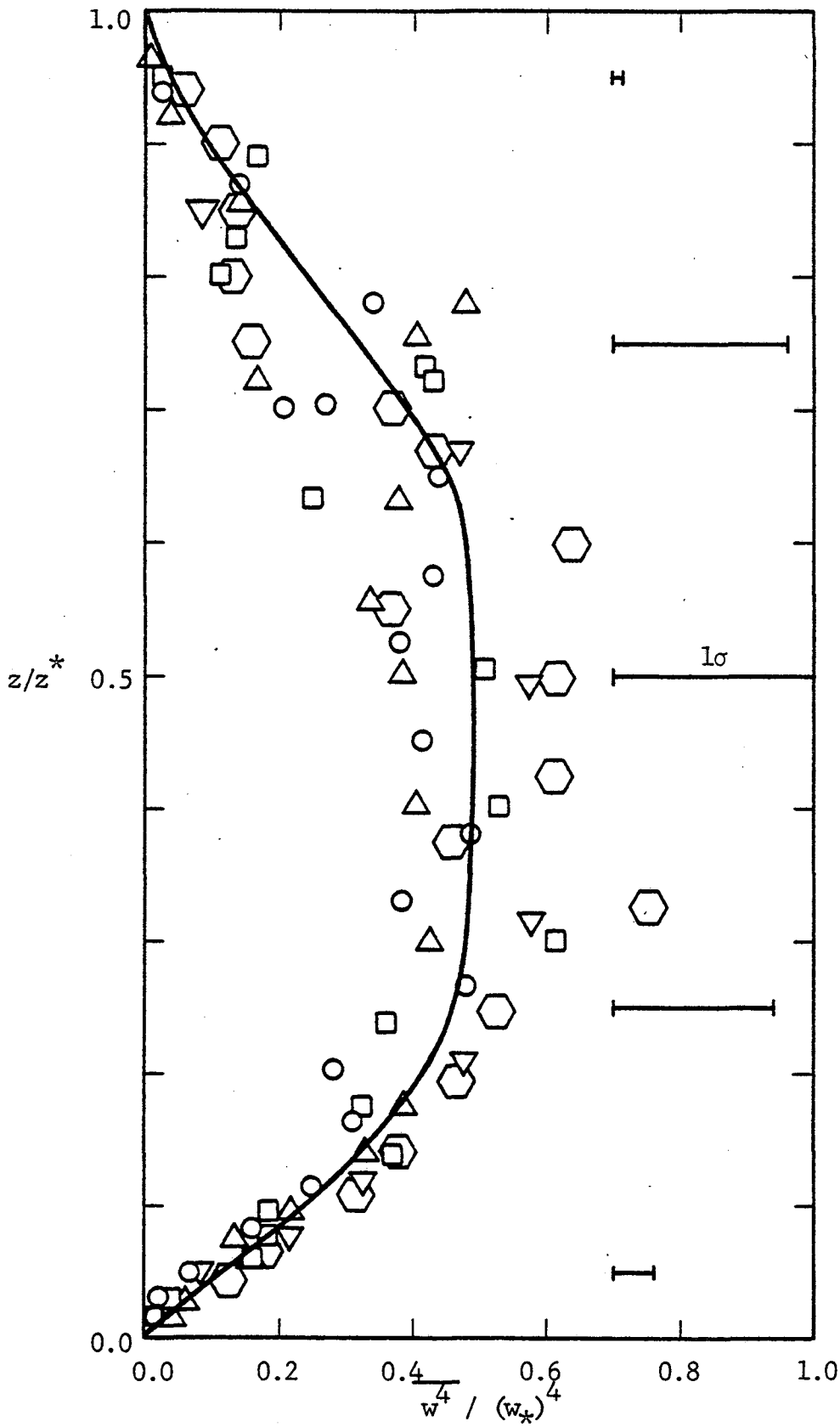

Figure 4.32 - Fourth order moment of vertical velocity. Symbols defined in Figure 4.25.

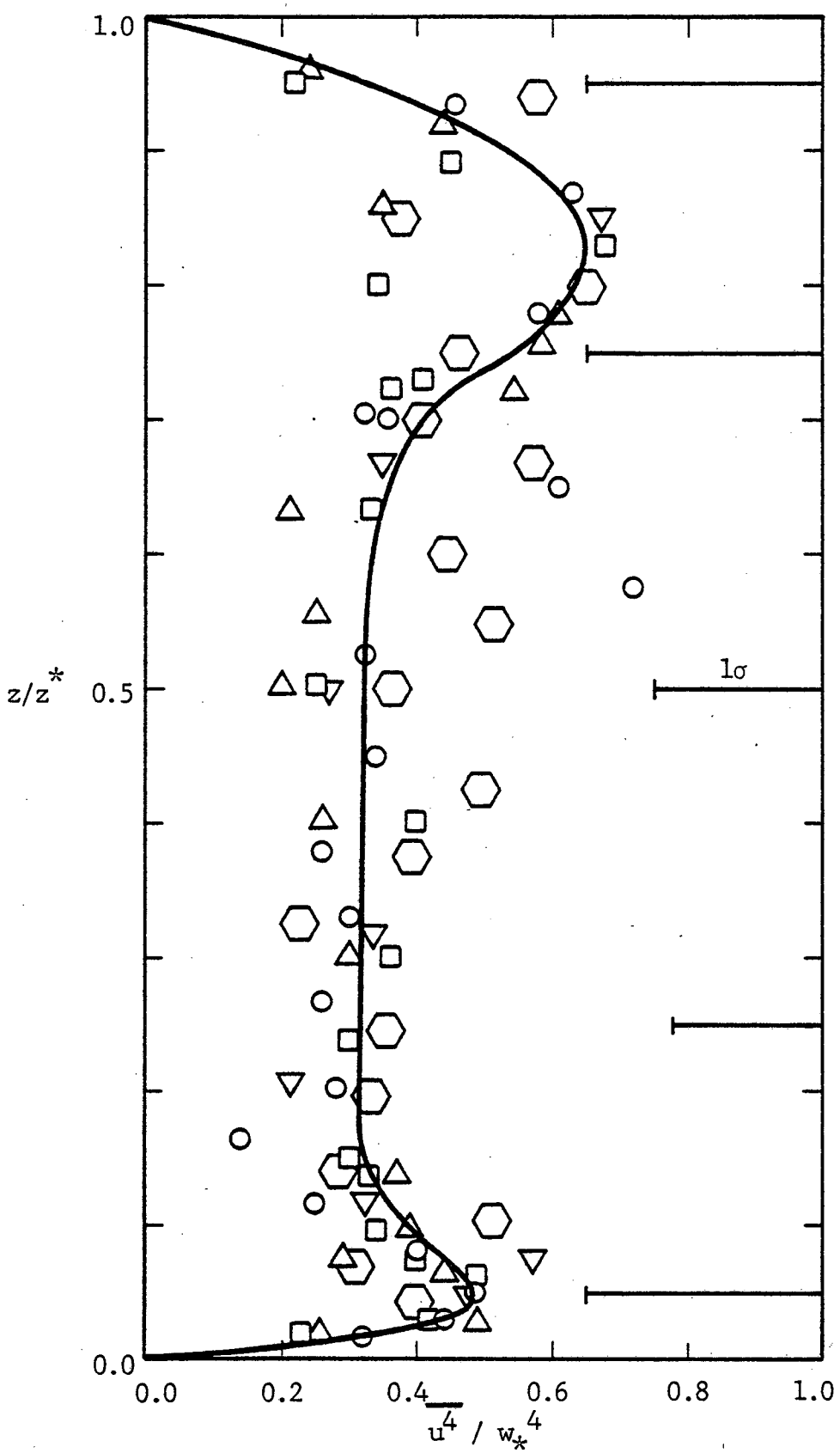

Figure 4.33 - Fourth order moment of horizontal velocity. Symbols defined in Figure 4.25.

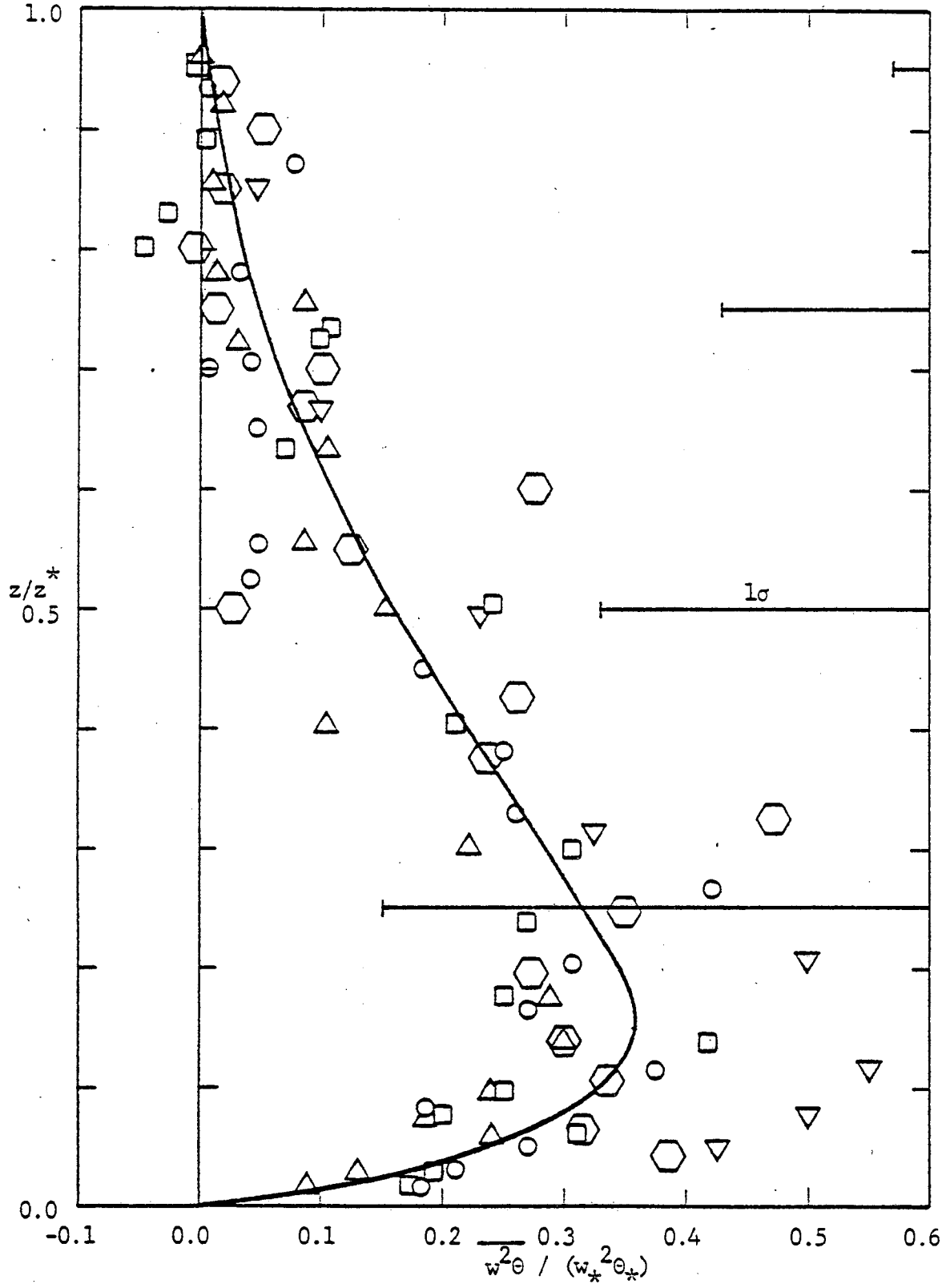

Figure 4.34 - Vertical transport of kinematic heat flux. Symbols defined in Figure 4.25.

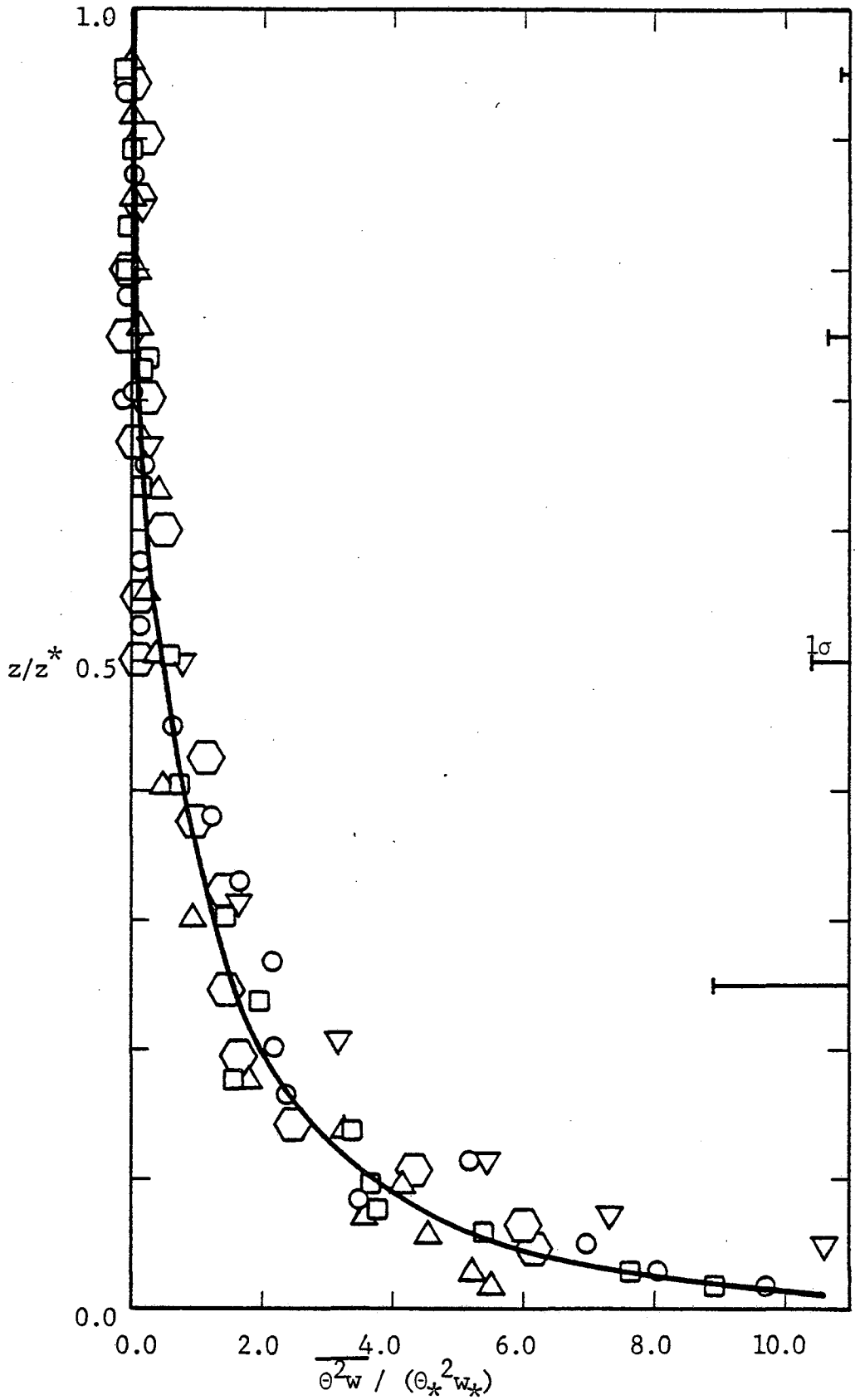

Figure 4.35 - Vertical transport of temperature fluctuations. Symbols defined in Figure 4.25.

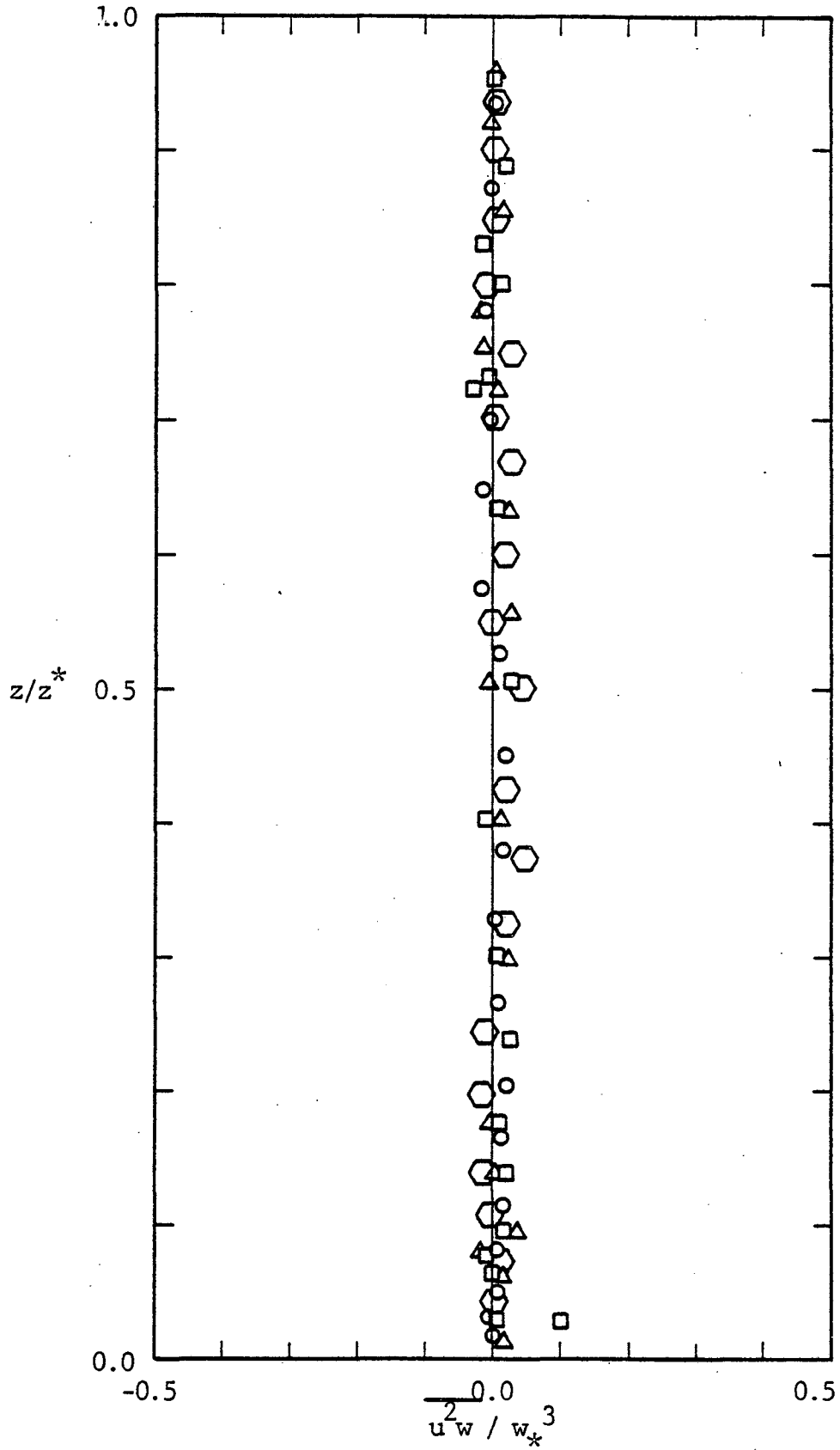

Figure 4.36 - Vertical transport of horizontal fluctuations. Symbols defined in Figure 4.25.

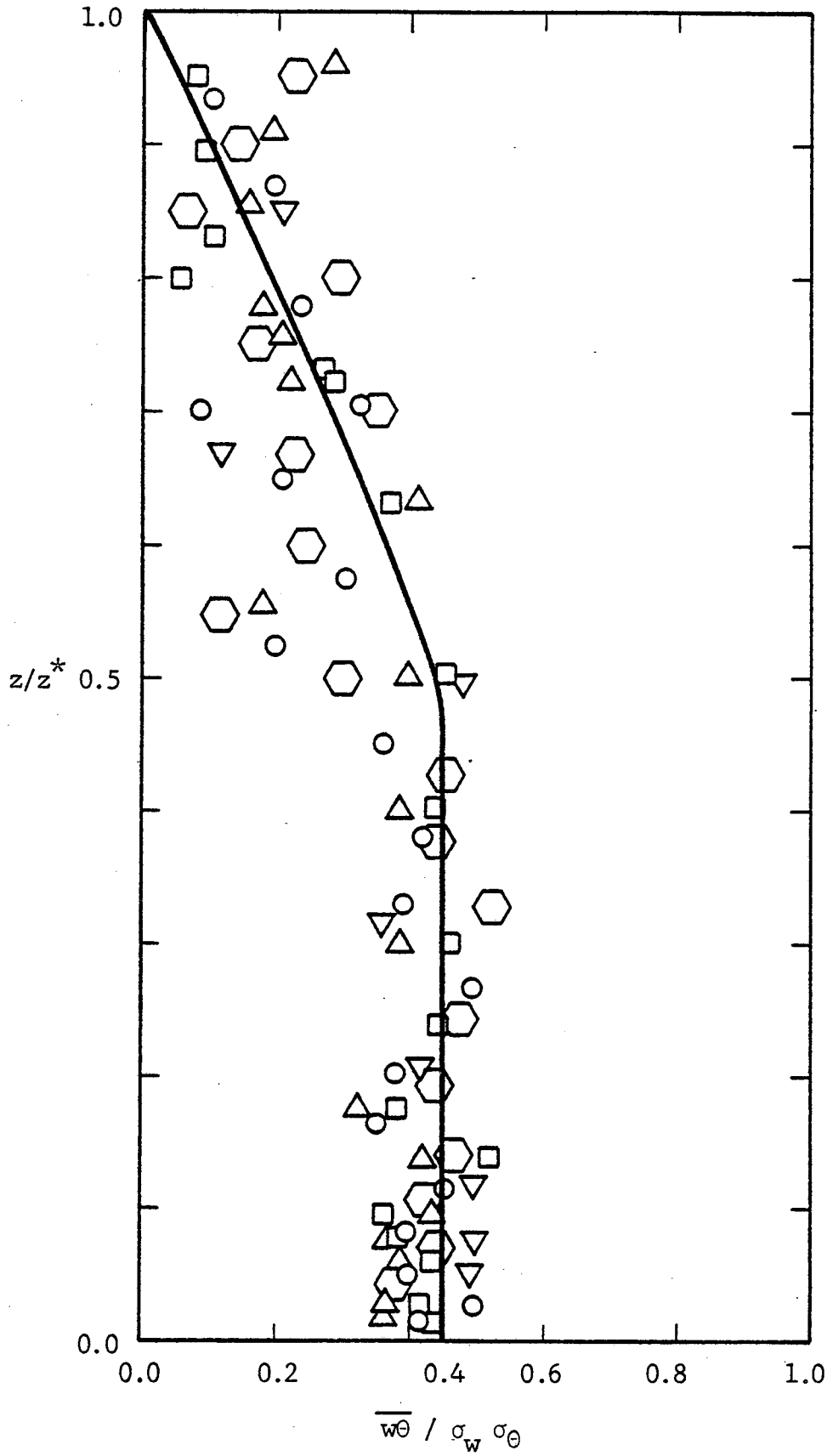

Figure 4.37 - w-θ correlation coefficient. Symbols defined in Figure 4.25.

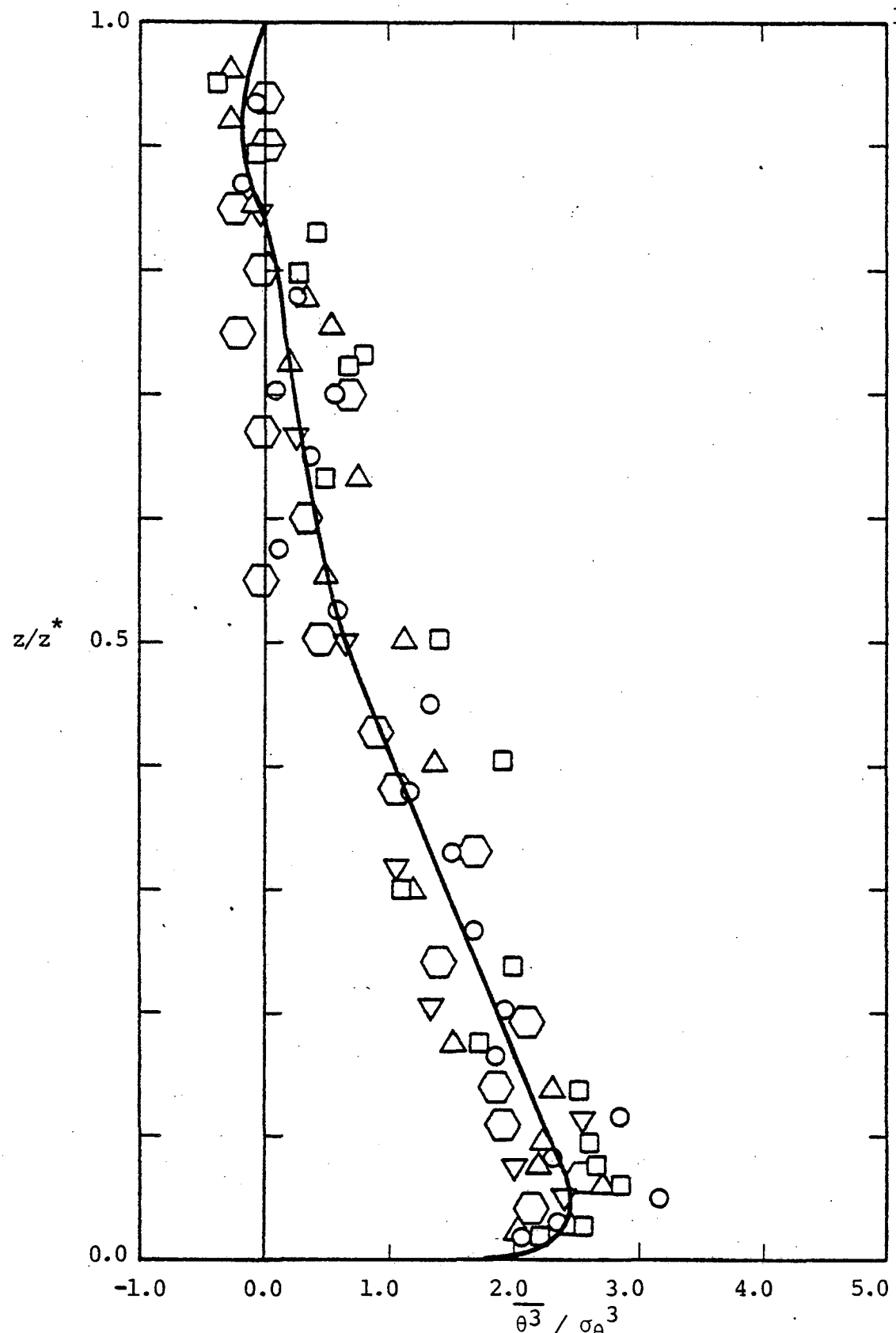

Figure 4.38 - Skewness of temperature fluctuations. Symbols defined in Figure 4.25.

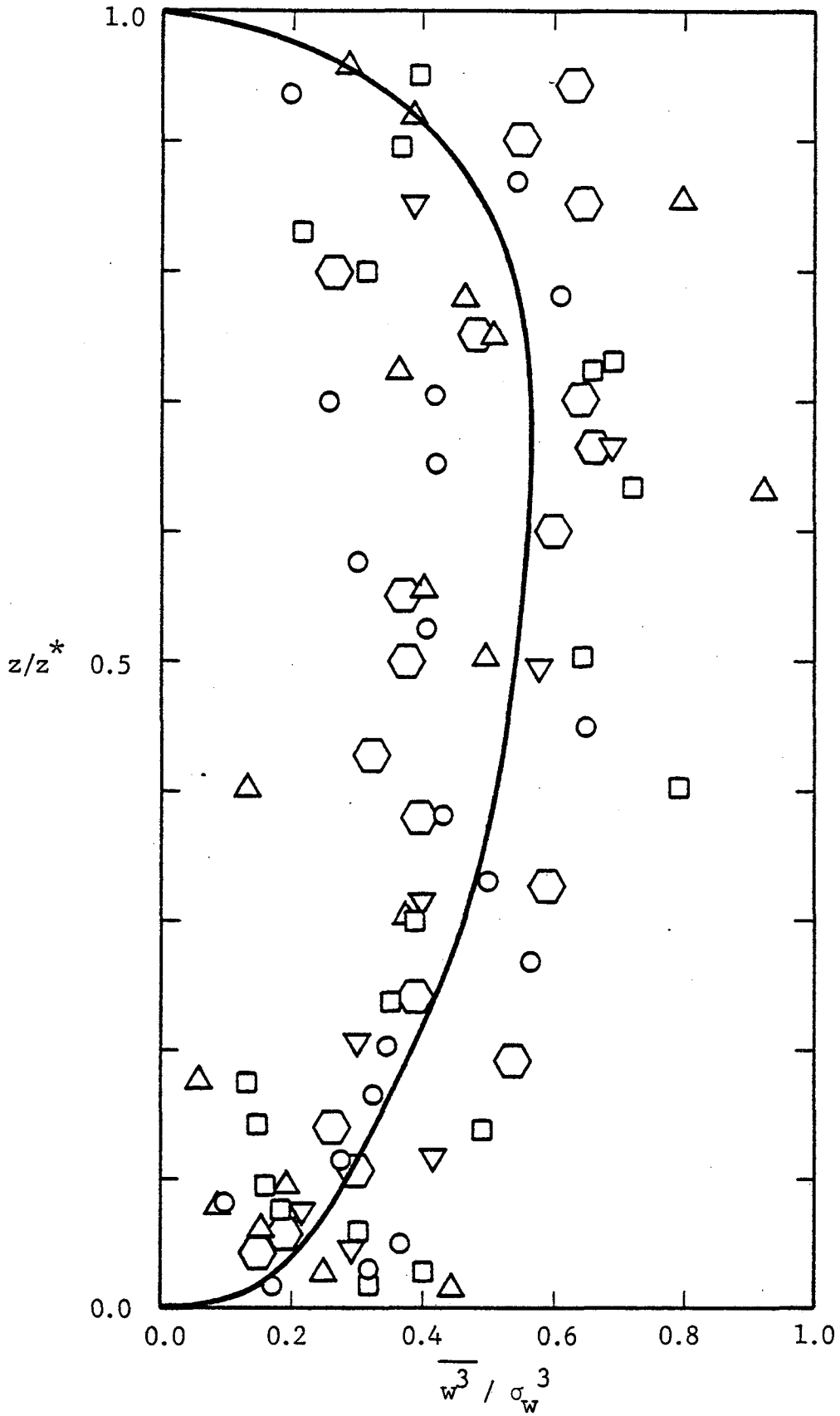

Figure 4.39 - Skewness of vertical velocity fluctuations. Symbols defined in Figure 4.25.

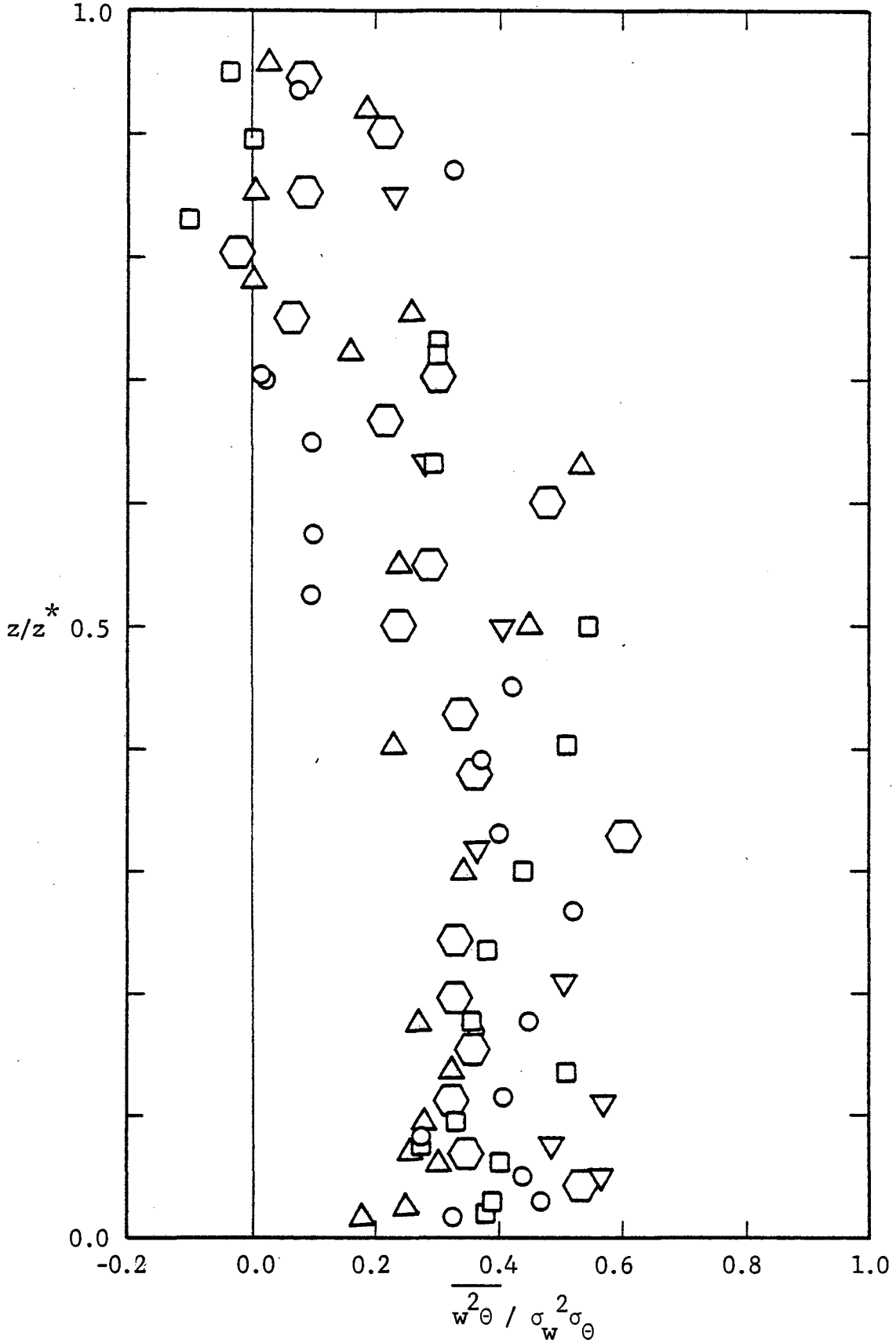

Figure 4.40 - Vertical transport of kinematic heat flux scaled by RMS values. Symbols defined in Figure 4.25.

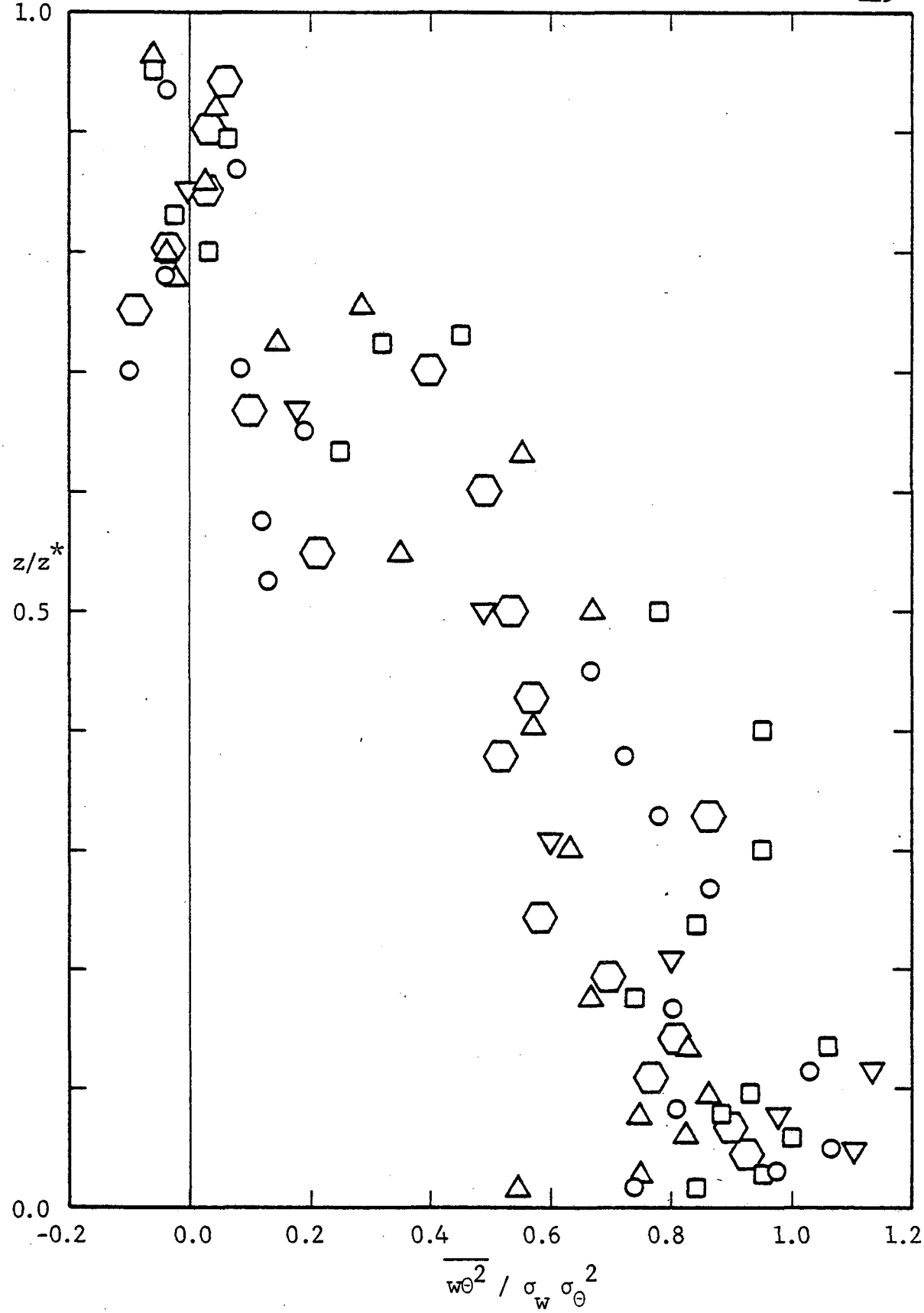

Figure 4.41 - Vertical transport of temperature fluctuations scaled by RMS values. Symbols defined in Figure 4.25.

Analyzing the vertical profiles of the central moments, three distinct regions can be identified in the convective layer:

Region I - Accelerating Region - This region extends from the lower boundary, or better, from the edge of the conduction layer up to $z/z^* \simeq 0.2$. It is dominated by elevated exchanges of heat and momentum between the plumes and the cold fluid. The hot parcel has temperature excess substantially decreased, as they rise in the region, while its positive vertical velocity is increased. The upward motion of high velocity hot fluid is accompanied by the downward displacement of large amounts of low velocity cold fluid. As the hot elements go up they carry surrounding cold fluid along resulting a continuous thickening. Due to the higher efficiency in the momentum transfer compared with the thermal transfer, the horizontal dimensions of the rising elements are bigger in the vertical velocity trace than in the temperature trace.

Region II - Central Region - The central region is characterized by small variations in the vertical profile of almost all the moments and it extends from about $z/z^* = 0.2$ up to 0.6. Due to the destruction of the plumes by the highly turbulent field, the kinematic heat flux $\overline{(w\theta)}$ and its vertical transport are linearly decreasing in this region. The upward and downward movements of hot and cold fluids respectively are well balanced resulting in vertical velocites of the same order of magnitude up and down.

Region III - Decelerating Region - This region extends from $z/z^* = 0.6$ to the upper plate and it is characterized by the gradual diminution of all the moments involving the vertical velocity. The

moments involving the horizontal velocity show maximum values there indicating the conversion of the vertical velocity to the horizontal movement, due to the presence of the upper boundary.

The existence of a non-zero third order moment of the horizontal velocity in the accelerating and decelerating regions indicate the predominance of the horizontal flow in certain directions. This is consistent with the non-zero cross-correlation of the horizontal and vertical velocities. A kinematic heat flux lower than the expected theoretical value can also be associated with a mean flow circulation. If a mean flow exists, its contribution to the turbulence is very small. Its estimation is difficult but as all moments were calculated from fluctuations about the ensemble averaged mean, it is reasonable to affirm that only the mean temperature and velocity values were influenced.

Instead of using Q_o for the calculation of the convective scales, using the kinematic heat flux at the lower boundary resulted in much better collapse of the data as shown in Figures 4.42 through 4.44.

In order to calculate $\overline{(w\theta)}_o$, a straight line parallel to the theoretical prediction was adjusted to each set of data and the point where it crossed the horizontal axis at $z/z^* = 0$ was used to compute the convective scales. Values are shown below:

Condition	Q_o {^oKcm/s }	z^* { cm }	$\overline{(w\theta)}_o/Q_o$
I	0.0153	20	0.82
II	0.0330	20	0.77
III	0.0568	20	0.70
IV	0.0450	15	0.84
V	0.0141	12	0.95

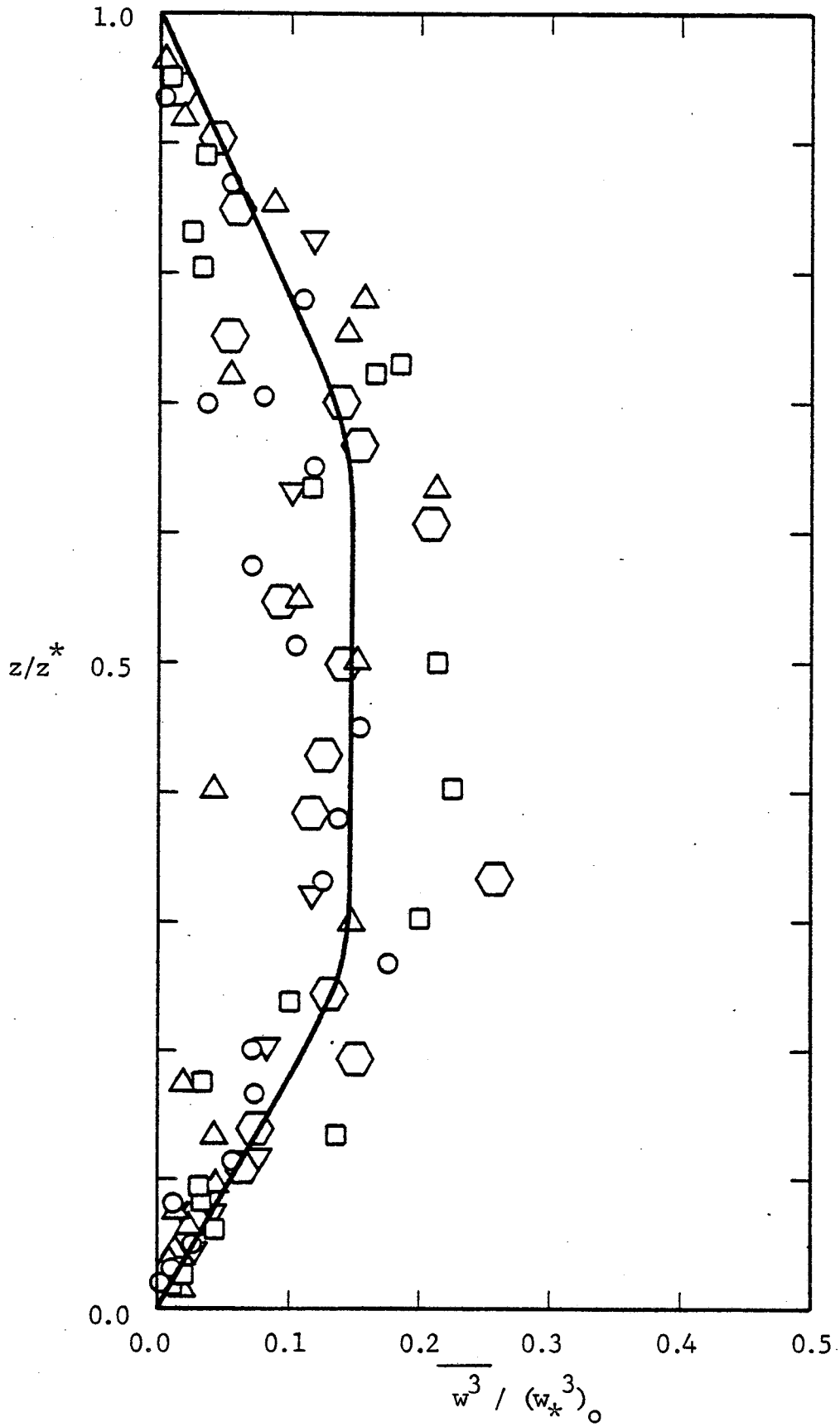

Figure 4.42 - Vertical transport of vertical velocity fluctuations using $(\overline{w\theta})_o$ to compute the convective scales. Symbols defined in Figure 4.25.

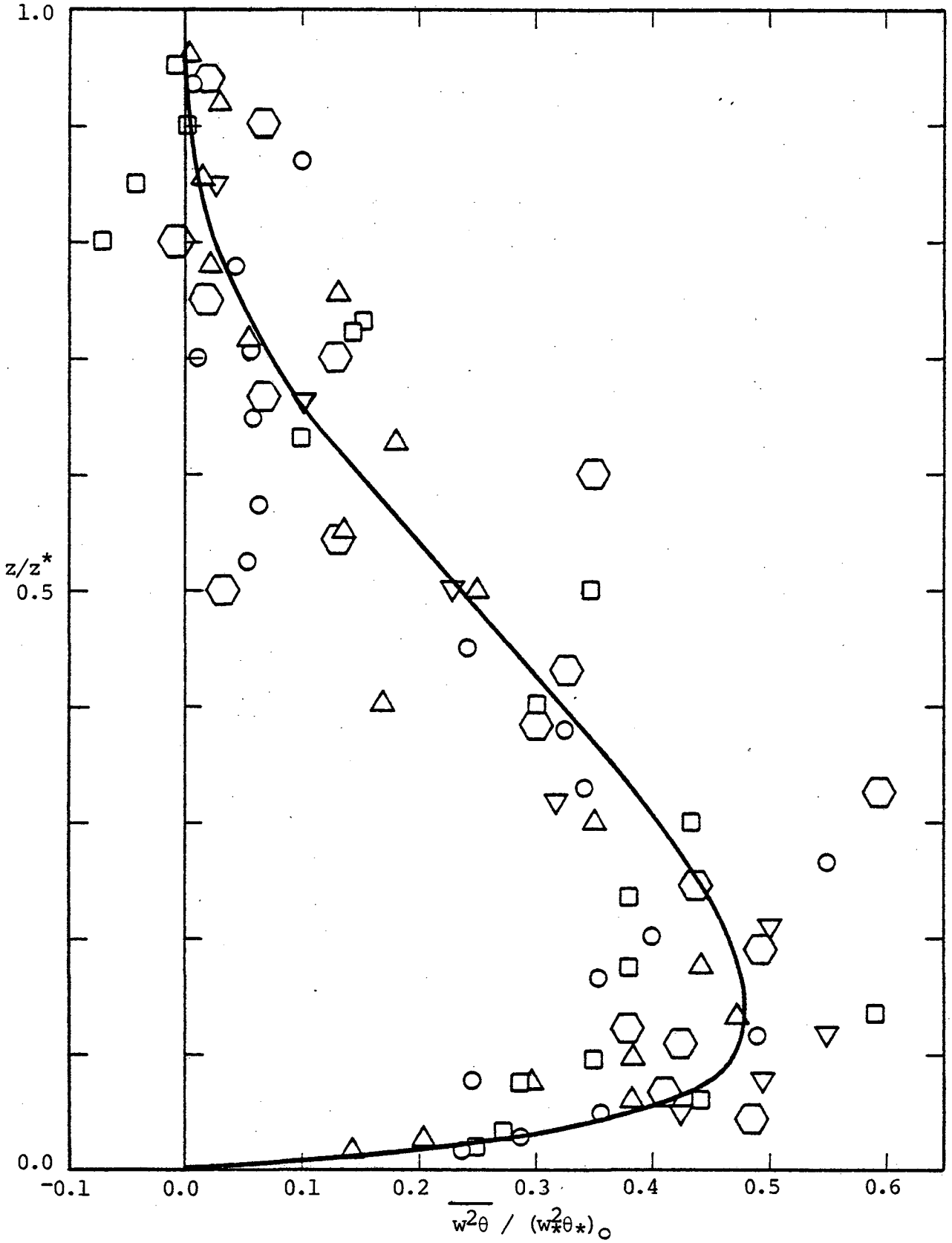

Figure 4.43 - Vertical transport of kinematic heat flux using $(\overline{w\theta})_o$ to compute the convective scales. Symbols defined in Figure 4.25.

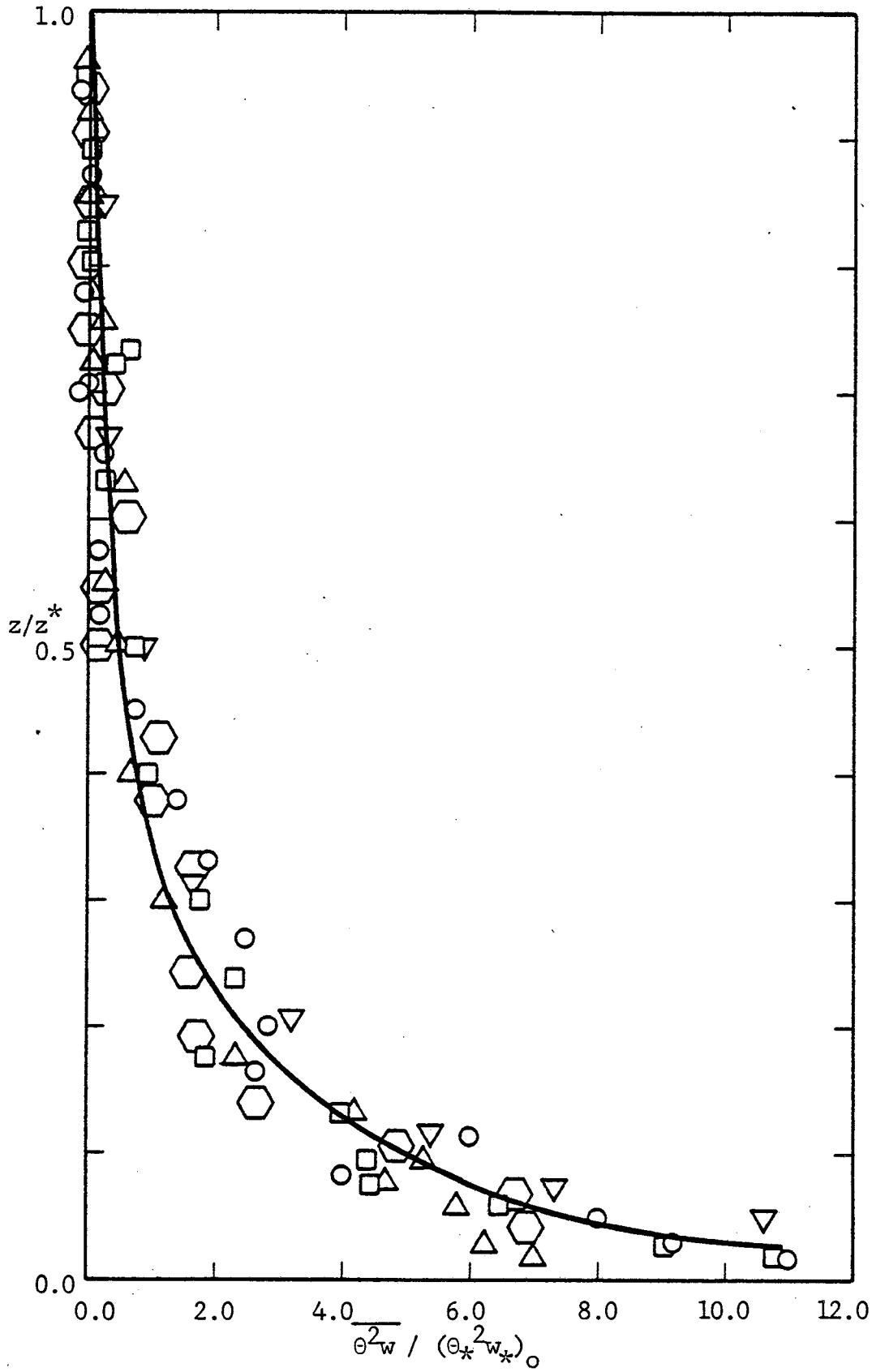

Figure 4.44 - Vertical transport of temperature fluctuations using $(\overline{w\theta})_o$ to compute the convective scales. Symbols defined in Figure 4.25.

4.5 Power Laws

Power law behavior of the moments in the matching region was investigated by plotting the data up to $z/z^* = 0.35$ on log-log graph paper. As pointed out by Townsend (1976), the thickness of the equilibrium layer is a small fraction of the total depth of the turbulent flow, and consequently the variation of kinematic heat flux across the layer is small compared with the heat flux at the wall.

In the equilibrium layer, both z_* and z_0 scaling must match so

$$\frac{\sigma_\theta}{\theta_*} = C \left(\frac{z}{z_*}\right)^n \tag{4.2a}$$

$$\frac{\sigma_\theta}{\theta_0} = C \left(\frac{z}{z_0}\right)^n \tag{4.2b}$$

$$\frac{\sigma_w}{w_*} = C_1 \left(\frac{z}{z_*}\right)^m \tag{4.3a}$$

$$\frac{\sigma_w}{w_0} = C_1 \left(\frac{z}{z_0}\right)^m \tag{4.3b}$$

Multiplying equation (4.2) by (4.3) yields

$$\frac{\sigma_\theta \sigma_w}{\theta_* w_*} = \frac{\sigma_\theta \sigma_w}{\theta_0 w_0} = CC_1 \left(\frac{z}{z_*}\right)^{n+m} = CC_1 \left(\frac{z}{z_0}\right)^{n+m} \tag{4.4}$$

Hence

$$\left(\frac{z}{z_*}\right)^{n+m} = \left(\frac{z}{z_0}\right)^{n+m} \tag{4.5}$$

Equation (4.5) holds only when $m+n = 0$ or $m = -n$. From the relation of convective and conduction scales defined in equations (2.21) and (2.22)

$$\frac{w^*}{w_0} = \left(\frac{z_*}{z_0}\right)^{1/3} \tag{4.6}$$

Comparing equation (4.6) with the relation of (4.3b) and (4.3a) one gets $m = \frac{1}{3}$ and $n = -\frac{1}{3}$. Hence

$$\frac{\sigma_w}{w_*} = C_1 \left(\frac{z}{z_*}\right)^{1/3} \tag{4.7}$$

$$\frac{\sigma_\theta}{\theta_*} = C \left(\frac{z}{z_*}\right)^{-1/3} \tag{4.8}$$

Similar arguments applied to the other moments permit us to write

$$\frac{\overline{w^3}}{w_*^3} = C_2 \left(\frac{z}{z_*}\right)^1 \tag{4.9}$$

$$\frac{\overline{\theta^3}}{\theta_*^3} = C_3 \left(\frac{z}{z_*}\right)^{-1} \tag{4.10}$$

$$\frac{\overline{w^2\theta}}{Q_0 w_*} = C_4 \left(\frac{z}{z_*}\right)^{1/3} \tag{4.11}$$

$$\frac{\overline{w\theta^2}}{Q_0 \theta_*} = C_5 \left(\frac{z}{z_*}\right)^{-1/3} \tag{4.12}$$

When the RMS values of temperature and velocity fluctuations scaled by the convective scales were plotted against z/z_*, a power law of -1/2 was found for σ_θ/θ_* and no characteristic power law was detected for σ_w/w_* as presented in Figures 4.45 and 4.46 respectively.

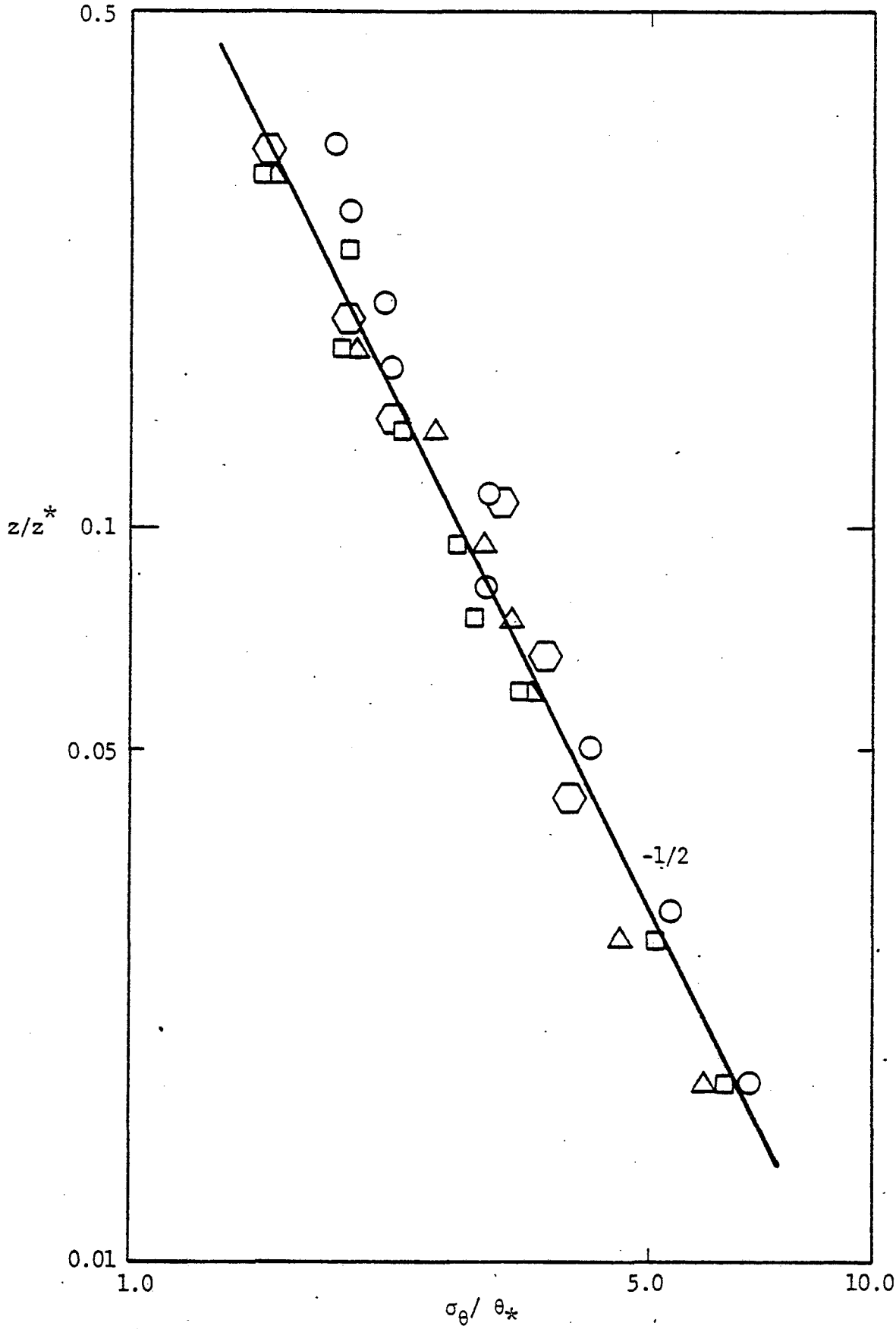

Figure 4.45 - RMS temperature power law - no shift in the vertical direction. Symbols defined in Figure 4.25.

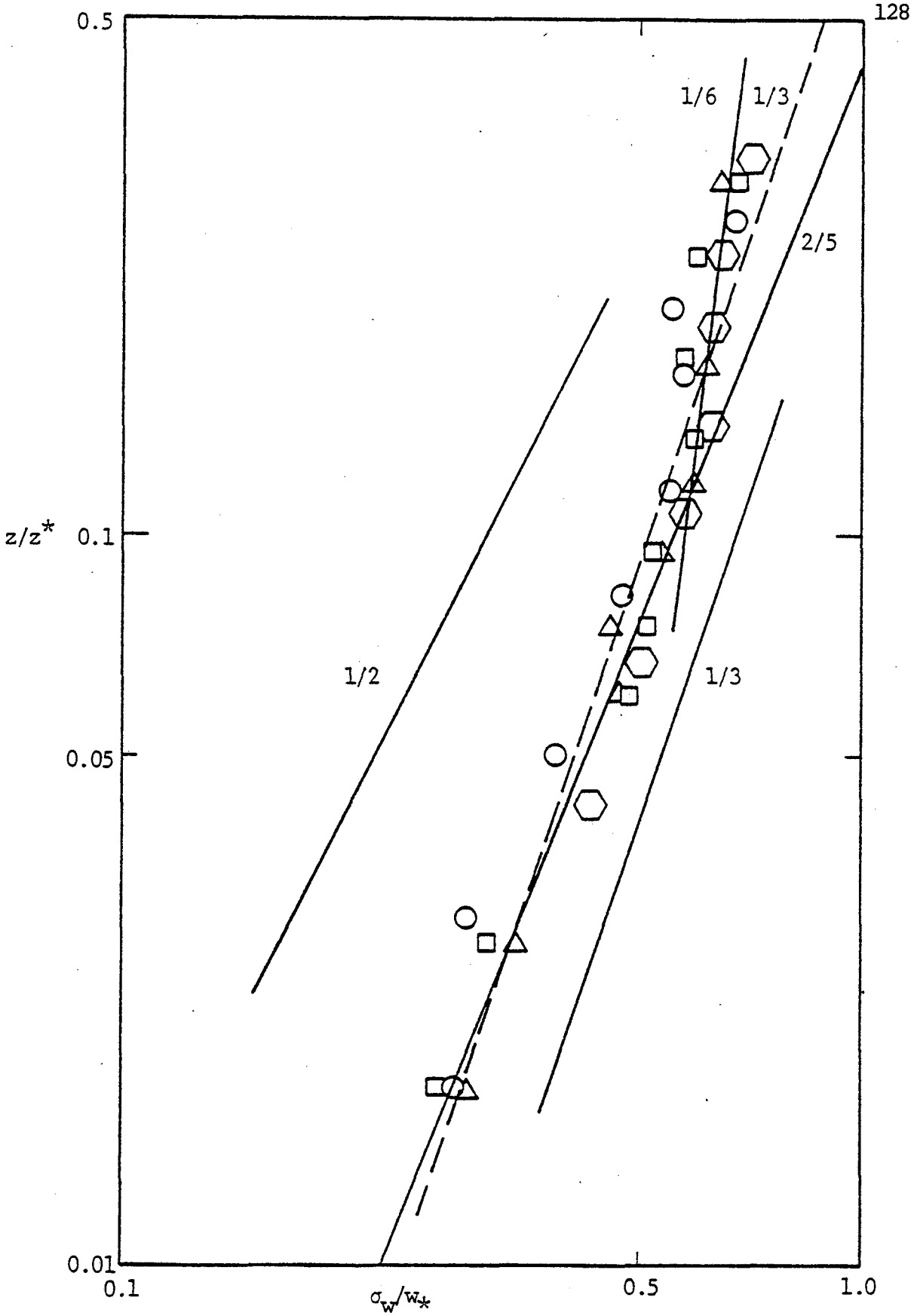

Figure 4.46 - RMS vertical velocity power law - no shift in the vertical direction. Symbols defined in Figure 4.25.

As suggested in Boberg (1977), a shift of ($8\ z_0/z_*$) was applied in the vertical dimension scale. The idea is to scale the moments with the distance to the edge of the conduction layer instead of with the distance to the wall. The numerical factor of 8 has been determined empirically by reference to the mean temperature data. The flow constraint at the conduction layer prevents eddies from having scales in the vertical direction that are larger than the distance from the margin of the conduction layer to the eddies centre. Figures 4.47 through 4.52 show the power laws of the central moments with the shift in the height.

The scatter in the data for the third order single and crossed moments precludes accurate verification of the power laws in the equilibrium layer but any change in the dependence can be clearly detected.

From the graphs, the equilibrium layer extends up to $\frac{z-8z_0}{z_*} \cong 0.1$ for each moment.

4.6 Conditional Averages

In an effort to understand the low values of kinematic heat flux obtained from the moments calculation, conditional averaging techniques were used to examine the statistics of w and θ more closely.

Data points in the w-θ plane were classified into five groups as pointed out in section 3.3.

Plots of the conditional averaging results for the kinematic heat fluxes are presented in Figures 4.53 through 4.60 for all runs. Figures 4.53 through 4.56 show the conditionally averaged mean heat

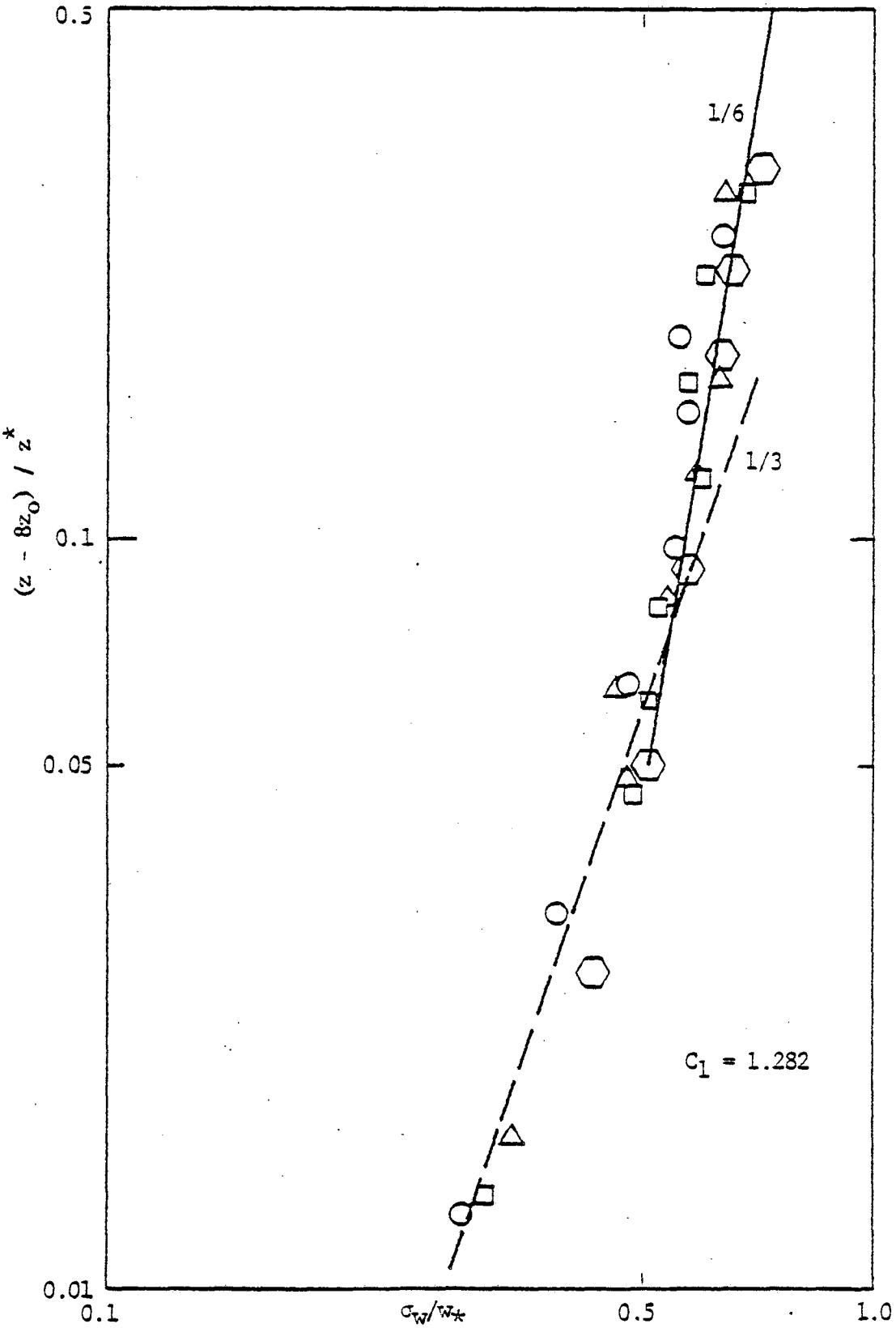

Figure 4.47 - RMS vertical velocity power law with $8z_o$ shift. Symbols defined in Figure 4.25.

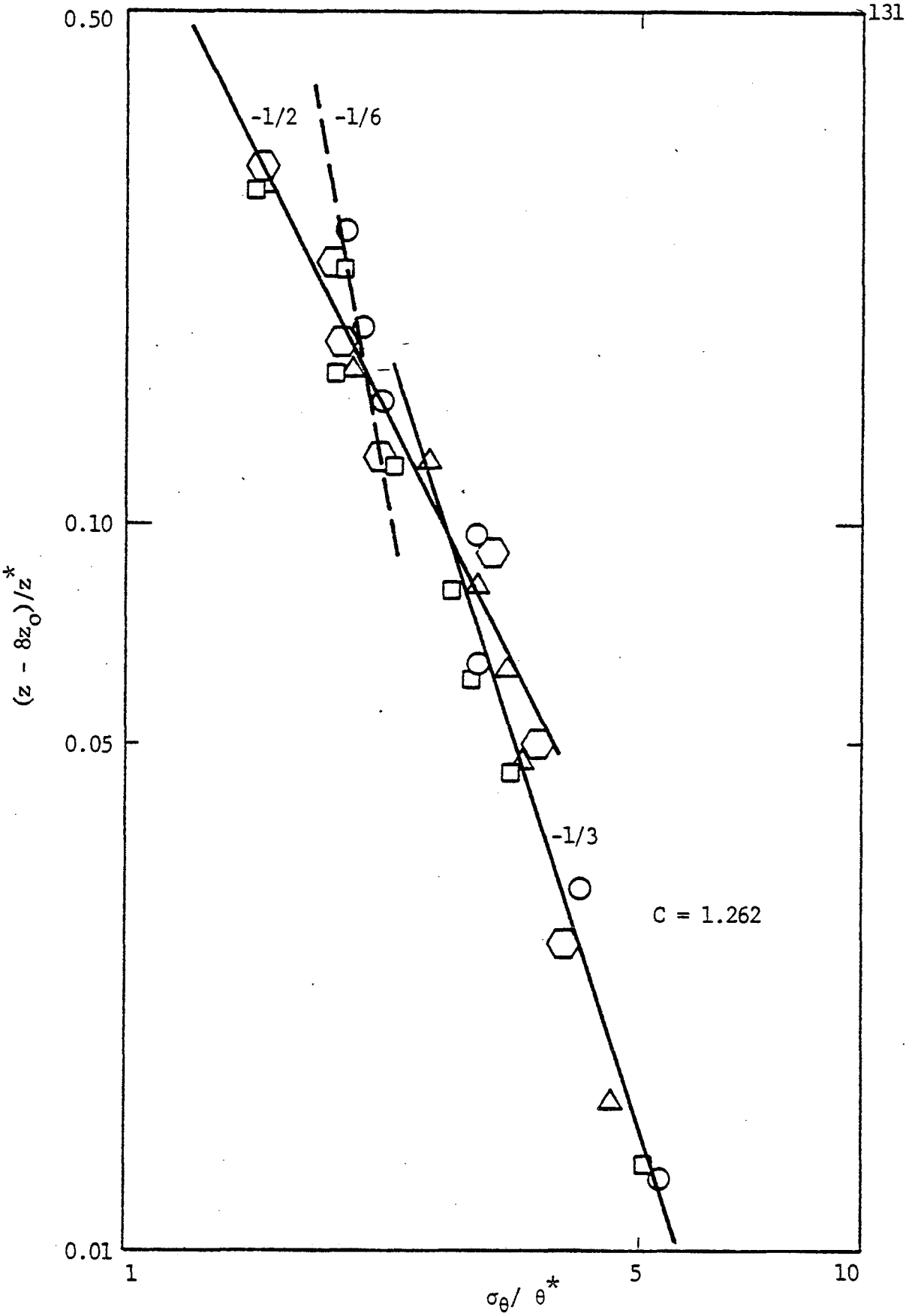

Figure 4.48 - RMS temperature power law with $8z_o$ shift. Symbols defined in Figure 4.25.

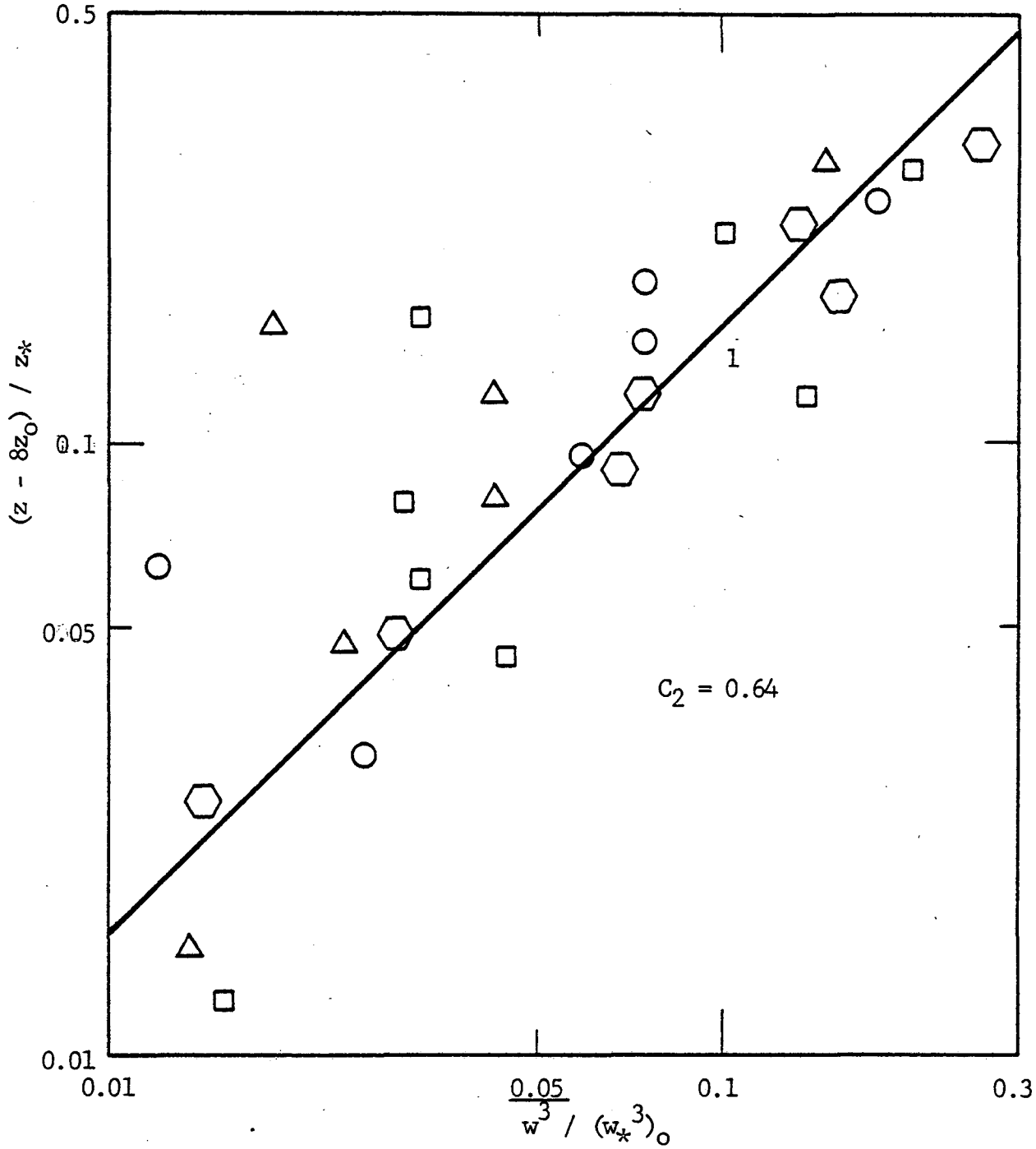

Figure 4.49 - Third order moment of vertical velocity power law with $8z_o$ shift and scales defined by kinematic heat flux at the lower boundary $(\overline{w\theta})_o$. Symbols defined in Figure 4.25.

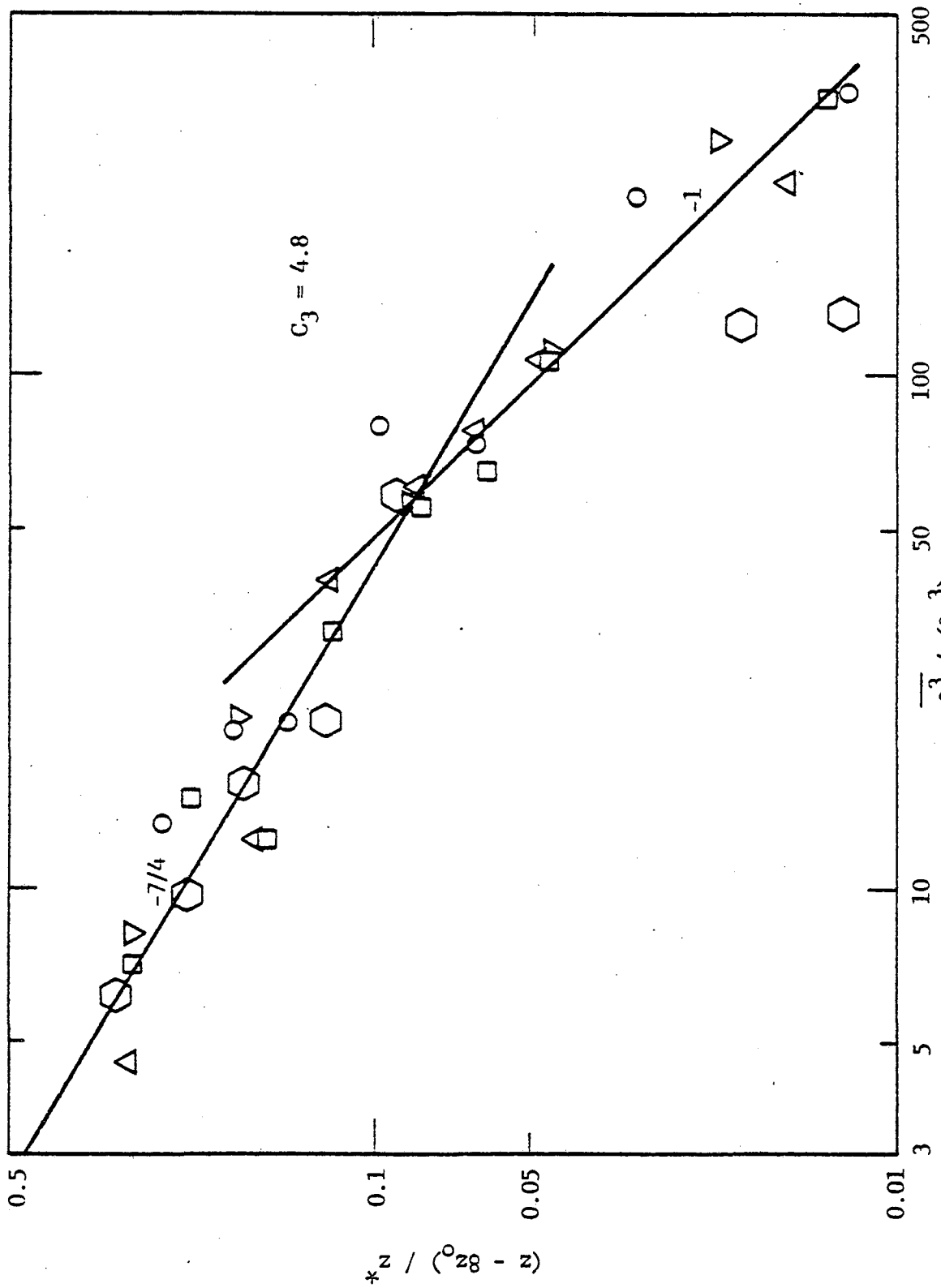

Figure 4.50 - Third order moment of temperature fluctuations. Same comments as in Figure 4.49.

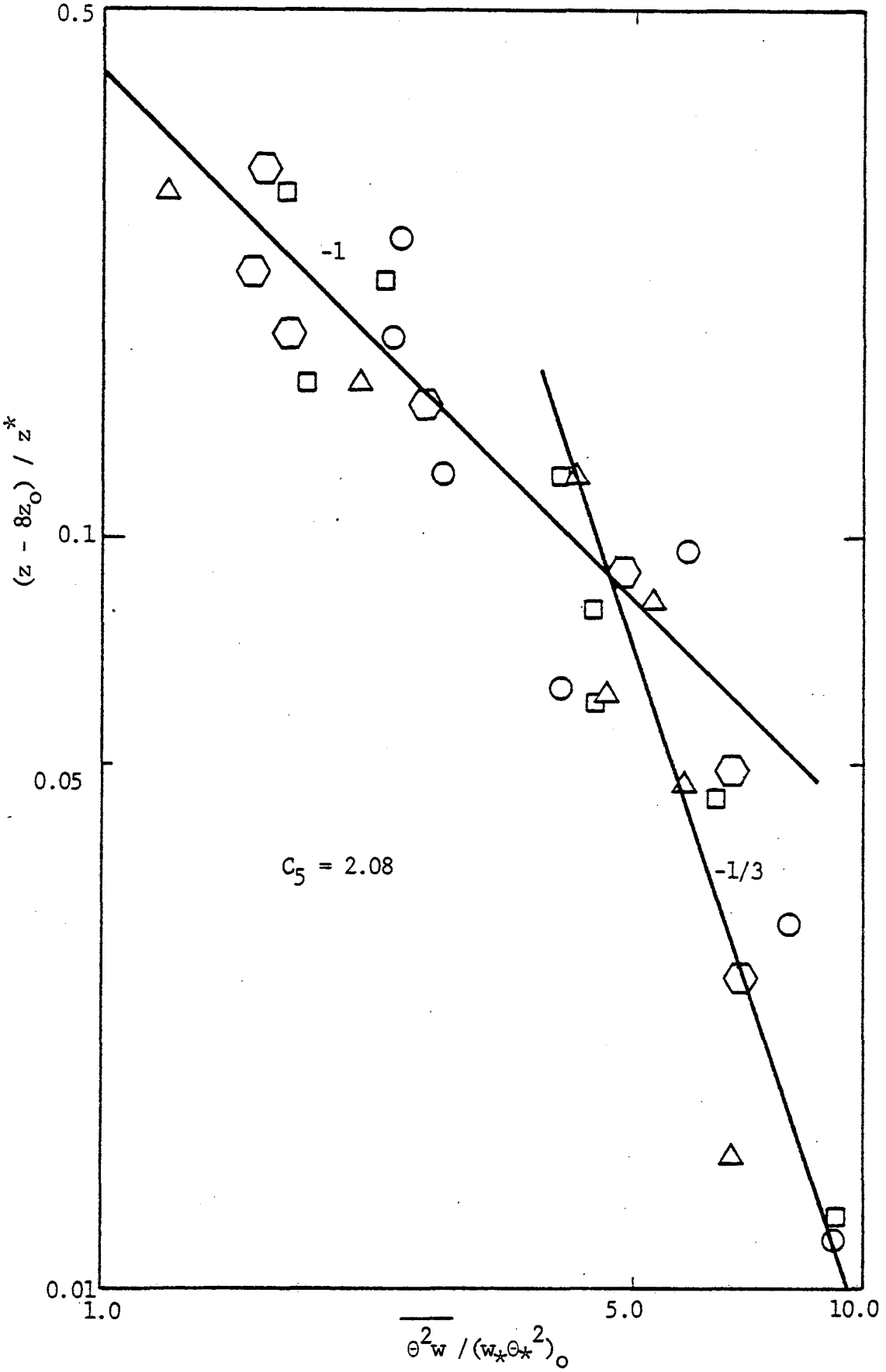

Figure 4.51 - Vertical transport of temperature fluctuations. Same comments as in Figure 4.49.

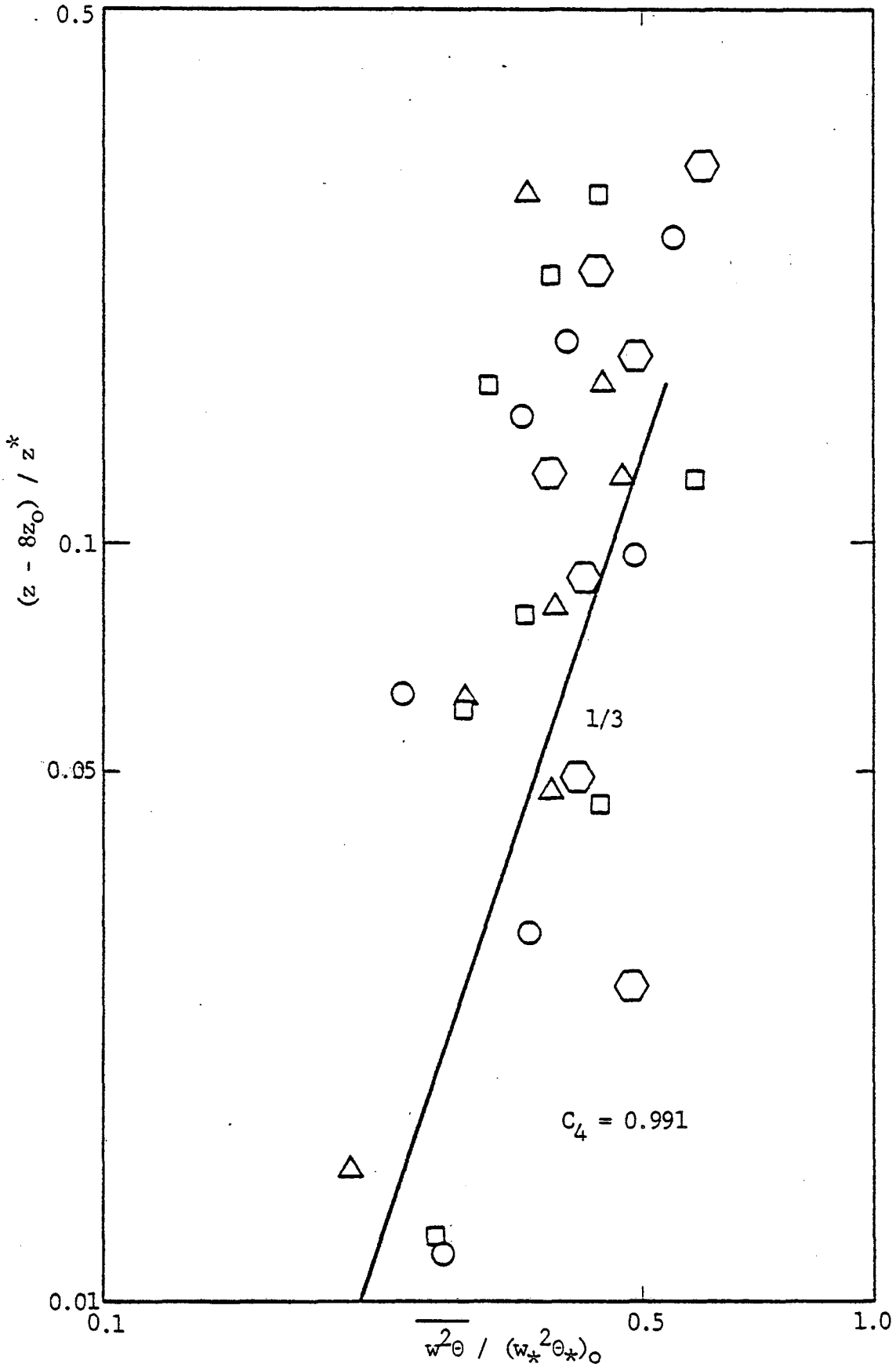

Figure 4.52 - Vertical transport of kinematic heat flux. Same comments as in Figure 4.49.

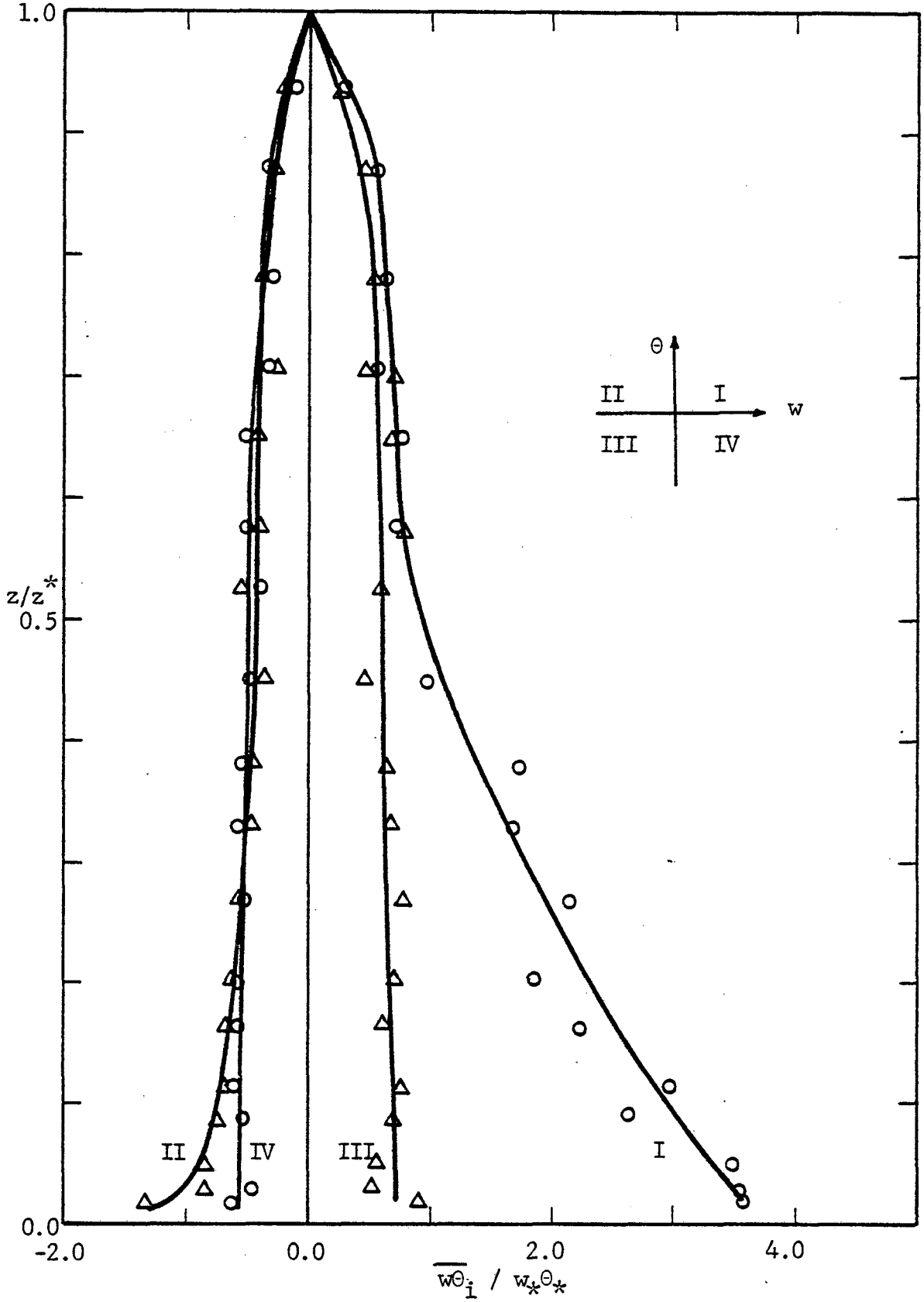

Figure 4.53 - Conditionally averaged kinematic heat flux. Flow condition I - $Pe_* = 6090$.

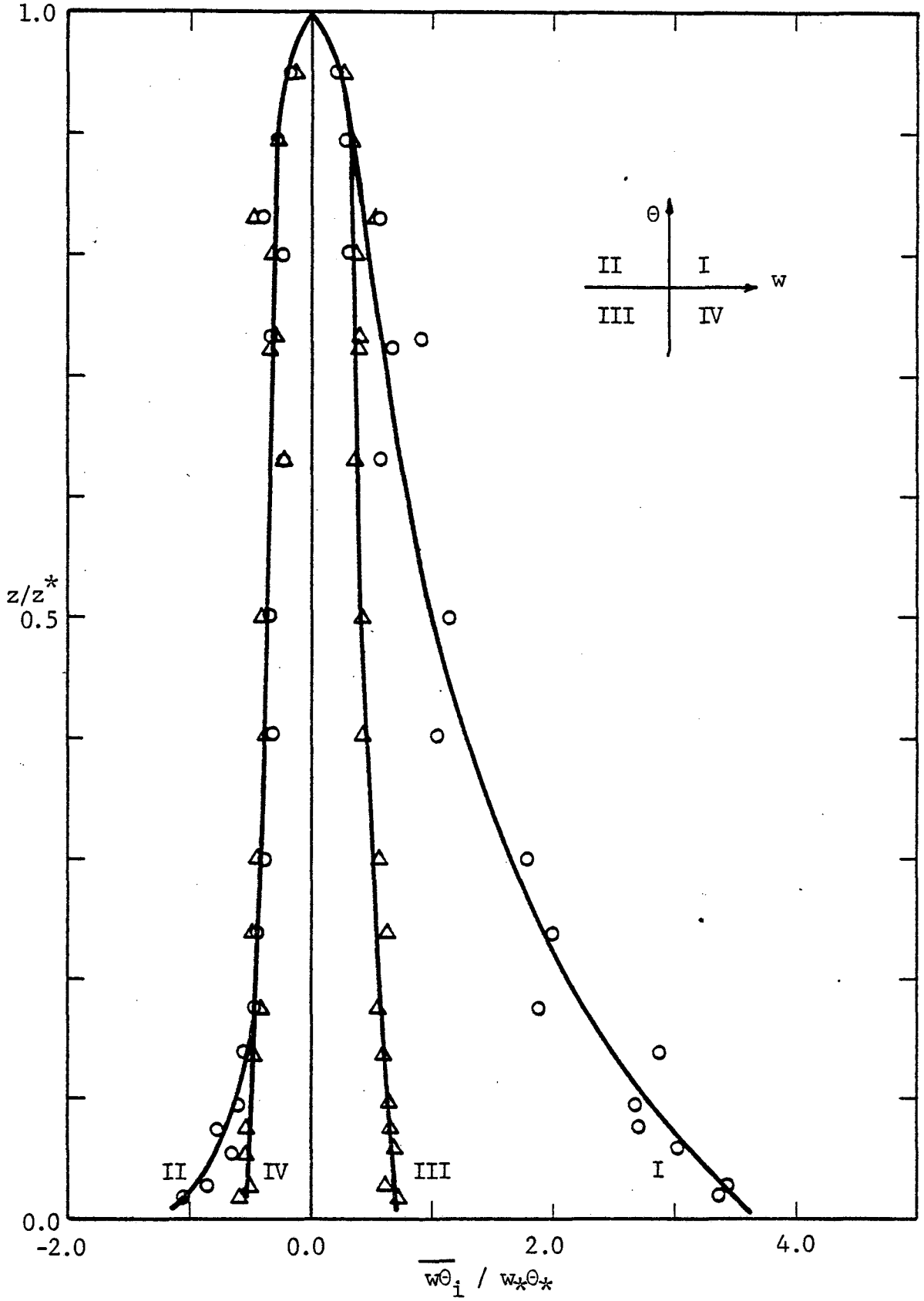

Figure 4.54 - Conditionally averaged kinematic heat flux. Flow condition II - $Pe_* = 7840$.

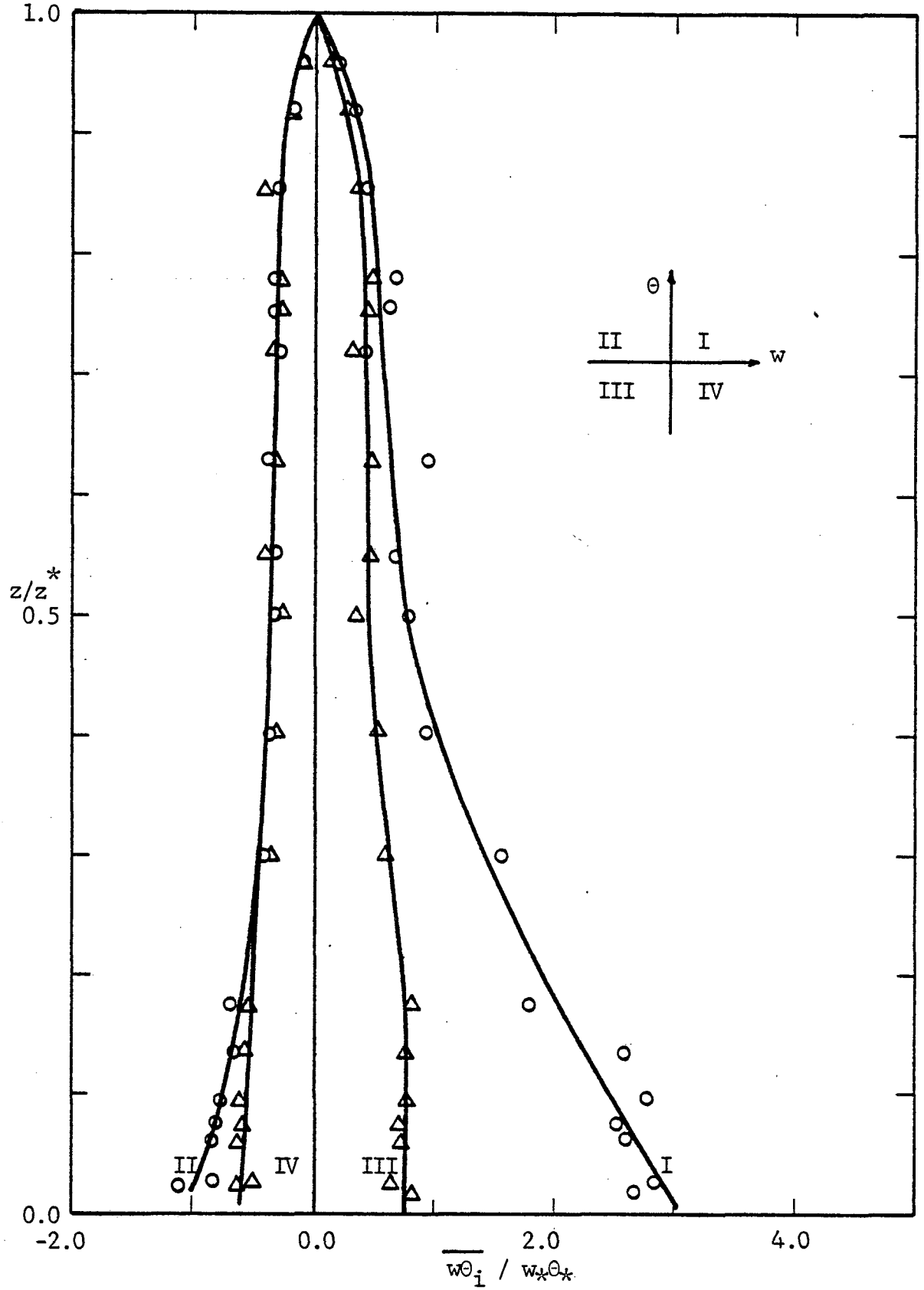

Figure 4.55 - Conditionally averaged kinematic heat flux. Flow condition III. $Pe_* = 9370$.

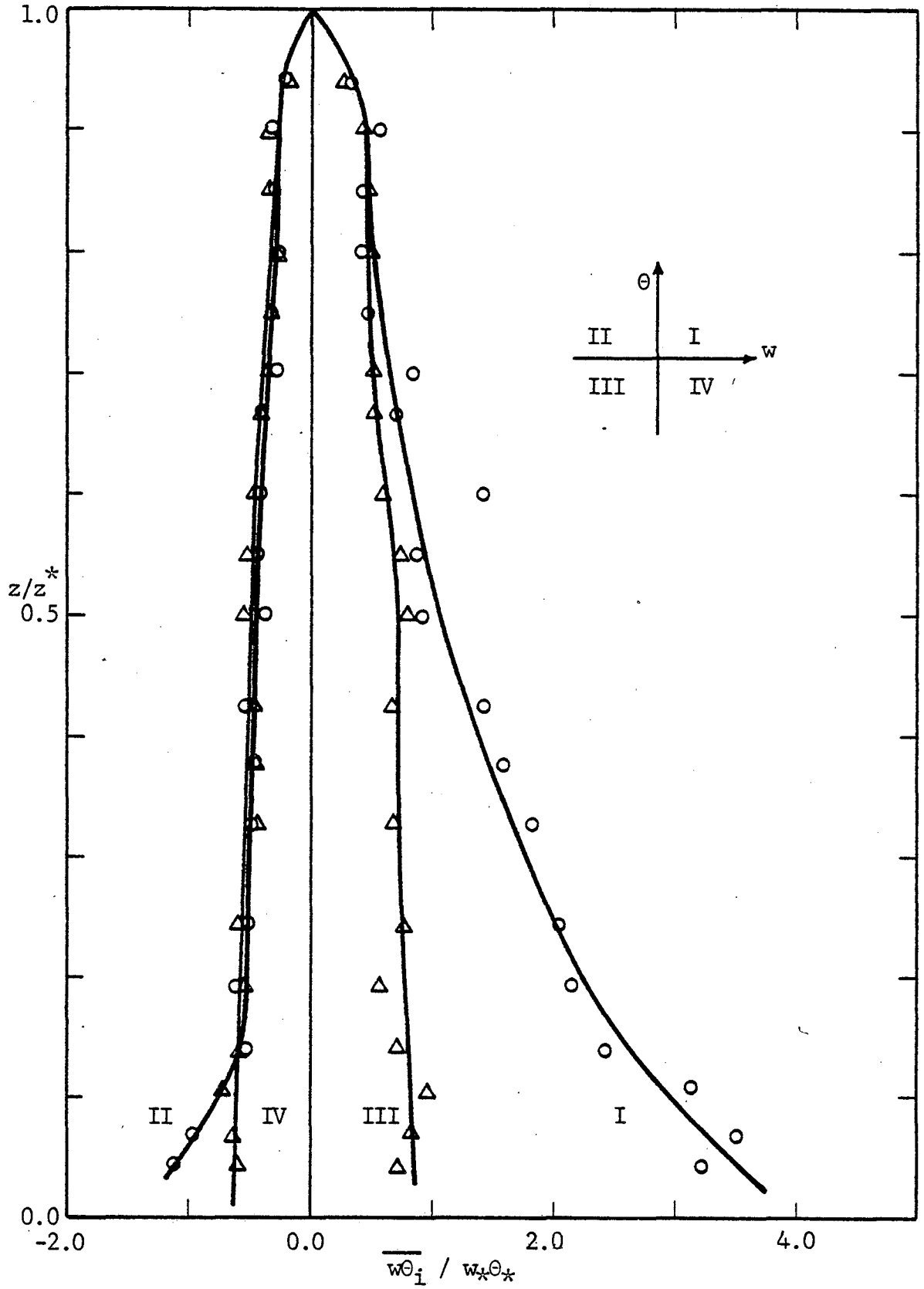

Figure 4.56 - Conditionally averaged kinematic heat flux. Flow condition IV $Pe_* = 6000$.

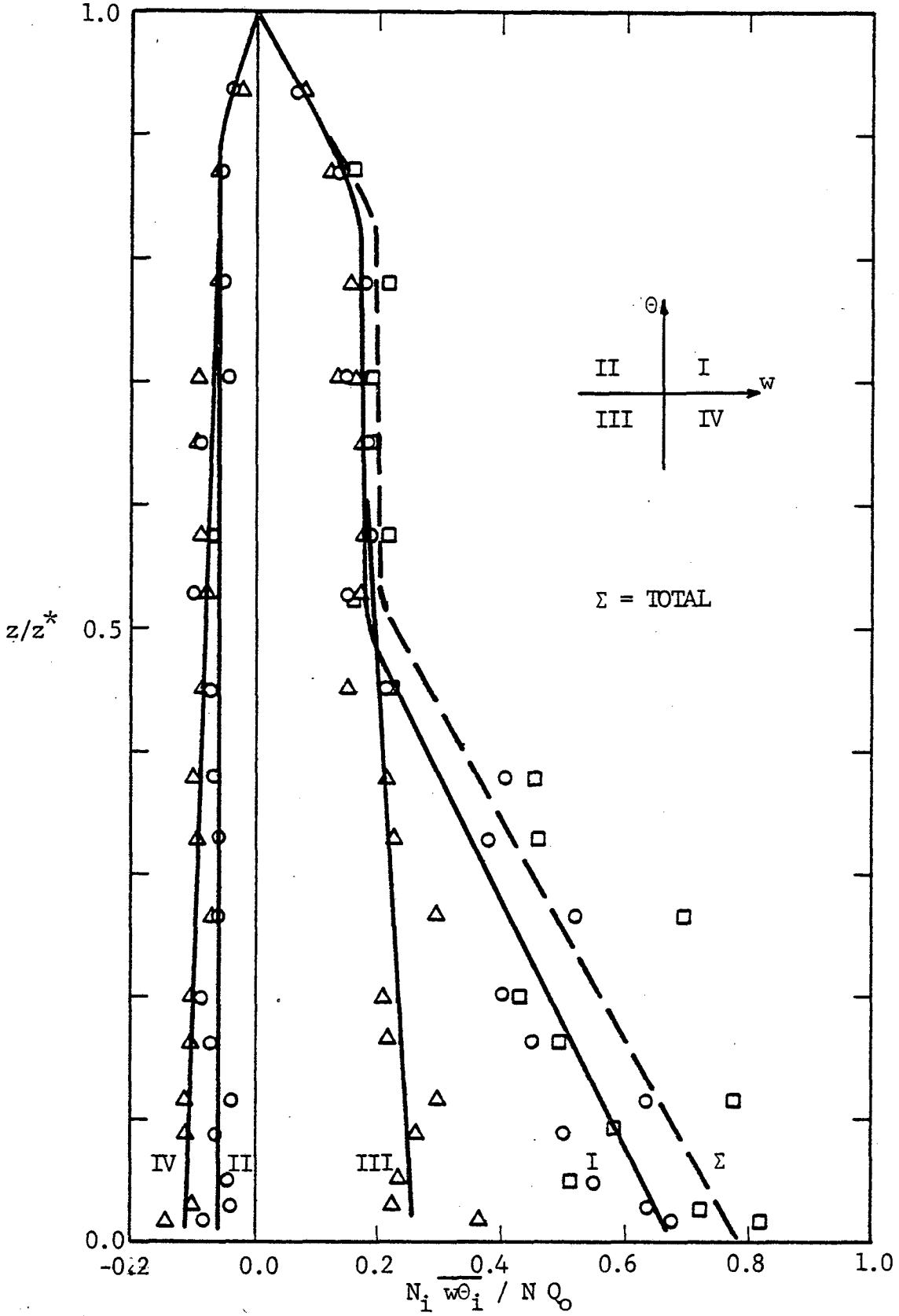

Figure 4.57 - Fraction of the kinematic heat flux associated with groups I to V - $Pe_* = 6090$.

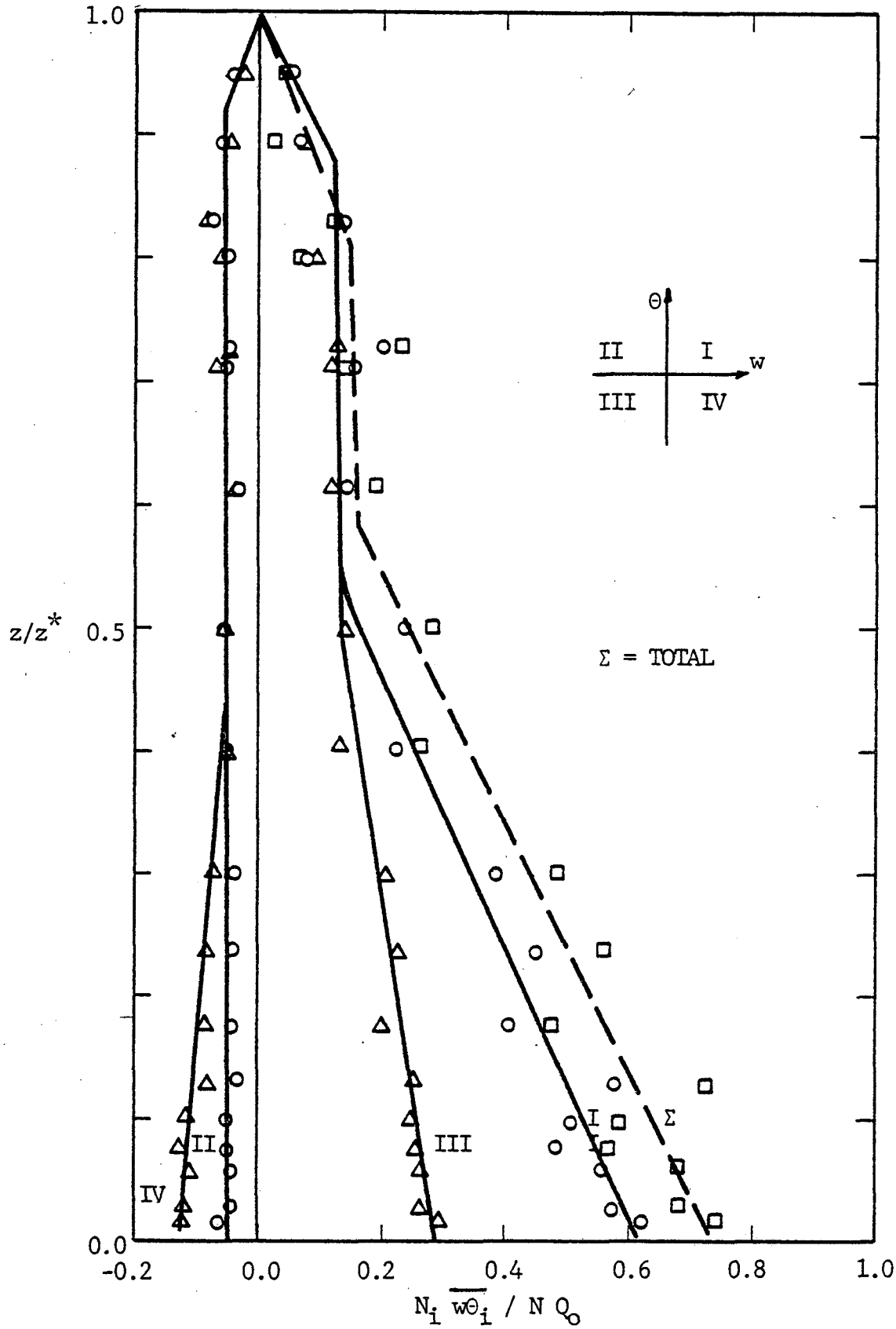

Figure 4.58 - Fraction of the kinematic heat flux associated with groups I to V - $Pe_* = 7840$.

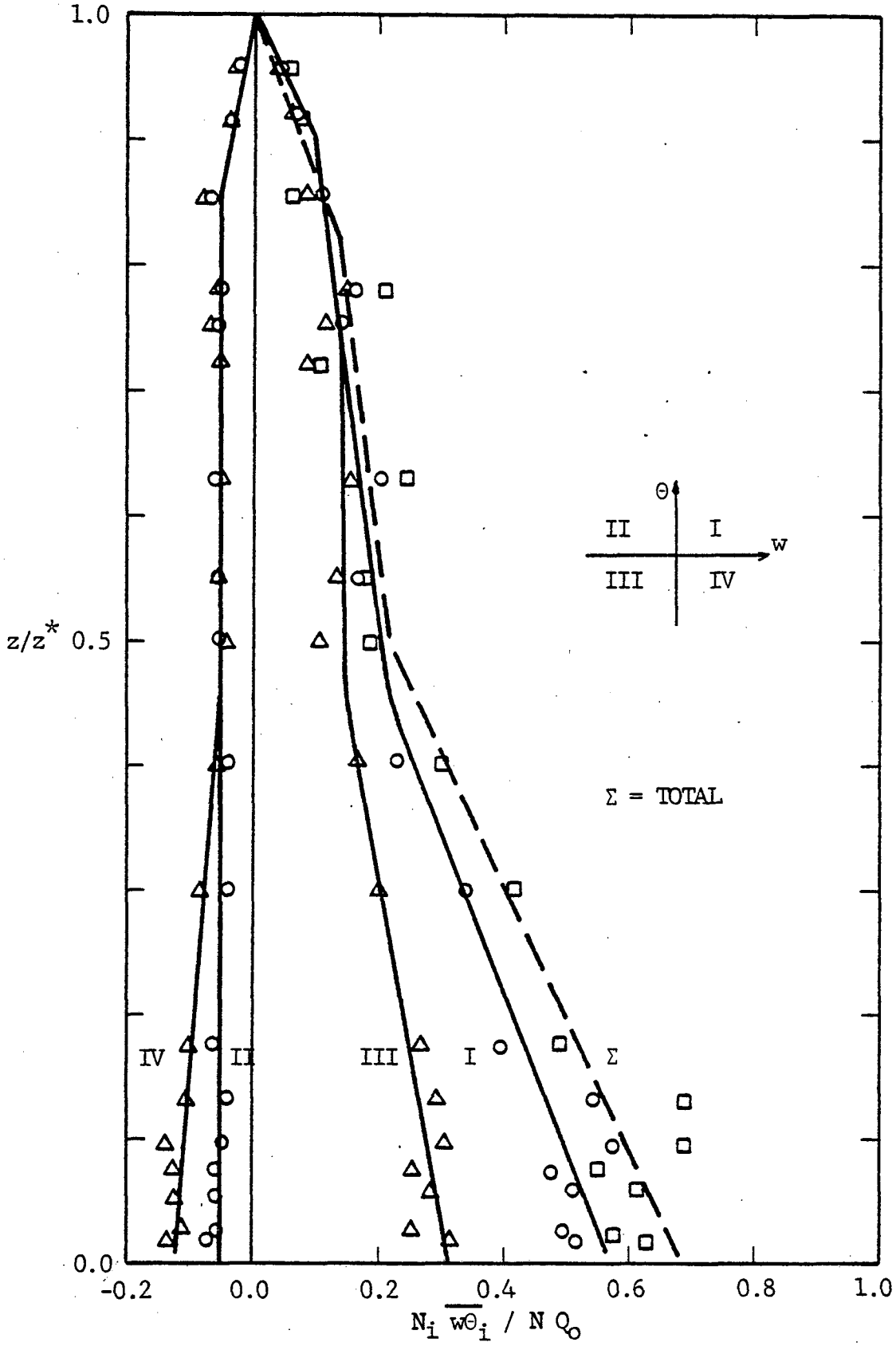

Figure 4.59 - Fraction of the kinematic heat flux associated with groups I to V - $Pe_* = 9370$.

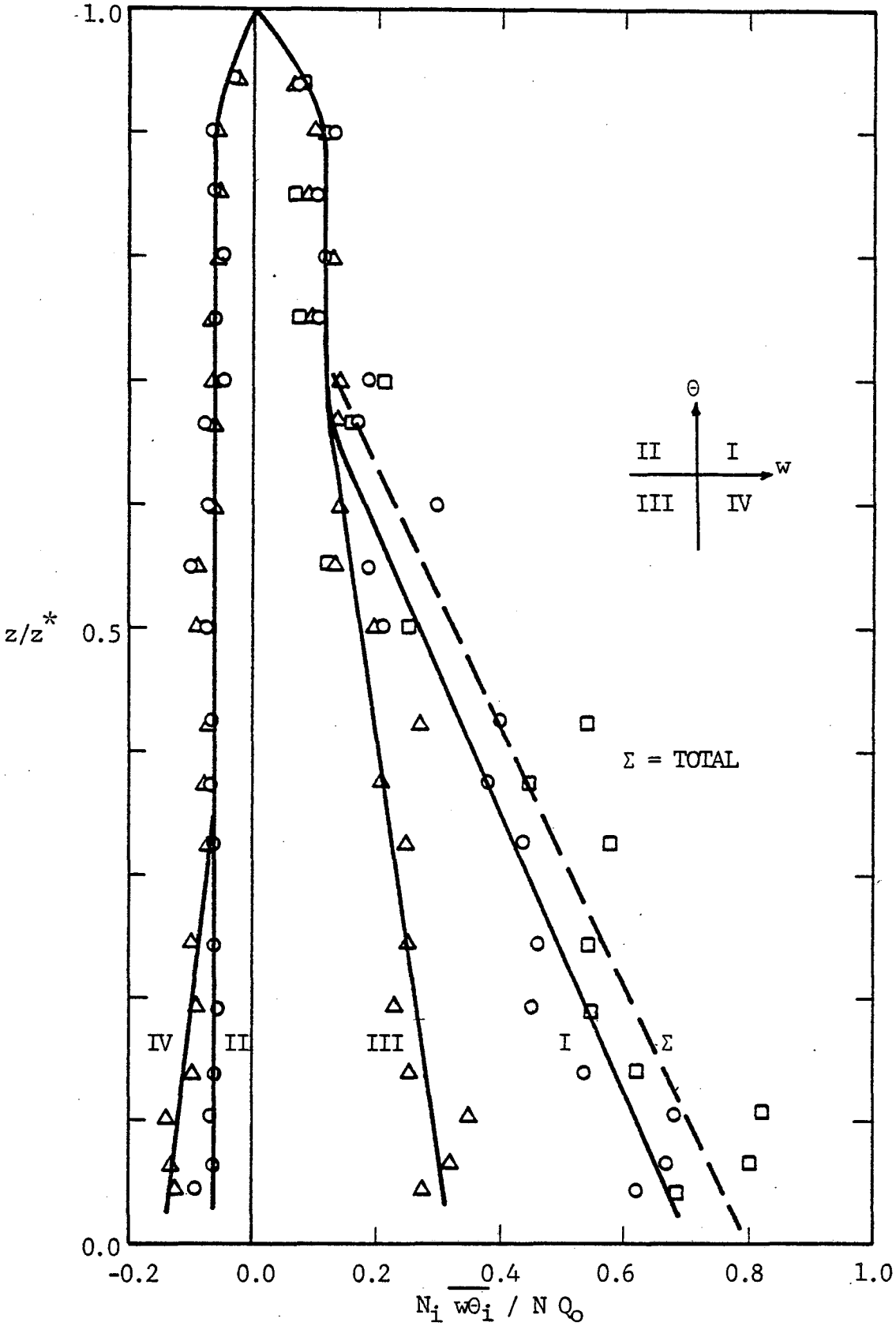

Figure 4.60 - Fraction of the kinematic heat flux associated with groups I to V - $Pe_* = 6000$.

fluxes in each quadrant, calculated according to

$$\frac{\overline{w\theta}_i}{w_*\theta_*} = \left(\frac{\sigma_w}{w_*}\right)\left(\frac{\sigma_\theta}{\theta_*}\right)\left(\frac{N}{N_i}\right)\left[\frac{1}{N}\sum_{a\in i}\left(\frac{w}{\sigma_w}\right)_a\left(\frac{\theta}{\sigma_\theta}\right)_a\right]. \qquad (4.13)$$

Figures 4.57 through 4.60 contain the information about the partial contribution of the points in each quadrant for the total heat flux, or, in other words, the fraction of the kinematic heat flux associated with groups I-V. These are related to the conditional averages by

$$\frac{N_i}{N}\frac{\overline{w\theta}_i}{w_*\theta_*} = \frac{1}{Q_0 r_{w\theta}}\left[\frac{1}{N}\sum_{a\in i}\left(\frac{w}{\sigma_w}\right)_a\left(\frac{\theta}{\sigma_\theta}\right)_a\right]. \qquad (4.14)$$

This analysis did not yield definite conclusions about the low kinematic heat flux. However, the important point was the existence of two gradients for the heat flux in the layer. Generally speaking, the fraction of the III quadrant nearly balances the negative contributions of the II and IV which are almost constants throughout the layer. It appears that the contribution from the I quadrant should have been bigger. The change in inclination of the heat flux moment happens close to $z/z_* = 0.6$, coinciding with the division of the convective layer as presented in section 4.4

4.7 Energy Budget

Smooth curves faired through the graphs of the central moments in section 4.4 were used to evaluate all measurable terms in the budget of kinetic energy, thermal variance and kinematic heat flux. Neglecting the contribution of the terms involving the pressure

fluctuations, the following dimensionless equations were used to evaluate the rate of dissipation terms as residuals in the balances:

$$\frac{\varepsilon}{\varepsilon^*} = -\frac{\partial}{\partial z_+}\left[w\left(\overline{\frac{1}{2}q^2}\right)\right]^+ + \overline{w\theta}^+ + \frac{1}{Re_*}\frac{\partial^2}{\partial z_+^2}\left[\overline{\frac{1}{2}q^2}\right]^+ \tag{4.15}$$

$$\frac{\varepsilon_\theta}{\varepsilon_{\theta_*}} = \frac{1}{Pe_*}\left[\frac{\partial^2\left(\overline{\frac{1}{2}\theta^2}\right)}{\partial z_+^2}\right]^+ - \left[\overline{w\theta}^+\frac{\partial T^+}{\partial z^+}\right] - \frac{1}{2}\frac{\partial}{\partial z_+}\left[\overline{(\theta^2 w)}^+\right] \tag{4.16}$$

$$\frac{\varepsilon_{w\theta}}{\varepsilon^*_{w\theta}} = \frac{\partial}{\partial z_+}\left[\overline{w^2\theta}\right]^+ + \left[\overline{w^2}^+\frac{\partial T^+}{\partial z^+}\right] + \left[\overline{\theta^2}^+\right] \tag{4.17}$$

All third order moments were non-dimensionalized using the kinematic heat flux at the lower boundary in the scales.

Figures 4.61 through 4.63 show the variation of the various terms of equations (4.16), (4.17) and (4.18) throughout the layer. The important points to be emphasized are that the terms involving the molecular transport are only important close to the lower boundary, the terms involving the mean temperature gradient vanish around $z/z_* = 0.20$ and the dissipation of kinetic energy is approximately equal to the production term throughout the layer. The rate of dissipation of kinetic energy and thermal variance calculated from power spectrum analysis using the hypothesis of local isotropy are presented in Figures 4.61 and 4.62 and the agreement with the values calculated from energy budget is very good.

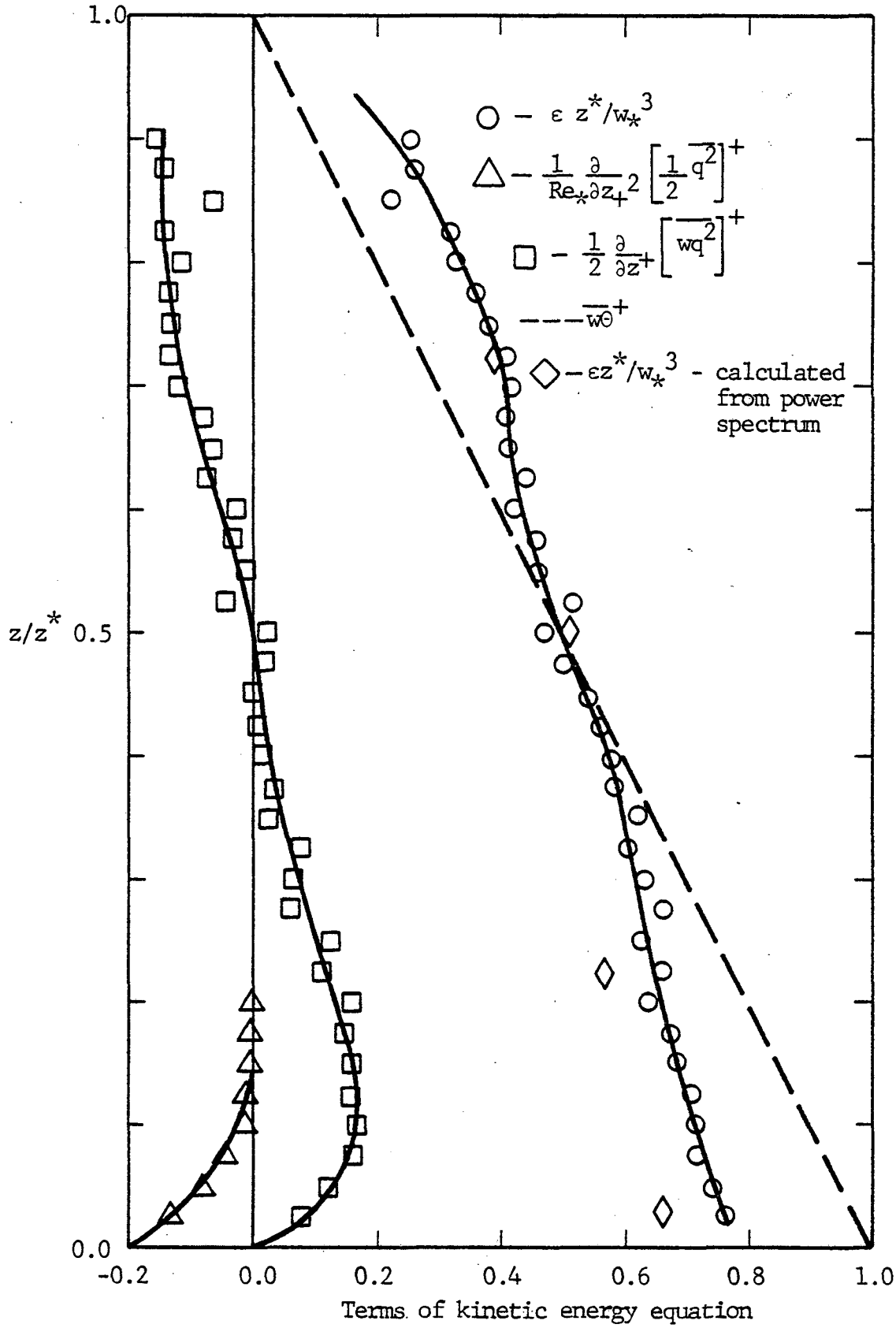

Figure 4.61 - Kinetic energy balance.

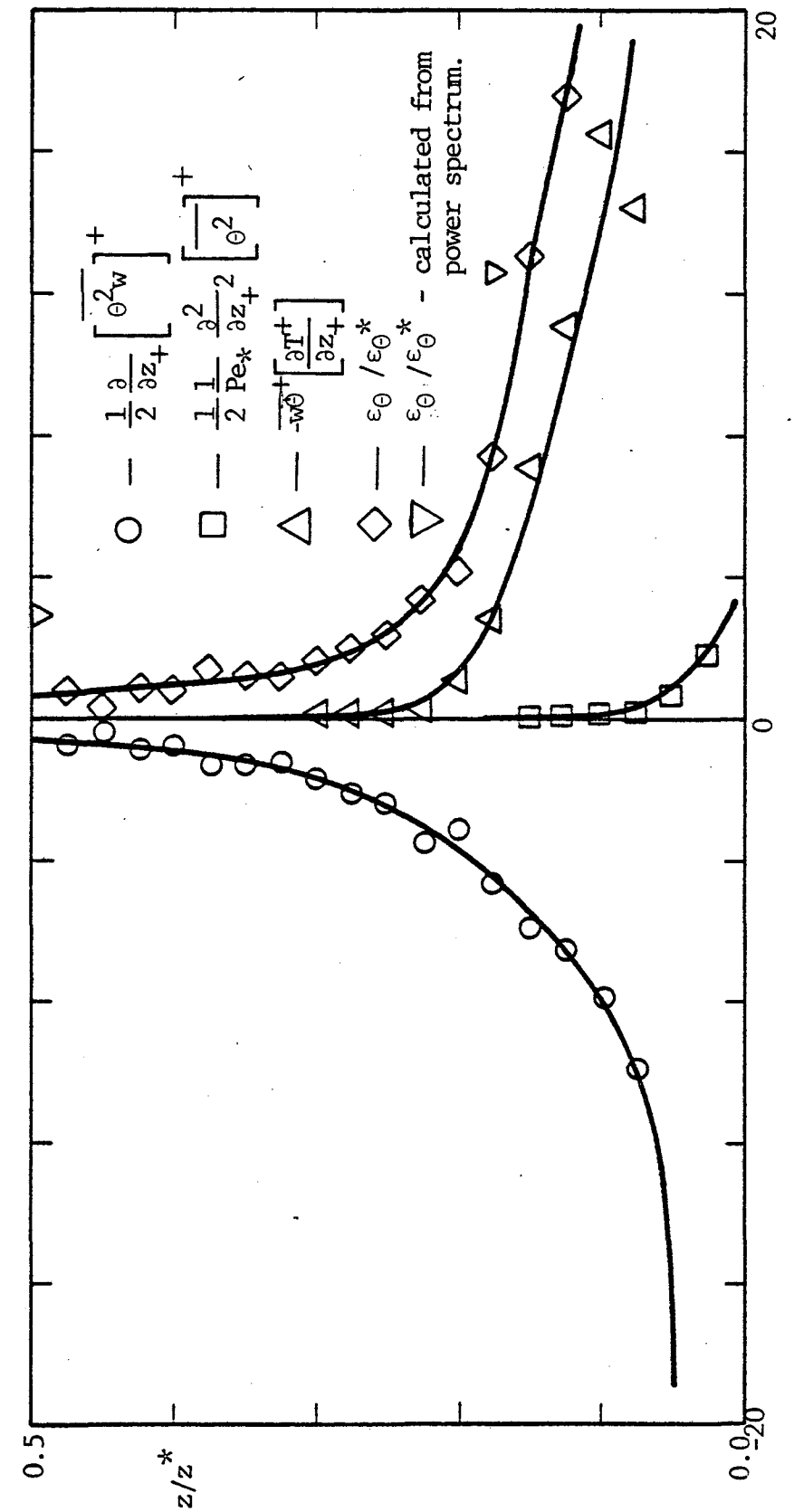

Terms of temperature variance equation

Figure 4.62 - Thermal energy balance.

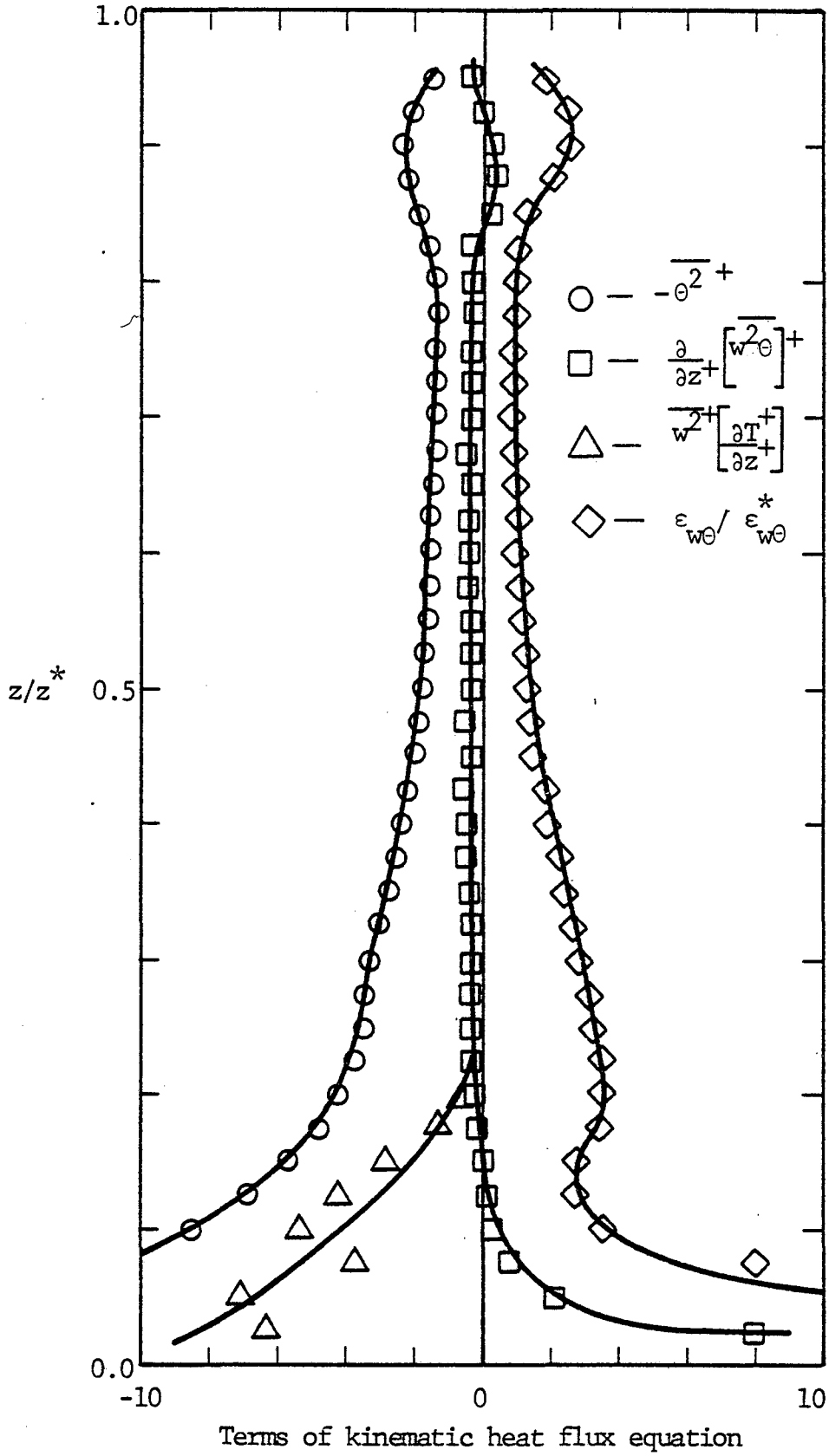

Figure 4.63 - Kinematic heat flux balance.

4.8 Prandtl Number Dependence

In order to check the calculated central moments for any dependence with respect to the Prandtl number due to the variation of the mean temperature from one set of data to the other, special runs were taken with the following characteristics

$z/z^* = 0.070$

$z^* = 200$ mm

$Q_0 = 0.033$ °K cm/s

Number of runs in each set = 16

Dwell time = 5000 μs

Number of Channels = 4

Resolution = 9 bits

Vertical Display Settings

Channel	Variable	Volts Full Scale	LP Filter [ms]
A	w	$\pm$ 2	10
B	θ	$\pm$ 1/4	10
C	u	$\pm$ 2	10

Six sets of independent runs were taken with mean core temperatures in each one ranging from 31.50°C up to 40.95°C as shown in Table 4.

The calculated central moments showed no evident Prandtl number dependence. The calculated values varied within the normal experimental uncertainty when compared with the results obtained in section 4.4.

Table 4

Prandtl Number Dependence of the Central Moments

Mean Temp °C	Pr #	σ_w/w_*	σ_θ/θ_*	σ_u/w_*	$\overline{w\theta}/Q_0$	$\overline{w^3}/w_*^3$	$\overline{u^3}/w_*^3$	$\overline{w^4}/w_*^4$	$\overline{u^4}/w_*^4$	$\overline{w^2\theta}/w_*Q_0$	$\overline{\theta^2 w}/\theta_*Q_0$
31.50	5.20	0.543	3.306	0.771	0.738	0.046	0.133	0.263	0.820	0.245	4.22
33.35	4.90	0.538	3.518	0.609	0.764	0.028	0.017	0.261	0.407	0.381	6.25
35.20	4.75	0.507	3.499	0.673	0.720	0.034	0.064	0.222	0.565	0.314	4.97
37.15	4.55	0.522	3.265	0.619	0.667	0.044	0.020	0.208	0.433	0.257	4.89
39.00	4.40	0.542	3.738	0.640	0.739	0.031	-0.059	0.237	0.534	0.281	5.82
40.95	4.20	0.523	3.634	0.603	0.766	0.026	-0.042	0.228	0.366	0.206	3.84

4.9 Power Spectrum Analysis

The power spectra of w, θ and u signals of some of the sets, used to calculate the central moments, were computed in order to identify possible characteristic subranges in the wave number space and, if an inertia subrange exists, to calculate the dissipation function of thermal and kinetic energy. The graphs of the power spectrum are shown in Figures 4.64 to 4.75. They represent the average value of all the spectra in one set (typically 14 runs). The calculation was done according to the description given in section 3.3.

The -5/3 region of the inertia subrange of horizontal and vertical velocities is reasonably well defined in the sets located away from the lower boundary. For large Prandtl number liquids, the temperature spectrum is expected to show a viscous-convective subrange with a -1 power law after an inertia subrange with a -5/3 power law. In the viscous convective subrange the molecular viscosity is important and the energy spectrum is dropping off sharply, while molecular thermal diffusivity has not yet become effective. Some of the temperature spectra did not show the viscous-convective subrange (-1) right after the inertial subrange and vice-versa.

The one-dimensional spectrum function was made dimensionless using the convective scales and transformed from frequency spectrum to wave number spectrum using the scanning speed U. The vertical log axis in the graphs corresponds to $\frac{UF_u(f)}{2\pi w^{*2} z_*}$ or $\frac{UF_\theta(f)}{2\pi \theta_*^2 z_*}$ or $\frac{UF_w(f)}{2\pi w_*^2 z_*}$ and the horizontal log axis is $\frac{2\pi z^* f}{U}$ where f is the frequency at which the spectrum is calculated, and given by $f = \frac{1}{N\Delta t}$ where Δt is the interval between points in the digitizer, and $1 \leq N \leq L/2$ and L is

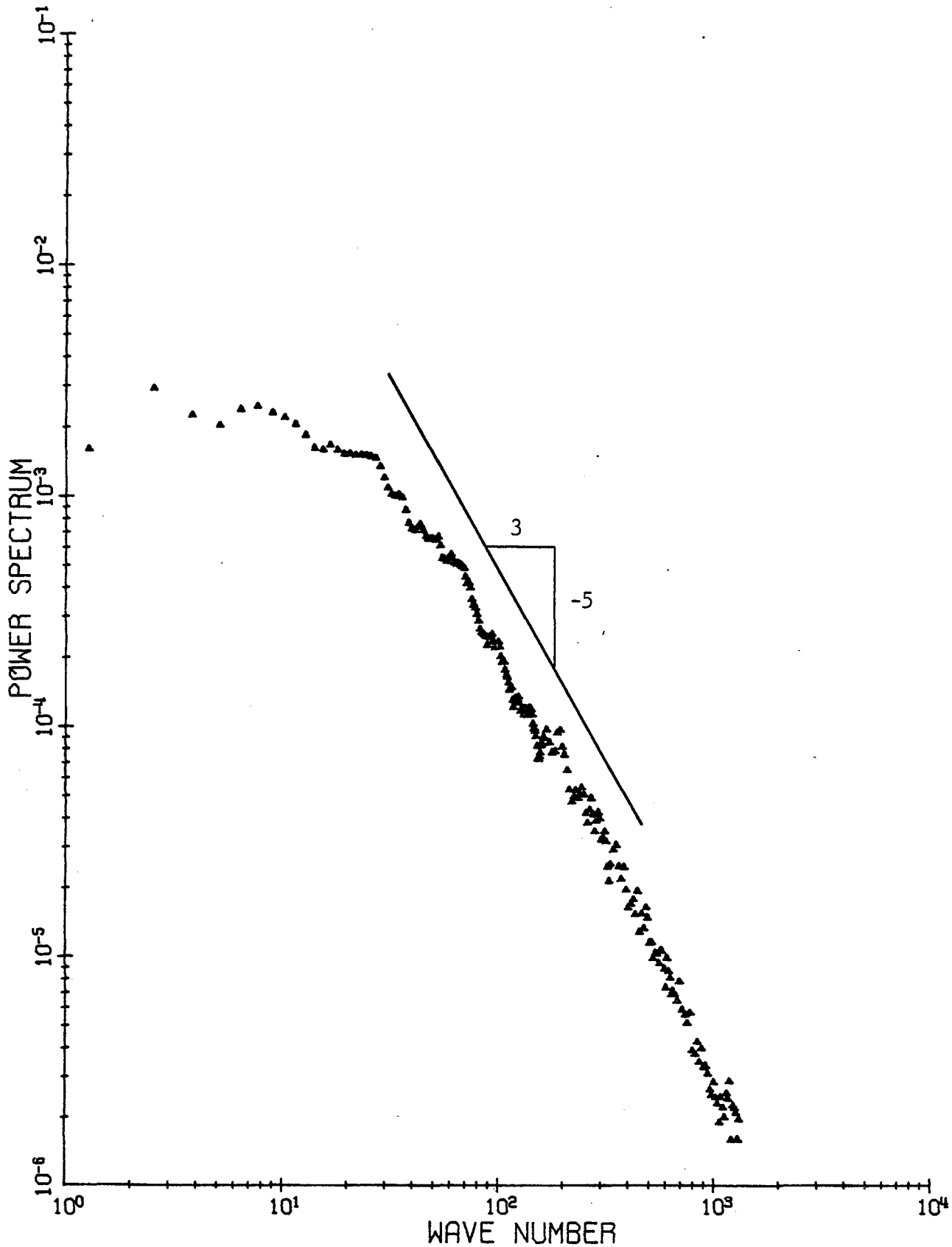

Figure 4.64 - Power spectrum of the vertical velocity fluctuations. Condition III, $Pe_* = 9370$, $z = 5.5$ mm.

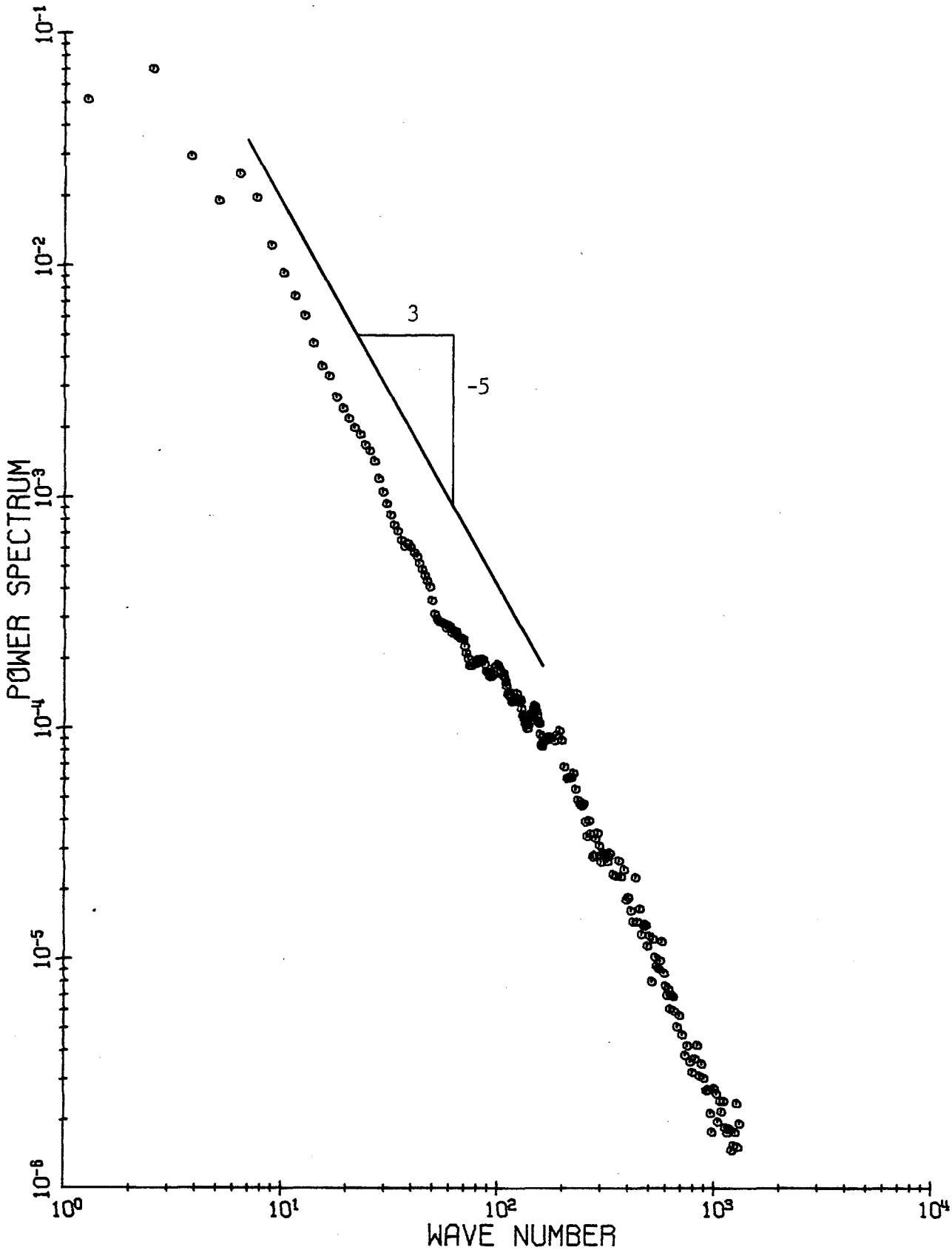

Figure 4.65 - Power spectrum of the horizontal velocity fluctuations. Condition III, $Pe_* = 9370$, $z = 5.5$ mm.

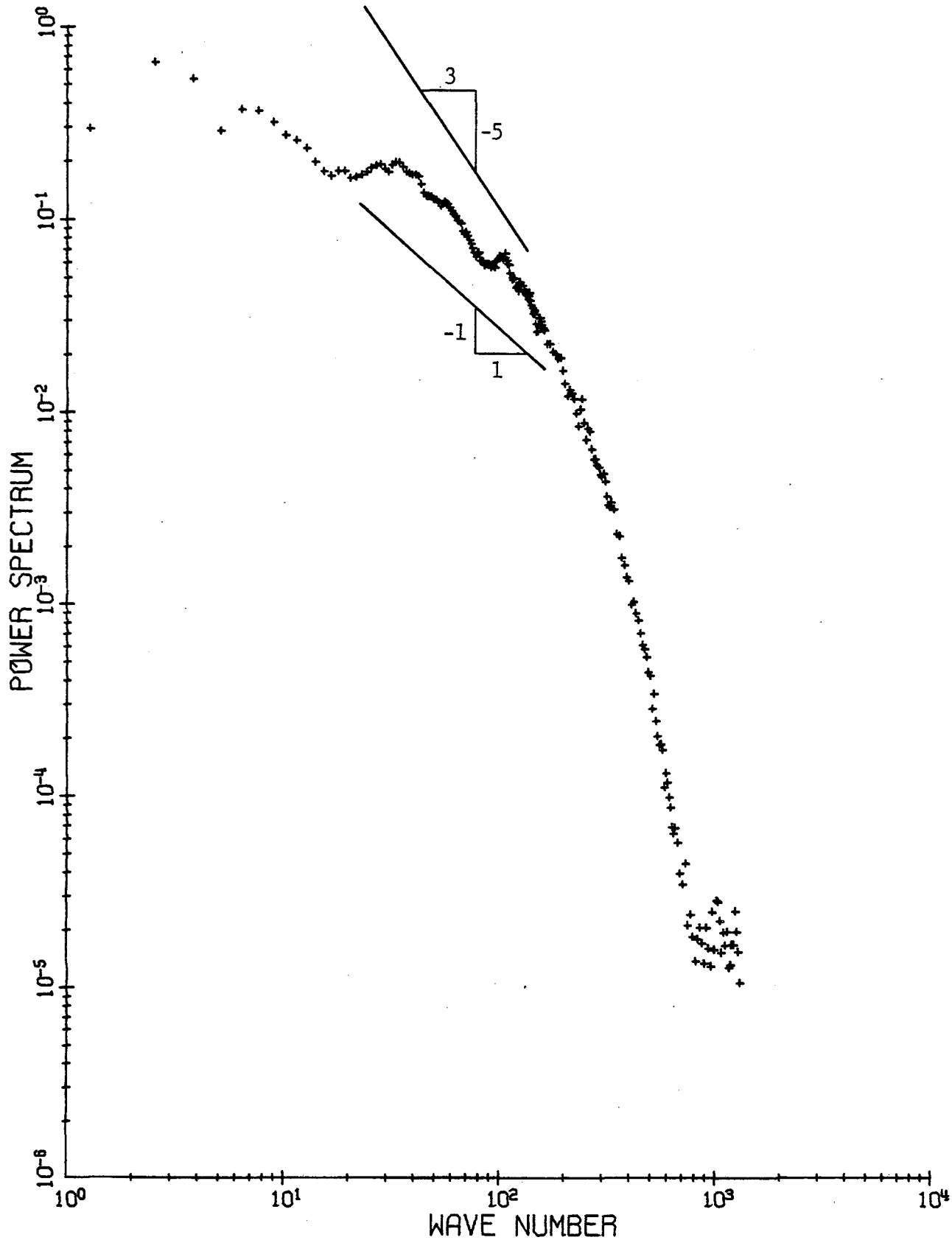

Figure 4.66 - Power spectrum of the temperature fluctuations. Condition III, Pe_{*} = 9370, z = 5.5 mm.

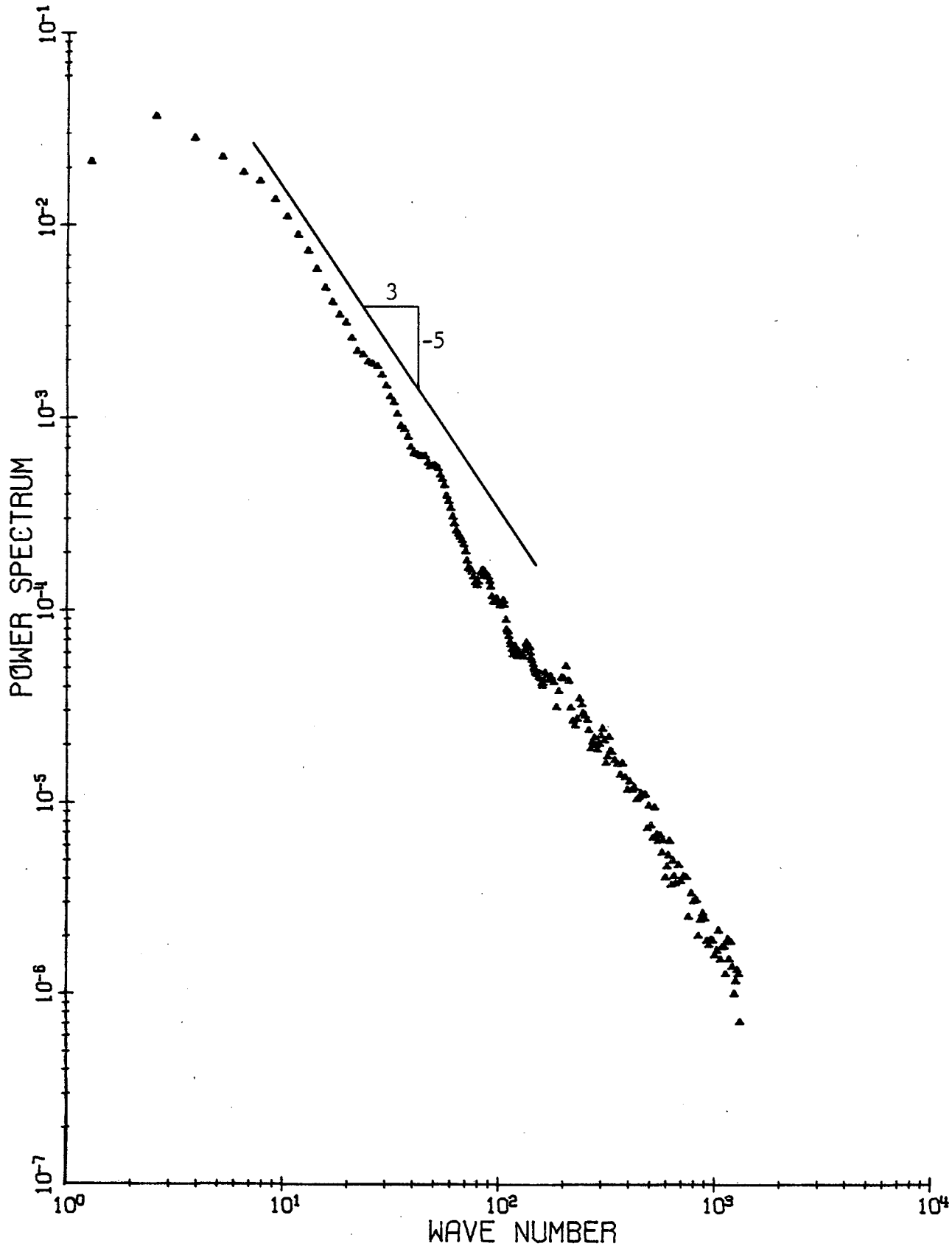

Figure 4.67 - Power spectrum of vertical velocity. Condition III, $Pe_* = 9370$, $z = 100.5$ mm.

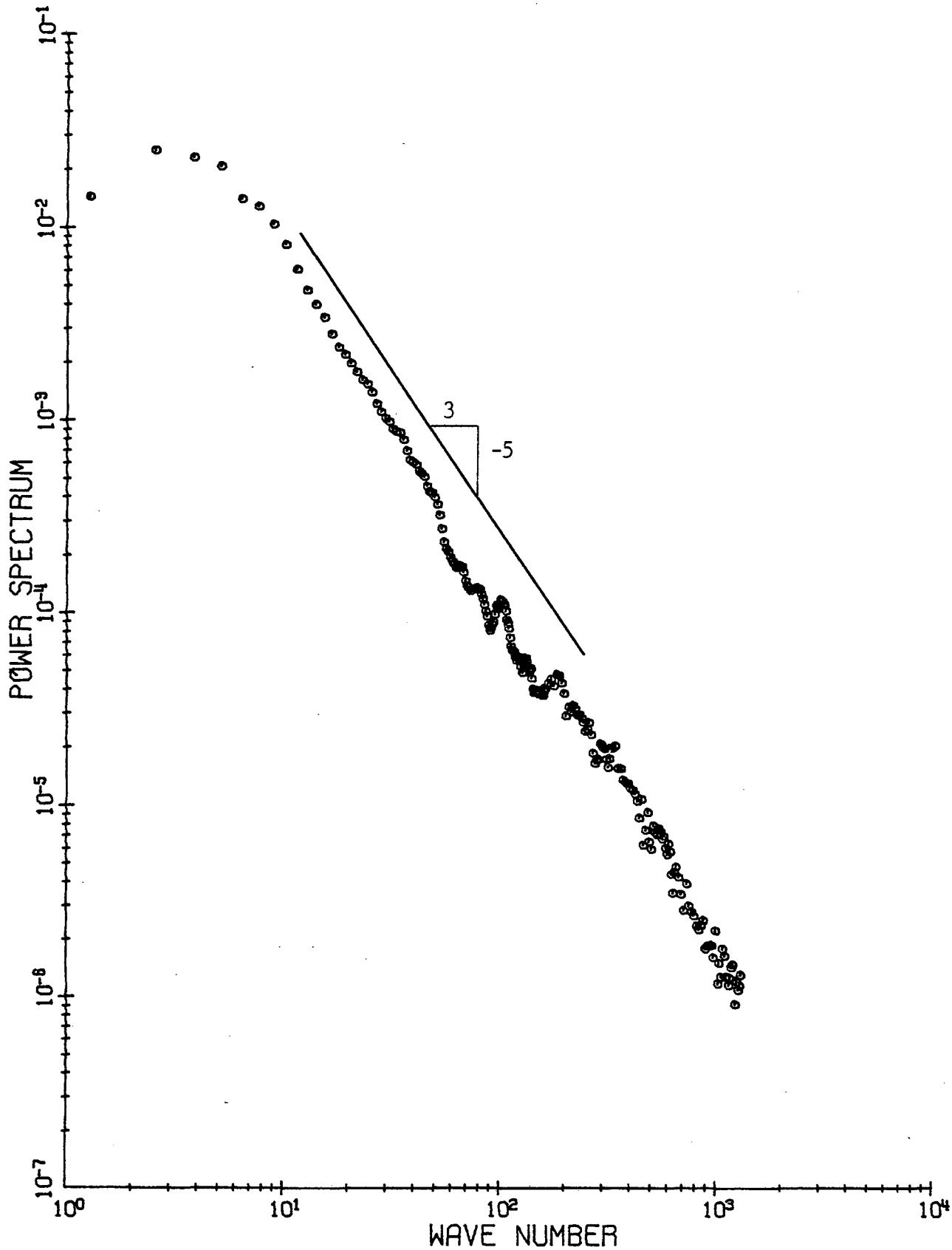

Figure 4.68 - Power spectrum of the horizontal velocity fluctuations. Pe_{*} = 9370, z = 100.5 mm. condition III.

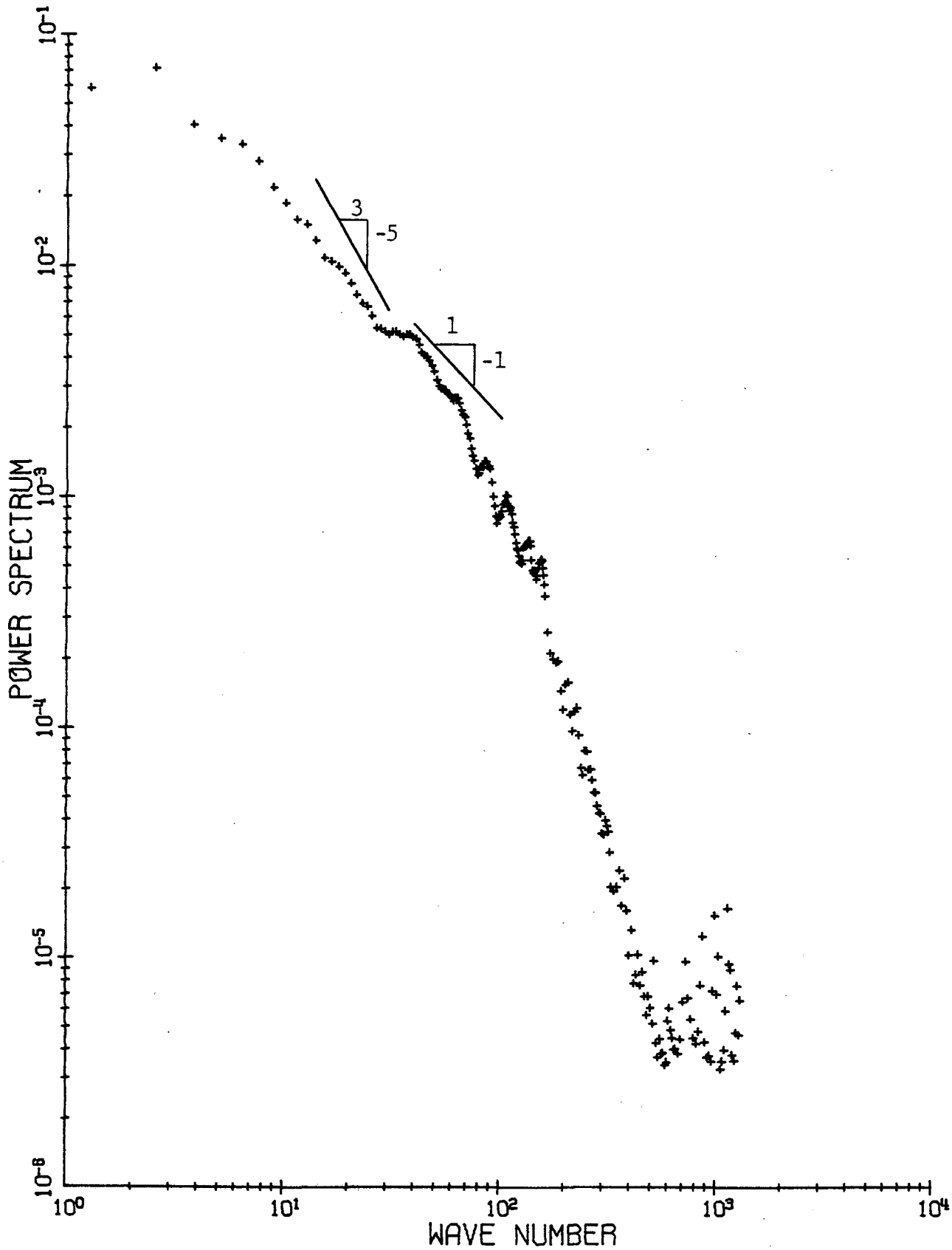

Figure 4.69 - Power spectrum of temperature fluctuations. Condition III, $Pe_{\lambda} = 9370$, z = 100.5 mm.

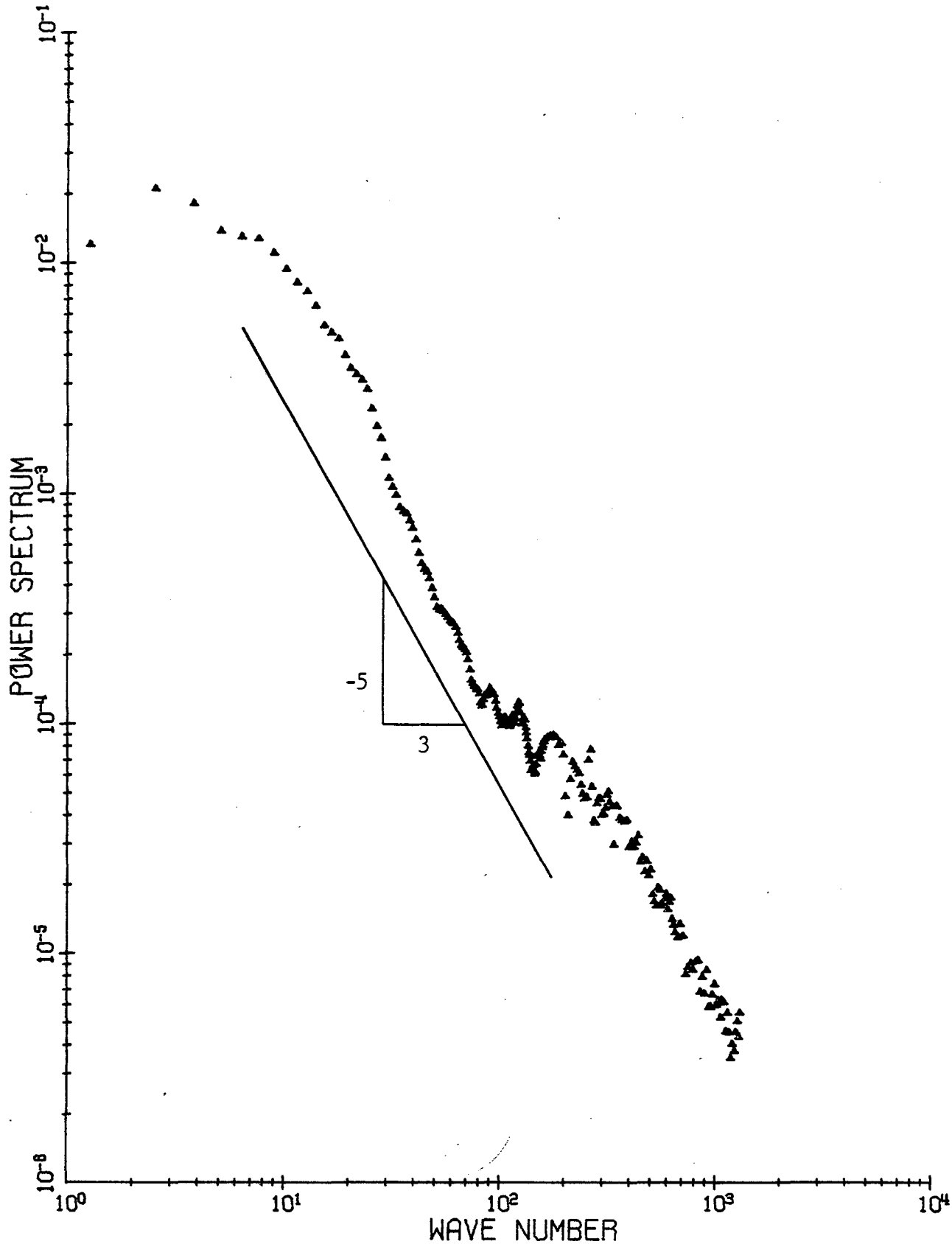

Figure 4.70 - Power spectrum of the vertical velocity fluctuations. Condition I, Pe_{*} = 6090, z = 130 mm.

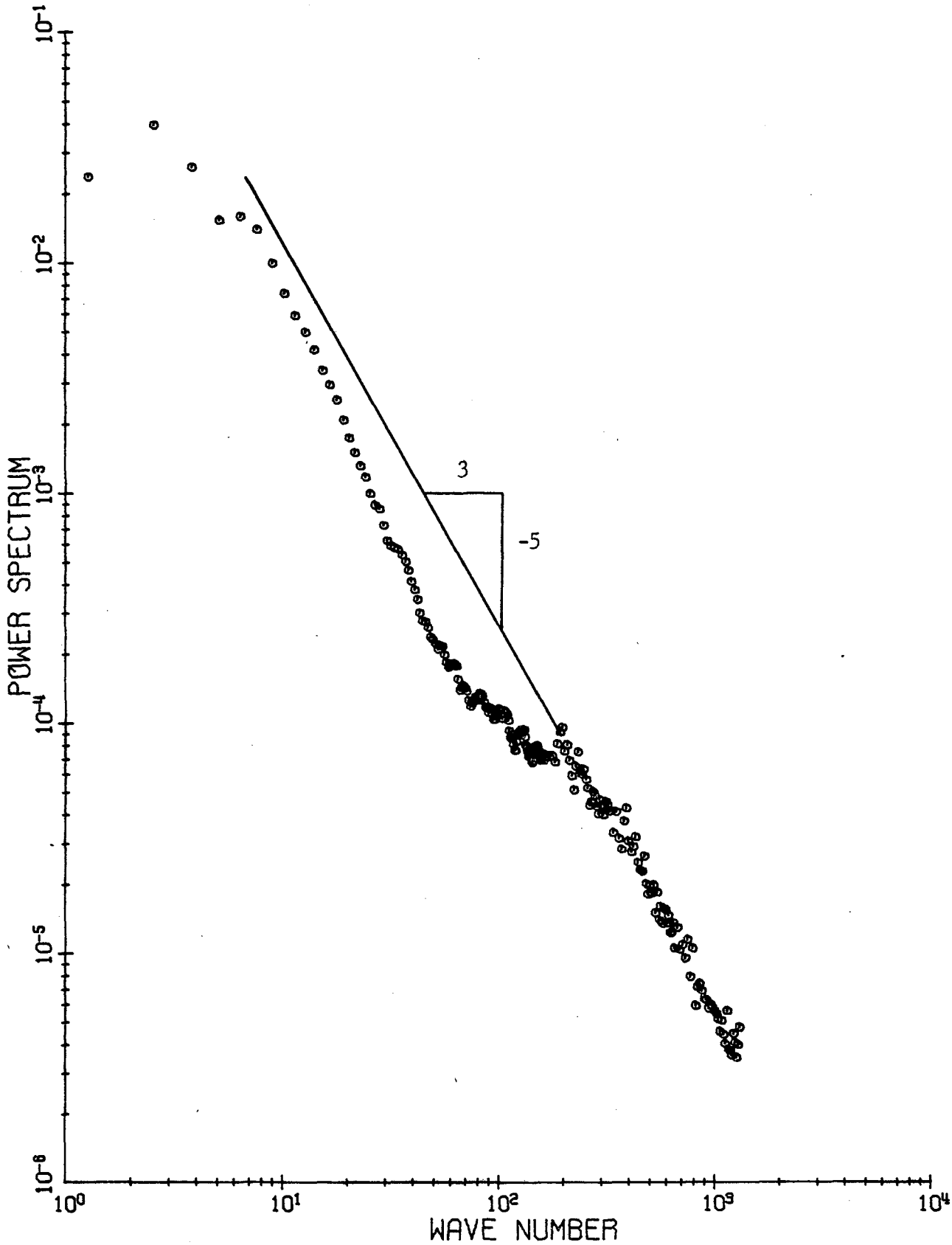

Figure 4.71 - Power spectrum of the horizontal velocity fluctuations. Condition I, $Pe_* = 6090$, $z = 130$ mm.

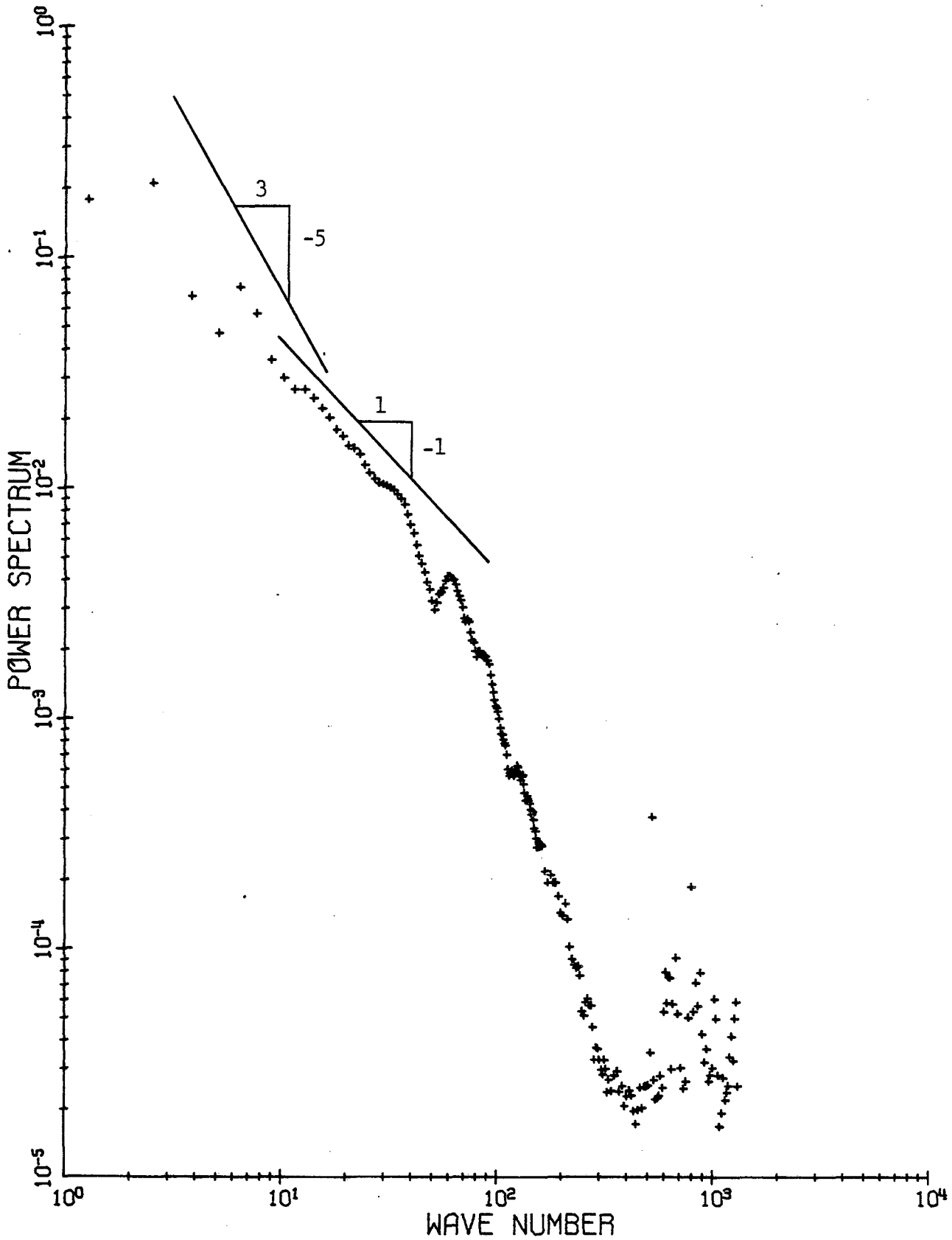

Figure 4.72 - Power spectrum of the temperature fluctuations. Condition I, Pe_{*} = 6090, z = 130 mm.

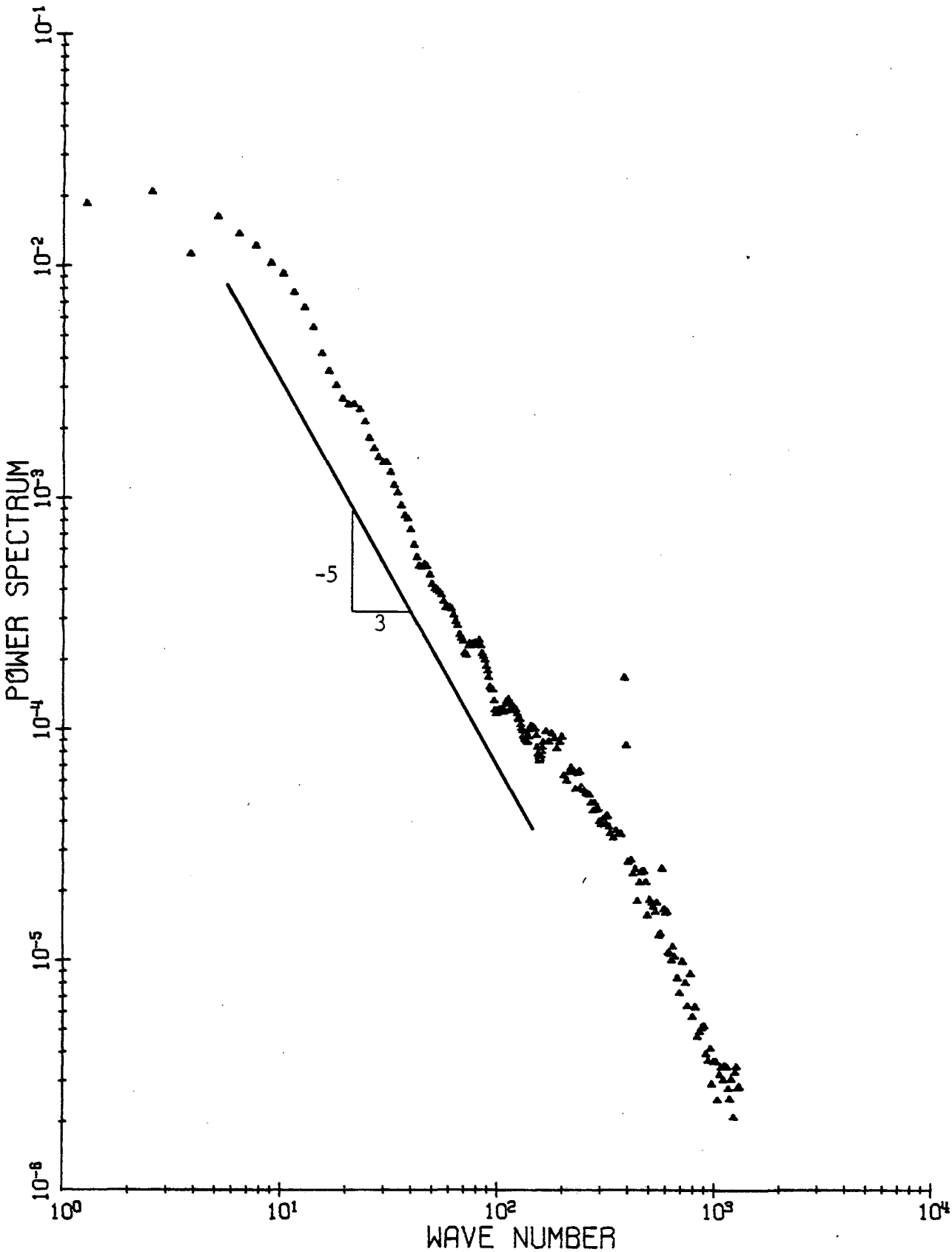

Figure 4.73 - Power spectrum of the vertical velocity fluctuations. Condition II, Pe_{*} = 7840, z = 144.5 mm.

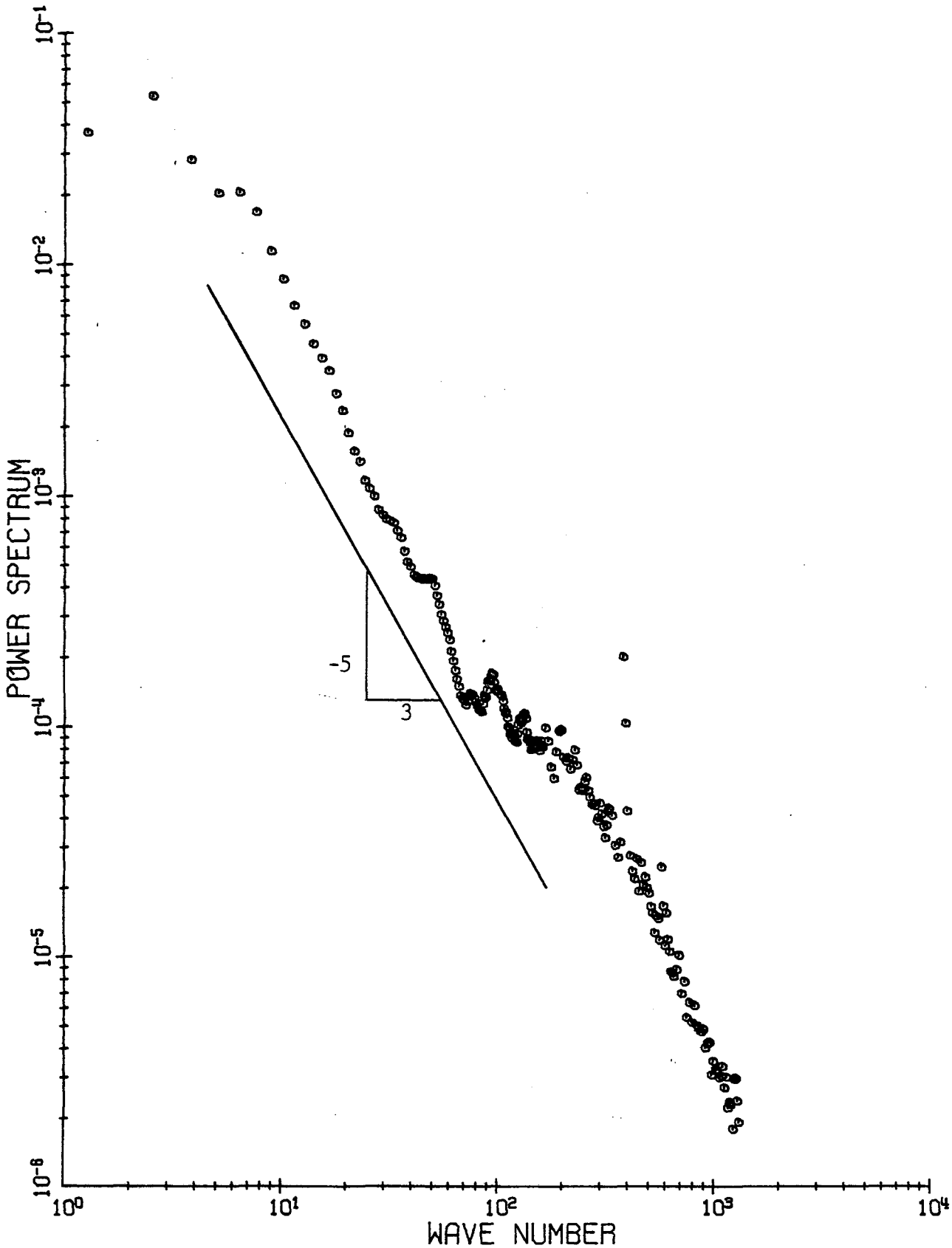

Figure 4.74 - Power spectrum of the horizontal velocity fluctuations. Condition II, Pe_{*} = 7840, z = 144.5 mm.

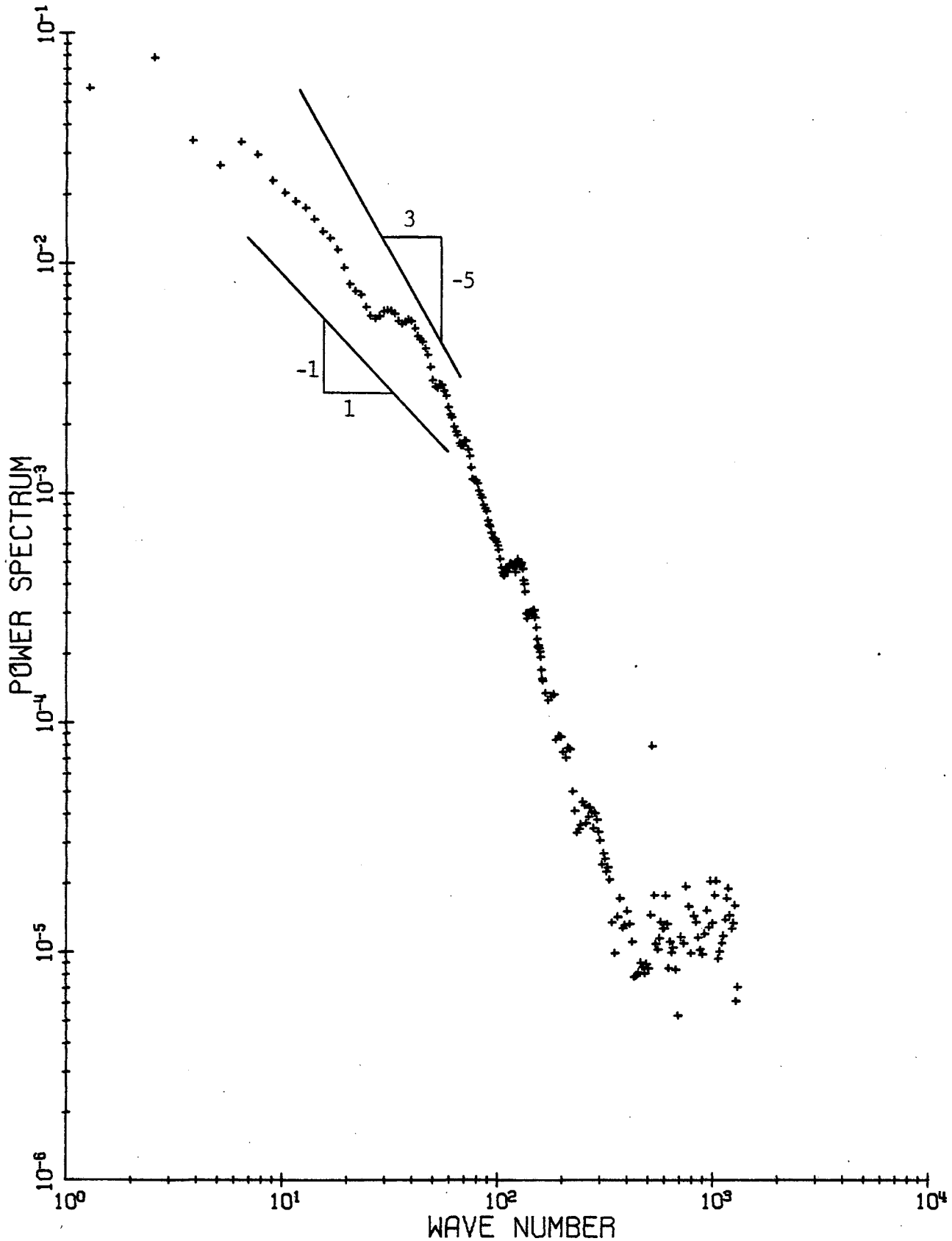

Figure 4.75 - Power spectrum of the temperature fluctuations. Condition II, $Pe_* = 7840$, $z = 144.5$ mm.

the total number of points of the record.

The rate of dissipation functions were calculated using the following expressions:

$$\frac{\varepsilon}{\varepsilon^*} = \left[\frac{F_u(k)\,(kz_*)^{5/3}}{a}\right]^{3/2} \tag{4.18}$$

and

$$\frac{\varepsilon_\theta}{\varepsilon_\theta^*} = \frac{F_\theta(k)\,(\varepsilon/\varepsilon^*)^{1/3}(kz^*)^{5/3}}{b} \tag{4.19}$$

where F_u and F_θ are the dimensionless spectra of horizontal velocity and temperature and a and b are universal constants. The values $a = 0.50$ and $b = 0.40$ were used in the calculations. Table 5 compares the values $\varepsilon/\varepsilon^*$ and $\varepsilon_\theta/\varepsilon_\theta^*$ calculated from the energy spectrum using the data taken at 5.5 mm, 35 mm, 100.5 mm and 144.5 mm and $Q_0 = 0.0568$°K cm/s, and the values computed from the energy balance described in section 4.7.

Table 5

Comparison of Rate of Dissipation Values

z [mm]	Calculated from spectrum		Calculated from energy balance	
	$\varepsilon/\varepsilon^*$	$\varepsilon_\theta/\varepsilon_\theta^*$	$\varepsilon/\varepsilon^*$	$\varepsilon_\theta/\varepsilon_\theta^*$
5.5	0.654	211.6	0.763	180.2
35.0	0.565	12.6	0.640	7.4
100.5	0.509	2.9	0.490	0.8
144.5	0.396	2.4	0.412	0.5

The agreement is very good for the dissipation of kinetic energy. The differences in the dissipation of mean square temperature fluctuations may be due to the difficulty in identifying an inertial and/or viscous-convective subrange. The values for $\varepsilon_\theta/\varepsilon_\theta^*$ away from the lower boundary are very small compared with the values close to it, therefore the importance of the discrepancies in the upper half of the layer is very small.

Figure 4.76 presents the power spectrum of the vertical velocity at different heights from the lower plate and a heat flux of 0.0153°K cm/s for a layer depth of $z^* = 200$ mm, and Figures 4.77 and 4.78 show the power spectrum of the horizontal and vertical velocities at the same height and different heat fluxes.

The fluctuations of the horizontal velocity are generated by a combination of motions of a turbulent nature and periodic oscillations as could be expected from the visualization studies.

The power spectrum of the horizontal component of the velocity should exhibit peaks associated with the wave like motion of the fronts sweeping the lower plate.

The structure associated with the vertical component of the velocity depends appreciably on the distance from the lower boundary, limiting the integral length scale of the flow. Therefore, the power spectrum should have a maximum at the wave number corresponding to this distance.

Unfortunately, due to the smoothing routine, those features are not well identified and yet if no smoothing routine were used, the scatter of the spectral estimates would swamp those characteristics.

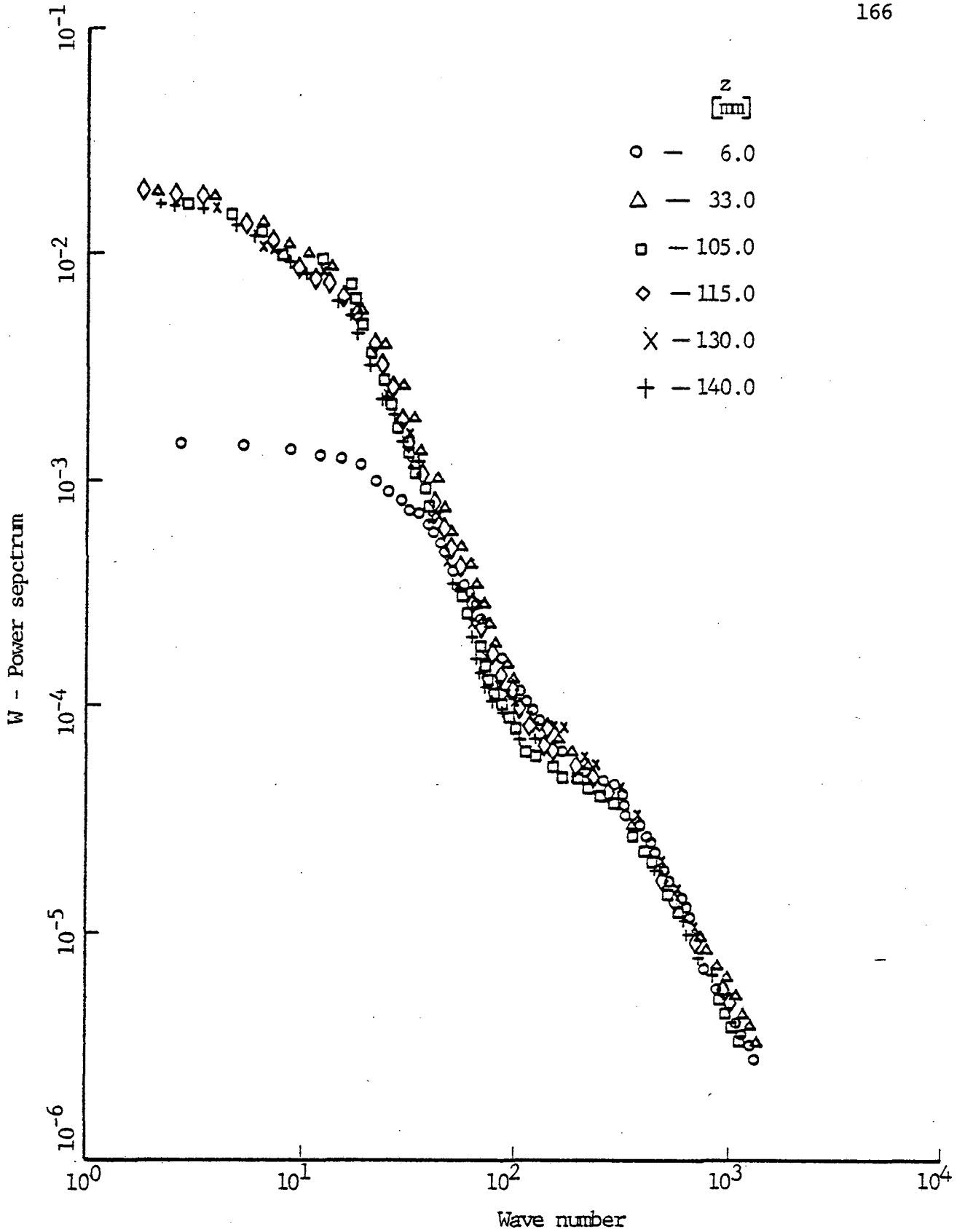

Figure 4.76 - Power spectrum of the vertical velocity for different heights. Condition I, $Pe_* = 6090$.

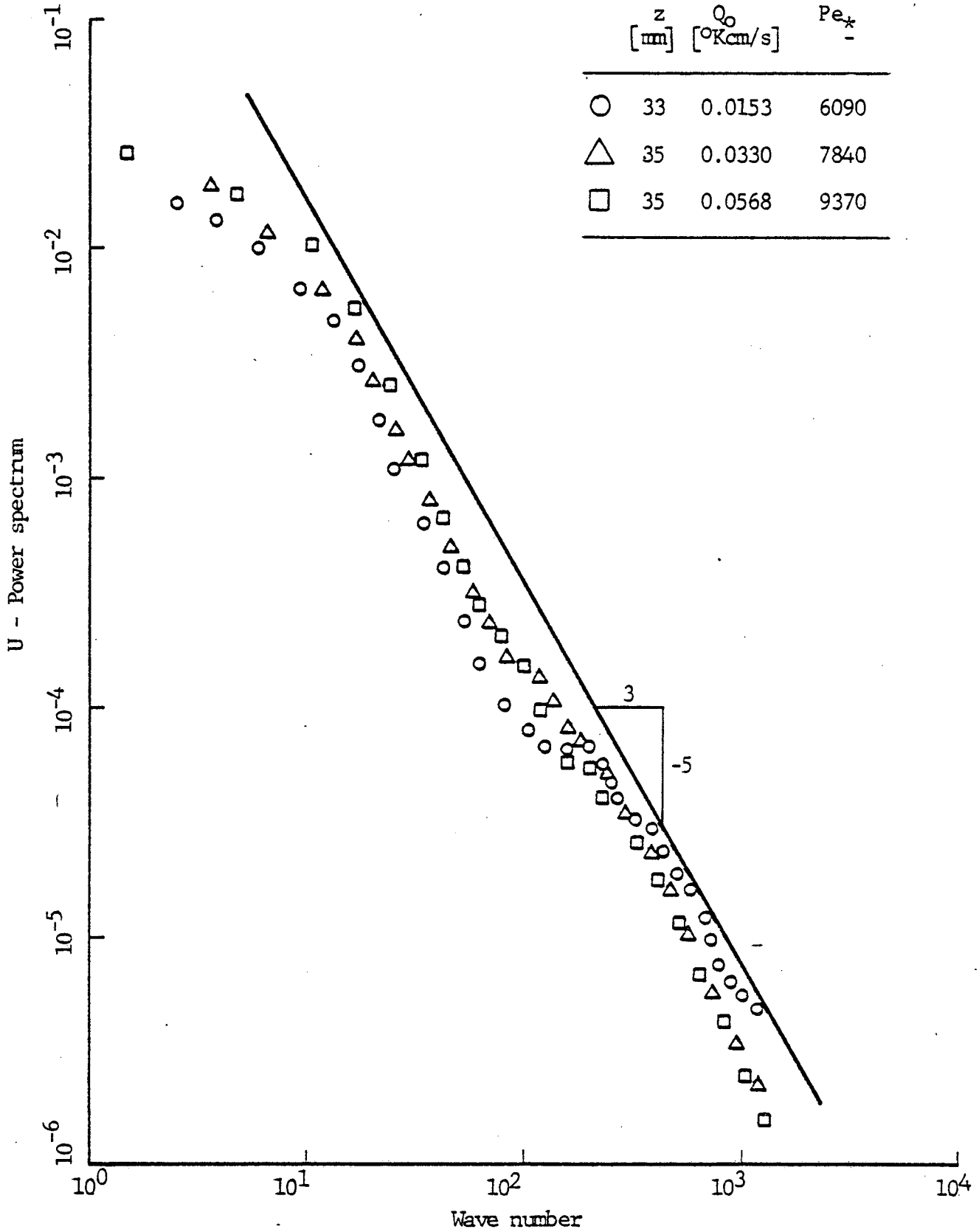

Figure 4.77 - Power spectrum of the horizontal velocity.

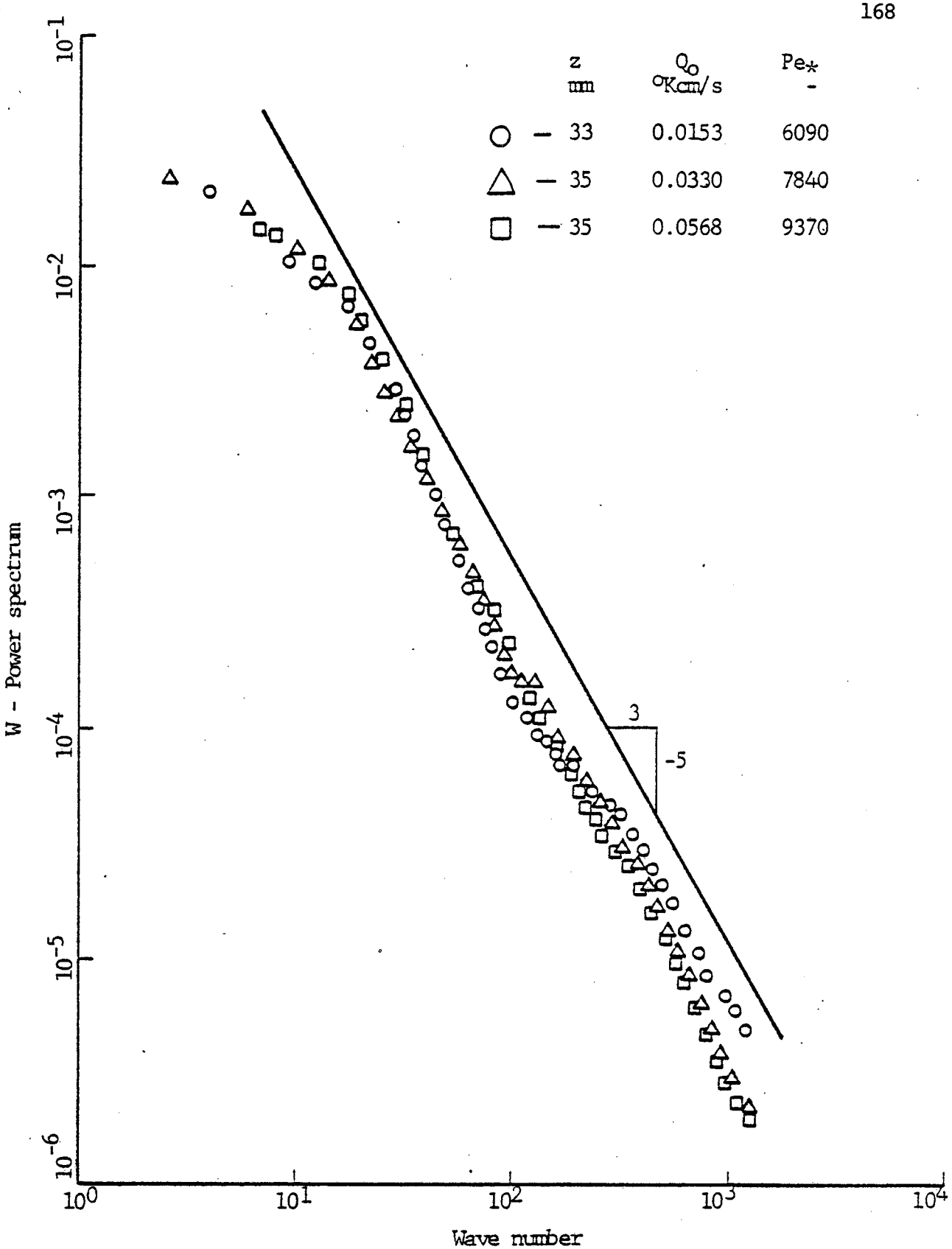

Figure 4.78 - Power spectrum of the vertical velocity.

4.10 Space-Time Cross Correlation

As pointed out in section 3.3, in order to generate a correction factor for the convective heat flux calculation and 3rd order cross moments, due to the horizontal spatial separation of the thermocouple probe and the measurement volume, special horizontal scans using half of the memory for the vertical velocity trace and the other half for the fluctuating temperature signal were performed and the cross correlation function using the Fast Fourier techniques was computed.

$$\overline{w\theta(\tau,\ell)} = \frac{1}{N}\sum_{t} w(x_1,x_2,x_3;t)\,\theta(x_1+\ell,x_2,x_3;t+\tau)$$

Figures 4.79 to 4.81 show the plots of the cross correlation against the horizontal separation using the scanning speed and Taylor's frozen field hypothesis for this conversion.

It was expected that the locus of the maximum points of the cross correlation was a slowly exponentially decaying curve as the separation between probes increased. The existence of maxima at larger separations greater than the maxima at small separations prohibited the use of the correction factor for the cross moments by extrapolating the envelope of the cross correlation curves up to the axis of ordinates.

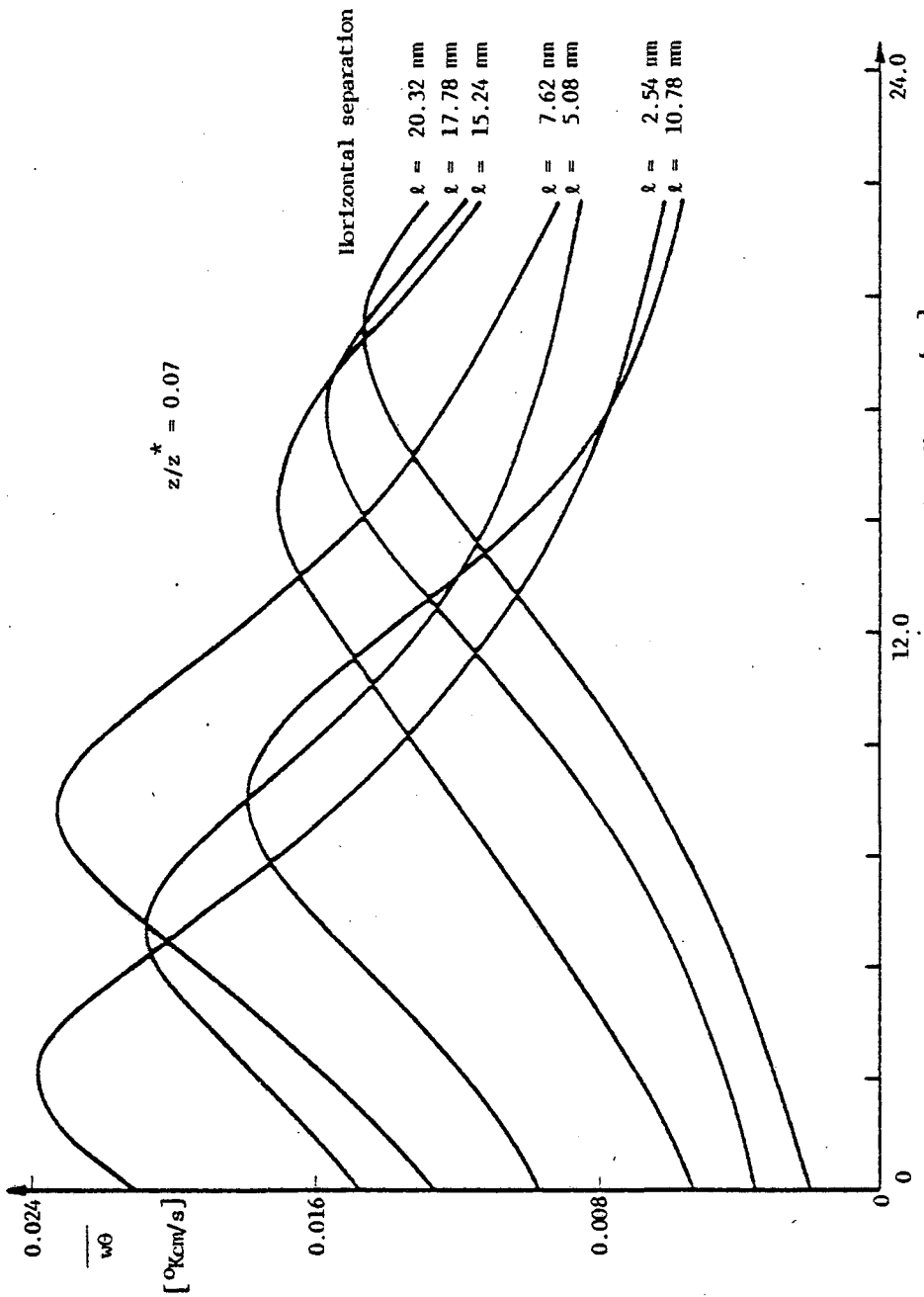

Figure 4.79 - Space time cross-correlation w-θ. Condition II.

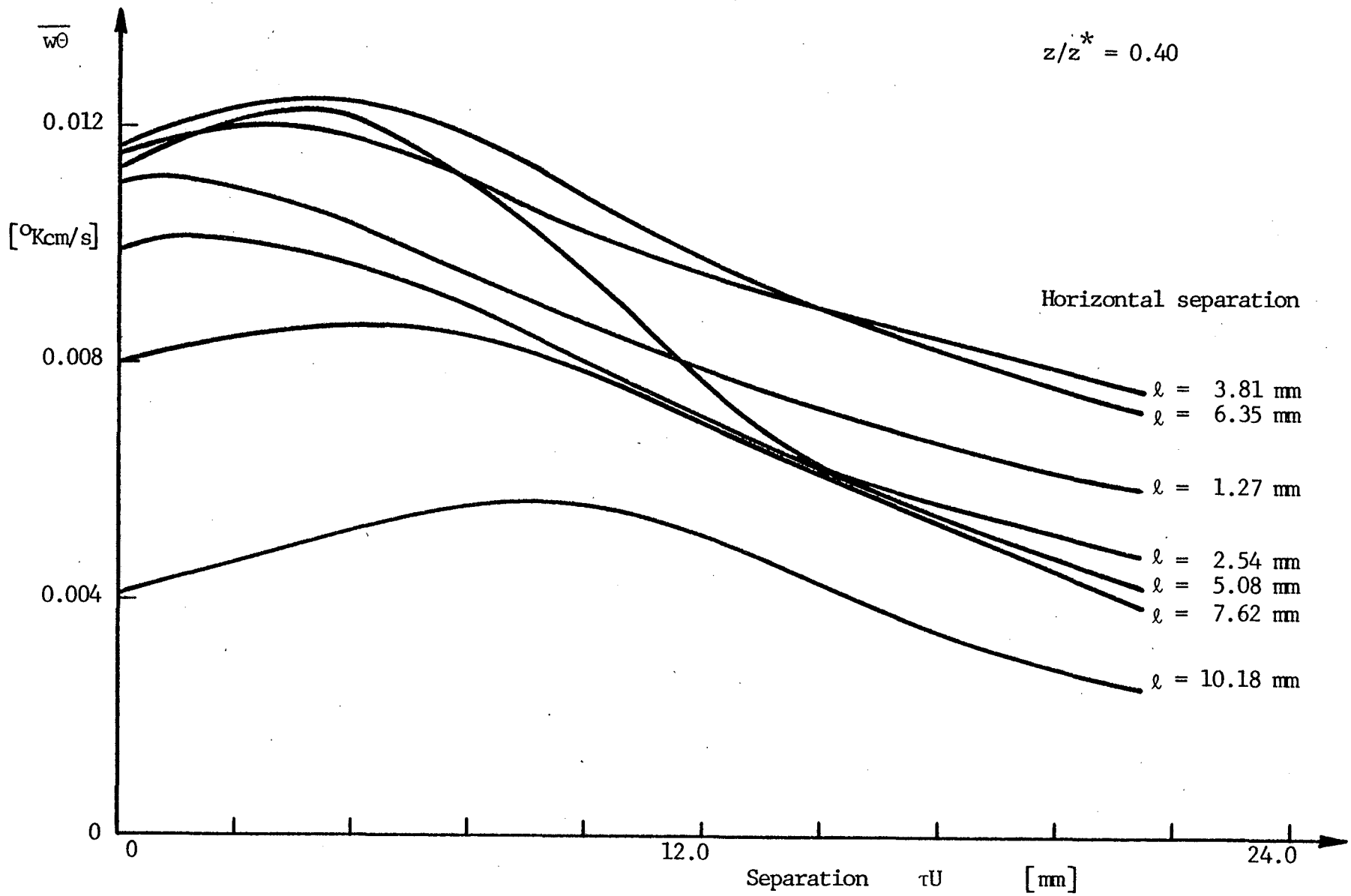

Figure 4.80 - Space time cross-correlation w-θ. Condition II

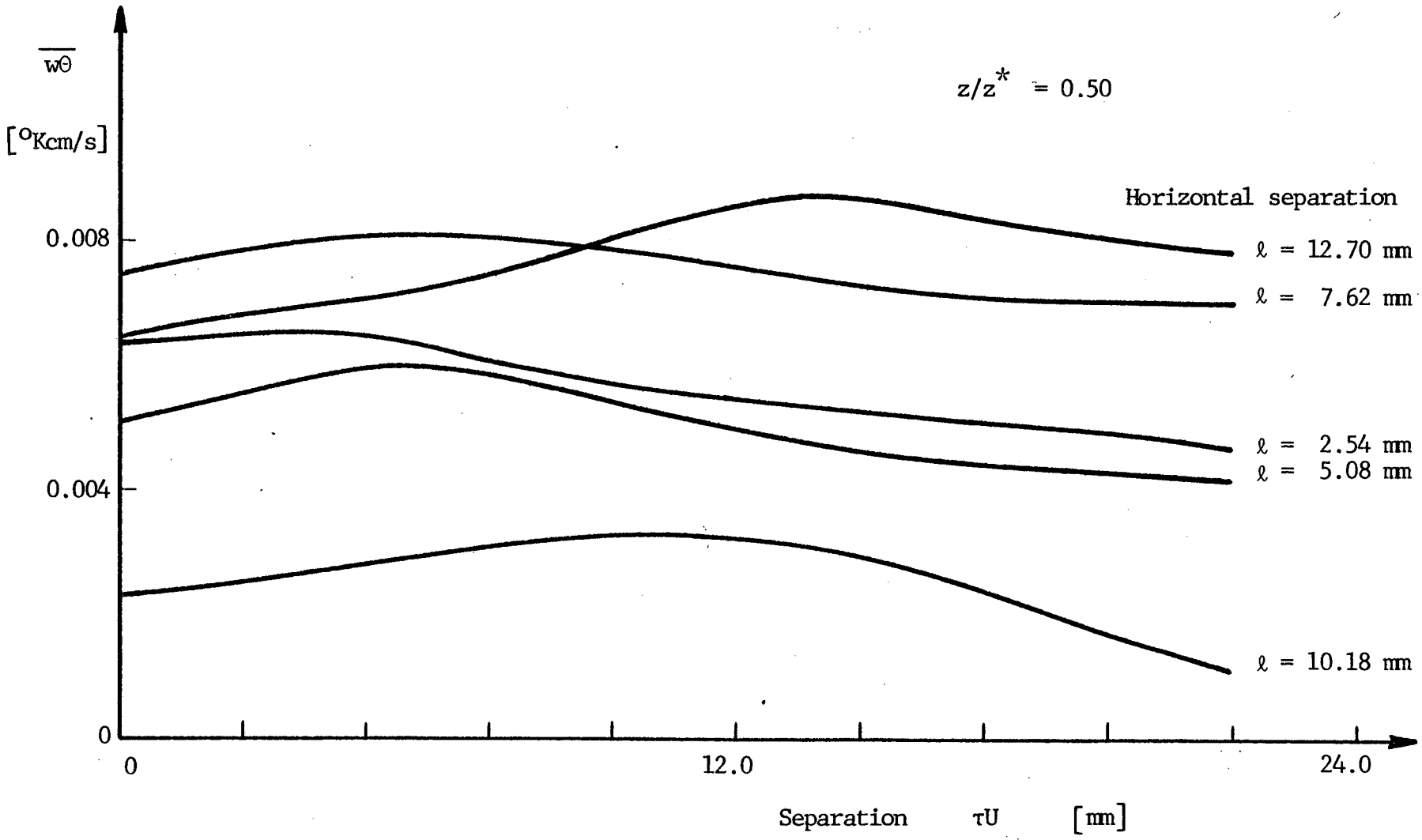

Figure 4.81 - Space time cross-correlation w-Θ Condition II

CHAPTER V

COMPARISON OF THE RESULTS WITH EXPERIMENTAL AND NUMERICAL STUDIES

The vertical profile of some of the moments of the laboratory experiment of Willis and Deardorff (1974), the aircraft measurements of Lenschow (1970, 1974) and Telford and Warner (1964), the data from the Minnesota experiment reported by Kaimal et al. (1977) and the numerical studies of Andre´ et al. (1977) and Zeman and Lumley (1976) were used for comparison with the calculated moments of the present study.

Figures 5.1 to 5.6 present the vertical profile of the moments for the different works.

The same constants of the numerical studies reported in the references, were used to compute the moments.

As can be seen, the agreement of the atomospheric measurements of the RMS values of the vertical velocity and temperature fluctuations with this study is very good. Beyond $z/z_* = 0.1$ the agreement is better with the data from Telford and Warner (1964) and Lenschow (1970, 1974) than with the data from the Minnesota experiment. Within the surface layer, some differences would be expected due to the effects of the mean wind. The laboratory measurements of Willis and Deardorff are also in good agreement for those moments up to $z/z_* = 0.8$ or may be up to a lower height in the layer due to the different upper boundary conditions.

The vertical profile of the RMS of the horizontal velocity agrees well with Lenschow's data but Willis and Deardorff's results are about 75% lower. This discrepancy may be due to the larger aspect ratio

Table 5A

Legend for Figures 5.1 through 5.6

Symbol	Reported by	Observations
●	Willis and Deardorff (1974)	Case S1
▲	Willis and Deardorff (1974)	Case S2
□	Telford and Warner (1964)	Aircraft measurements
▽	Lenschow (1974)	Aircraft measurements as reported by Willis and Deardorff (1974)
◇	Lenschow (1970)	Same as above
▷	Kaimal et al. (1977)	Minnesota experimental data
—·—	Andre et al. (1976)	Clipping approximation - Numerical study
— — —	Zeman and Lumley (1976)	Second order modeling - Numerical study
———	Present study	-

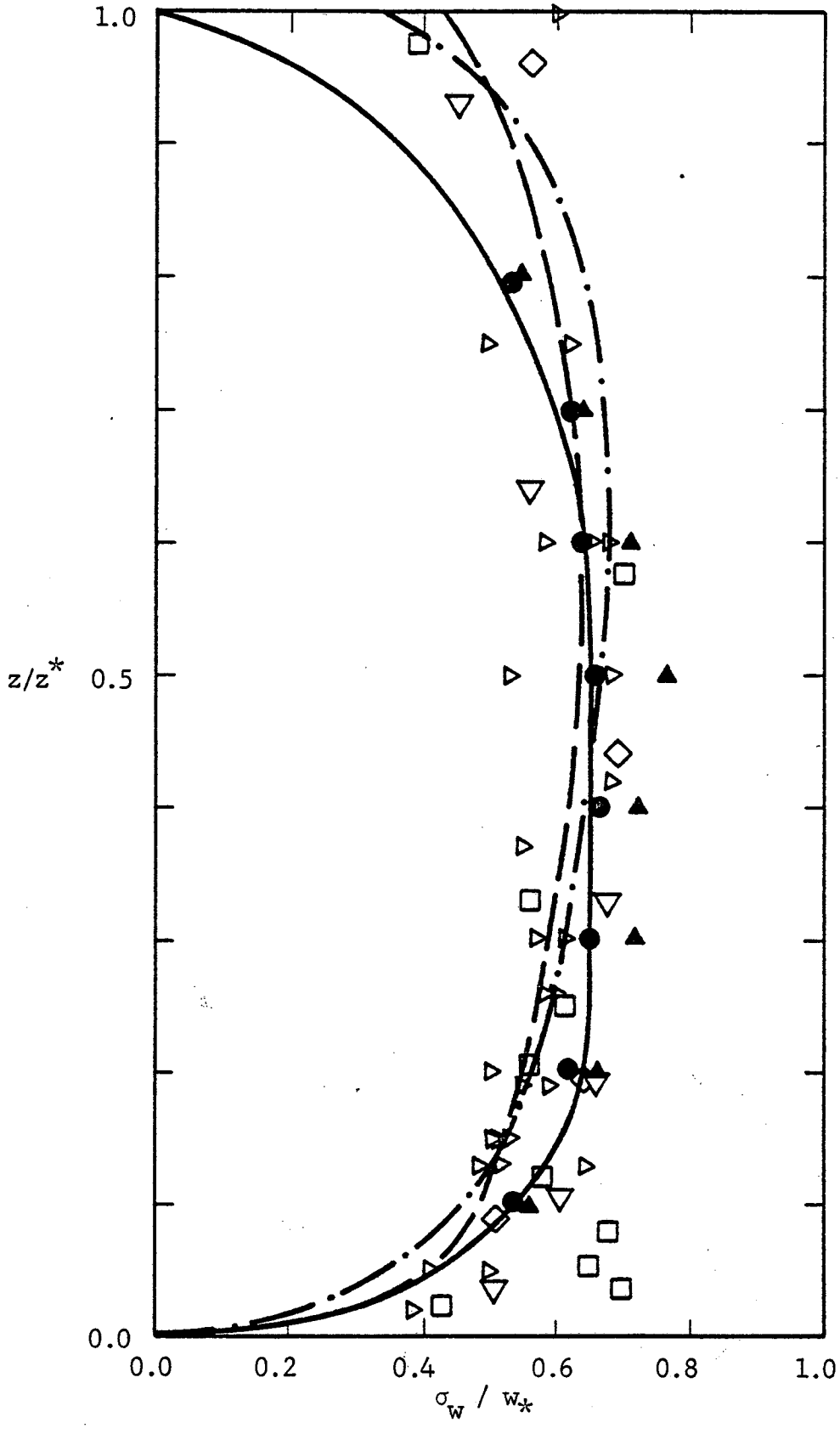

Figure 5.1 - Comparison of RMS vertical velocity with experimental and numerical studies. Legend presented in Table 5A.

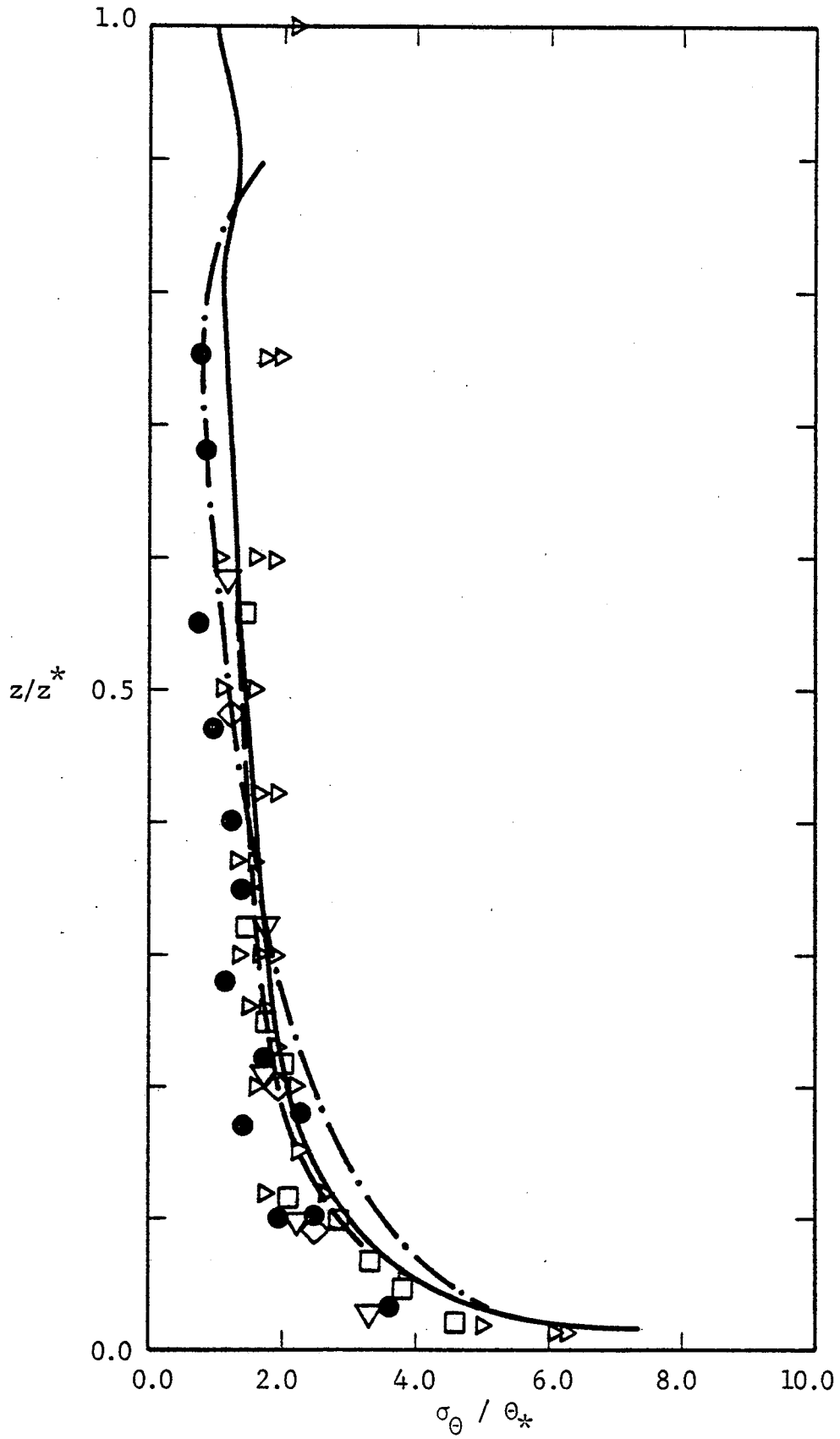

Figure 5.2 - Comparison of RMS temperature fluctuations with experimental and numerical studies. Legend presented in Table 5A.

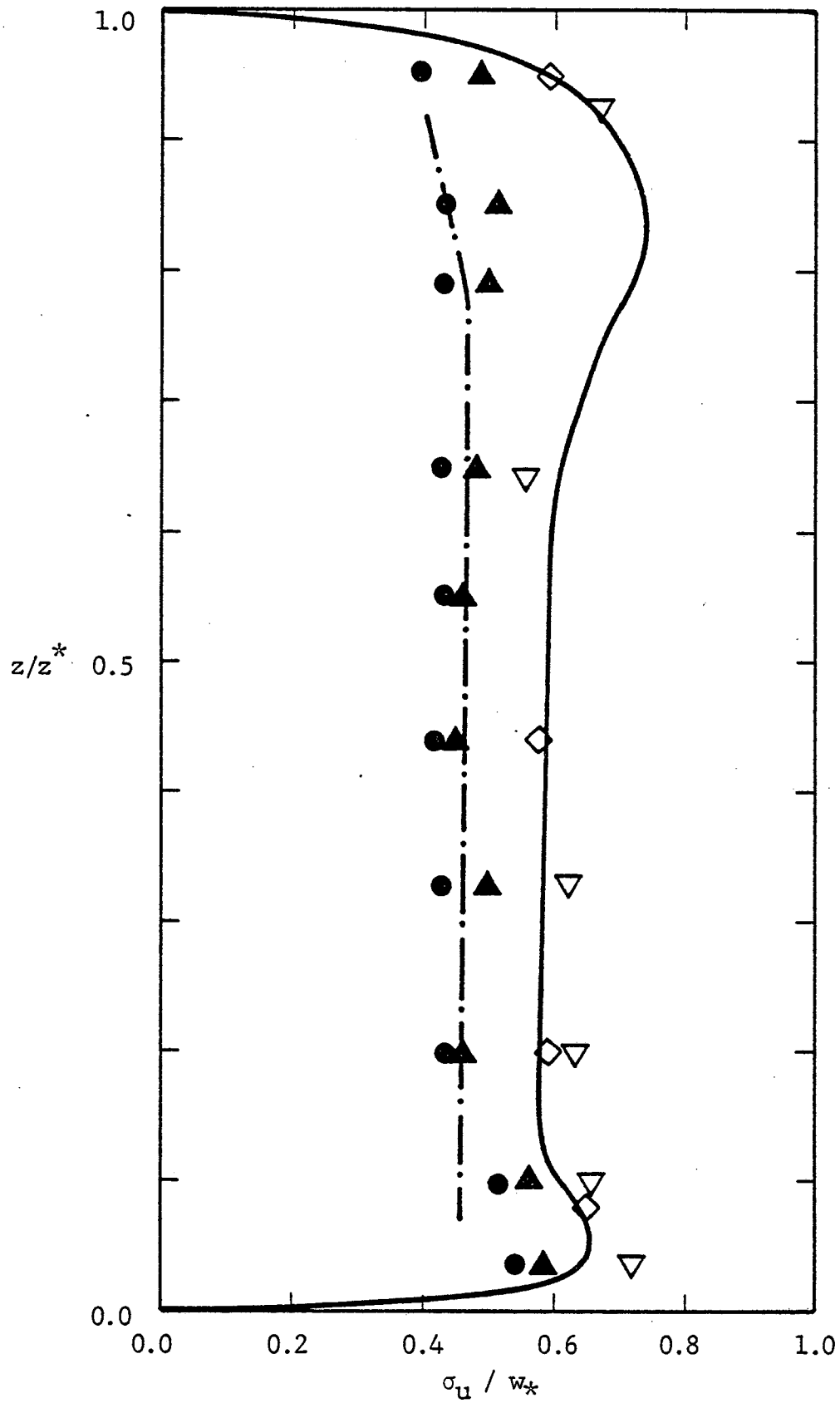

Figure 5.3 - Comparison of RMS horizontal velocity with experimental and numerical studies. Legend presented in Table 5A.

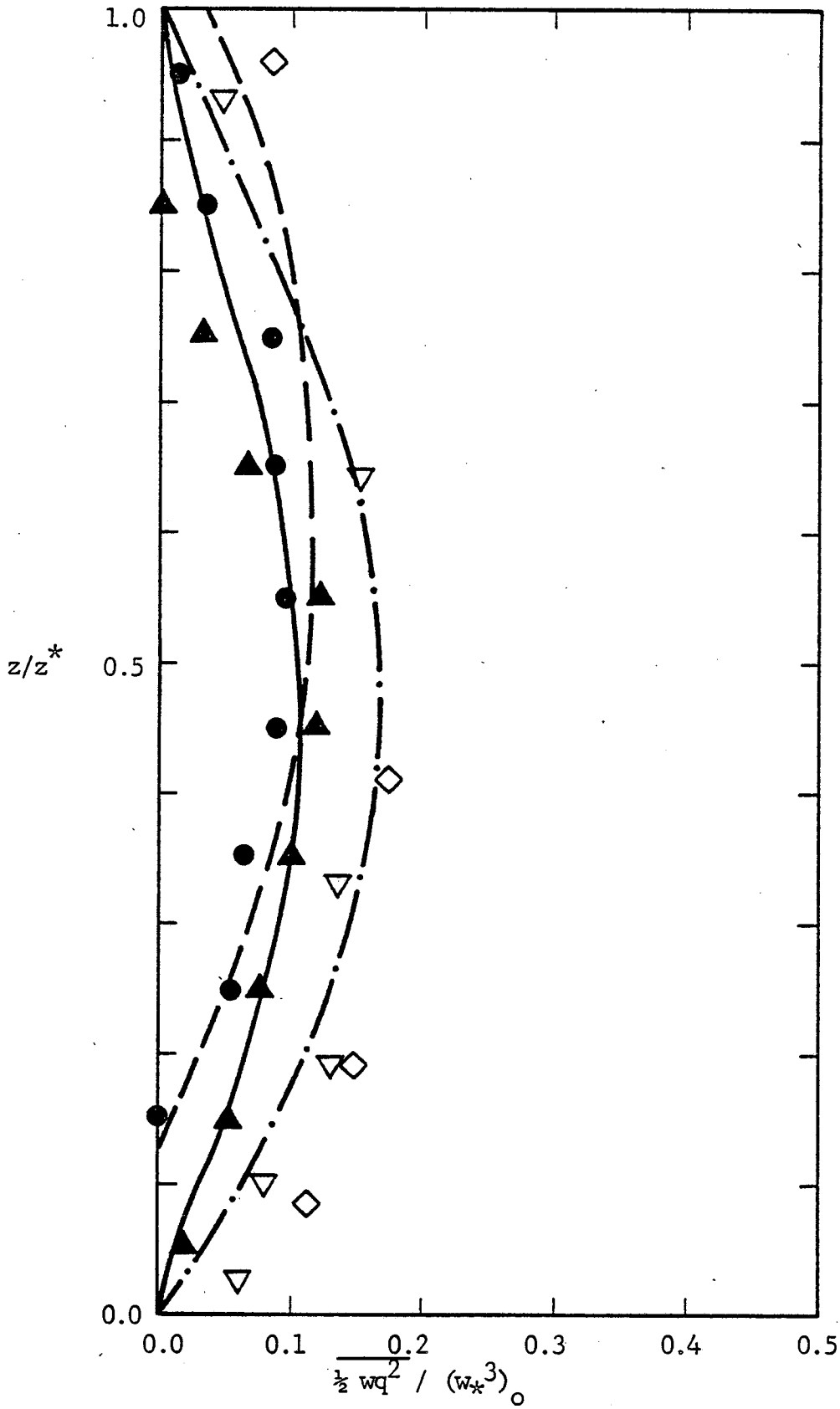

Figure 5.4 - Comparison of vertical transport of kinetic energy with experimental and numerical studies. Legend presented in Table 5A.

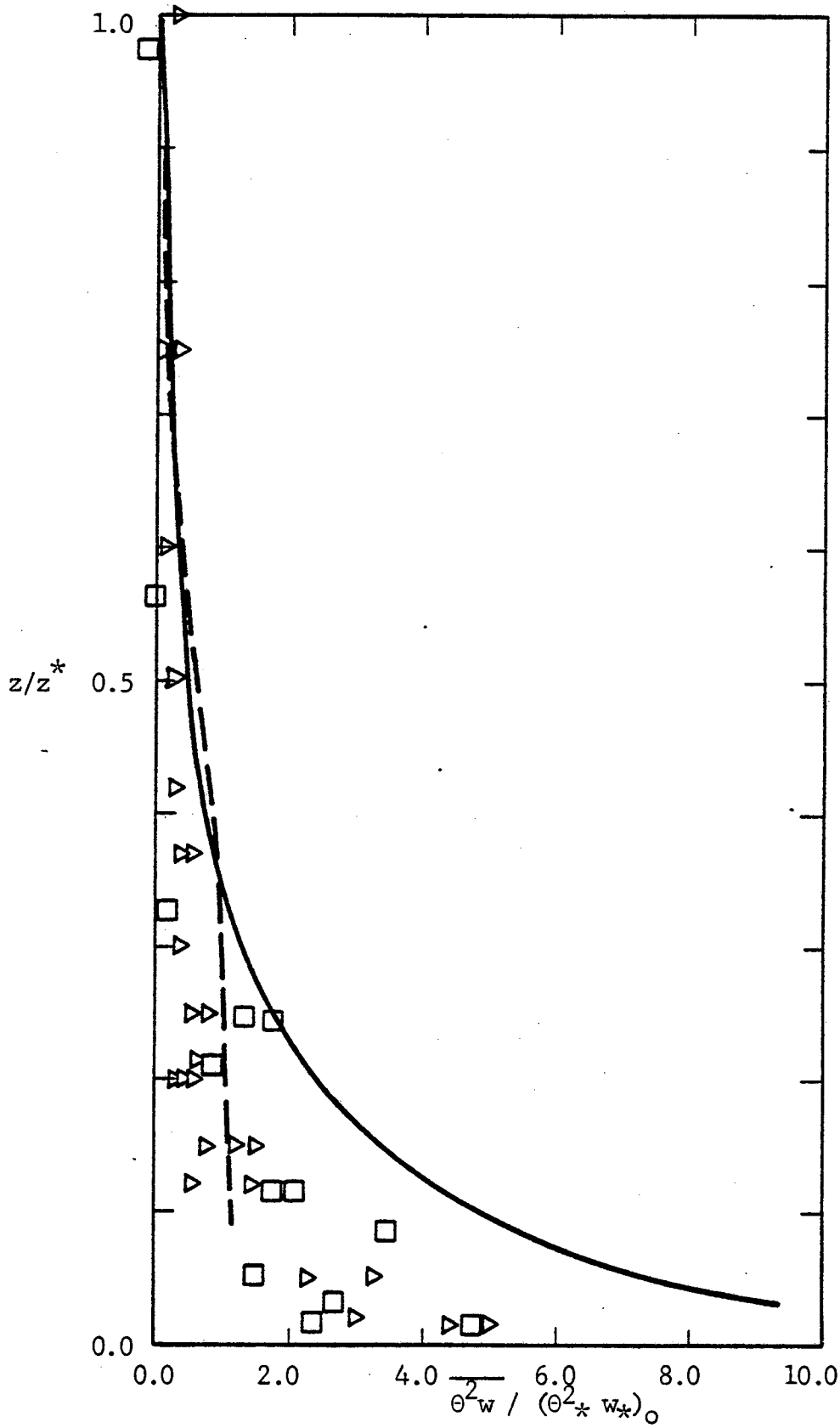

Figure 5.5 - Comparison of vertical transport of RMS temperature fluctuations with experimental and numerical studies. Legend presented in Table 5A.

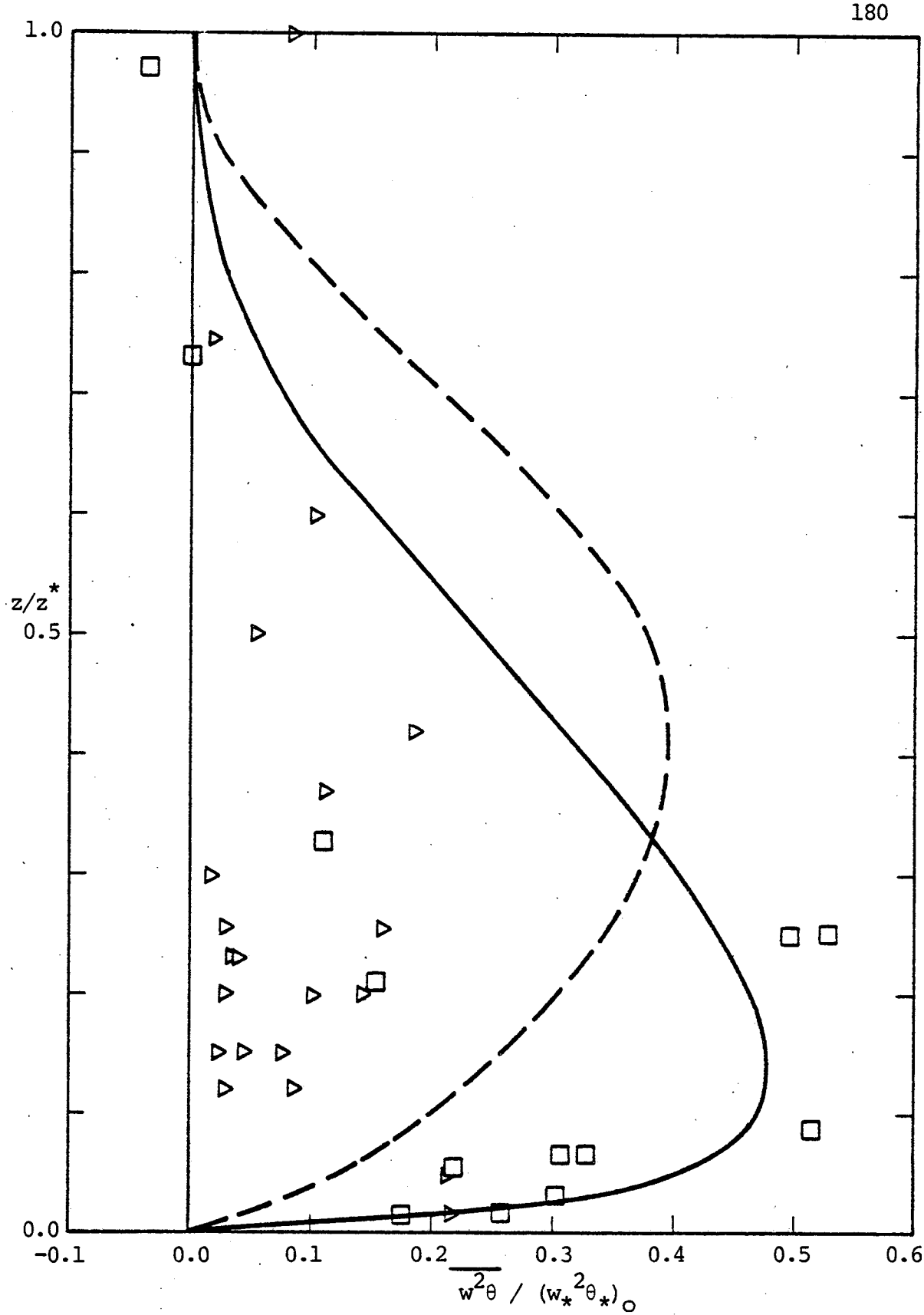

Figure 5.6 - Comparison of vertical transport of kinematic heat flux with experimental and numerical studies. Legend presented in Table 5A.

of the test section in this experiment and/or to the accuracy of their measuring method used to compute this moment.

The third order moments, or better, the vertical transport of kinetic and thermal energies do not agree as well with the atmospheric measurements. The vertical transport of kinetic energy compares well with Willis and Deardorff's measurements but are lower than Lenschow's data. This discrepancy is due to the fact that the vertical contribution to the turbulence of the horizontal velocity is bigger in the atmosphere than in the laboratory. The existence of a mean wind generating turbulence increases the amount of kinetic energy emerging from the surface layer which has to be convected upwards in the convective region. The shape of the vertical profiles is the same but the magnitude of the laboratory experiments is about 30% lower.

The major discrepancy was found in the vertical transport of mean square temperature fluctuations and of kinematic heat flux. Once more, the forced convection of the atmosphere produced different lower boundary conditions for the convective region. The measurements of Telford and Warner (1964) agreed reasonably well with unsteady turbulent thermal convection experiment, but the Minnesota data is quite different for the vertical transport of kinematic heat flux.

The shape of the curves of the vertical transport of the temperature variance is about the same for the laboratory and atmospheric case, but the magnitudes differ by about 100% up to $z/z_* = 0.2$.

The constants of both numerical studies need to be adjusted in order to fit better the available data. It is hoped that this work

produce enough information to test the planetary boundary layer numerical models.

The reader is referred to the cited works for further details on the calculations of the numerical and atmospheric studies.

CHAPTER VI

CONCLUSIONS AND SUGGESTIONS

The main conclusions and suggestions obtained from this study are related as follows:

i) It is feasible to use a laser Doppler velocimeter to measure the instantaneous components of the velocity in a thermal convection experiment, provided that the signal - to - noise ratio is high (recommend ~ 5 or higher). Refractive index fluctuations are the most restrictive factor for the velocity measurements close to the lower plate.

ii) Signal - to - noise ratio could be improved by

a) using a more powerful laser,

b) avoiding induced vibrations in the optical system by isolating the table from the vibrations coming through the floor; changing the mechanical drive to an hydraulic drive, or using a 4-pole electric motor to drive the lead screw of the lathe and redesigning the coupling carriage-lead screw and stiffening the prisms assembly mount,

c) proper grounding and shielding the electronic circuits and cables in order to keep the hum pick up low.

iii) The vertical profiles of the central moments are in good agreement with the atmospheric measurements, although larger ensembles are required to compute the third and fourth order moments.

iv) Large turbulent Reynolds number are achieved in this experiment and local isotropy hypothesis are valid in certain regions of the spectrum. Therefore the rate of dissipation of kinetic energy,

thermal variance and kinematic heat flux can be inferred from the harmonic analysis. It is recommended that a larger number of points in the records be used for this type of analysis.

v) The atmospheric forced convection data can be reproduced in the laboratory if the effects of the mean wind confined to the surface layer are adequately taken into account. Cold and hot regions can be easily generated in the lower plate of the thermal convection test section and the effects of the mean wind can be studied more intensively.

vi) The hypothesis of horizontal homogeneity is valid in this experiment and the data reported here are valid for this situation. The test section could be easily tilted and the influence of inclined ground convection can be studied.

vii) The performance of the upper plate as an insulated boundary is very good but its warpage should be corrected in order to reduce the possibility of mean flow generation.

viii) A more detailed noise study is desired in order to quantitatively account for the effects of the refractive index fluctuations. Measurements of the cross-correlation of the noise generated by the field of thermals and the temperature fluctuations at the measurement volume indicated no correlation at all. This was expected because the distortion of the beams at the measurement volume is dependent upon the whole history of the disturbances along the beams.

ix) The mean temperature measurements are in good agreement with other laboratory experiments. Beyond $z/z_* = 0.2$, the layer is

essentially isothermal. New measurements of mean temperature should be performed in order to decrease the dependence of the mean temperature profile on the time constant close to the lower boundary, by using a bare wire and a bigger supporting ring to produce better horizontal averages. Ensemble averaging many independent mean temperature measurements is the correct way to compute its vertical profile.

x) The kinetic energy, the temperature variance and the kinematic heat flux budgets produced reasonably good results when the terms containing the pressure fluctuations were neglected in regions away from the lower boundary. More investigations are needed to determine the influence of those terms.

xi) This experiment produced good experimental data that can be used as a check for the numerical models that try to study more complicated flows where convection plays an important role.

xii) The vertical profile of the central movements when scaled by the convective scales revealed an equilibrium layer extending up to $\frac{(z - \delta z_o)}{z_*} = 0.1$, where the power laws are reasonably defined when a shift of δz_o in the height scale is used.

LIST OF REFERENCES

Adrian, R. J., 1971: Analysis of a Laser Doppler Anemometer. J. Phys. E: Sci. Instrum., 4, 505-511.

Adrian, R. J., 1972: Statistics of Laser Doppler Velocimeter Signals Frequency Meausrements. J. Phys. E: Sci. Instrum., 5, 91-95.

Adrian, R. J., 1972: Turbulent Thermal Convection: Statistical Model Equation and Experiments on Convection Under Stable Layer. Ph.D. Thesis, University of Cambridge.

Adrian, R. J., 1973: LDV Measurements in Turbulent Free Convection. Proc. of Symp. on Turbulence in Liquids, Rolla, MO.

Adrian, R. J., 1975: Turbulent Water-Over-Ice Convection. J. Fluid Mech., 69, 753-781.

Adrian, R. J., 1975: A Bipolar Two Component Laser Doppler Velocimeter. J. Phys. E: Sci. Instrum., 8, 72-75.

André, J. C., G. DeMoor, P. Lacarrère, R. DuVachat, 1977a: Turbulence Approximation for Inhomogeneous Flows: Part I. The Clipping Approximation. J. Atmos. Sc., 33, 476-481.

André, J. C., G. DeMoor, P. Lacarrère, R. DuVachat, 1977b: Turbulence Approximation for Inhomogeneous Flows: Part II. The Numerical Simulation of a Penetrative Experiment. J. Atmos. Sc., 33, 482-491.

Adrian, R. J., M. K. Chung, 1978: The Mean Temperature Profile in Turbulent Thermal Convection, in preparation.

Adrian, R. J., 1977: Private Communication.

Boberg, T. E., 1977: An Experimental Study of Unsteady Free Convection from a Heated Horizontal Plate. MSc. Thesis, University of Illinois.

Bryson, R. A., 1955: Convective heat transfer with light winds. Trans. Amer. Geophys. Union, 36, 209-212.

Benech, B., 1976: Experimental Study of an Artificial Convective Plume Initiated from the Ground. J. Appl. Meteor. 15, 127-137.

Bendat, J. S., A. G. Piersol, 1971: Random Data: Analysis and Measurement Procedures. Wiley-Interscience.

Brumbach, R. P., 1968: Digital Computer Routines for Power Spectral Analysis. AC Electronics-Defense Research Laboratories Technical Report TR68-31.

Carrol, J. J., 1976: The Thermal Structure of Turbulent Convection. J. Atmos. Sci., 33, 642-659.

Chu, T. Y., R. J. Goldstein, 1973: Turbulent Convection on a Horizontal Layer of Water. J. Fluid Mech., 60, 141-159.

Croft, J. F., 1958: The Convective Regime and Temperature Distribution above a Horizontal Heated Surface. Q. J. Roy. Meteo. Soc., 84, 418-427.

Chao, B. T., 1964: Turbulent Transport Behavior of Small Particles in Dilute Suspension. Österreichisches Ingenieur Archiv., 18, 7-21.

Chung, M. K., 1978: Study of Second Order Turbulence Models with Variable Coefficients. Ph.D. Thesis, University of Illinois, Urbana, Illinois.

Deardorff, J. W., 1964: A Numerical Study of Two-Dimensional Parallel Plate Convection. J. Atmos. Sci., 21, 419-37.

Deardorff, J. W., 1965: A Numerical Study of Pseudo-Three-Dimensional Parallel Plate Convection. J. Atmos. Sci., 22, 419-34.

Deardorff, J. W., 1970: Convective Velocity and Temperature Scales for the Unstable Planetary Boundary Layer and Rayleigh Convection. J. Atmos. Sci., 27, 1211-13.

Deardorff, J. W., 1970: Preliminary Results from Numerical Integrations of the Unstable Planetary Boundary Layer. J. Atmos. Sci., 27, 1209-11.

Deardorff, J. W., 1972: Numerical Investigation of Neutral and Unstable Planetary Boundary Layer. J. Atmos. Sci., 29, 91-115.

Deardorff, J. W., 1974: Three-Dimensional Numerical Study of Turbulence in an Entraining Mixed Layer. Boundary Layer Meteorol., 7, 199-226.

Deardorff, J. W., 1974: Three-Dimensional Numerical Study of the Height and Mean Structure of a Heated Planetary Boundary Layer. Boundary-Layer Meteorol. 7, 81-106.

Deardorff, J. W., G. E. Willis, 1967: Investigation of Turbulent Thermal Convection between Horizontal Plates. J. Fluid Mech., 28, 675-701.

Deardorff, J. W., G. E. Willis, 1967: The Free-Convection Temperature Profile. Q. J. Roy. Meteo. Soc., 73, 166-175.

Deardorff, J. W., G. E. Willis, D. K. Lilly, 1969: Laboratory Investigation of Non-Steady Penetrative Convection. J. Fluid Mech., 35, 7-31.

Durst, F., A. Melling, J. H. Whitelaw, 1976: Principle and Practice of Laser-Doppler Anemometry. Academic Press.

Elder, J. W., 1969: The Temporal Development of a Model of High Rayleigh Number Convection. J. Fluid Mech., 35, 417-37.

Fitzjarrald, D. E., 1976: An Experimental Study of Turbulent Convection in Air. J. Fluid Mech., 73, 693-719.

Foster, T. D., 1965: Onset of Convection in a Layer of Fluid Cooled from Above. Phys. Fluids, 8, 1770-74.

Garon, A. M., R. J. Goldstein 1973: Velocity and Heat Transfer Measurements in Thermal Convection. Phys. Fluids, 16, 1818-25.

Globe, S., D. Dropkin, 1959: Natural Convection Heat Transfer in Liquids Confined by Two Horizontal Plates and Heated from Below. J. Heat Transfer, 81, 24-28.

George, W. K., J. L. Lumley, 1973: The Laser Doppler Velocimeter and its Application to the Measurement of Turbulence. J. Fluid Mech., 60, 321-62.

Goldstein, R. J., T. Y. Chu, 1969: Thermal Convection in a Horizontal Layer of Air. Prog. Heat & Mass Transfer, 2, 55-75.

Hall, F. F., J. G. Edinger, W. D. Neff, 1975: Convective Plumes in the Planetary Boundary Layer, Investigated with an Accoustic Echo Sounder. J. Appl. Meteor., 14, 513-23.

Herring, J. R., 1963: Investigation of Problems in Thermal Convection. J. Atmos. Sci., 20, 325-338.

Herring, J. R., 1964: Investigation of Problems in Thermal Convection: Rigid Boundaries. J. Atmos. Sci., 21, 277-90.

Herring, J. R., 1966: Some Analytic Results in The Theory of Thermal Convection. J. Atmos. Sci., 23, 672-77.

Herring, J. R., 1969: Statistical Theory of Thermal Convection at Large Prandtl Number. Phys. Fluids, 12, 39-52.

Hinze, J. O., 1975: Turbulence. McGraw Hill Book Co., 2nd Ed.

Howard, L. N., 1963: Heat Transport by Turbulent Convection. J. Fluid Mech., 17, 425-32.

Kraichnan, R. H., 1959: Isotropic Turbulence at Very High Reynolds Numbers. J. Fluid Mech. 5, 497-543.

Kraichnan, R. H., 1962: Turbulent Thermal Convection at Arbitrary Prandtl Number. Phys. Fluids, 5, 1374-89.

Kaimal, J. C., J. C. Wyngaard, D. A. Haugen, O. R. Coté Y. Izumi, S. J. Caughey, C. J. Readings, 1976: Turbulence Structure in the Convective Boundary Layer. J. Atmos. Sci. 33, 2152-2169.

Long, R. R., 1976: Relation Between Nusselt Number and Rayleigh Number in Turbulent Thermal Convection. J. Fluid Mech., 73, 445-51.

Lundgren, T. S., 1967: Distribution Functions in the Statistical Theory of Turbulence. Phys. Fluids, 10, 969-75.

Lundgren, T. S., 1969: Model Equations for Nonhomogeneous Turbulence. Phys. Fluids, 12, 485-97.

Lenschow, D. H., 1970: Airplane Measurements of Planetary Boundary Layer Structure. J. Appl. Meteor., 9, 874-884.

Lenschow, D. H., 1974: Model of the Height Variation of the Turbulence Kinetic Energy Budget in the Unstable Planetary Boundary Layer. J. Atmos. Sci., 31, 465-474.

Lenschow, D. H., W. B. Johnson, Jr., 1968: Concurrent Airplane and Ballon Measurements of Atmospheric Boundary-Layer Structure over a Forest. J. Appl. Meteor., 7, 79-89.

Malkus, W. V. R., 1954: The Heat Transport and Spectrum of Thermal Turbulence. Proc. Roy. Soc., London, A225, 195-212.

Malkus, W. V. R., 1954: Discrete Transitions in Turbulent Convection. Proc. Roy. Soc., London, A225, 185-194.

Manton, M. J., 1975: Penetrative Convection Due to a Field of Thermals. J. Atmos. Sci., 32, 2272-77.

Mieghem, J. V., 1973: Atmospheric Energetics, Oxford Univ. Press.

Mellor, G. L., 1973: Analytic Predictions of the Properties of Stratified Planetary Surface Layers. J. Atmos. Sci., 30, 1061-69.

Manton, M. J., W. R. Cotton, 1977: Parameterization of the Atmospheric Surface Layer. J. Atmos. Sci., 34, 331-34.

Millionshchikov, M. 1941: On the Theory of Homogeneous and Isotropic Turbulence. C. R. Acad. Sci. URSS 32, 615-618.

O'Brien, E. E., G. C. Francis, 1962: A Consequence of the Zero-Fourth-Cumulant Approximation. J. Fluid Mech., 13, 369-375.

Ogura, Y., 1962a: Energy Transfer in a Normally Distributed and Isotropic Turbulent Velocity Field in Two Dimensions. Phys. Fluids, 5, 395-401.

Ogura, Y., 1962b: Energy Transfer in Isotropic Turbulent Flow. J. Geophys. Res., 67, 3143-49.

Ogura, Y., 1963: A Consequence of the Zero-Fourth-Cumulant Approximation in the Decay of Isotropic Turbulence. J. Fluid Mech., 16, 33-40.

Petersen, E. L., 1976: A Model for the Simulation of Atmospheric Turbulence. J. Appl. Meteor., 15, 571-87.

Priestley, C. H. B., 1954: Convection from a Large Horizontal Surface. Aust. J. Phys., 7, 1176-201.

Priestley, C. H. B., 1953: Buoyant Motion in a Turbulent Environment. Aust. J. Phys., 6, 279-90.

Plate, E. J., 1971: Aerodynamic Characteristics of Atmospheric Boundary Layers. U.S. Atomic Energy Commission.

Proudman, I., W. H. Reid, 1954: On the Decay of a Normally Distributed and Homogeneous Turbulent Velocity Field. Phil. Trans. Roy. Soc. London, A247, 163-189.

Silveston, P. L., 1958: Wärmedurchgang inWaagerechten Flüssigkeiksschichten. Forsch. Ing., Wes. 24, 29-32 and 59-69.

Sommerscales, E. F. C., D. Dropkin, 1966: Experimental Investigation of the Temperature Distribution in a Horizontal Layer of Fluid Heated from Below. Int. J. Heat Mass Transfer, 9, 1189-1204.

Sommerscales, E. F. C., I. W. Gazda, 1969: Thermal Convection in High Prandtl Number Liquids at High Rayleigh Number. Int. J. Heat Mass Transfer, 12, 1491-1511.

Spiegel, E. A., 1962: On the Malkus Theory of Turbulence. Mécanique de la Turbulence, 181-205.

Telford, J. W., 1966: The Convective Mechanism in Clear Air. J. Atmos. Sci., 23, 652-666.

Telford, J. W., 1970: Convective Plumes in a Convective Field. J. Atmos. Sci., 27, 347-358.

Thomas, D. B., A. A. Townsend, 1958: Turbulent Convection Over a Heated Horizontal Surface. J. Fluid Mech., 2, 473-92.

Townsend, A. A., 1959: Temperature Fluctuations Over a Heated Horizontal Surface. J. Fluid Mech., 5, 209-241.

Townsend, A. A., 1964: Turbulent Convection in Water Over Ice. Q. J. Roy. Meteo. Soc., 90, 248-259.

Townsend, A. A., 1962: Remarks on the Malkus Theory of Turbulent Flow. Mécanique de la Turbulence, 1967-180.

Townsend, A. A., 1975: The Structure of Turbulent Shear Flow. Cambridge University Press, 2nd Edition.

Turner, J. S., 1963: The Motion of Buoyant Elements in Turbulent Surroundings. J. Fluid Mech., 16, 1-16.

Turner, J. S., 1969: Buoyant Plumes and Thermals. Annual Rev. Fluid Mech. I, 29-44.

Turner, J. S., 1973: Buoyancy Effects in Fluids. Cambridge University Press.

Tatsumi, T., 1957: The Theory of Decay Process of Incompressible Isotropic Turbulence. Proc. Roy. Soc. London, A239, 16-45.

Telford, J. W., J. Warner, 1964: Fluxes of Heat and Vapor in the Lower Atmosphere Derived from Aircraft Observations. J. Atmos. Sci., 21, 539-48.

Warner, J., J. W. Telford, 1967: Convection Below Cloud Base. J. Atmos. Sci., 24, 374-82.

Willis, G. E., J. W. Deardorff, 1974: Laboratory Model of the Unstable Planetary Boundary Layer. J. Atmos. Sci., 31, 1297-1307.

Wyngaard, J. C., O. R. Coté, 1974: The Evolution of a Convective Planetary Boundary Layer - A Higher-Order Closure Model Study. Boundary-Layer Meteorol., 7, 289-308.

Warner, J., 1972: The Structure and Intensity of Turbulence in Air over the Sea. Quart. J. R. Met. Soc. 98, 175-186.

White, F. M., 1974: Viscous Fluid Flow. McGraw Hill Book Co.

Willis, G. E., J. W. Deardorff, 1976: Visual Observations of Horizontal Planforms of Penetrative Convection. Private communication to R. J. Adrian.

Zeman, O., J. L. Lumley, 1976: Modeling Buoyancy Driven Mixed Layers. J. Atmos. Sci., 33, 1974-88.

Zeman, O., H. Tennekes, 1977: Parameterization of the Turbulent Energy Budget at the Top of the Daytime Atmospheric Boundary Layer. J. Atmos. Sci., 34, 111-23.

APPENDIX A-1

CONVERSION FACTORS FOR VELOCITY MEASUREMENTS

The calculation of the conversion factors for velocity measurements refer to Figure 3.5 for the definition of the quantities used. For the geometry used close to the lower boundary, the frequency of the signal at the output of the radio frequency band pass filters is given by

$$\nu_{31} = 30 - \left[\frac{\sin\kappa_3}{\lambda_{H_2O}} u + \frac{\cos\kappa_3 - \cos\kappa_1}{\lambda_{H_2O}} v + \frac{\sin\kappa_1}{\lambda_{H_2O}} w\right] \tag{1a}$$

$$\nu_{21} = 40 - \left[-\frac{\sin\kappa_2}{\lambda_{H_2O}} u + \frac{\cos\kappa_2 - \cos\kappa_1}{\lambda_{H_2O}} v + \frac{\sin\kappa_1}{\lambda_{H_2O}} w\right] \tag{1b}$$

where the angles refer to those in water. The corresponding voltage of the signal at the output of the signal processor TSI 1090 after frequency mixing at 30.025 MHz and 39.975 MHz is

$$V_{30} = V_A = S_A(30025 - \nu_{31}) =$$

$$= S\{25 + \frac{n}{\lambda}[(\sin\kappa_3)u + (\cos\kappa_3 - \cos\kappa_1)v +$$

$$+ (\sin\kappa_1)w]\} \tag{2a}$$

$$V_{40} = V_B = S_B(\nu_{21} - 39975) =$$

$$= S\{25 + \frac{n}{\lambda}[(\sin\kappa_2)u - (\cos\kappa_2 - \cos\kappa_1)v - (\sin\kappa_1)w]\} \tag{2b}$$

where $S = S_A = S_B$ is the sensitivity scale of the signal processor and n is the refractive index of the water.

Adding and subtracting both signals

$$V_A + V_B = 50S + \frac{nS}{\lambda} [(\sin\kappa_3+\sin\kappa_2)u+(\cos\kappa_3-\cos\kappa_2)v] \tag{3a}$$

$$V_A - V_B = \frac{nS}{\lambda} [(\sin\kappa_3-\sin\kappa_2)u+(\cos\kappa_3+\cos\kappa_2-2\cos\kappa_1)v + 2(\sin\kappa_1)w] \tag{3b}$$

Using the signal conditioner TSI 1057 to suppress the DC component of the sum of the signals, then

$$u = \frac{\lambda}{nS} [V_A+V_B-50S] \frac{1}{\sin\kappa_3+\sin\kappa_2} - \frac{\cos\kappa_3-\cos\kappa_1}{\sin\kappa_3+\sin\kappa_2} v \tag{4a}$$

$$w = \frac{\lambda}{nS} [V_A-V_B] \frac{1}{2\sin\kappa_1} - \frac{\sin\kappa_3-\sin\kappa_2}{2\sin\kappa_1} u - \frac{\cos\kappa_3+\cos\kappa_2-2\cos\kappa_1}{2\sin\kappa_1} v \tag{4b}$$

The coefficients of the v component of the velocity are at least one order of magnitude smaller than the other terms, therefore the final expressions are

$$u = \frac{\lambda}{nS} [V_A+V_B-50S] \frac{1}{\sin\kappa_3+\sin\kappa_2} \tag{5a}$$

$$w = \frac{\lambda}{nS} [V_A -V_B] \frac{1}{2\sin\kappa_1} - \frac{\sin\kappa_3-\sin\kappa_2}{2\sin\kappa_1} u \tag{5b}$$

At the beginning of the experiment, the angles of the beams were $\kappa_1 = 4.1718°$, $\kappa_2 = 4.3259°$, $\kappa_3 = 3.8686°$ and S = 20V/100kHz, resulting

$$u = 1.3505\ [V_A+V_B-10] \tag{6a}$$

and

$$w = 1.3264\ [V_A-V_B] + 0.0739[V_A+V_B-10]\ . \tag{6b}$$

Reassembly of the prism beam splitter changed the angles to $\kappa_1 = \kappa_2 = \kappa_3 = \kappa = 4.121$, in water, resulting in

$$u = 1.3458\ [V_A+V_B-10]\ , \tag{7a}$$

and

$$w = 1.3458[V_A-V_B]\ . \tag{7b}$$

In order to measure the velocity components close to the upper plate the beams are diffracted to the opposite side at the Bragg cell and the prisms assembly is rotated 180° in a vertical plane. The frequency shifts in the beams will be (ν_0-30 MHz) and (ν_0-40 MHz). Following the same steps, equations (7a) and (7b) will apply for this new configuration where the u and w coordinates are the same as before.

APPENDIX A-2

CHARACTERISTICS OF THE LASER DOPPLER VELOCIMETER

Assuming that each beam is Gaussian, the nominal measurement volume is the volume corresponding to e^{-2} dimensions. The dimensions of the ellipsoid corresponding to e^{-2} contour of two beams intersection are given by

$$dm = d_{e^{-2}}/\cos\kappa \tag{1}$$

$$lm = d_{e^{-2}}/\sin\kappa \tag{2}$$

$$hm = d_{e^{-2}}$$

where dm is the transverse dimension in the plane of the axis of the two beams, hm is the height of the e^{-2} contour perpendicular to this plane, at mid-point, lm is the length contained in the plane of the axis of the two beams and $d_{e^{-2}}$ is the diameter of the beam at the focal plane of the objective lens. It is given by

$$d_{e^{-2}} = \frac{4\lambda f}{\pi D_{e^{-2}}} \tag{4}$$

where f is the focal length of the lens and $D_{e^{-2}}$ is the diameter of the beam ahead of the lens L_4.

The estimated diameters of the three beams ahead of lens L_4 are $D_{0_{main}} = D_{0_{30}} = D_{0_{40}} = 2.1$ mm. Therefore $d_{e^{-2}} = 147.3$ μm, hm = 147.3 μm, dm = 147.7 μm and lm = 2050 μm, yielding a volume

of 23.35×10^6 μm^3. The number of fringes is given by

$$N_{FR} = \frac{d_e - 2}{d_f} \tag{5}$$

Using equation (3.2), the distance between fringes is 2.47 μm and approximately 60 fringes are formed by the intersection of each two beams.

Using an aperture with ϕ = 0.35 mm and a magnification of the collecting lenses of 2.486, the pin hole will see 1.03 mm in the transverse direction and 1.62 mm in the plane of the axis of the two beams of the measurement volume for 32.5° off axis back scatter.

Assuming that all the particles in the suspension had the same diameter of 5 μm, for the condition of dillution used during the measurements (c.f. Chapter 3), there was in average one particle per measurement volume.

As reported by Durst et al (1976), the number of fringes seen by the photodetector, N_{ph}, could be calculated by

$$N_{ph} = \frac{2}{M} d_{ph} \sin\kappa \tag{6}$$

where M is the magnitification of the collecting system and d_{ph} is the diameter of the pinhole A_2. Substituting the numerical values, there were 52.3 fringes seen by the photodetector.

With an average of one particle in the measurement volume, the probability of signals from two or more particles overlapping is significant. Since the particles arrive at random times, their signals have random phases and the superposition of such signals

creates a random frequency modulation of the instantaneous frequency of the sum signal. Upon frequency demodulation, this appears as a random noise in the output voltage of the frequency trackers referred as "phase noise" or "Doppler ambiguity noise" after George and Lumley (1973).

For the case in which the mean number of particles in the measurement volume is much greater than unity, the statistics of the phase noise are well understood and given in George and Lumley (1973). However, the signal in the present experiment does not correspond to this condition, so the extent to which phase noise is a major contributor to the total noise in the output of the frequency trackers is not clear. We shall, however, evaluate the phase noise for reference.

The RMS value of the equivalent input phase noise at the frequency tracker output is

$$\text{RMS } [\frac{\dot{\Phi}}{2\pi}] = \sqrt{\Delta f_D f_c} \tag{7}$$

where f_c is the frequency of the low pass filter on the frequency tracker output and Δf_D is the e^{-1} bandwidth of the power spectrum of the photocurrent due to transit time broadening.

The equation for Δf_D is

$$\beta = \frac{\Delta f_D}{f_D} = \frac{1.8}{N_{ph}} \tag{8}$$

which gives approximately 3.5% bandwidth.

The low pass frequency used in the experiment was f_c = 16 Hz so the RMS phase noise would be about 50 Hz for a speed of 2 cm/s, corresponding to an equivalent input noise of 0.13 mm/s.

APPENDIX A-3

ABILITY TO FOLLOW THE FLOW

The motion of particles suspended in a moving fluid is mainly affected by the particle shape, the particle size, the relative density of particle and fluid, the concentration of the suspension and body forces.

Assuming spherical particles with negligible effect on the fluid flow and applying D'Alembert's principle in a Lagrangian coordinate system, the equation of motion for the particle can be written as

$$\frac{4}{3}\pi a^3 \rho_p \frac{du_{pi}}{dt} = F_{1i}(\text{drag force}) + F_{2i}(\text{Basset memory term}) + F_{3i}(\text{apparent mass acceleration}) + F_{4i}(\text{local pressure gradient effect}) + F_{5i}(\text{local velocity shear effect}) + F_{6i}(\text{body force due to gravity})$$

The force vector due to drag, using Oseen's approximation can be expressed as

$$(F_1)_i = \frac{\pi}{2} \rho_f a^2 (u_{fi}-u_{pi})^2 \left[\frac{24}{Re}\left(1 + \frac{3}{16} Re\right)\right] \qquad (2a)$$

or using Stokes approximation for creeping flow on a sphere

$$(F_1)_i = - 6\pi \mu a (u_{pi}-u_{fi}) \qquad (2b)$$

where

a - particle radius

ρ_f - fluid density

u_f - fluid velocity

$Re = \frac{2(u_f - u_p)a}{\nu}$

μ = fluid viscosity

The Basset memory term takes into account the effect of the deviation in flow pattern from steady state and is the fluid resistance due to relative acceleration of the particle.

$$(F_2)_i = 6a^2\rho_f\sqrt{\pi\nu}\int_{t_0}^{t}\frac{(\frac{du_{fi}}{d\tau} - \frac{du_{pi}}{d\tau})}{\sqrt{t-\tau}}\,d\tau \qquad (3)$$

The apparent mass acceleration is the force vector due to the acceleration of the mass of fluid displaced by the particle relative to the local fluid acceleration.

$$(F_3)_i = \frac{2}{3}\pi a^3\rho_f\frac{d}{dt}(u_{fi}-u_{pi}) \qquad (4)$$

The local pressure gradient effect is the force vector due to the local static pressure field around the particle.

$$(F_4)_i = \frac{4}{3}\pi a^3(-\frac{\partial p}{\partial x_i}) \qquad (5)$$

In order to consider the force due to the local velocity shear it is assumed that the particle is spinning due to the shear and then, with this Magnus effect, it is possible to calculate the forces on the particle. In general, the three components of the force due to

the local shear effects are given by the cross product of the velocity vector and the vorticity vector (Ω_i)

$$(F_5)_i = -\frac{4}{3}\pi \rho_f a^3 \epsilon_{ijk}(u_{fj}-u_{pj})\ \Omega_k \tag{6}$$

The body force on the particle exerted by gravity is

$$(F_6)_i = \frac{4}{3}\pi a^3 \rho_f g_i \tag{7}$$

In a turbulent flow, in order to draw some conclusions about the behavior of the particles in representing the flow field, further assumptions are necessary: homogeneous and time invariant turbulence, particles smaller than the turbulence microscale, Stokes drag law for spherical particles, one particle is always surrounded by the same fluid molecules and no interaction between particles.

Using the solution of equation (1) derived by Chao (1964), which was obtained by Fourier transform techniques, estimates of the relation of the mean square velocity of the particle and the mean square velocity of the fluid can be calculated by

$$\frac{\overline{u^2}}{\overline{u_f^2}} = \int_0^\infty \frac{\Omega^{(1)}}{\Omega^{(2)}} F(\omega)\ d\omega \tag{8}$$

where $F(\omega)$ is the normalized Lagrangian energy spectrum density function of the fluid motion,

$$\Omega^{(1)}\ (\tfrac{\omega}{\alpha}) = (\tfrac{\omega}{\alpha})^2 + \sqrt{6}\ (\tfrac{\omega}{\alpha})^{3/2} + 3(\tfrac{\omega}{\alpha}) + \sqrt{6}\ (\tfrac{\omega}{\alpha})^{1/2} + 1 \tag{9}$$

$$\Omega^{(2)}\ (\tfrac{\omega}{\alpha},\beta) = \frac{1}{\beta^2}\ (\tfrac{\omega}{\alpha})^2 + \frac{\sqrt{6}}{\beta}\ (\tfrac{\omega}{\alpha})^{3/2} + 3(\tfrac{\omega}{\alpha}) + \sqrt{6}\ (\tfrac{\omega}{\alpha})^{1/2} + 1 \tag{10}$$

$$\alpha = \frac{3\nu}{a^2} \tag{11}$$

$$\beta = \frac{\rho_p + \rho_f/2}{\rho_p + \rho_f/2} \tag{12}$$

For Dow Saran particles of 5 μm diameter and $\frac{\rho_p}{\rho_f} = 1.33$, at T = 30°C then $\alpha = 9.768 \times 10^4/s$ and $\beta = 0.818$. The maximum frequency of the fluctuations expected from the experiment is on the order of 200 s^{-1}. For this range of frequencies $\Omega^{(1)}/\Omega^{(2)} = 1$ and using the definition of normalized power spectrum $\int_0^\infty F(\omega)\,d\omega = 1$. Therefore, $\frac{\overline{u_p^2}}{\overline{u_f^2}} = 1$ and the particles follow the turbulent flow continuously, and the mean square particle velocity fluctuation is the mean square velocity fluctuation.

The terminal settling velocity calculated based on

a) Solid particles in a Newtonian fluid

b) No collision between the particles

c) Uniform, smooth, spherical particles of density ρ_p, diameter d and fluid of density ρ_f and viscosity μ

d) System in the gravitational field is given by

$$V = \frac{d^2(\rho_p - \rho_f)g}{18\mu} \tag{13}$$

Substituting the numerical values, V = 5.6 μm/s which is very small compared to the characteristic values encountered in the flow (1.0 cm/s).

APPENDIX A4

TIME CONSTANT OF THE RESISTANCE WIRE PROBE

In order to correct the values indicated by the resistance wire probe due to its time lag, special calibrations to determine the time constant were performed using two different methods:

i) Passing the probe and a thermocouple with much smaller time constant ($\sim$5ms) through a temperature discontinuity, at a constant speed of 0.475 cm/s.

ii) Moving the resistance wire and the thermocouple in a constant temperature gradient medium.

Assuming negligible spatial variations of temperature within the sensor, neglecting lead wire conduction to or from the sensor and neglecting viscous dissipation effects, an energy balance yields

$$mc \frac{dT_{RW}}{dt} = hA_s (T_f - T_{RW}) \tag{1}$$

where mc is the capacitance heat mass of the sensor, A_s is the external area, h is the mean heat transfer coefficient, T_f is the fluid temperature and T_{RW} is the temperature indicated by the resistance wire.

Considering a step change in the fluid temperature from T_{f0} to T_f, then the response of the resistance wire is given by

$$\frac{T_{RW} - T_f}{T_{f0} - T_f} = e^{-(hA_s/mc)t} \tag{2}$$

For the case in which the fluid temperature increases linearly with time

$$T_f - T_{f0} = \beta t \tag{3}$$

Therefore the temperature difference of the fluid and resistance wire will be, at any time

$$T_f - T_{RW} = \beta \frac{mc}{hA_s} = \beta\tau \tag{4}$$

where $\tau = \frac{mc}{hA_s}$ is the time constant of the probe.

As the thermocouple probe, used to measure the instantaneous temperature in the thermal convection experiment, has a frequency response on the order of 50 Hz, its temperature indication was assumed to be the fluid temperature. Therefore, having the records for T_{RW} and T_f at each time, τ can be evaluated from equation (1) directly.

At the starting point, before the run has been initiated, both resistance wire and thermocouple read the same temperature. Therefore this is the reference temperature for both records. The problem is if one considers the temperature just before entering the discontinuity, as a reference, it will be different for the thermocouple and resistance wire.

Figures A4.1 and A4.2 show the typical indications of temperature through a discontinuity and in a constant gradient medium.

The time constant calculation is

$$\tau = \frac{(T_f - T_{f0}) - (T_{RW} - T_{RW0})}{\frac{d\,T_{RW}}{dt}} \tag{5}$$

Sixteen scans of each method yielded an average time constant of 0.228 ± 0.24 s.

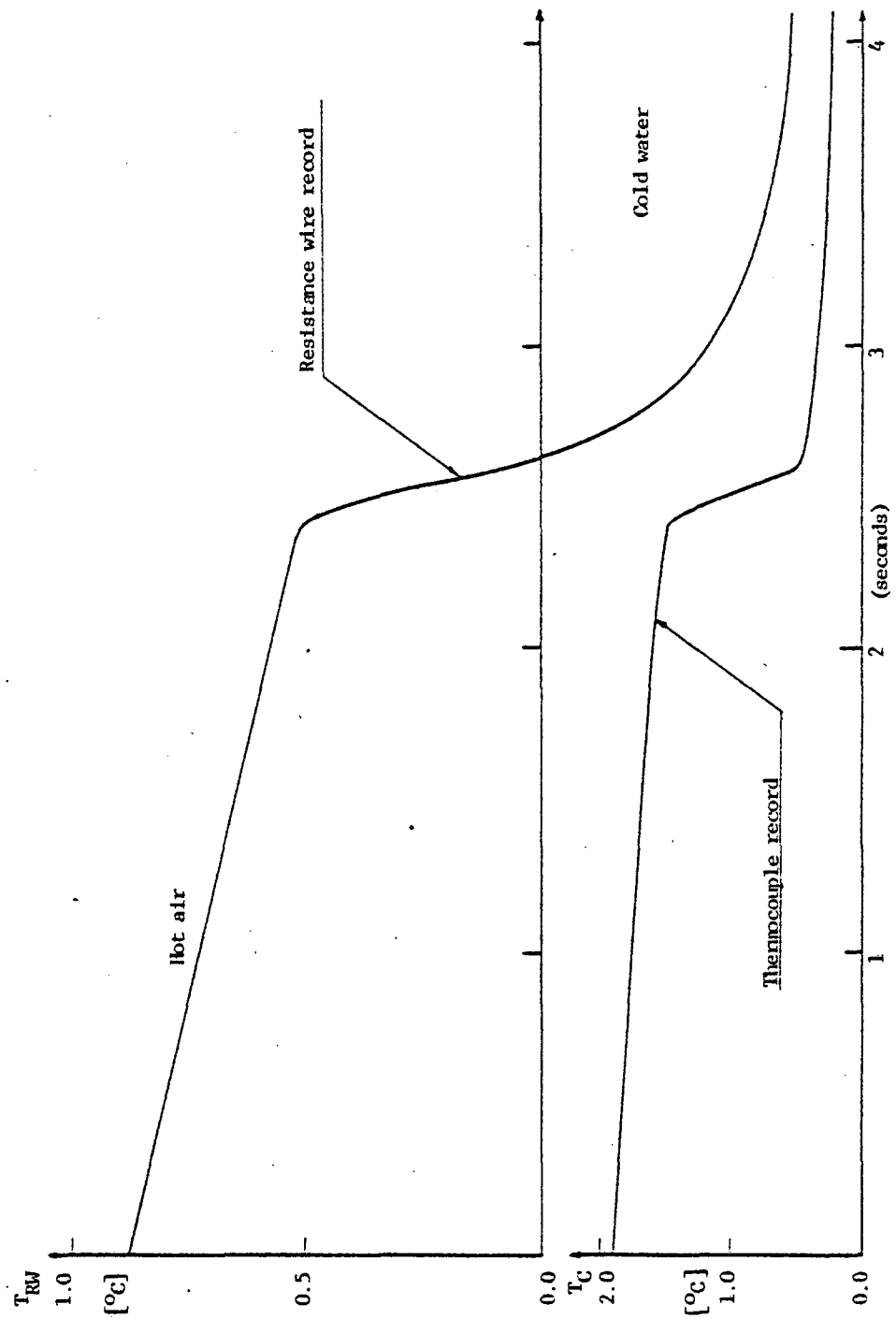

Figure A4.1 - Typical records of resistance wire and thermocouple through a temperature discontinuity.

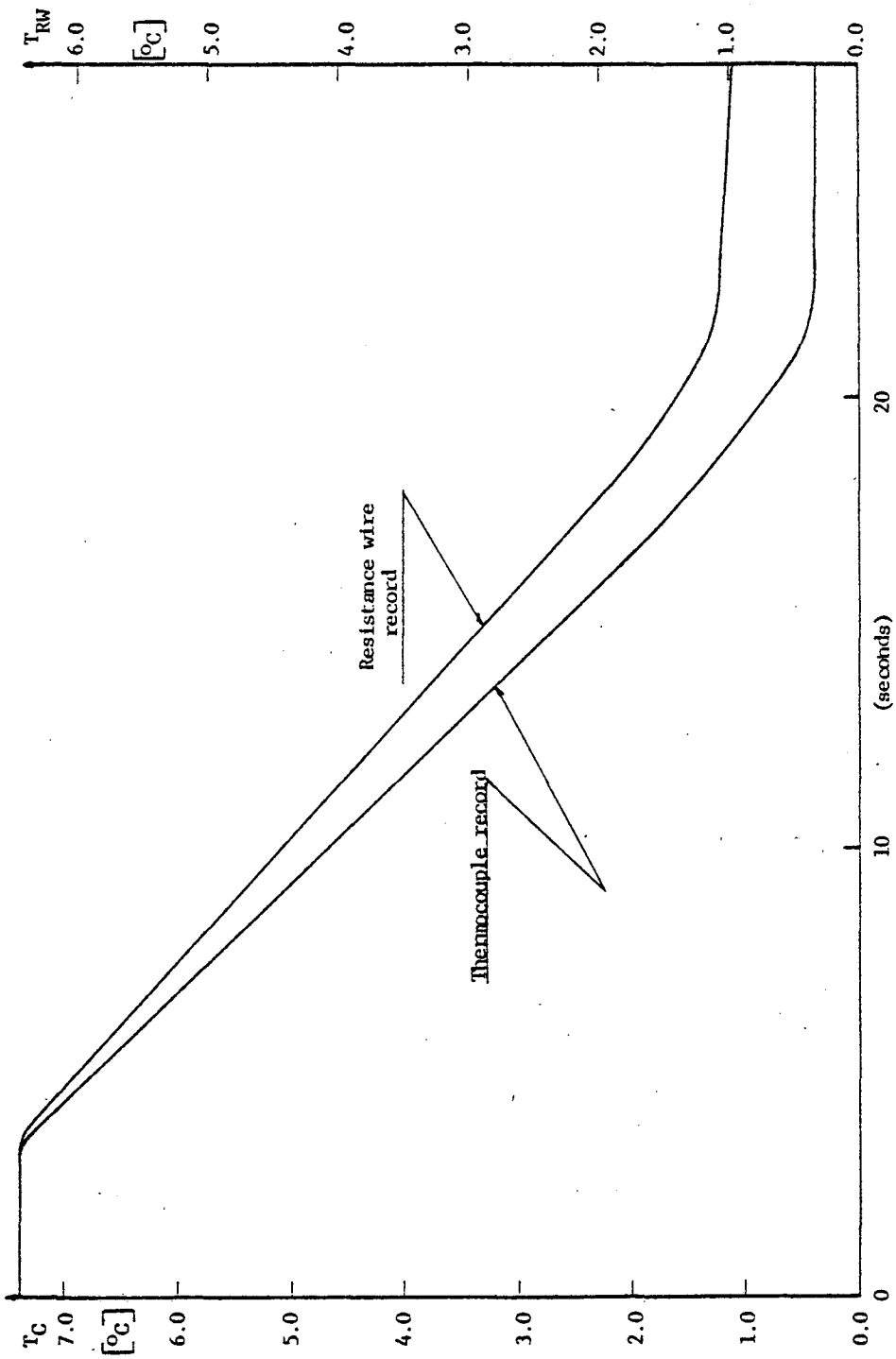

Figure A4.2 - Typical records of resistance wire and thermocouple through a constant gradient medium.

APPENDIX A-5

NUMERICAL VALUES OF THE CALCULATED CENTRAL MOMENTS

All the data used to compute the central moments are related in Table 6 with the specification of the main parameters of the runs, tag word 1, number of runs and tape in which it is recorded. The mean temperature is the temporal mean during the whole set of runs for a certain condition. Close to the lower plate (up to $z/z_* = 0.10$), the temporal mean was added to half of the total spatial mean temperature drop to produce the mean temperature.

Tables 7 and 8 present the numerical values of the moments resulting from ensemble averaging the spatial averages of the independent runs and scaling them with respect to the convection scales and to the RMS values respectively.

Table 9 presents the standard deviation of all the spatial means of one set.

Table 6

Main Characteristics of the Runs

Tap Name	Tag Word 1 Octal	Tag Word 1 Decimal	Number of runs	Heat Flux-Q_0 [°K cm/s]	Mean Temp. [°C]	z^* [mm]	z [mm]
100004	151611	54153	11	0.0330	32.50	200	19.0
	151612	54154	13	0.0568	38.50	200	19.0
	152301	54465	12	0.0330	35.00	200	35.0
	152302	54466	14	0.0568	39.50	200	35.0
	153201	54913	19	0.0330	37.00	200	47.5
	153301	54977	14	0.0330	33.00	200	60.0
	153302	54978	14	0.0568	39.50	200	60.0
	153401	55041	13	0.0330	34.00	200	80.5
	153402	55042	15	0.0568	39.00	200	80.5
	153501	55105	12	0.0330	31.00	200	100.5
	153502	55106	12	0.0568	36.00	200	100.5
	153503	55107	14	0.0568	39.00	200	111.0
100005	152001	54273	12	0.0330	32.50	200	12.0
	152002	54274	15	0.0568	38.50	200	12.0
	152101	54337	13	0.0330	32.50	200	15.0
	152102	54338	15	0.0568	38.25	200	15.0
	152201	54401	14	0.0330	34.25	200	27.5
	152202	54402	15	0.0568	39.50	200	27.5
	153601	55169	13	0.0330	33.50	200	126.5
	153602	55170	15	0.0568	39.50	200	126.5
	153701	55233	14	0.0330	32.50	200	144.5
	153702	55234	13	0.0568	37.00	200	144.5
100007	100601	33153	14	0.0330	33.00	200	5.5
	100602	33154	16	0.0568	38.00	200	5.5
	100701	33217	12	0.0153	31.50	200	6.0
	100702	33218	14	0.0153	33.00	200	3.5
	100703	33219	14	0.0330	36.50	200	3.5
	100704	33220	15	0.0568	42.15	200	3.5
	101101	33345	14	0.0153	27.75	200	10.0
	101102	33346	14	0.0153	28.15	200	16.5
	101103	33347	14	0.0153	29.65	200	23.0
	101104	33348	13	0.0153	31.25	200	33.0
	101105	33349	15	0.0153	32.75	200	40.5
	101106	33350	14	0.0153	34.25	200	53.5
	101107	33351	14	0.0153	36.00	200	66.0
	101110	33352	16	0.0153	37.75	200	76.0
	101201	33409	14	0.0153	33.50	200	90.0
	101202	33410	14	0.0153	35.75	200	105.0
	101203	33411	14	0.0153	38.00	200	115.0
	101204	33412	14	0.0153	40.25	200	130.0
	101205	33413	16	0.0153	41.75	200	140.0

Table 6 (cont.)

Tape Name	Tag Word 1 Octal	Tag Word 1 Decimal	Number of runs	Heat Flux [°K cm/s]	Mean Temp. [°C]	z* [mm]	z [mm]
100010	112601	38273	15	0.0450	34.55	150	21.0
	112602	38274	15	0.0450	39.40	150	16.0
	112701	38337	13	0.0450	35.00	150	10.0
	112703	38339	17	0.0450	40.25	150	6.5
	113001	38401	14	0.0450	34.35	150	29.0
	113002	38402	15	0.0450	37.85	150	36.5
	113101	38465	14	0.0450	33.25	150	49.0
	113102	38466	14	0.0450	36.75	150	56.5
	113103	38467	15	0.0450	40.50	150	64.0
	113201	38529	11	0.0450	37.25	150	74.5
	113202	38530	15	0.0450	40.60	150	82.0
100011	113601	38785	14	0.0450	38.75	150	90.0
	113701	38849	13	0.0450	36.50	150	100.0
	114001	38913	14	0.0450	37.00	150	105.0
	114002	38914	15	0.0450	40.50	150	112.5
	114101	38977	13	0.0450	33.60	150	120.5
	114102	38978	14	0.0450	36.60	150	127.5
	114103	38979	14	0.0450	40.50	150	135.0
100012	115301	39617	14	0.0450	23.50	150	141.0
	115302	39618	15	0.0450	26.50	150	141.0
	115401	39681	13	0.0153	26.75	200	141.0
	115402	39682	15	0.0330	31.00	200	146.0
	115403	39683	15	0.0568	35.25	200	151.0
	115404	39684	15	0.0568	38.35	200	155.5
	115501	39745	14	0.0153	30.75	200	155.5
	115502	39746	15	0.0330	34.00	200	160.5
	115503	39747	15	0.0330	36.75	200	166.0
	115504	39748	15	0.0568	41.00	200	171.0
	115601	39809	14	0.0153	31.15	200	173.5
	115602	39810	15	0.0330	34.75	200	178.5
	115603	39811	15	0.0568	40.75	200	183.5
	115701	39873	14	0.0153	33.75	200	187.0
	115702	39874	14	0.0330	36.50	200	189.5
	115703	39875	15	0.0568	40.30	200	192.0
100013	117701	40897	15	0.0141	26.00	120	102.0
	117702	40898	16	0.0141	34.75	120	80.0
	117703	40899	14	0.0141	37.20	120	59.0
	120001	40961	15	0.0141	35.25	120	59.0
	120002	40962	16	0.0141	38.15	120	38.0
	120003	40963	16	0.0141	39.85	120	25.0
	120101	41025	15	0.0141	33.00	120	14.0
	120102	41026	16	0.0141	35.50	120	9.0
	120103	41027	16	0.0141	37.75	120	5.5
	120201	41090	16	0.0330	39.90	200	21.0
	120202	41153	15	0.0330	32.70	200	21.0

Table 7

Central Moments Scaled by Convective Scales
Condition I: $z^* = 20cm$, $Q_0 = 0.0153$ °K cm/s

z/z_*	σ_w/w_*	σ_θ/θ_*	σ_u/w_*	$\overline{w\theta}/Q_0$	$\overline{w^3}/w_*^3$	$\overline{u^3}/w_*^3$	$\overline{uw}/w_*^2$	$\overline{u\theta}/Q_0$	$\overline{w^4}/w_*^4$	$\overline{u^4}/w_*^4$	$\overline{w^2\theta}/w_*Q_0$	$\overline{w\theta^2}/\theta_*Q_0$	$\overline{u^2w}/w_*^3$
0.0175	0.288	6.76	0.580	0.808	0.004	-0.006	-0.001	0.010	0.022	0.321	0.182	9.70	-0.004
0.0300	0.292	5.30	0.639	0.763	0.008	0.056	-0.001	-0.163	0.024	0.437	0.212	8.08	-0.005
0.050	0.388	4.12	0.659	0.634	0.021	-0.044	-0.003	-0.180	0.068	0.492	0.273	7.02	0.002
0.0825	0.476	3.01	0.630	0.566	0.010	-0.032	-0.014	-0.058	0.160	0.396	0.187	3.49	0.006
0.115	0.551	3.03	0.546	0.754	0.046	0.018	-0.058	-0.185	0.249	0.252	0.375	5.20	0.012
0.165	0.572	2.25	0.469	0.445	0.061	-0.007	-0.019	-0.071	0.307	0.140	0.271	2.34	0.010
0.2025	0.555	2.20	0.554	0.466	0.059	0.002	-0.080	0.029	0.284	0.281	0.305	2.10	0.020
0.2675	0.637	1.99	0.534	0.622	0.145	-0.024	-0.046	0.652	0.478	0.261	0.422	2.17	0.006
0.330	0.593	1.89	0.562	0.437	0.103	-0.010	-0.083	-0.018	0.386	0.299	0.260	1.66	-0.001
0.380	0.642	1.62	0.544	0.443	0.113	0.002	-0.102	-0.012	0.492	0.262	0.248	1.22	0.013
0.450	0.578	1.30	0.603	0.273	0.126	-0.009	-0.050	0.067	0.418	0.343	0.184	0.65	0.019
0.525	0.596	1.24	0.577	0.147	0.086	-0.042	-0.093	0.090	0.381	0.324	0.042	0.12	0.008
0.575	0.582	1.40	0.720	0.248	0.059	-0.094	-0.068	0.137	0.425	0.722	0.048	0.14	-0.014
0.650	0.613	1.33	0.705	0.171	0.097	-0.034	-0.103	0.249	0.437	0.614	0.046	0.21	-0.012
0.700	0.489	1.57	0.620	0.065	0.030	-0.018	-0.077	0.191	0.207	0.355	0.008	-0.13	-0.001
0.705	0.536	1.02	0.574	0.176	0.065	0.026	-0.038	-0.029	0.269	0.324	0.042	0.05	0.007
0.780	0.528	1.15	0.700	0.144	0.090	-0.089	0.027	0.269	0.371	0.581	0.033	-0.03	-0.016
0.870	0.439	1.23	0.705	0.107	0.046	-0.039	0.007	-0.110	0.164	0.630	0.078	0.05	-0.001
0.935	0.258	1.21	0.644	0.033	0.003	0.005	0.021	0.012	0.017	0.456	0.006	-0.01	0.003

Table 7 (Cont.)

Central Moments Scaled by Convective Scales
Condition II: $z^* = 20$ cm, $Q_0 = 0.0330$ °K cm/s

z/z_*	σ_w/w_*	σ_θ/θ_*	σ_u/w_*	$\overline{w\theta}/Q_0$	$\overline{w^3}/w_*^3$	$\overline{u^3}/w_*^3$	$\overline{uw}/w_*^2$	$\overline{u\theta}/Q_0$	$\overline{w^4}/w_*^4$	$\overline{u^4}/w_*^4$	$\overline{w^2\theta}/w_*Q_0$	$\overline{w\theta^2}/\theta_*Q_0$	$\overline{u^2w}/w_*^3$
0.0175	0.269	6.32	0.527	0.725	0.006	0.016	-0.005	-0.090	0.019	0.232	0.175	8.97	0.000
0.0275	0.310	5.10	0.628	0.651	0.012	-0.030	0.019	-0.042	0.037	0.418	0.190	7.65	-0.003
0.0600	0.485	3.33	0.640	0.699	0.034	-0.055	0.004	-0.290	0.162	0.494	0.312	5.36	0.006
0.0750	0.511	2.90	0.578	0.574	0.025	-0.057	0.002	-0.035	0.180	0.402	0.206	3.75	-0.007
0.0950	0.521	2.76	0.566	0.519	0.023	-0.070	0.003	-0.024	0.186	0.341	0.249	3.67	0.017
0.134	0.595	2.31	0.574	0.716	0.104	0.012	0.051	-0.039	0.371	0.333	0.417	3.39	0.019
0.175	0.572	1.91	0.572	0.414	0.025	-0.025	0.070	-0.183	0.317	0.303	0.254	1.55	0.004
0.238	0.598	1.97	0.569	0.523	0.077	0.018	-0.013	-0.066	0.360	0.295	0.267	1.96	0.025
0.300	0.680	1.50	0.581	0.471	0.152	0.048	-0.020	-0.086	0.613	0.365	0.307	1.44	0.008
0.402	0.603	1.14	0.618	0.300	0.174	0.026	-0.015	0.017	0.529	0.401	0.212	0.75	-0.011
0.500	0.635	1.11	0.557	0.317	0.164	0.003	-0.050	-0.095	0.510	0.249	0.244	0.61	0.028
0.632	0.501	0.94	0.600	0.174	0.091	-0.017	-0.017	0.003	0.248	0.359	0.070	0.11	0.009
0.722	0.591	0.96	0.608	0.161	0.127	-0.002	0.009	0.023	0.429	0.365	0.101	0.17	-0.031
0.730	0.591	1.01	0.648	0.164	0.143	-0.001	0.065	-0.043	0.408	0.408	0.105	0.27	-0.006
0.800	0.428	0.96	0.572	0.023	0.025	-0.062	-0.040	0.162	0.120	0.340	-0.049	0.01	0.013
0.830	0.447	1.41	0.715	0.063	0.019	-0.028	-0.040	0.206	0.135	0.680	-0.029	-0.02	-0.014
0.890	0.380	0.95	0.640	0.033	0.020	-0.055	-0.024	0.138	0.082	0.454	0.003	0.02	0.019
0.950	0.217	1.29	0.542	0.026	0.004	-0.034	-0.004	0.151	0.010	0.224	-0.005	-0.04	0.000

Table 7 (Cont.)

Central Moments Scaled by Convective Scales
Condition III: $z^* = 20$ cm, $Q_0 = 0.0568$ °K cm/s

z/z_*	σ_w/w_*	σ_θ/θ_*	σ_u/w_*	$\overline{w\theta}/Q_0$	$\overline{w^3}/w_*^3$	$\overline{u^3}/w_*^3$	$\overline{uw}/w_*^2$	$\overline{u\theta}/Q_0$	$\overline{w^4}/w_*^4$	$\overline{u^4}/w_*^4$	$\overline{w^2\theta}/w_*Q_0$	$\overline{w\theta^2}/\theta_*Q_0$	$\overline{u^2w}/w_*^3$
0.0175	0.289	5.92	0.542	0.606	0.011	0.032	0.014	0.002	0.035	0.251	0.087	5.51	0.002
0.0275	0.338	4.53	0.643	0.556	0.009	0.047	0.014	-0.130	0.057	0.488	0.129	5.22	0.048
0.060	0.477	3.41	0.639	0.625	0.017	-0.006	0.038	0.024	0.165	0.438	0.236	4.57	-0.006
0.075	0.458	3.27	0.561	0.556	0.009	-0.025	0.033	0.033	0.132	0.286	0.181	3.64	-0.010
0.095	0.532	3.00	0.605	0.692	0.029	-0.034	-0.012	-0.196	0.214	0.390	0.238	4.16	0.022
0.134	0.589	2.58	0.598	0.642	0.029	-0.031	0.082	0.052	0.333	0.373	0.293	3.27	0.006
0.175	0.618	2.04	0.568	0.405	0.013	-0.003	0.039	-0.077	0.390	0.311	0.274	1.71	-0.006
0.300	0.641	1.53	0.536	0.377	0.099	0.014	0.084	0.034	0.427	0.301	0.217	0.95	0.011
0.402	0.617	1.20	0.550	0.282	0.030	-0.002	-0.055	-0.122	0.403	0.262	0.104	0.50	0.009
0.500	0.597	0.96	0.523	0.225	0.105	0.023	0.007	0.020	0.385	0.199	0.154	0.37	-0.007
0.550	0.573	1.06	0.548	0.178	0.075	-0.008	-0.060	0.041	0.336	0.245	0.085	0.22	0.027
0.632	0.544	1.22	0.523	0.270	0.147	0.018	0.049	-0.071	0.376	0.207	0.112	0.45	0.021
0.722	0.469	0.92	0.664	0.094	0.037	-0.044	-0.026	0.195	0.162	0.544	0.032	0.06	0.008
0.755	0.582	0.99	0.685	0.119	0.099	0.052	0.043	-0.126	0.402	0.583	0.086	0.16	-0.015
0.780	0.615	1.03	0.710	0.113	0.108	0.051	0.065	-0.089	0.479	0.608	0.013	-0.01	-0.018
0.855	0.427	1.11	0.613	0.075	0.062	0.003	-0.035	0.052	0.141	0.350	0.010	0.01	0.012
0.920	0.307	1.06	0.593	0.064	0.011	-0.127	0.003	0.123	0.039	0.441	0.018	0.01	-0.005
0.960	0.164	1.23	0.533	0.057	0.001	-0.001	0.010	0.207	0.005	0.234	0.001	-0.01	0.001

Table 7 (cont.)

Central Moments Scaled by Convective Scales
Condition IV: $z^* = 15$ cm, $Q_0 = 0.0450$ °K cm/s

z/z_*	σ_w/w_*	σ_θ/θ_*	σ_u/w_*	$\overline{w\theta}/Q_0$	$\overline{w^3}/w_*^3$	$\overline{u^3}/w_*^3$	$\overline{uw}/w_*^2$	$\overline{u\theta}/Q_0$	$\overline{w^4}/w_*^4$	$\overline{u^4}/w_*^4$	$\overline{w^2\theta}/w_*Q_0$	$\overline{\theta^2 w}/\theta_*Q_0$	$\overline{u^2 w}/w_*^3$
0.043	0.430	3.94	0.596	0.643	0.012	-0.013	0.002	-0.089	0.127	0.397	0.385	6.14	-0.012
0.067	0.506	3.63	0.588	0.810	0.024	0.028	-0.004	-0.074	0.175	0.308	0.325	5.99	0.006
0.107	0.573	3.14	0.641	0.760	0.057	0.092	-0.028	0.198	0.138	0.510	0.335	4.32	0.006
0.140	0.614	2.25	0.578	0.646	0.061	0.034	-0.062	-0.181	0.373	0.284	0.300	2.51	0.013
0.193	0.618	1.96	0.608	0.532	0.127	0.000	-0.002	-0.0178	0.466	0.330	0.391	1.66	0.020
0.243	0.655	1.92	0.587	0.595	0.110	0.032	-0.070	-0.078	0.523	0.355	0.347	1.40	-0.010
0.327	0.713	1.54	0.528	0.573	0.215	0.009	-0.069	-0.011	0.754	0.224	0.471	1.46	0.012
0.377	0.628	1.68	0.617	0.458	0.098	-0.006	-0.057	-0.038	0.465	0.391	0.235	0.91	0.043
0.427	0.693	1.61	0.634	0.508	0.107	-0.060	-0.107	0.101	0.609	0.491	0.259	1.01	0.019
0.500	0.685	1.21	0.580	0.247	0.120	-0.046	-0.093	0.000	0.619	0.369	0.027	0.18	0.034
0.547	0.584	1.24	0.655	0.084	0.077	0.011	-0.098	0.106	0.364	0.513	0.125	0.19	0.006
0.600	0.664	1.29	0.624	0.209	0.175	-0.049	-0.076	0.032	0.640	0.448	0.277	0.54	0.019
0.667	0.582	1.16	0.654	0.154	0.130	0.047	-0.067	0.034	0.431	0.571	0.085	0.08	0.029
0.700	0.565	1.09	0.623	0.217	0.116	-0.008	-0.033	0.049	0.387	0.410	0.102	0.27	-0.010
0.750	0.451	1.08	0.620	0.084	0.044	-0.082	-0.025	0.054	0.154	0.457	0.014	-0.05	0.029
0.800	0.440	1.15	0.711	0.148	0.023	-0.107	0.026	0.319	0.125	0.652	-0.005	-0.02	-0.011
0.850	0.426	1.15	0.611	0.033	0.050	-0.070	-0.022	-0.076	0.132	0.374	0.018	0.01	0.003
0.900	0.414	1.41	0.775	0.082	0.039	-0.133	-0.025	0.109	0.116	1.095	0.053	0.03	0.011
0.940	0.242	1.26	0.652	0.072	0.010	-0.006	0.018	0.216	0.026	0.586	0.018	0.02	0.001

Table 7 (Cont.)

Central Moments Scaled by Convective Scales
Condition V: $z^* = 12$ cm, $Q_0 = 0.0141$ °K cm/s

z/z_*	σ_w/w_*	σ_θ/θ_*	σ_u/w_*	$\overline{w\theta}/Q_0$	$\overline{w^3}/w_*^3$	$\overline{u^3}/w_*^3$	$\overline{uw}/w_*^2$	$\overline{u\theta}/Q_0$	$\overline{w^4}/w_*^4$	$\overline{u^4}/w_*^4$	$\overline{w^2\theta}/w_*Q_0$	$\overline{\theta^2 w}/\theta_* Q_0$	$\overline{u^2 w}/w_*^3$
0.050	0.389	4.97	0.644	0.945	0.017	0.032	0.011	0.092	0.076	0.480	0.426	10.57	-0.004
0.075	0.520	3.79	0.658	0.981	0.030	-0.015	0.011	-0.130	0.218	0.574	0.500	7.32	-0.004
0.117	0.582	2.85	0.580	0.818	0.081	0.022	-0.025	-0.050	0.323	0.325	0.550	5.37	0.030
0.208	0.627	2.52	0.519	0.658	0.074	0.021	-0.065	-0.037	0.477	0.216	0.499	3.17	-0.009
0.317	0.667	2.00	0.590	0.480	0.119	-0.004	-0.071	0.177	0.576	0.334	0.327	1.59	0.007
0.495	0.635	2.05	0.666	0.424	0.149	0.008	-0.110	-0.026	0.574	0.510	0.232	0.73	-0.005
0.667	0.590	1.52	0.585	0.105	0.142	-0.070	-0.060	-0.075	0.471	0.350	0.098	0.24	0.028
0.850	0.382	1.42	0.727	0.119	0.016	-0.138	-0.025	0.214	0.086	0.676	0.048	0.00	0.010

Table 8

Central Moments Scaled by RMS Values
Condition I: $z^* = 20$ cm, $Q_0 = 0.0153$ °K cm/s

z/z_*	$\overline{w\theta}/\sigma_w\sigma_\theta$	$\overline{w^3}/\sigma_w^3$	$\overline{\theta^3}/\sigma_\theta^3$	$\overline{u^3}/\sigma_u^3$	$\overline{uw}/\sigma_u\sigma_w$	$\overline{u\theta}/\sigma_u\sigma_\theta$	$\overline{w^4}/\sigma_w^4$	$\overline{\theta^4}/\sigma_\theta^4$	$\overline{u^4}/\sigma_u^4$	$\overline{w^2\theta}/\sigma_w^2\sigma_\theta$	$\overline{w\theta^2}/\sigma_w\sigma_\theta^2$	$\overline{u^2w}/\sigma_u^2\sigma_w$
0.0175	0.412	0.169	2.06	-0.033	-0.005	0.003	3.27	7.46	2.82	0.325	0.738	-0.044
0.030	0.492	0.317	2.34	0.216	-0.003	-0.048	3.30	8.82	2.61	0.467	0.982	-0.044
0.050	0.396	0.363	3.18	-0.153	-0.013	-0.066	3.00	15.12	2.60	0.440	1.065	0.0137
0.0825	0.395	0.090	2.32	-0.127	-0.047	-0.031	3.13	11.44	2.51	0.274	0.811	0.0336
0.115	0.452	0.276	2.84	0.112	-0.191	-0.112	2.69	14.53	2.83	0.408	1.030	0.075
0.165	0.346	0.323	1.85	-0.064	-0.072	-0.067	2.86	9.11	2.89	0.368	0.807	0.078
0.2025	0.382	0.344	1.92	0.011	-0.259	0.024	2.99	11.56	2.97	0.450	0.785	0.120
0.2675	0.491	0.561	1.68	-0.156	-0.136	0.061	2.90	7.99	3.20	0.522	0.862	0.035
0.330	0.390	0.497	1.50	-0.054	-0.249	-0.017	3.12	6.64	3.00	0.392	0.785	-0.0036
0.380	0.425	0.427	1.15	0.011	-0.293	-0.013	2.90	4.80	2.98	0.371	0.724	0.070
0.450	0.363	0.652	1.32	-0.043	-0.144	0.086	3.73	7.49	2.59	0.424	0.669	0.089
0.525	0.199	0.407	0.60	-0.217	-0.272	0.126	3.02	4.29	2.91	0.094	0.136	0.039
0.572	0.304	0.299	0.11	-0.252	-0.163	0.136	3.71	3.12	2.69	0.102	0.122	-0.046
0.650	0.209	0.422	0.37	-0.098	-0.239	0.264	3.10	3.92	2.48	0.091	0.192	-0.040
0.700	0.085	0.253	0.58	-0.077	-0.253	0.197	3.61	3.80	2.40	0.022	-0.106	-0.005
0.705	0.324	0.420	0.09	0.137	-0.125	-0.050	3.26	2.90	2.98	0.145	0.085	0.041
0.780	0.237	0.608	0.27	-0.260	0.073	0.334	4.78	3.18	2.42	0.104	-0.040	-0.061
0.870	0.199	0.543	-0.17	-0.110	0.022	-0.127	4.42	3.85	2.54	0.330	0.078	-0.003
0.935	0.107	0.192	-0.08	-0.017	0.128	0.015	3.76	3.00	2.66	0.074	-0.037	0.025

Table 8 (Cont.)

Central Moments Scaled by RMS Values
Condition II: $z^* = 20$ cm, $Q_0 = 0.0330$ °K cm/s

z/z_*	$\overline{w\theta}/\sigma_w\sigma_\theta$	$\overline{w^3}/\sigma_w^3$	$\overline{\theta^3}/\sigma_\theta^3$	$\overline{u^3}/\sigma_u^3$	$\overline{uw}/\sigma_u\sigma_w$	$\overline{u\theta}/\sigma_u\sigma_\theta$	$\overline{w^4}/\sigma_w^4$	$\overline{\theta^4}/\sigma_\theta^4$	$\overline{u^4}/\sigma_u^4$	$\overline{w^2\theta}/\sigma_w^2\sigma_\theta$	$\overline{w\theta^2}/\sigma_w\sigma_\theta^2$	$\overline{u^2w}/\sigma_u^2\sigma_w$
0.0175	0.426	0.316	2.23	0.111	-0.033	-0.027	3.54	8.61	3.02	0.381	0.836	0.005
0.0275	0.412	0.396	2.55	-0.120	0.097	-0.013	3.98	10.15	2.69	0.387	0.950	-0.026
0.060	0.434	0.296	2.85	-0.208	0.013	-0.136	2.94	14.06	2.93	0.399	1.000	0.031
0.075	0.387	0.186	2.67	-0.294	-0.008	-0.021	2.63	11.91	3.61	0.273	0.873	-0.038
0.095	0.362	0.159	2.61	-0.388	0.012	-0.015	2.52	12.65	3.32	0.332	0.928	0.104
0.134	0.520	0.494	2.53	0.061	0.149	-0.029	2.96	11.76	3.06	0.510	1.064	0.097
0.175	0.379	0.132	1.72	-0.134	0.213	-0.167	2.98	8.31	2.84	0.356	0.740	0.022
0.238	0.443	0.358	1.95	0.098	-0.038	-0.059	2.81	11.15	2.82	0.379	0.842	0.129
0.300	0.462	0.483	2.10	-0.246	-0.050	-0.099	2.87	9.28	3.19	0.444	0.945	0.036
0.402	0.435	0.791	1.89	0.111	-0.040	0.024	3.99	9.80	2.75	0.511	0.956	-0.048
0.500	0.499	0.641	1.40	0.015	-0.142	-0.153	3.13	6.56	2.59	0.546	0.781	0.142
0.632	0.369	0.720	0.48	-0.077	-0.057	0.005	3.94	3.64	2.77	0.296	0.250	0.048
0.722	0.285	0.615	0.66	-0.011	0.026	0.040	3.53	4.59	2.68	0.302	0.319	-0.014
0.730	0.273	0.692	0.79	-0.004	0.171	-0.066	3.35	4.89	2.32	0.298	0.453	-0.026
0.800	0.055	0.318	0.28	-0.329	-0.162	0.297	3.59	3.11	3.17	-0.278	0.033	0.092
0.830	0.100	0.217	0.44	-0.078	-0.122	0.205	3.39	3.33	2.60	-0.104	-0.026	-0.060
0.890	0.092	0.365	-0.06	-0.209	-0.100	0.226	3.95	3.08	2.71	0.022	0.062	0.121
0.950	0.081	0.393	-0.38	-0.214	-0.312	0.155	4.63	1.24	2.60	-0.034	-0.059	0.000

Table 8 (Cont.)

Central Moments Scaled by RMS Values
Condition III: $z^* = 20$ cm, $Q_0 = 0.0568$ °K cm/s

z/z_*	$\overline{w\theta}/\sigma_w\sigma_\theta$	$\overline{w^3}/\sigma_w^3$	$\overline{\theta^3}/\sigma_\theta^3$	$\overline{u^3}/\sigma_u^3$	$\overline{uw}/\sigma_u\sigma_w$	$\overline{u\theta}/\sigma_u\sigma_\theta$	$\overline{w^4}/\sigma_w^4$	$\overline{\theta^4}/\sigma_\theta^4$	$\overline{u^4}/\sigma_u^4$	$\overline{w^2\theta}/\sigma_w^2\sigma_\theta$	$\overline{w\theta^2}/\sigma_w\sigma_\theta^2$	$\overline{u^2w}/\sigma_u^2\sigma_w$
0.0175	0.355	0.446	2.06	0.204	0.088	0.001	5.12	8.08	2.91	0.177	0.546	0.026
0.0275	0.363	0.243	2.49	0.178	0.066	-0.044	4.39	10.51	2.85	0.248	0.752	0.034
0.060	0.384	0.153	2.70	-0.025	0.123	0.011	3.17	13.28	2.63	0.304	0.823	-0.030
0.075	0.371	0.091	2.20	-0.014	0.130	0.018	3.00	9.23	2.89	0.264	0.745	-0.074
0.095	0.434	0.195	2.23	-0.153	-0.036	-0.108	2.67	10.75	2.91	0.280	0.868	0.112
0.134	0.422	0.144	2.30	-0.146	0.233	0.033	2.76	11.25	2.92	0.326	0.832	-0.031
0.175	0.323	0.545	1.51	-0.015	0.111	-0.067	2.68	7.56	2.99	0.268	0.667	-0.029
0.300	0.384	0.374	1.26	0.075	0.232	0.039	2.53	7.75	2.94	0.345	0.633	0.055
0.402	0.382	0.129	1.36	-0.012	-0.161	-0.186	2.78	7.53	2.87	0.229	0.571	0.046
0.500	0.392	0.493	1.18	0.159	0.022	0.040	3.04	5.52	2.67	0.449	0.669	-0.042
0.550	0.294	0.400	0.49	-0.050	-0.192	0.071	3.12	4.60	2.72	0.244	0.348	0.157
0.632	0.408	0.916	0.75	0.130	0.173	-0.112	4.30	4.02	2.76	0.534	0.553	0.142
0.722	0.217	0.359	0.21	-0.149	-0.084	0.319	3.33	2.75	2.80	0.160	0.144	0.040
0.755	0.207	0.504	0.53	0.160	0.107	-0.186	3.49	3.40	2.65	0.256	0.286	-0.055
0.780	0.179	0.465	0.27	0.142	0.149	-0.122	3.36	3.73	2.40	0.034	-0.019	-0.060
0.855	0.158	0.792	-0.07	0.013	-0.133	0.076	4.26	3.17	2.48	0.051	0.027	0.077
0.920	0.196	0.386	-0.28	-0.610	0.017	0.195	4.38	3.78	3.57	0.184	0.044	-0.046
0.960	0.282	0.290	-0.29	0.039	0.109	0.317	6.90	2.84	2.91	0.029	-0.055	0.028

Table 8 (Cont.)

Central Moments Scaled by RMS Values
Condition IV: $z^* = 15$ cm, $Q_0 = 0.0450$ °K cm/s

z/z_*	$\overline{w\theta}/\sigma_w\sigma_\theta$	$\overline{w^3}/\sigma_w^3$	$\overline{\theta^3}/\sigma_\theta^3$	$\overline{u^3}/\sigma_u^3$	$\overline{uw}/\sigma_u\sigma_w$	$\overline{u\theta}/\sigma_u\sigma_\theta$	$\overline{w^4}/\sigma_w^4$	$\overline{\theta^4}/\sigma_\theta^4$	$\overline{u^4}/\sigma_u^4$	$\overline{w^2\theta}/\sigma_w^2\sigma_\theta$	$\overline{w\theta^2}/\sigma_w\sigma_\theta^2$	$\overline{u^2w}/\sigma_u^2\sigma_w$
0.043	0.380	0.152	2.13	-0.063	0.007	-0.038	3.74	9.27	3.14	0.530	0.922	-0.082
0.067	0.441	0.188	2.55	0.136	-0.015	-0.035	2.67	10.93	2.57	0.349	0.898	0.034
0.107	0.423	0.301	1.90	0.350	-0.076	0.098	2.95	10.14	3.03	0.325	0.766	0.024
0.140	0.467	0.265	1.85	0.175	-0.175	-0.139	2.62	7.94	2.54	0.353	0.806	0.063
0.193	0.438	0.537	2.10	0.000	0.004	-0.015	3.19	6.59	2.83	0.330	0.696	0.086
0.243	0.473	0.391	1.38	0.156	-0.182	-0.069	2.84	6.47	2.99	0.328	0.579	-0.046
0.327	0.522	0.592	1.66	0.063	-0.182	-0.014	2.92	7.92	2.88	0.602	0.822	0.061
0.377	0.435	0.395	1.03	-0.027	-0.147	-0.037	3.00	4.53	2.69	0.356	0.518	0.178
0.427	0.456	0.322	0.83	-0.237	-0.243	0.100	2.64	5.16	3.03	0.336	0.567	0.067
0.500	0.299	0.374	0.45	-0.236	-0.235	0.000	2.82	4.83	2.47	0.234	0.537	0.147
0.547	0.114	0.369	-0.06	0.040	-0.253	0.131	2.93	2.98	2.80	0.286	0.213	0.025
0.600	0.244	0.598	0.32	-0.203	-0.184	0.040	3.29	4.27	2.95	0.485	0.490	0.074
0.667	0.228	0.661	-0.02	0.168	-0.177	0.045	3.76	3.23	3.11	0.216	0.101	0.115
0.700	0.352	0.642	0.67	-0.031	-0.095	0.073	2.94	4.62	2.72	0.293	0.396	-0.044
0.750	0.171	0.481	-0.22	-0.345	-0.088	0.080	3.72	2.76	3.09	0.065	-0.094	0.168
0.800	0.294	0.267	-0.05	-0.296	0.082	0.391	3.34	2.80	2.55	-0.023	-0.034	-0.048
0.850	0.068	0.642	-0.26	-0.305	-0.083	-0.108	4.01	4.00	2.67	0.085	0.026	0.021
0.900	0.140	0.550	0.01	-0.286	-0.078	0.100	3.95	2.88	3.03	0.217	0.031	0.044
0.940	0.227	0.655	0.01	-0.021	0.107	0.263	3.52	2.93	3.25	0.087	0.057	0.010

Table 8 (Cont.)

Central Moments Scaled by RMS Values
Condition V: $z^* = 12$ cm, $Q_0 = 0.0141$ °K cm/s

z/z_*	$\overline{w\theta}/\sigma_w\sigma_\theta$	$\overline{w^3}/\sigma_w^3$	$\overline{\theta^3}/\sigma_\theta^3$	$\overline{u^3}/\sigma_u^3$	$\overline{uw}/\sigma_u\sigma_w$	$\overline{u\theta}/\sigma_u\sigma_\theta$	$\overline{w^4}/\sigma_w^4$	$\overline{\theta^4}/\sigma_\theta^4$	$\overline{u^4}/\sigma_u^4$	$\overline{w^2\theta}/\sigma_w^2\sigma_\theta$	$\overline{w\theta^2}/\sigma_w\sigma_\theta^2$	$\overline{u^2w}/\sigma_u^2\sigma_w$
0.050	0.489	0.293	2.35	0.120	0.044	0.029	3.35	9.64	2.78	0.567	1.102	-0.027
0.075	0.497	0.215	2.00	-0.053	0.032	-0.052	2.98	8.41	3.06	0.487	0.978	-0.019
0.117	0.493	0.411	2.54	0.115	-0.073	-0.030	2.82	12.20	2.87	0.570	1.135	0.153
0.208	0.415	0.299	1.34	0.148	-0.200	-0.028	3.09	6.40	2.97	0.503	0.794	-0.051
0.317	0.359	0.399	1.01	-0.017	-0.179	0.150	2.91	5.78	2.76	0.367	0.594	0.028
0.495	0.325	0.580	0.42	0.026	-0.260	-0.019	3.53	3.53	2.60	0.280	0.271	-0.018
0.667	0.118	0.691	0.25	-0.350	-0.174	-0.085	3.89	3.20	2.98	0.185	0.178	0.136
0.850	0.210	0.289	-0.011	-0.360	0.089	0.207	4.01	3.16	2.43	0.232	0.005	0.049

Table 9

Standard Deviation of Central Moments
Condition I: $z^* = 20$ cm, $Q_0 = 0.0153$ °K cm/s

z/z^*	$S(\sigma_w/w_*)$	$S(\sigma_\theta/\theta_*)$	$S(\sigma_u/w_*)$	$S(\overline{w\theta}/Q_0)$	$S(\overline{w^3}/w_*^3)$	$S(\overline{u^3}/w_*^3)$	$S(\overline{w^4}/w_*^4)$	$S(\overline{u^4}/w_*^4)$	$S(\overline{w^2\theta}/w_*Q_0)$	$S(\overline{w\theta^2}/\theta_*Q_0)$
0.0175	0.016	0.841	0.093	0.323	0.007	0.232	0.005	0.161	0.144	4.87
0.030	0.035	0.684	0.116	0.198	0.013	0.286	0.009	0.351	0.152	4.08
0.050	0.033	0.961	0.120	0.280	0.032	0.211	0.020	0.325	0.263	5.25
0.0825	0.082	0.585	0.134	0.240	0.097	0.283	0.125	0.311	0.282	3.02
0.115	0.048	0.735	0.091	0.261	0.070	0.175	0.085	0.229	0.271	3.10
0.165	0.046	0.473	0.083	0.238	0.128	0.142	0.078	0.089	0.279	1.44
0.2025	0.063	0.613	0.133	0.306	0.110	0.255	0.137	0.251	0.413	2.58
0.2675	0.119	0.491	0.120	0.400	0.282	0.265	0.292	0.241	0.618	2.93
0.330	0.122	0.391	0.093	0.404	0.249	0.234	0.324	0.191	0.607	2.62
0.380	0.112	0.276	0.118	0.223	0.221	0.241	0.278	0.193	0.275	1.01
0.450	0.134	0.401	0.109	0.299	0.261	0.218	0.449	0.186	0.293	1.10
0.525	0.163	0.290	0.127	0.270	0.281	0.327	0.294	0.330	0.298	0.76
0.575	0.147	0.305	0.166	0.255	0.295	0.685	0.411	0.735	0.318	0.84
0.650	0.130	0.290	0.137	0.273	0.375	0.543	0.384	0.425	0.307	0.95
0.700	0.146	0.603	0.103	0.270	0.099	0.350	0.222	0.182	0.151	0.47
0.705	0.097	0.176	0.123	0.147	0.169	0.236	0.191	0.239	0.164	0.36
0.780	0.149	0.208	0.160	0.177	0.222	0.501	0.494	0.419	0.243	0.40
0.870	0.098	0.291	0.138	0.116	0.108	0.587	0.150	0.485	0.232	0.45
0.935	0.039	0.215	0.162	0.062	0.014	0.390	0.009	0.342	0.042	0.09

Table 9 (Cont.)

Standard Deviation of Central Moments
Condition II: $z^* = 20$ cm, $Q_0 = 0.0330$ °K cm/s

z/z^*	$S(\sigma_w/w_*)$	$S(\sigma_\theta/\theta_*)$	$S(\sigma_u/w_*)$	$S(\overline{w\theta}/Q_0)$	$S(\overline{w^3}/w_*^3)$	$S(\overline{u^3}/w_*^3)$	$S(\overline{w^4}/w_*^4)$	$S(\overline{u^4}/w_*^4)$	$S(\overline{w^2\theta}/w_*Q_0)$	$S(\overline{w\theta^2}/\theta_*Q_0)$
0.0175	0.022	0.968	0.062	0.210	0.097	0.163	0.008	0.124	0.137	4.45
0.0275	0.035	0.865	0.148	0.233	0.020	0.215	0.029	0.335	0.142	3.13
0.060	0.043	0.765	0.140	0.276	0.080	0.233	0.064	0.448	0.324	4.07
0.075	0.050	0.663	0.130	0.220	0.079	0.276	0.066	0.403	0.261	3.21
0.095	0.051	0.612	0.138	0.206	0.108	0.259	0.068	0.373	0.243	2.81
0.134	0.062	0.499	0.103	0.272	0.165	0.145	0.164	0.211	0.402	2.32
0.175	0.076	0.395	0.108	0.159	0.159	0.275	0.172	0.201	0.269	1.31
0.238	0.104	0.462	0.125	0.278	0.229	0.281	0.240	0.220	0.459	2.76
0.300	0.112	0.366	0.085	0.242	0.308	0.271	0.403	0.167	0.158	1.34
0.402	0.124	0.313	0.155	0.228	0.319	0.442	0.478	0.419	0.305	0.92
0.500	0.140	0.244	0.132	0.217	0.313	0.229	0.393	0.171	0.235	0.61
0.632	0.126	0.180	0.126	0.130	0.185	0.308	0.242	0.254	0.186	0.37
0.722	0.146	0.155	0.137	0.184	0.385	0.251	0.512	0.350	0.235	0.55
0.730	0.124	0.242	0.091	0.186	0.228	0.317	0.404	0.203	0.175	0.43
0.800	0.093	0.236	0.151	0.122	0.098	0.297	0.109	0.343	0.118	0.19
0.830	0.081	0.490	0.154	0.113	0.070	0.602	0.097	0.500	0.199	0.32
0.890	0.075	0.230	0.153	0.064	0.057	0.392	0.058	0.386	0.085	0.15
0.950	0.051	0.175	0.103	0.046	0.008	0.198	0.008	0.150	0.032	0.08

Table 9 (Cont.)

Standard Deviation of Central Moments
Condition III: $z^* = 20$ cm, $Q_0 = 0.0568$ °K cm/s

z/z^*	$S(\sigma_w/w_*)$	$S(\sigma_\theta/\theta_*)$	$S(\sigma_u/w_*)$	$S(\overline{w\theta}/Q_0)$	$S(\overline{w^3}/w_*^3)$	$S(\overline{u^3}/w_*^3)$	$S(\overline{w^4}/w_*^4)$	$S(\overline{u^4}/w_*^4)$	$S(\overline{w^2\theta}/w_*Q_0)$	$S(\overline{w\theta^2}/\theta_*Q_0)$
0.0175	0.052	0.696	0.083	0.218	0.028	0.167	0.049	0.168	0.139	3.60
0.0275	0.041	0.605	0.150	0.152	0.025	0.177	0.058	0.452	0.115	2.52
0.060	0.070	0.865	0.162	0.225	0.106	0.269	0.102	0.341	0.326	4.15
0.075	0.062	0.530	0.082	0.186	0.058	0.200	0.065	0.171	0.165	2.10
0.095	0.061	0.517	0.132	0.258	0.072	0.208	0.105	0.346	0.287	2.78
0.134	0.074	0.536	0.112	0.264	0.150	0.253	0.140	0.270	0.324	2.27
0.175	0.106	0.467	0.114	0.332	0.229	0.208	0.207	0.207	0.388	1.86
0.300	0.105	0.472	0.101	0.270	0.232	0.251	0.210	0.193	0.440	1.48
0.402	0.106	0.265	0.098	0.200	0.235	0.184	0.288	0.214	0.200	0.74
0.500	0.118	0.227	0.085	0.185	0.219	0.160	0.284	0.115	0.225	0.41
0.550	0.116	0.230	0.116	0.218	0.236	0.253	0.268	0.203	0.286	0.53
0.632	0.165	0.291	0.085	0.247	0.285	0.146	0.560	0.114	0.436	1.00
0.722	0.097	0.168	0.165	0.174	0.113	0.335	0.100	0.456	0.129	0.24
0.755	0.154	0.185	0.194	0.135	0.251	0.580	0.336	0.476	0.189	0.44
0.780	0.119	0.268	0.128	0.171	0.277	0.365	0.393	0.369	0.233	0.38
0.855	0.154	0.299	0.136	0.130	0.191	0.361	0.255	0.268	0.108	0.26
0.920	0.074	0.254	0.165	0.070	0.025	0.350	0.045	0.476	0.066	0.19
0.960	0.049	0.271	0.147	0.037	0.003	0.180	0.011	0.258	0.024	0.12

Table 9 (Cont.)

Standard Deviation of Central Moments
Condition IV: $z^* = 20$ cm, $Q_0 = 0.0450$ °K cm/s

z/z^*	$S(\sigma_w/w_*)$	$S(\sigma_\theta/\theta_*)$	$S(\sigma_u/w_*)$	$S(\overline{w\theta}/Q_0)$	$S(\overline{w^3}/w_*^3)$	$S(\overline{u^3}/w_*^3)$	$S(\overline{w^4}/w_*^4)$	$S(\overline{u^4}/w_*^4)$	$S(\overline{w^2\theta}/w_*Q_0)$	$S(\overline{w\theta^2}/\theta_*Q_0)$
0.043	0.032	0.734	0.100	0.253	0.054	0.251	0.045	0.273	0.257	3.80
0.067	0.053	0.777	0.100	0.267	0.040	0.274	0.064	0.200	0.210	3.28
0.107	0.065	0.595	0.127	0.380	0.163	0.377	0.212	0.328	0.494	4.35
0.140	0.076	0.392	0.118	0.224	0.156	0.213	0.149	0.167	0.342	1.77
0.193	0.120	0.402	0.071	0.305	0.171	0.247	0.398	0.136	0.461	1.71
0.243	0.064	0.259	0.095	0.222	0.196	0.273	0.227	0.225	0.289	1.11
0.327	0.124	0.269	0.076	0.353	0.410	0.200	0.496	0.136	0.637	1.59
0.377	0.106	0.593	0.118	0.307	0.187	0.325	0.268	0.212	0.608	1.86
0.427	0.080	0.410	0.165	0.318	0.436	0.466	0.441	0.551	0.497	1.83
0.500	0.068	0.150	0.102	0.202	0.210	0.287	0.228	0.395	0.325	0.74
0.547	0.088	0.252	0.155	0.210	0.209	0.438	0.226	0.439	0.245	0.33
0.600	0.088	0.254	0.017	0.195	0.217	0.141	0.256	0.195	0.390	0.71
0.667	0.126	0.239	0.174	0.205	0.206	0.526	0.364	0.617	0.305	0.49
0.700	0.108	0.220	0.143	0.175	0.215	0.386	0.381	0.315	0.221	0.39
0.750	0.082	0.311	0.176	0.106	0.064	0.436	0.102	0.473	0.143	0.19
0.800	0.080	0.203	0.174	0.0093	0.081	0.408	0.090	0.640	0.094	0.20
0.850	0.097	0.267	0.127	0.121	0.123	0.352	0.160	0.331	0.112	0.27
0.900	0.105	0.356	0.182	0.118	0.056	0.729	0.104	1.058	0.124	0.22
0.940	0.034	0.215	0.141	0.066	0.011	0.520	0.009	0.653	0.034	0.11

Table 9 (Cont.)

Standard Deviation of Central Moments
Condition V: $z^* = 12$ cm, $Q_0 = 0.0141$ °K cm/s

z/z^*	$s(\sigma_w/w_*)$	$S(\sigma_\theta/\theta_*)$	$S(\sigma_u/w_*)$	$S(\overline{w\theta}/Q_0)$	$S(\overline{w^3}/w_*^3)$	$S(\overline{u^3}/w_*^3)$	$S(\overline{w^4}/w_*^4)$	$S(\overline{u^4}/w_*^4)$	$S(\overline{w^2\theta}/w_*Q_0)$	$S(\overline{w\theta^2}/\theta_*Q_0)$
0.050	0.030	0.840	0.092	0.215	0.018	0.293	0.020	0.222	0.302	5.62
0.075	0.046	0.678	0.201	0.335	0.067	0.271	0.078	0.575	0.550	5.46
0.117	0.046	0.342	0.092	0.235	0.119	0.166	0.102	0.159	0.466	3.36
0.208	0.101	0.571	0.062	0.426	0.154	0.132	0.295	0.096	0.622	3.93
0.317	0.073	0.266	0.095	0.273	0.222	0.219	0.257	0.212	0.529	1.93
0.495	0.122	0.521	0.103	0.433	0.301	0.337	0.564	0.262	0.588	2.20
0.667	0.102	0.307	0.110	0.253	0.227	0.276	0.383	0.282	0.283	0.67
0.850	0.046	0.210	0.118	0.080	0.066	0.360	0.093	0.504	0.113	0.35

VITA

Rogerio Tadeu da Silva Ferreira was born in Lages, Santa Catarina, Brazil, on May 20, 1946. Upon graduation from Colegio Naval in 1964, he entered Escola Naval and in 1968 he changed his major and entered the Universidade Federal de Santa Catarina. He was awarded a Bachelor of Science degree in Mechanical Engineering in 1970. He received his Master of Science degree in Mechanical Engineering from the Universidade Federal de Santa Catarina in 1973.

In 1971 he joined the staff of the Mechanical Engineering Department of the Universidade Federal de Santa Catarina as an assistant professor being promoted to associate professor in 1977.

Since 1975, he has been in a leave of absence from the Universidade Federal de Santa Catarina in order to pursue the Doctor of Philosophy degree in Mechanical Engineering at the University of Illinois, Urbana. He will resume his teaching activities after the completion of the degree.

He currently is a member of the honorary society of Phi Kappa Phi, the American Society of Mechanical Engineering - ASME and the American Society of Heating, Refrigeration and Air Conditioning - ASHRAE.

UNIVERSITY OF ILLINOIS AT URBANA-CHAMPAIGN

THE GRADUATE COLLEGE

September, 1978

WE HEREBY RECOMMEND THAT THE THESIS BY

ROGERIO TADEU DA SILVA FERREIRA

ENTITLED UNSTEADY TURBULENT THERMAL CONVECTION

BE ACCEPTED IN PARTIAL FULFILLMENT OF THE REQUIREMENTS FOR

THE DEGREE OF DOCTOR OF PHILOSOPHY

Ronald J Adrian
Director of Thesis Research

James W. Baughn
Head of Department

Committee on Final Examination†

Barclay G. Jones
Chairman

Ronald J Adrian

Melvin L. Kent

Wilbur M. Phillips

† Required for doctor's degree but not for master's.

O-517